D-A141 658   THE USE OF SATELLITE AND AIRCRAFT SAR TO DETECT AND   1/4
              CHART HAZARDS TO NAVI..(U) ENVIRONMENTAL RESEARCH INST
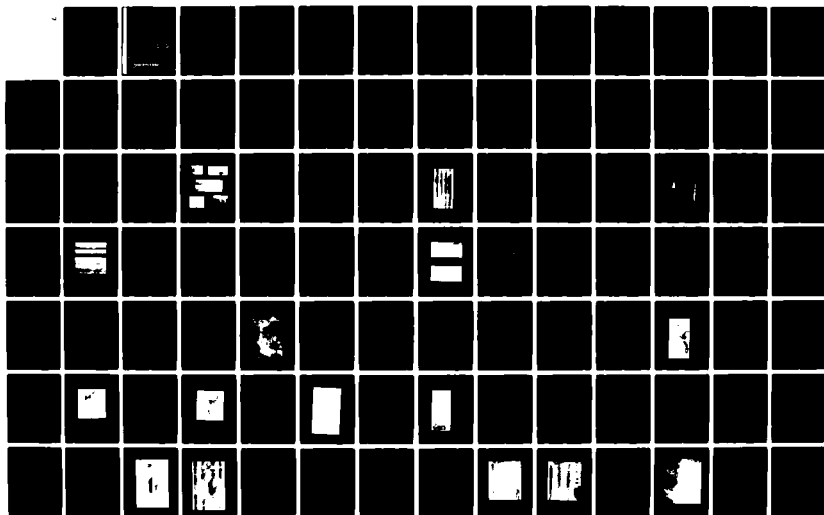   OF MICHIGAN ANN ARBOR RADAR DIV E S KASISCHKE ET AL.
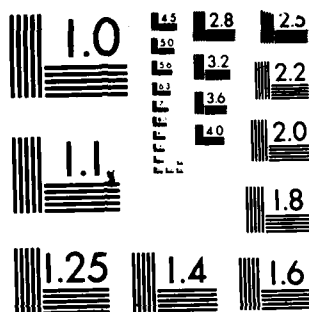UNCLASSIFIED AUG 83 ERIM-163000-2-F N00014-82-C-2308   F/G 8/3   NL

MICROCOPY RESOLUTION TEST CHART
NATIONAL BUREAU OF STANDARDS-1963-A

AD-A141 658

163000-2-F

Final Report

THE USE OF SATELLITE AND AIRCRAFT SAR TO DETECT AND CHART HAZARDS TO NAVIGATION

AUGUST 1983

E.S. KASISCHKE
R.A. SHUCHMAN
J.D. LYDEN
G.A. MEADOWS
D.R. LYZENGA
E.M. JURECKI

Radar Division

DTIC
SELECTED
MAY 3 1 1984

A

ENVIRONMENTAL
RESEARCH INSTITUTE OF MICHIGAN
BOX 8618 ● ANN ARBOR ● MICHIGAN 48107

84 05 29 026

SECURITY CLASSIFICATION OF THIS PAGE *(When Data Entered)*

REPORT DOCUMENTATION PAGE		READ INSTRUCTIONS BEFORE COMPLETING FORM
1 REPORT NUMBER	2. GOVT ACCESSION NO. AD· P141658	3 RECIPIENT'S CATALOG NUMBER
4. TITLE *(and Subtitle)* THE USE OF SATELLITE AND AIRCRAFT SAR TO DETECT AND CHART HAZARDS TO NAVIGATION		5 TYPE OF REPORT & PERIOD COVERED Final Report August 1982 to August 1983
		6. PERFORMING ORG REPORT NUMBER 163000-2-F
7. AUTHOR(s) E.S. Kasischke, R.A. Shuchman, J.D. Lyden, G.A. Meadows, D.R. Lyzenga, E.M. Jurecki		8. CONTRACT OR GRANT NUMBER(s) N00014-82-C-2308
9 PERFORMING ORGANIZATION NAME AND ADDRESS Radar Division, Environmental Research Institute of Michigan, P.O. Box 8618, Ann Arbor, MI 48107		10 PROGRAM ELEMENT PROJECT TASK AREA & WORK UNIT NUMBERS
11 CONTROLLING OFFICE NAME AND ADDRESS Naval Research Laboratory 4555 Overlook Drive Washington, D.C. 20375		12 REPORT DATE August 1983
		13. NUMBER OF PAGES 318
14 MONITORING AGENCY NAME AND ADDRESS *(if different from Controlling Office)*		15 SECURITY CLASS *(of this report)* Unclassified
		15a DECLASSIFICATION/DOWNGRADING SCHEDULE

16 DISTRIBUTION STATEMENT *(of this Report)*

Distribution of this report is unlimited.

17 DISTRIBUTION STATEMENT *(of the abstract entered in Block 20, if different from Report)*

18 SUPPLEMENTARY NOTES

The technical monitor for this project was Mr. Peter A. Mitchell

19 KEY WORDS *(Continue on reverse side if necessary and identify by block number)*

Synthetic Aperture Radar
Bottom Features
Seasat
SIR-A

APD-10
Data Survey
Modeling
Digital Analysis

20. ABSTRACT *(Continue on reverse side if necessary and identify by block number)*

A total survey of Seasat and SIR-A L-band Synthetic Aperture Radar (SAR) imagery for the presence of bottom-related surface patterns was completed. Aircraft X-band SAR data collected by an APD-10 system was also reviewed. Examples from these three SAR systems are presented which further illustrate the types of bottom-related surface patterns which appear on SAR imagery. A comparison of digital SAR image intensities versus depth data demonstrates

DD FORM 1 JAN 73 1473 EDITION OF 1 NOV 65 IS OBSOLETE

SECURITY CLASSIFICATION OF THIS PAGE *(When Data Entered)*

20. ABSTRACT (Continued)

the correlation of the SAR surface patterns to bottom features, and when combined with ancillary envi~onmental data, demonstrates the dependence of SAR surface patterns on the ambient environmental conditions. First order hydrodynamic/electromagnetic models are presented which demonstrate how bottom-related surface patterns appear on SAR images.

PREFACE

The work described in this report was conducted by the Radar Division of the Environmental Research Institute of Michigan. This work was completed under the technical supervision of the Naval Research Laboratory (NRL) under Contract No. N00014-82-C-2308 and was supported by the Defense Mapping Agency and the Naval Ocean Research and Development Activity. The technical monitor for this contract was Peter A. Mitchell.

The Principal Investigators for this project were Eric S. Kasischke and Robert A. Shuchman. Other ERIM scientists who made significant contributions to this report included James D. Lyden, David R. Lyzenga, Susan C. Crane, Elizabeth M. Jurecki, Barbara A. Burns, Jacquelyn S. Ott and Fred J. Tanis. Guy A. Meadows of the University of Michigan, Ann Arbor, Michigan also contributed to this study.

Finally, Dynamics Technology, Inc. (Dynatech), of Torrance, California, supported this research effort through a subcontract to ERIM. Anthony K. Liu and Steven A. Borchardt performed the Dynatech analysis.

iii

ACKNOWLEDGEMENTS

TABLE OF CONTENTS

TABLE OF CONTENTS (CONCLUDED)

LIST OF FIGURES

LIST OF FIGURES (CONTINUED)

LIST OF FIGURES (CONTINUED)

LIST OF FIGURES (CONTINUED)

LIST OF FIGURES (CONCLUDED)

LIST OF TABLES

LIST OF TABLES (CONCLUDED)

THE USE OF SATELLITE AND AIRCRAFT SAR TO DETECT
AND CHART HAZARDS TO NAVIGATION

1
INTRODUCTION

This report presents the results of a continuation of previous research conducted for the Naval Research Laboratory under the sponsorship of the Defense Mapping Agency and the Naval Ocean Research and Development Activity (Kasischke, et al., 1980; 1982). It represents the culmination of a series of studies to evaluate the utility of aircraft and spacecraft synthetic aperture radar (SAR) data for detecting and locating submerged features in shallow and deep water regions which could be hazardous to navigation. These studies were carried out through an examination of data collected by three separate SAR systems. These systems were the Seasat and SIR-A spaceborne (L-band) SARs and the APD-10 aircraft (X-band) SAR.

During the initial investigation of the Seasat SAR imagery, Kasischke, et al. (1980) demonstrated that certain surface patterns present on Seasat SAR imagery occurred over distinct bottom topographic features. This analysis utilized data collected over five study sites during four Seasat passes. Through this investigation, and several others conducted at ERIM (Shuchman, et al., 1979; Shuchman and Kasischke, 1979; 1981), five distinct types of SAR-observed surface patterns were identified which are believed to be bottom related.

During the follow-on study to the initial investigation (see Kasischke, et al., 1982; 1983; Shuchman, et al. 1981; Shuchman, 1982), Seasat SAR imagery collected over nine test sites from 35 orbits were analyzed. The purpose of this study was to further document the occurrence of bottom-related SAR surface patterns as well as to investigate the mechanisms which cause these patterns to appear. It is necessary to understand these mechanisms in order to

understand the limitations of SAR as a hydrographic survey and mapping tool.

In addition, during this study, Seasat SAR data from a deep-water test site were analyzed and a previously unrecognized type of bottom-related surface pattern was identified. Techniques employed in this investigation included several multi-temporal analyses, a multi-sensor analysis and a statistical correlation of digital depth data with digitally recorded SAR image intensity.

The goal of the present study is to define the practical limitations of SAR data for the detection and mapping of bottom features. In order to fulfill this objective, this investigation addresses three major areas. These areas are: (1) a complete survey of all Seasat and SIR-A imagery, as well as available APD-10 X-band data, to determine how frequently depth-related surface patterns appear on SAR imagery; (2) a digital analysis of Seasat SAR imagery, including SAR image intensity versus charted depth comparisons, SAR image intensity versus Landsat comparisons and digital enhancement of Seasat SAR imagery; and (3) the development of first-order theoretical models to provide explanations of the hydrodynamic mechanisms responsible for SAR detection of bottom features.

This report is divided into six chapters, including this introduction. Chapter 2 presents an executive summary which discusses the results of the present analysis and the limitations of SARs for bottom feature detection. Chapter 3 discusses the results of the survey of Seasat, SIR-A and APD-10 SAR imagery, along with discussions of specific test case studies. Chapter 4 describes the results of the digital analyses of the Seasat data. Chapter 5 presents a discussion of possible hydrodynamic mechanisms responsible for the detection of bottom features on SAR imagery. Finally, Chapter 6 presents the conclusions of the longer term DMA/NRL program along with recommendations for future investigations.

Appendix A of this report contains a table which summarizes the complete survey of Seasat SAR imagery. Appendix B contains a copy of the report prepared by Dynamics Technology under sub-contract to ERIM. Appendix C contains copies of one journal and three symposium articles which were based largely on results obtained from the present and past DMA/NRL sponsored investigations.

2
EXECUTIVE SUMMARY

Since the mid-1970s, the Defense Mapping Agency (DMA), the Naval Research Laboratory (NRL) and the Naval Ocean Research and Development Activity (NORDA) have sponsored research to explore the use of remote sensing techniques to aid in updating nautical charts. The goals of using remote sensing in hydrography are, in order of priority:

1. To detect uncharted or mis-positioned submerged features which are potentially hazardous to surface navigation,

2. To define the boundary and location of these hazards in either an absolute or relative sense, and

3. To extract accurate, detailed and complete water depth information.

Early research on the use of remote sensing techniques focused on sensors which detected or measured reflected solar radiation (i.e., aerial photography and multispectral scanners) and on active laser systems. Since the launch of the Seasat satellite in 1978, the research has been expanded to include active microwave sensors, specifically synthetic aperture radar (SAR).

This report presents the results of an investigation on the utility of SAR imagery for detecting and charting of submerged navigation hazards. This investigation is the third in a series of studies sponsored by DMA, NRL, and NORDA on this topic. The overall goal of these studies is to define the practical limitations of SAR as a hydrographic mapping tool.

The microwave energy emitted by a SAR does not penetrate appreciably beyond the water surface; therefore, the surface expressions of bathymetric features observed on SAR imagery are due to surface roughness variations which are caused by a hydrodynamic interaction

5

between the bottom feature and short wavelength, wind-driven surface waves in the 1 to 40 cm wavelength region. Two major classes of ocean processes result in SAR observation of bottom features: (1) gravity waves propagating into shallow water; and (2) ocean currents flowing over distinct bottom features. These processes result in six types of surface patterns on SAR images, as summarized in Table 1.

The research conducted during the past year and discussed in this report can be divided into three major activities: (1) a survey of Seasat, SIR-A and APD-10 SAR imagery, (2) digital processing of Seasat SAR data, and (3) definition of the basic hydrodynamic mechanisms responsible for the bottom-related surface patterns observed on SAR imagery.

A survey of Seasat SAR data was completed during the past year. A total of 212 passes of imagery were examined. This survey revealed that on over 80 percent of the occasions the when Seasat SAR passed over a deep-water bottom feature (i.e., seamount, ridge, shelf, bank or edge of a continental shelf), an associated internal wave or frontal boundary was present on the imagery. For shallow-water features (sand banks, shoals, coral reefs, and bank edges in the Carribean), the correlation rate was approximately 60 percent. Four separate areas were further investigated through test case analyses. Two areas (Cay Sal Bank and Dry Tortugas) were used to further document the occurrence of bottom-related surface patterns on Seasat SAR imagery in shallow-water regions. The third test case study area involved analyzing imagery collected over coral reefs in the Bahamas. Analysis of this study area revealed that bottom-related surface patterns were present less than 30 percent of the occasions when the Seasat SAR imaged a coral reef area. Surface patterns were present only over those reefs located at the edges of banks where a shallow water depth or a tidal current existed. The fourth test case study area was located in the eastern North Atlantic ocean where an

TABLE 1
SUMMARY OF TYPES OF BOTTOM-RELATED SURFACE
PATTERNS ON SEASAT SAR IMAGERY

Surface Pattern Type	Bottom/Ocean Interaction	Bottom Feature	Result on Ocean Surface	Result on SAR Imagery
I	Gravity Wave Propagating into Shallow Water	Gradual Shoaling Shelf (10 to 50 m)	Refraction of Gravity Waves	Change in Gravity Wavelength and Direction of Propagation
II		Sand, Shoal, Shoal Surrounding an Island, Coral Reef (3 to 60 m)	Non-Linear Gravity Wave Interaction	Distinct Change in Radar Backscatter (Change in Image Tone Over Bottom Feature)
III	Current Flowing Over a Bottom Feature	Sand Banks, Large Banks in Bahamas (5 to 40 m)	Change in Current Velocity	Distinct Change in Radar Backscatter (Banded Pattern or Stripe over the Bottom Feature)
IV		Continental Shelf (50 to 100 m)	Generation of Internal Waves in Shallow Water	Internal Waves
V		Deep Water Banks, Shelves, Seamounts, Ridges (100 to 1500 m)	Generation of Internal (Lee) Waves in Deep Water	Internal Waves
VI		Deep Water Banks, Shelves, Seamounts Ridges (100 to 1500 m)	Deep Water Upwelling	Striped Pattern

analysis of Seasat SAR imagery collected over deep-water bottom fea-
tures was conducted. This analysis supported previous research which
revealed a high correlation between the occurrence of internal wave
patterns and deep-water bottom features.

Imagery collected by the Shuttle Imaging Radar-A (SIR-A) were
also examined. All of the passes or data takes (a total of 20) of
imagery were reviewed. The SIR-A SAR's system parameters were opti-
mized for collection of data over land areas. SIR-A's incidence
angle of ~50° resulted in a radar return from the water surface which
was theoretically 15 dB lower than the return using Seasat's 20° in-
cidence angle. Compared with Seasat, SIR-A imagery contained less
dramatic patterns over water areas, and relatively few bottom-related
surface patterns. Several areas where bottom-related surface pat-
terns did occur were studied during the present investigation. These
areas were Crooked Island, Mayaguana Island, the Caicos Islands, the
Tongue of the Ocean, and eastern Australia. Despite the relative
infrequency of these events, the analysis did demonstrate the poten-
tial of using shuttle-based SAR data for detection of submerged nav-
igation hazards.

X-Band SAR imagery, collected by an aircraft-mounted APD-10 sys-
tem during two SAR/oceanography experiments, were also examined.
These two experiments were the Maritime Remote Sensing (MARSEN) ex-
periment, conducted over the Dutch and German coasts of the North
Sea in 1979, and the NRL Remote Sensing Experiment, conducted over
Phelps Bank in the Nantucket Shoals area in 1982. Both data sets
contained surface patterns which were determined to be bottom-
related. The NRL Remote Sensing Experiment imagery was also compared
to Seasat imagery collected over the same region. The bottom-related
surface patterns on the APD-10 (X-band) imagery were found to be
similar in appearance to those observed by the Seasat SAR (L-band)
imagery.

Three separate analyses were conducted on digital Seasat SAR data. Seasat data collected over Cook Inlet, Alaska were cross-correlated to digitally-recorded depth data from the region. Unlike similar previous analyses, low cross-correlations were found (0.50). These low correlations were believed to be due to the environmental conditions present at the time the Seasat SAR data were collected, including low current velocities and high wind speed.

Seasat data collected on two separate dates over the Tongue of the Ocean (TOTO) were compared to Landsat multispectral scanner (MSS) data collected within six weeks of the Seasat data. In this analyses, a digital depth profile was produced using the Landsat MSS data due to the absence of adequate bathymetry data for the TOTO region. Previous analyses have shown that accurate, relative depth profiles from Landsat MSS data can be generated in areas of low turbidity water such as is found in the Bahamas. Although the two Seasat scenes contained similar patterns over the tidal bar belts in the TOTO, a significant difference between the images existed in the form of a tonal reversal between the Seasat images. This reversal is believed to be due to the different current directions at the times the images were collected. Comparisons of the Seasat data to the digital depth profile produced from the MSS data revealed a high cross correlation between depth and radar image intensity for limited areas.

The digital correlations between water depth and radar image intensity performed during the present study reinforce concepts concerning extraction of water depth information from SAR imagery where currents are flowing over bottom features. In these cases, the radar image intensity is dependent on several factors, including the direction and magnitude of the current, the depth of the water over the feature, the ambient gravity wave field, and the magnitude and direction of the surface wind. In developing a hydrodynamic/electromagnetic model to predict radar image intensity as a function of water depth, all these factors must be accounted for.

In the third digital analysis performed during the past year, four speckle reduction algorithms were evaluated for their utility in improving the detectability of SAR-observed ocean surface patterns. A median filter was found to be the best all-around image smoothing algorithm, and a convex hull filter was found to work best for improving the detectability of large-scale surface patterns.

The final area of research pursued during this investigation was the determination of plausible hydrodynamic mechanisms responsible for the appearance of bottom-related surface patterns on SAR imagery. The causes of types I and III surface patterns (see Table 1) were determined during previous studies (see Shuchman and Kasischke, 1981; Kasischke, et al., 1983). The hydrodynamic mechanisms for types II, IV, V and VI surface patterns were determined during the present study. Each type of hydrodynamic mechanism is discussed in detail in Chapter 5 of this report.

Seasat SAR imagery collected during Rev. 762 around North Rona Rock was used in the analysis of the type II surface patterns. The change in radar backscatter over the shoal or sill surrounding North Rona Rock is believed to be caused by the trapping of long wave energy around the island due to the bottom topography at the edge of the shoal or sill.

Both shallow and deep water internal waves were studied using Seasat imagery from Revs. 974 and 762, respectively. Shallow water internal waves (type IV) observed on the U.S. East Coast in the New York Bight region appear to be generated at the edge of the continental shelf by shear flow instability at the bottom of the mixed layer. The internal wave then propagates up onto the shelf until the mixed layer almost intersects the bottom. The SAR-observed features suggest that the internal waves in each packet are probably rank-ordered solitary waves. A two-layer solitary wave model combined with a spectral transport model was used to simulate the ocean structure

10

present when Rev. 974 data were collected. Inputs from this model were used to simulate Seasat SAR imagery of internal waves, and demonstrated the capability to provide a first order description of the internal wave field observed by Seasat during Rev. 974.

The deep-water internal waves (type V) observed during Rev. 762 over the eastern North Atlantic ocean were shown to be generated by a lee wave formation as the diurnal tide flows over the saddle-like valley in the Wyville-Thomson Ridge. Although the generation mechanism is different than for shallow-water internal waves, the hydrodynamic/electromagnetic interaction responsible for the deep water internal waves appearing on Seasat SAR imagery are believed to be the same.

Finally, type VI surface patterns were also explained using imagery collected during Rev. 762. The frontal boundary over the Faeroe Bank Channel appears to be generated by deep-water upwelling. The tidal current *flowing over the* Wyville-Thomson Ridge through another saddle-like valley on the west side of the ridge forces the deep water isotherms up toward the surface. Therefore, the frontal boundary may simply represent a surface intersection of the seasonal thermocline. The mechanism for frontal boundaries appearing on SAR images is possibly due to an interaction of the capillary and ultra-gravity waves with the current shear at the boundary or to the temperature variations between the two water masses.

Studies at ERIM have led to an understanding of the limitations of SAR as a hydrographic mapping tool. There are physical limitations as to when SAR data can be used to detect bottom-related surface patterns. In all cases, a surface wind with a magnitude greater than 1 m/sec must be present in order to generate the small surface waves which are primarily responsible for the radar return from a water surface. In some cases, wind magnitudes above a certain threshold (approximately 8 m/sec) may reduce the chances of detecting

11

bottom-related surface patterns on SAR imagery. In addition, a suitable oceanic disturbance or flow regime must be present, such as a current or gravity wave field. In order to correctly interpret the imagery, the hydrographer should ascertain the ambient environmental conditions at the time of the SAR data collection. The absence of a surface pattern on a SAR image does not always indicate absence of a bottom feature, but may be due to the lack of the favorable environmental conditions necessary to create the SAR observed signature.

The measurement of refracting gravity waves on SAR imagery in some instances can be used to estimate water depth. This method, however, is limited to areas where there is gradually shoaling water, between 15 and 50 meters of depth, and to conditions where the SAR can detect gravity waves.

Gravity wave/bottom interactions result in several SAR surface patterns. These patterns often outline the edges of shoals and coral reefs, and thus can be used to plot their locations and general shapes. The detection of these features on SAR imagery is limited to those instances where a gravity wave field is present and where shoals and coral reefs lie between two and fifty meters in depth. No water depth information can be extracted from these patterns.

Currents flowing over shallow water bottom features not only can give the exact location of a feature, but in some cases give an indication of that feature's structure. The depths of features detected in this manner range between 1 and 30 meters. Strong statistical correlations have been found between radar backscatter and water depth in some cases. However, in these cases, radar backscatter is also dependent on current speed and wind speed and direction. If these parameters can be measured or estimated, then the potential exists to extract water depth information from radar image intensity.

Although a high correlation exists between the occurrence of internal waves and the presence of a deep water bottom feature, the

internal waves give only a limited indication of the type or exact location of the bottom feature. At the present time, all that can be inferred from the presence of an internal wave on a SAR image is the presence of a bottom feature in the region. The same general statements are true for frontal boundaries which are due to deep-water upwelling.

The studies conducted over the past four years at ERIM have demonstrated the potential of SAR imagery for the detection and location of bottom features which may be hazardous to surface and subsurface navigation. Although there is no spaceborne SARs in operation today, a significant number of new systems are scheduled for the near future, insuring a world wide source of data. These systems include both Shuttle-borne (Spacelab, SIR-B, SAR-FACILITY, SIR-C) as well as satellite-borne (ERS-1 [ESA], ERS-1 [Japan], Radarsat [Canada]) SARs. Therefore, in the near future SAR imagery will represent a viable and continual source of information for use by hydrographers in the updating of navigation charts.

3
SURVEY OF SAR DATA

The approach taken during previous research efforts (e.g., Kasischke, et al., 1980; 1982) was to conduct in-depth analyses of a limited number of Seasat test sites in order to determine the types of bottom-related surface patterns which appear on SAR imagery as well as begin to understand the mechanisms responsible for their appearance. During the present study, a survey of the Seasat SAR data set was completed and a survey of he SIR-A SAR data set conducted. Two aircraft data sets were also reviewed. The purpose of these surveys was two-fold: to determine the frequency that bottom-related surface patterns appear on SAR imagery, and to determine how SARs with different sensor parameters detect bottom-related surface patterns. In the following sections, results of the surveys will be presented along with case studies from each SAR system.

3.1 SEASAT SAR DATA

The characteristics of the Seasat SAR have been discussed in a past report (Kasischke, et al., 1982) and will not be reviewed here. The Seasat satellite collected SAR imagery during approximately 370 of the 1500 orbits it was in operation. SAR imagery from a total of 212 Seasat orbits were reviewed during the survey performed during this study. The remaining Seasat imagery was not included in the survey for one or more of the following reasons:

1. The imagery was not processed,
2. The imagery was of land areas only, or
3. The imagery was collected over ice covered regions, or deep water regions where few deep-water bottom features existed.

The first step in the Seasat survey was to develop a uniform classification code for both bottom feature types and bottom-related surface patterns on SAR images.

15

Ten separate classes of bottom features were identified. These are:

1. Deep Water Banks (banks in water deeper than 100 meters),

2. Deep Water Ridges (submarine ridges in water deeper than 100 meters),

3. Deep Water Shelves (shelves in water deeper than 100 meters),

4. Sea Mounts,

5. Continental Shelves (continental shelves in water shallower than 100 meters),

6. Sand Banks and Shallow Water Shoals,

7. Shoal Areas Surrounding Islands,

8. Shallow Water Banks (large banks, generally in the Carribean, with depths shallower than 20 meters),

9. Coral Reefs, and

10. Mud Banks (often submerged at high tide, but can be detected and charted at low water).

In Table 1, six distinct types of SAR-observed bottom-related surface patterns were identified. Surface pattern types V and VI from Table 1 are both internal wave patterns and are quite similar in appearance. The distinction between these two types is that one occurs in shallow water (<100 m) while the other occurs in deep water. For recognition purposes, the six types of patterns identified in Table 1 can be grouped into five distinct classes: changes in radar backscatter (image tone), frontal boundary patterns, internal wave patterns, striped patterns and striated or banded patterns. Table 2 summarizes the types of bottom features each class of surface patterns are associated with. Examples of the five classes of patterns are presented in Figure 1.

16

TABLE 2
SUMMARY OF BOTTOM FEATURES ASSOCIATED
WITH SAR SURFACE PATTERNS

SAR Surface Patterns	Bottom Features
Change in Radar Backscatter	Sand Banks and Shallow Water Shoals Shoal Areas Surrounding Islands Shallow Water Banks Coral Reefs Mud Banks
Frontal Boundaries	Deep Water Banks Deep Water Ridges Deep Water Shelves Seamounts
Internal Waves	Deep Water Banks Deep Water Ridges Deep Water Shelves Seamounts Continental Shelves
Striped Pattern	Sand Banks and Shallow-Water Shoals Shoal Area Surrounding Islands Shallow-Water Banks Coral Reefs
Banded Pattern	Sand Banks and Shallow Water Shoals Shallow-Water Banks

Change in Radar Backscatter

Frontal Boundary
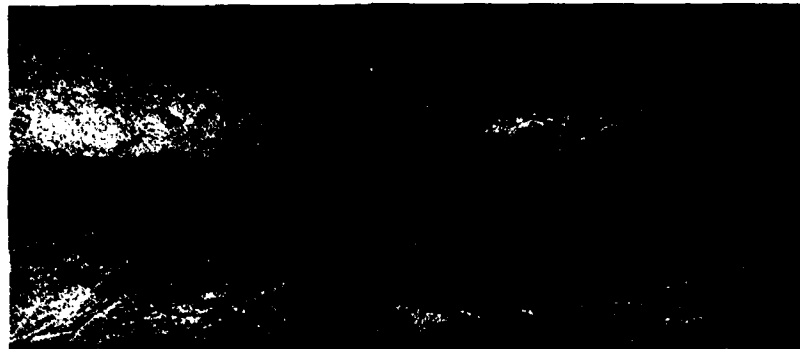
Internal Waves
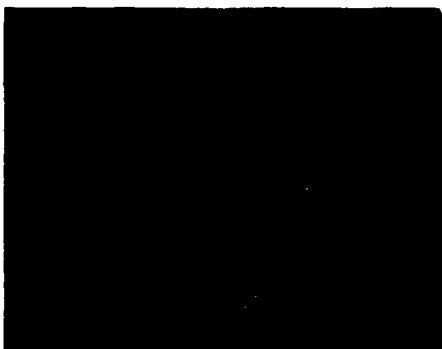
Striped Pattern
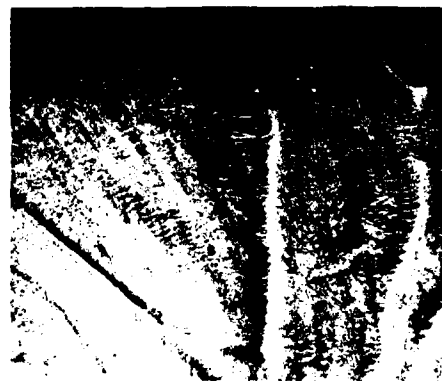
Banded Pattern

Figure 1. Five Classes of Bottom-Related Surface Patterns Observed
on Seasat SAR Imagery

18

For consistency, during this year's study all passes of Seasat SAR imagery were reviewed, including those passes used in past studies. The following procedure was used during the survey of Seasat SAR imagery: first, the ground track of each of the 212 passes was marked on a hydrographic chart. The Seasat SAR imagery of each pass was interpreted, and the position of each pattern which resembled a bottom-related surface patterns was plotted on the chart. The position of the SAR surface patterns were then compared to the position of the known bottom features. In addition, those bottom features which did not have an associated SAR surface pattern were noted as well as those surface patterns which did not correlate to any known bottom feature (i.e., possible false alarms).

Appendix A to this report contains the complete survey of the 212 Seasat passes in tabular form. These tables list, for each Seasat pass, the names of the bottom features within the ground track of that pass, the type of each bottom feature, and the associated SAR surface pattern for each specific feature.

Table 3 presents a summary of the survey of Seasat SAR data presented in Appendix A. This table contains a summary of the number of times a SAR surface pattern was associated with a given type of bottom feature. From Table 3, it can be seen that the deep water bottom features (banks, ridges, shelfs, and seamounts) had an associated surface pattern on Seasat SAR imagery well over 80 percent of the time. Most of the deep water features surveyed were located in the eastern North Atlantic Ocean. This area is discussed in more detail in Section 3.1.1.4.

Shallow water bottom features (sand banks, shoals, and large shallow bank edges such as the Great Bahama Bank) had an associated surface pattern on Seasat SAR imagery 67 percent of the time. Coral reefs were not well detected on Seasat SAR imagery. This bottom feature type will be discussed in more detail in Section 3.1.1.2.

TABLE 3
SUMMARY OF THE SURVEY OF SEASAT SAR
IMAGERY-DISTRIBUTION OF SAR SURFACE PATTERNS
BY BOTTOM FEATURE TYPE

Bottom Feature Type	SAR Surface Pattern	Number of Occurrences	Percent Occurrences
Deep Water Banks	Internal Wave	24	46
	Frontal Boundary	9	17.5
	Both*	10	19.
	Sub-Total	43	82.5
	No Pattern	9	17.5
Deep Water Ridges	Internal Wave	17	61
	Frontal Boundary	3	11
	Both*	4	14
	Sub-Total	24	86
	No Pattern	4	14
Deep Water Shelves	Internal Wave	6	46
	Frontal Boundary	1	8
	Both*	5	38
	Sub-Total	12	92
	None	1	8
Seamounts	Internal Wave	8	67
	Both*	1	8
	Sub-Total	9	75
	None	3	25
Continental Shelves	Internal Wave	117	59
	None	81	41
Sand Banks and Shallow Water Shoals	Band	46	39
	Stripe	5	4
	Change in Radar Backscatter	24	20
	Sub-Total	75	64
	None	43	36
Shoal Areas Surrounding Islands	Change in Radar Backscatter	30	91
	Stripe	2	6
	Sub-Total	32	97
	None	1	3
Shallow Water Banks	Stripe	90	56
	Change in Radar Backscatter	11	7
	Sub-Total	101	63
	None	60	37
Coral Reefs	Change in Radar Backscatter	18	28
	Stripe	1	2
	Sub-Total	19	30
	None	46	70
Mud Banks	Change in Radar Backscatter	26	100
	None	0	0

*Both Internal Waves and Frontal Boundary Patterns

20

The high detection rate of mud banks (100 percent) was entirely ex-
pected, since SARs can detect land/water boundaries well. However
obvious, the value of being able to chart the locations of mud banks,
which are often submerged during high tides, should not be
overlooked.

Numerous examples of bottom-related surface patterns observed on
Seasat SAR imagery have been presented in previous investigations
(see e.g., Kasischke, et al., 1980; 1982; 1983; Shuchman and
Kasischke, 1979; Lyzenga, 1981; Kenyon, 1981; 1983; Kasischke and
Lyzenga, 1983; Lodge, 1983; or Fu and Holt, 1982). Additional exam-
ples are also presented below.

3.1.1 TEST CASE STUDIES

Seasat SAR imagery from four areas were examined to further docu-
ment and study the occurrence of bottom-related surface patterns.
These areas were the Cay Sal Bank, Dry Tortugas, coral reefs in the
Bahamas, and deep-water bottom features in the eastern North Atlantic
Ocean.

3.1.1.1 Cay Sal Bank

Figure 2 presents Seasat SAR imagery collected over the Cay Sal
Bank during Rev. 809 on 22 August 1978 at approximately 13:25 GMT.
Corresponding bathymetry for this area is illustrated in Figure 3.
Cay Sal Bank is a 4000 km^2 bank which lies midway between Florida,
Cuba, and the Great Bahama Bank. The average depth of this bank is
about 8 meters, while the channels surrounding the bank are between
600 and 900 meters in depth.

The outline of the Cay Sal Bank is clearly visible on the Seasat
image (C7 to H9 to A13). Land features on the image include the
Florida Keys (C1 to J1), Cuba (J12 to E15), Cay Sal (H9), Anguilla
Cays (A12 to A13), Damas Cays (B9), Dog Rocks (B8) and Double Headed
Shot Cays (F7 to G8).
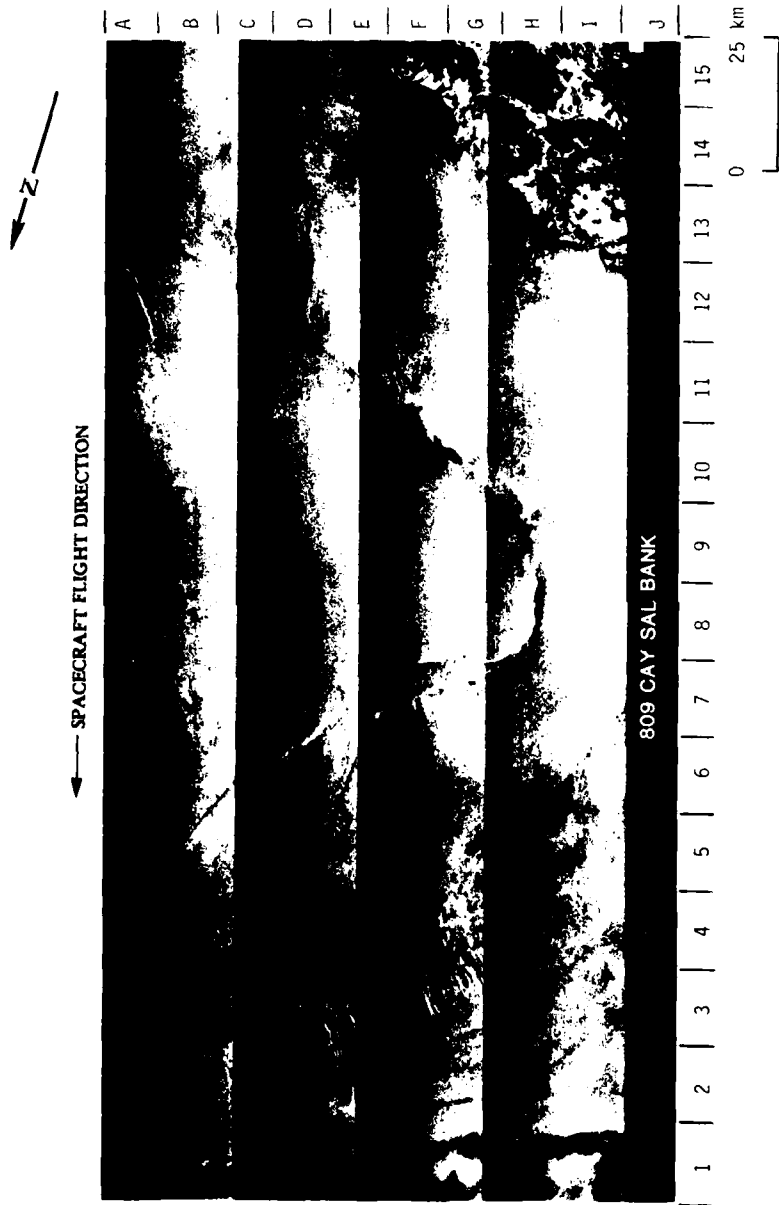
Figure 2. Seasat SAR Image of Cay Sal Bank (Rev. 309, 22 August 1978;
Optically Processed Imagery Courtesy of JPL)

22
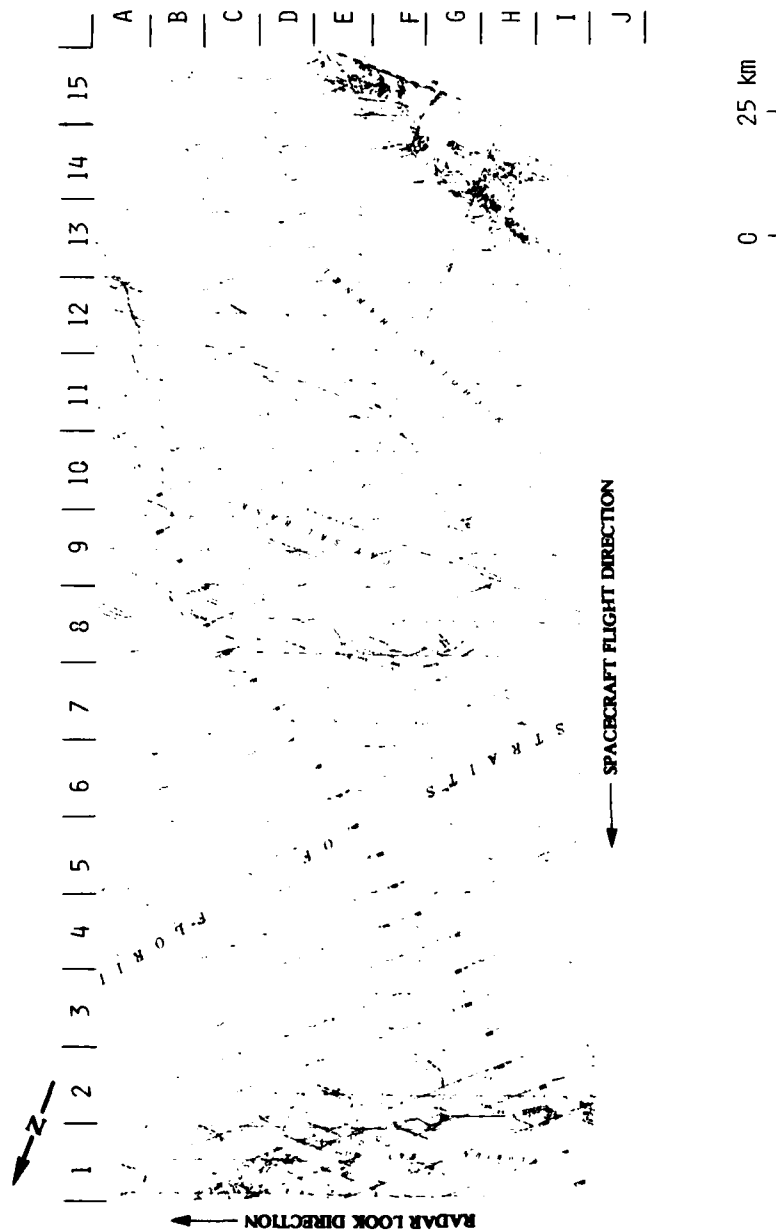
Figure 3. Ground Coverage of Seasat Rev. 809 Over Cay Sal Bank
(After DMA Chart No. 11461, Depth in Fathoms)

23
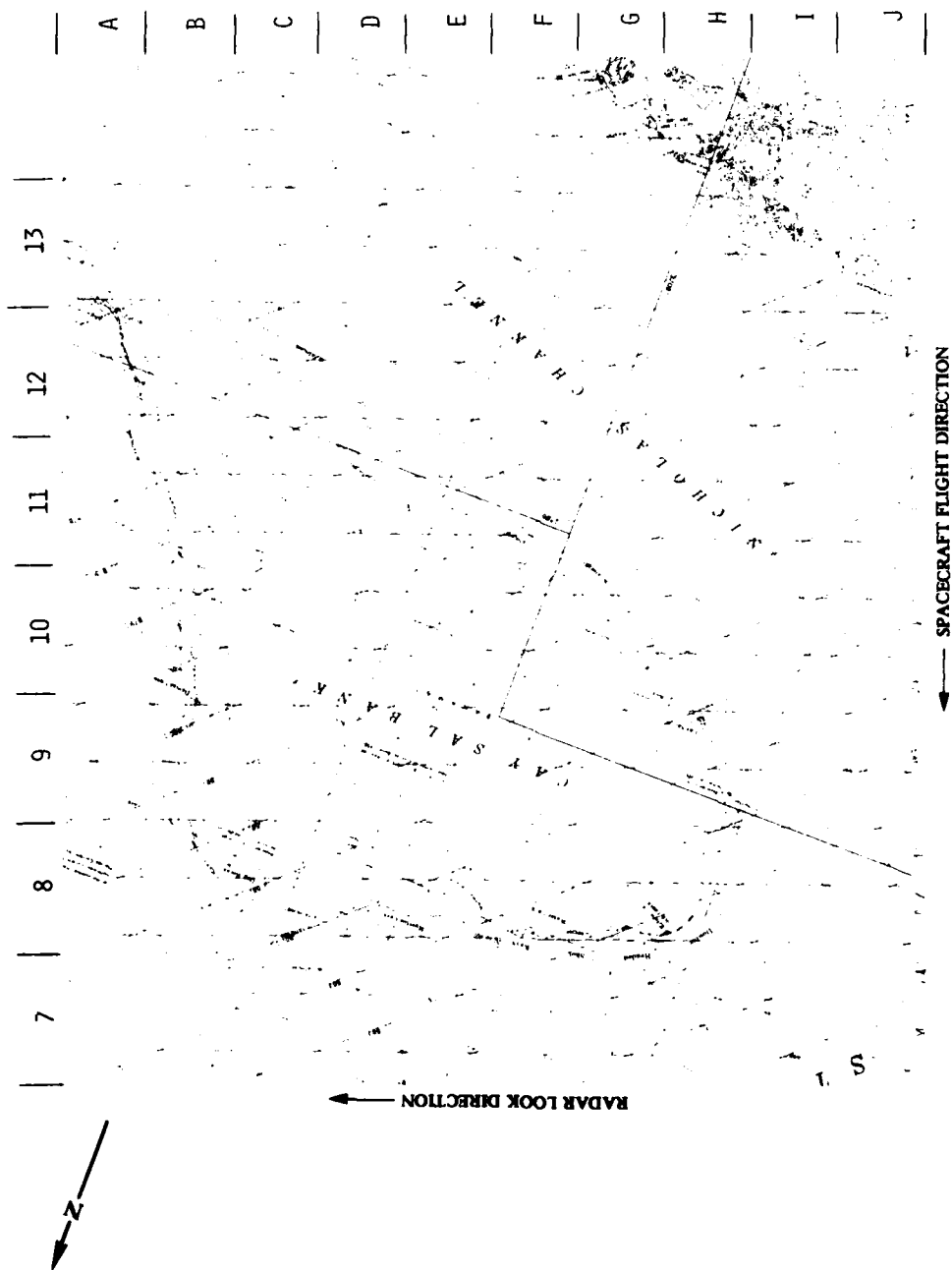
Figure 3a. Enlargement of Hydrographic Chart of Cay Sal Bank (After DMA Chart No. 11461, Depths In Fathoms)

As indicated on Figure 4, strong currents flow on all three sides of the Cay Sal Bank. These currents are believed to be responsible for many of the patterns present on the Seasat imagery in Figure 2. A small cyclonic vortex pattern can be seen at C13 to D13 in Figure 2. Vortices have been observed on other Seasat imagery (Fu and Holt, 1982; pg. 82). The wave-like patterns off the coast of Florida (D2 to H4) are believed to be the surface effects of the bottom boundary layer of the Gulf Stream adjusting to changes in the Stream's interior flow as it passes over the bottom. These patterns are similar to those observed by Fu and Holt (1982) and discussed by Mollo-Christensen (1981). Finally, the dark stripe along the Florida Keys (B1 to H2) can be seen to correspond to the edge of the continental shelf in this region.

The environmental conditions present at the time Rev. 809 Seasat SAR data were collected are summarized in Table 4. The meteorological data were estimated using National Weather Service weather observation summaries from Miami and Key West, Florida. The tide conditions were calculated using tide tables from Kline (1978) along with the generalized tide flow model developed in previous DMA/NRL sponsored studies (Kasischke, et al., 1982.). The dark stripe between Cay Sal and Anguila Cays (H9 to A13) in Figure 2, is believed to be caused by the flood tide flowing onto the bank. The other edges of the Cay Sal Bank are believed to be detected due to a combination of the flood tides flowing onto the bank as well as interactions between the strong currents (e.g., the Gulf Stream) in this area and the edge of the bank. The striated or banded patterns along the northern edge of the bank (G7 to H8) are quite similar to those typically found over sand banks. The chart of this area, however, reveals no sand banks at these points.

Seasat imaged all or portions of the Cay Sal Bank on five separate occasions. These occurrences are summarized in Table 4, along with the estimated wind speed and direction and tidal conditions for
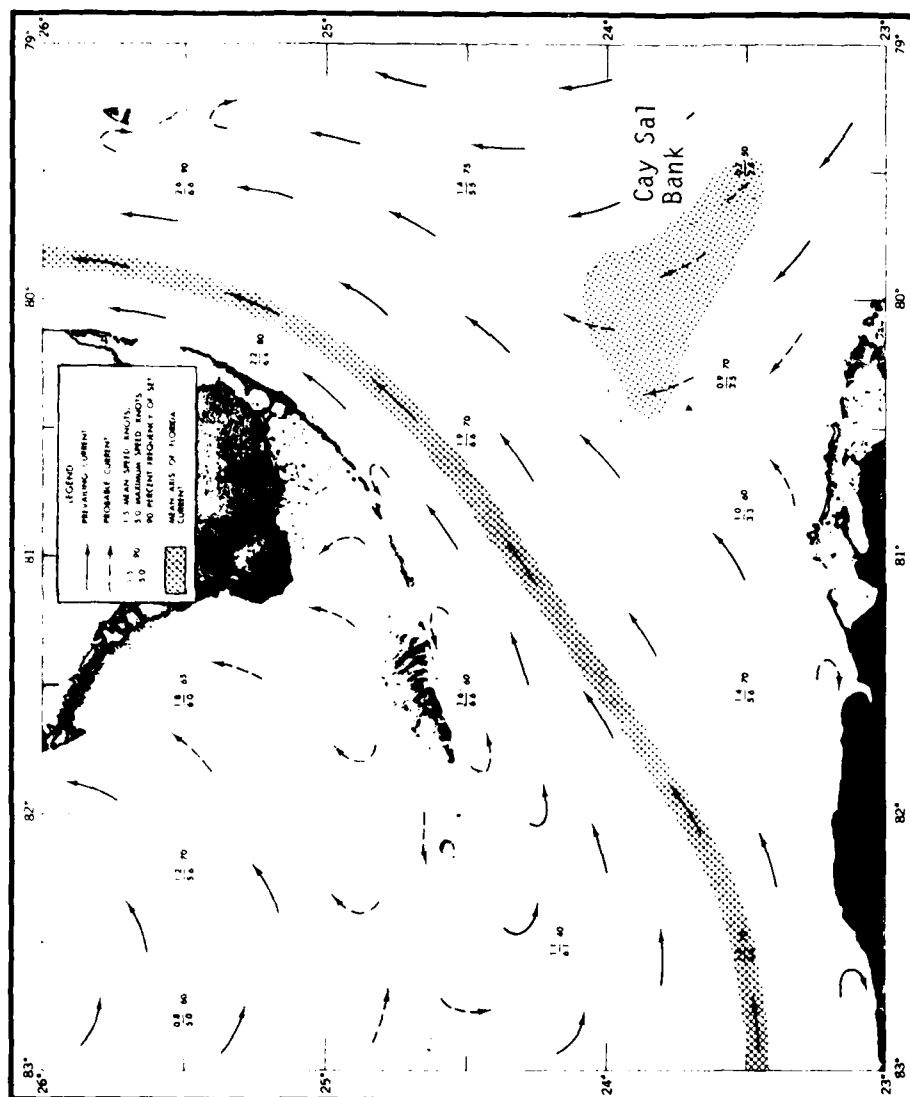
Figure 4.   Surface Currents Around Cay Sal Bank (From
U.S. Naval Oceanographic Office, 1977)

26

TABLE 4

SUMMARY OF ENVIRONMENTAL CONDITIONS AT CAY SAL BANK TEST SITE

Seasat Revolution	Date	Time (GMT)	Bottom-Related Surface Pattern Observed	Wind Speed (m/s)	Wind Direction	Tidal Conditions
565	5 August 1978	12:15	Yes	4.5	145°	Strong flood (3.5 hours after low water)
608	8 August 1978	12:25	No	5.5	125°	Moderate flood (2 hours after low water)
809	22 August 1978	13:25	Yes	3.8	142°	Strong flood (3 hours after low water)
1404	3 October 1978	05:00	Yes	2.5	160°	Strong ebb (4 hours after high water)
1490	9 October 1978	05:20	Yes	7.3	300°	Moderate ebb (4.5 hours after high water)

27

this area at these times. On four of the five times Seasat imaged the Cay Sal Bank, a bottom-related surface pattern similar to that in Figure 2 was present. Possible explanations why Seasat did not image the Cay Sal Bank during Rev. 608 (see Table 4) include insufficient currents at the time of the SAR overpass or too low of wind speeds to generate the small-scale surface waves necessary to detect a surface pattern.

A final observation on this data set is that on DMA Chart No. 11461, the following note is made regarding the position of the Dog Rocks and their surrounding shoals: "Reported to lie 1 1/2 miles eastward of charted position." Since these small islands are clearly detectable on the SAR imagery (B8), Seasat data can be used to verify the positions of these islands. This would require obtaining digitally-processed data from the area as well as using sophisticated geometric correction algorithms such as those developed by Curlander and Brown (1981).

3.1.1.2 Dry Tortugas

Seasat SAR imagery of the western end of the Florida keys is presented in Figure 5 (Seasat Rev. 766, 19 August 1978, 13:20 GMT). The bathymetry for this region is presented in Figure 6 (after NOS Chart No. 11434). This image covers the region from Key West (G1) to the Dry Tortugas (B10 to C9). There are many patterns in Figure 5 which occur directly over the sand ridges and shoals in this area. They include:

1. Distinct changes of radar return intensity and banded patterns are both present over the sand banks making up the Dry Tortugas (B10 to C9). The Dry Tortugas contain five small keys which are situated on three larger sand banks. These banks are located in water of 1 to 2 m in depth and are surrounded by 15 to 20 m deep water.

28

2. The Rebecca and Isaac Shoals (D 7/8) are indicated by small areas of distinct changes in image tone. These shoals are in water 3 to 5 m in depth and are surrounded by 10 m deep water.

3. The western edge of the Half Moon Shoal (E7) is visible on the Seasat image as a banded pattern. This shoal is approximately 5 m deep and is next to 15 m deep water.

4. Between Half Moon Shoal (E7) and the Marquesas Keys (F3), a large region of changes in image tone exists. This region corresponds to a large bank in water 2 to 3 m deep bordered by water which is over 10 meters deep.

5. There are several banded patterns between the Marquesas Keys (F2/3). These most likely correspond to tidally formed longitudinal sand ridges similar to those found in many areas of strong tidal action (e.g., the Tongue of the Ocean, Nantucket Shoals or the English Channel, see Kasischke, et al., 1980; 1982).

6. The small dark areas (low radar return) on the image (F4 and G1 to G2) most likely correspond to regions of exposed sand banks.

7. The subtle change in radar return at position E4 to D6 correlates to the location of the New Ground Shoal. This shoal is in water 3 to 5 m in depth, with the adjacent water over 15 m deep.

8. The edge of the continental shelf in this region (F9 to H1) is expressed as a subtle stripe or a change in image tone on the SAR imagery.

Ancillary environmental data for this region was obtained by consulting the weather records and tide tables from Key West, Florida. At the time of the Seasat overpass of this region, there were 10 knot
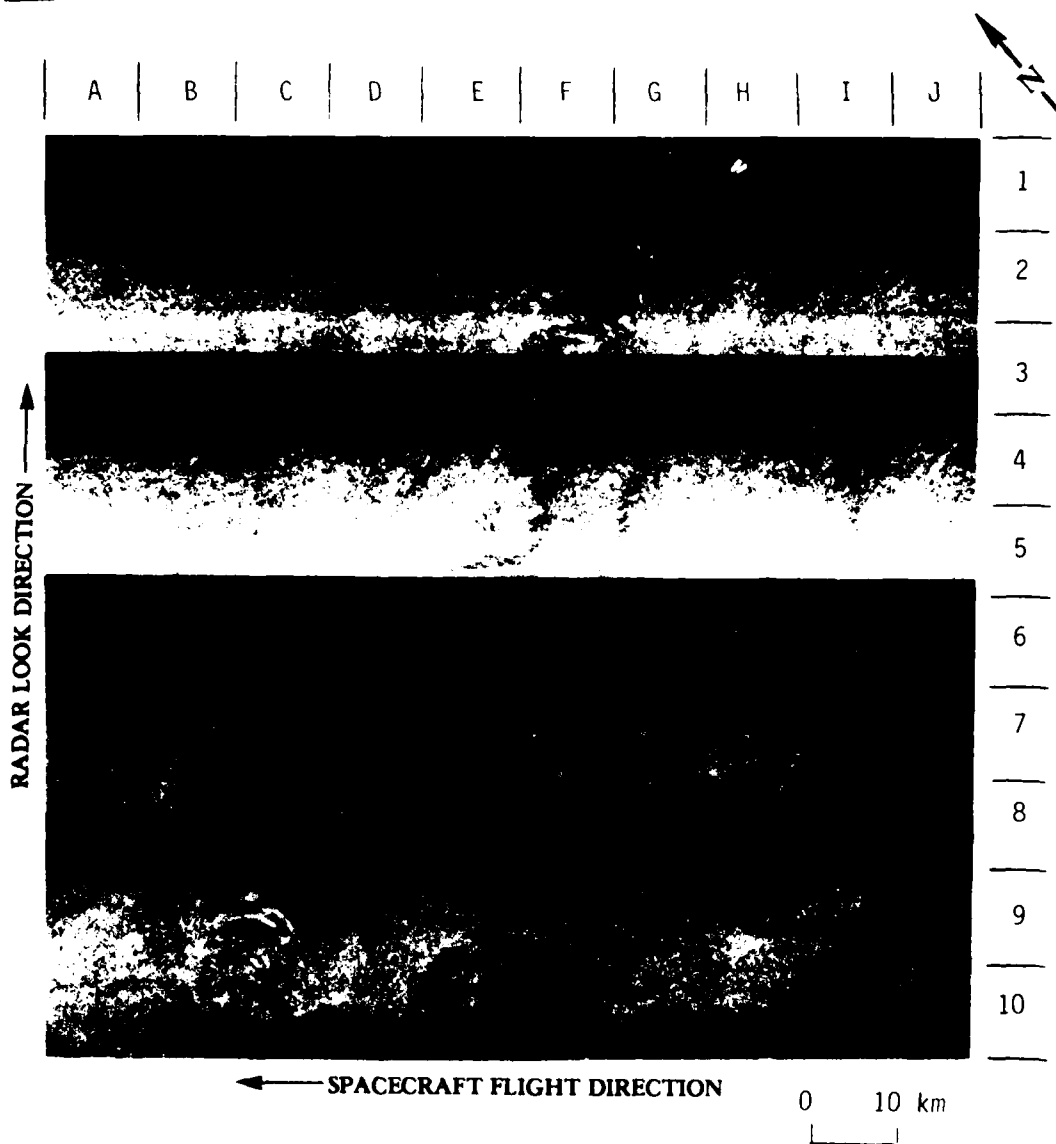
Figure 5.   Seasat SAR Image of Dry Tortugas (Rev. 766, 19 August 1978, Optically Processed Data Courtesy of JPL)
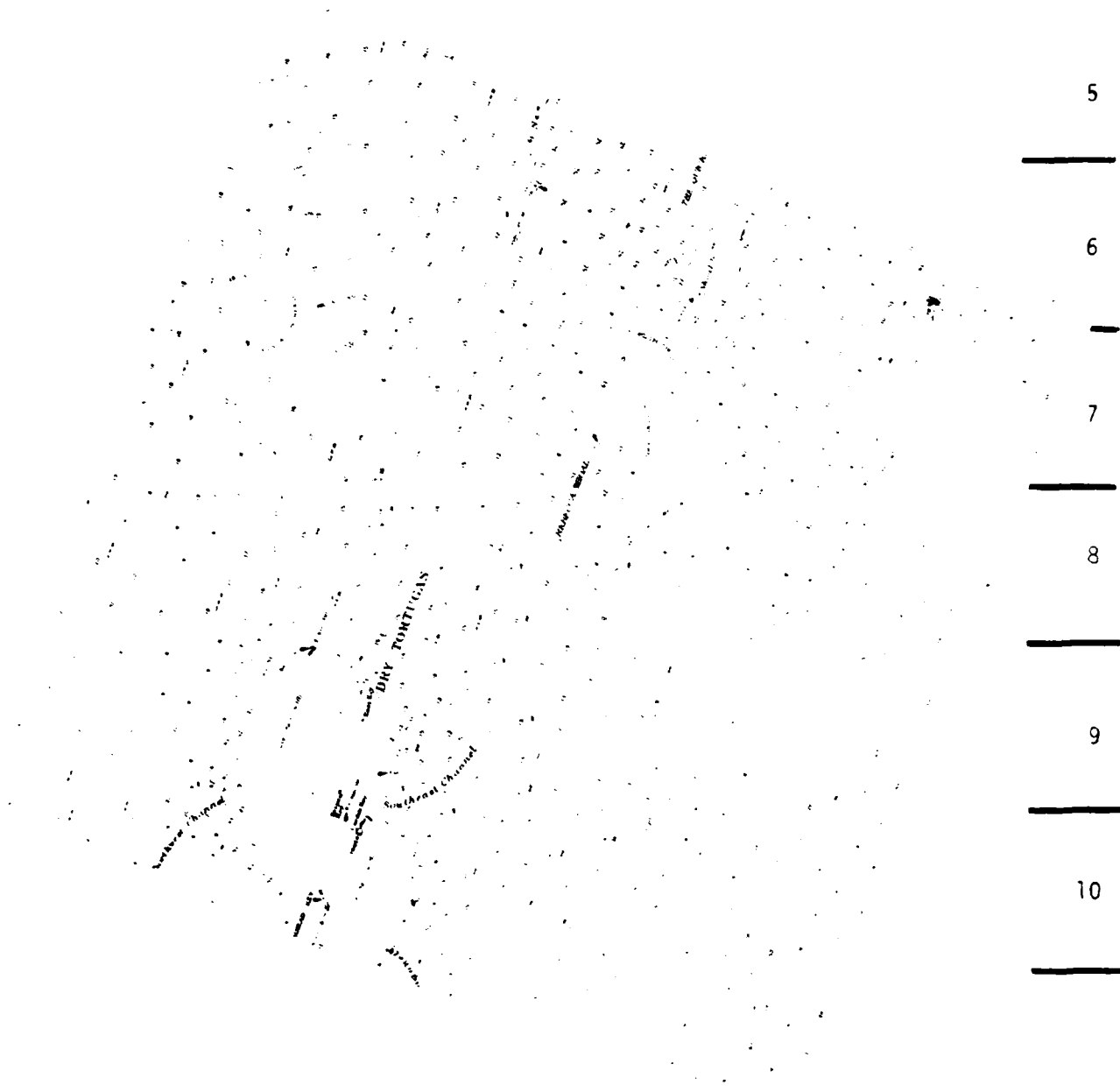
Figure 6a.   Hydrographic Chart of Key West to Quick Sands (Depths in Fathoms, After DMA Chart No. 11434, Sombrero Key to Dry Tortugas).

Figure 6b. Hydrographic Chart of Quick Sands to Dry Tortugas (Depths in Fathoms, After DMA Chart No. 11434, Sombrero Key to Dry Tortugas).

winds from 135° (T). Since the winds had been light (~10 knots) for the previous four days, the local sea present was most likely light. Tide tables for this area indicate the Seasat data were collected near maximum flood tide. Tidal currents at Key West were estimated to be 1.5 knots with a heading of 020° (T). From these data, we can conclude that the surface patterns present on the Seasat SAR images were most likely the result of the tidally driven currents flowing over the bottom features in this region.

Seasat imaged the Dry Tortugas region on two other occasions (Revs. 522 and 802). On both occasions, patterns similar to those present on Figure 4 were also visible on the Seasat images.

Finally, the image in Figure 5 presents an interesting case study of the detection of islands on Seasat SAR imagery. The Dry Tortugas are made up of five small keys, each between 0.1 to 0.3 km^2. These small keys are difficult to detect on the Seasat image. Loggerhead Key (C10) is the most apparent, and it is visible as a small dark patch on the image. In contrast, the small keys between Key West (G1) and the Marquesas Keys (F3) are quite visible on the SAR imagery as bright returns. Most of these keys are as small as those in the Dry Tortugas. The explanation to this apparent contradiction is obtained through examination of the smaller scale charts of these areas. DMA Chart No. 11439 (Sand Key to Rebecca Shoal) indicates that most of the keys in this region consist of mangrove swamps, while DMA Chart No. 11438 (Dry Tortugas) indicates these keys are essentially flat, sand spits. The mangrove swamps would appear bright on the Seasat SAR imagery because the vegetation would be detected as a rough surface by the SAR, whereas the sand covered keys would have a specular reflection for the L-band Seasat SAR wavelength, resulting in a dark return on the imagery.

3.1.1.3 Carribean Coral Reefs

During a previous year's effort (Kasischke, et al., 1982), Seasat SAR imagery of the eastern Great Bahama Bank was examined for surface patterns associated with the large patches of coral heads found in this region. It was concluded from this earlier analysis that the large regions of coral were not detectable on Seasat SAR imagery because of the absence of a physical ocean process (i.e., waves or currents) in these areas.

Figure 7 presents two Seasat images collected over nearly the same region of the Bahamas on two separate occasions. These images are of the northern edge of the Little Bahama Bank, including Sale Cay, and were collected during Seasat Revs. 450 and 1110. Examination of the corresponding hydrographic chart of this region in Figure 8 (after DMA Chart No. 26320: Northwest and Northeast Providence Channels) indicates that the dark stripe on the Rev. 450 image (A5 to D1) corresponds to the edge of the Little Bahama Bank, while the mottled line (C3 to E1) corresponds to a coral reef at the edge of the bank. On the Rev. 1110 image, a slight change in image tone is present at the coral reef (D2 to E1), but no pattern is detected at the edge of the bank.

The difference in the land/water contrast between these two images is probably due to differences in incidence angle as well as wind conditions. The portion of Rev. 450 shown in Figure 7 is from sub-swaths 1 and 2, while the portion of Rev. 1110 is from sub-swaths 3 and 4. Under some conditions such a contrast reversal is observed from subswath 1 to subswath 4 in the same image, due to the more rapid falloff of the radar cross section over water than over land. Additionally, or alternatively, the wind speed may have been higher during Rev. 450 than during Rev. 1110, causing a higher radar cross section over water in the former case. Changes in the radar cross section of the land surface (e.g., due to a recent rainfall) are also possible but less likely.

The region of the Little Bahama Bank presented in Figure 7 was imaged on ten different occasions by the Seasat SAR. It therefore offers an excellent opportunity to further analyze the appearance or absence of surface patterns associated with the types of coral reefs found in this region.

For this area, all ten passes of Seasat SAR imagery were examined for surface patterns. For each pass, the tidal stage was predicted from tide tables (Kline, 1978), the estimated water height above mean low water springs estimated, and a tidal current velocity predicted. These latter two parameters were estimated using the techniques developed during previous studies (Kasischke, et al., 1982). Presented in Table 5 are each Seasat Revolution, Date, Time (GMT), estimated water height (above mean low water springs), estimated current speed, and whether or not a surface pattern was present on the SAR imagery.

DMA Chart No. 26320 indicates that the reefs in the region being studied uncover at low water springs. However, we do not think the reefs uncovered during the times the imagery investigated during this analysis was collected. Our reasoning for this is as follows: The lowest predicted tide height was during Rev. 1110. If the reefs were exposed at this time, we would expect them to be clearly identifiable on the imagery. However, comparison of the Rev. 1110 imagery versus the Rev. 450 in Figure 7 imagery clearly shows that the more distinct pattern is present on the Rev. 450, which had a higher predicted water depth. It is believed this more distinct pattern is associated with a current flowing over the coral reef.

The estimated water depth versus current velocities listed in Table 5 were plotted for the ten passes in Figure 9. With one exception, no surface patterns were detected when the water depth was greater than two feet and the estimated current velocity was less than ~1 m/s. The only exception to this rule was Rev. 1239.

Rev. 450, 28 July 1978
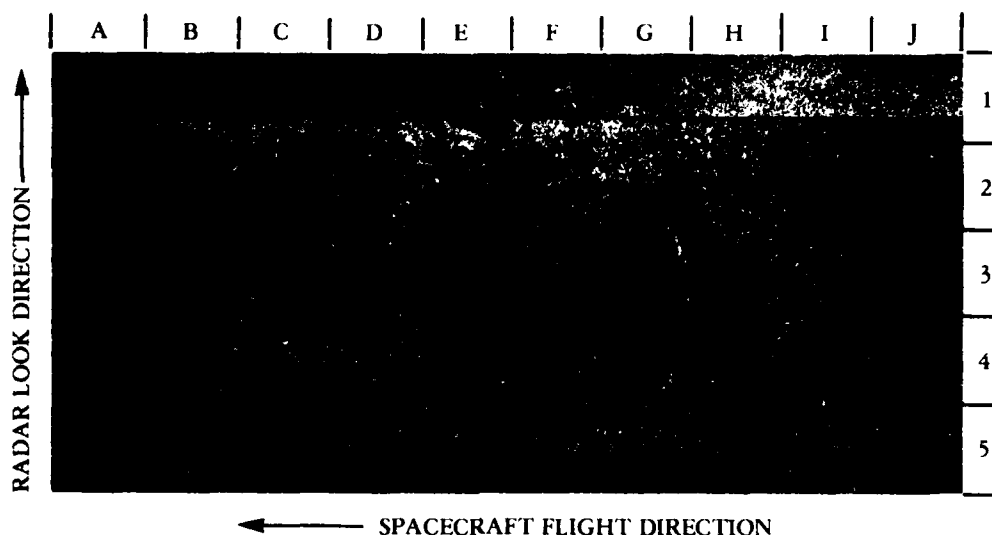
Rev. 1110, 12 September 1978
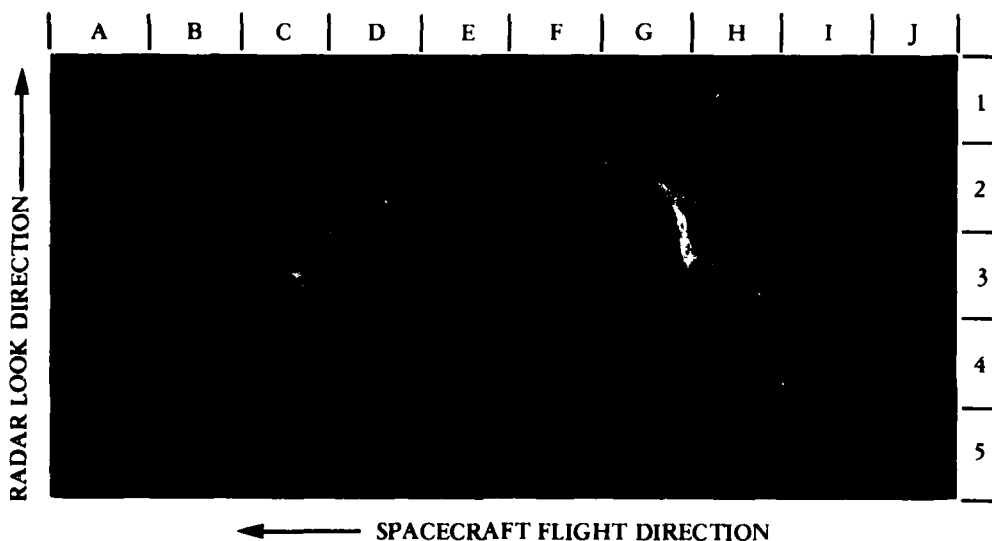
Figure 7. Seasat SAR Imagery Collected Over Northern Edge of Little
Bahama Bank (JPL Optically Processed Imagery)

36
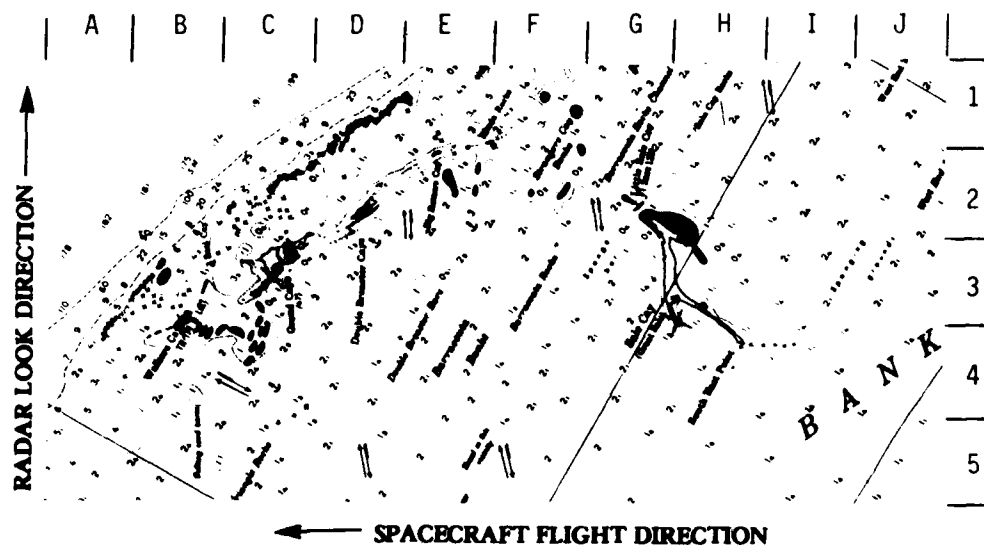
Figure 8. Hydrographic Chart of Northern Edge of
           Little Bahama Bank (DMA Chart No.
           26320, Soundings in Fathoms and Feet)
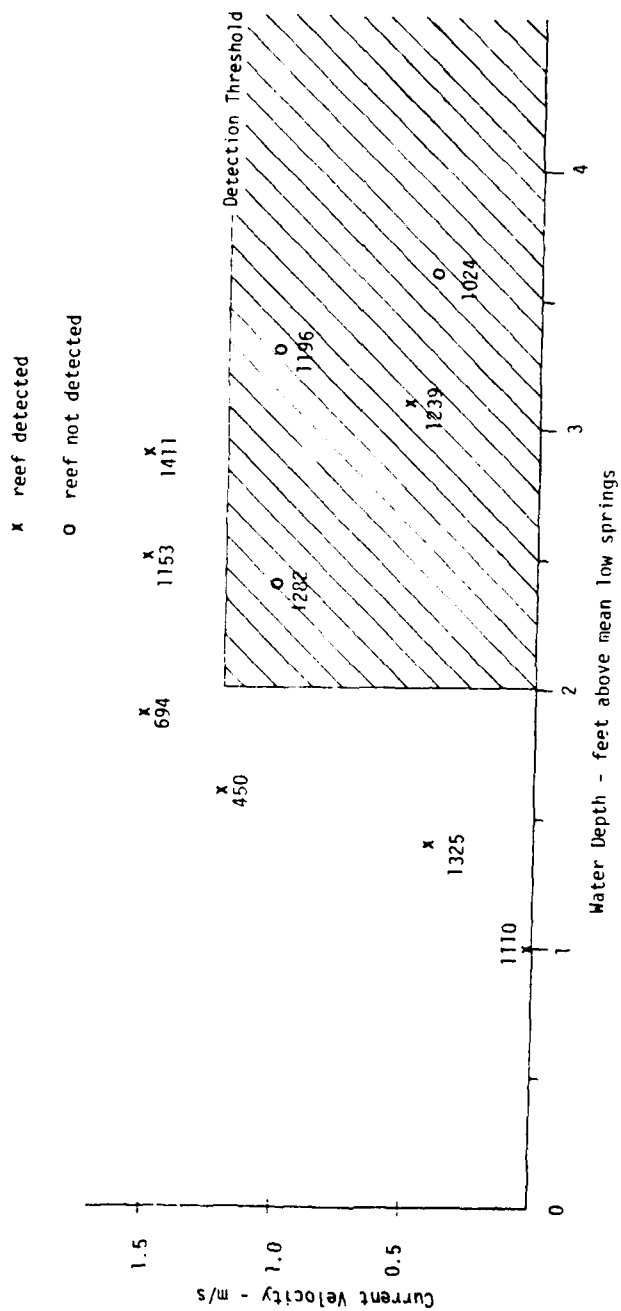
Figure 9. Relationship Between Water Depth, Current Speed and Detection Threshold on Seasat SAR Imagery for Sale Cay Coral Reefs

TABLE 5
SUMMARY OF LITTLE BAHAMA BANK CORAL REEF ANALYSIS

Seasat Revolution	Date	Time (GMT)	Estimated Water Height* (ft)	Estimated Current Velocity** (m/s)	Surface Pattern Visible
450	7-28-78	11:25	1.6	1.2 E	Yes
694	8-14-78	12:40	1.9	1.5 E	Yes
1024	9-06-78	14:20	3.6	0.4 F	No
1110	9-12-78	14:45	1.0	0.0	Yes
1153	9-15-78	14:55	2.5	1.5 E	Yes
1196	9-18-78	15:10	3.3	1.0 E	No
1239	9-21-78	15:20	3.1	0.5 F	Yes
1282	9-24-78	15:35	2.4	1.0 F	No
1325	9-27-78	15:45	1.4	0.4 F	Yes
1411	10-03-78	16:15	2.9	1.5 E	Yes

*Water height above mean low water springs.
**E = Ebb tide
  F = Flood tide

These observations seem to support the following hypothesis for detection of coral reefs in this region: when the water depth is less than two feet over the reefs, a current velocity of less than 1 m/s is necessary to generate a bottom-related surface pattern. When the water depth is greater than two feet, a current velocity of greater than 1 m/s is necessary. Explanations for the detection of a surface pattern during Rev. 1239 include the possibilities that the current velocity was higher than estimated or the water depth was lower than estimated.

Although the overall detection rate of coral reefs was low (30 percent from Table 3), this figure included nineteen cases from the interior of the Great Bahama Bank, where due to calm water conditions, one would anticipate no detectable surface patterns. If these cases are removed, the detection rates do increase to over 40 percent. The conclusion which can be drawn from the present analysis is that if SAR data are collected at the proper times (i.e., near low water when there are maximum tidal currents), then coral reefs at the edges of banks may be detected.

3.1.1.4 Eastern North Atlantic Ocean

During a previous year's study, Seasat SAR imagery collected during the JASIN experiment were examined for bottom-related surface patterns (see e.g., Kasischke, et al., 1982). This analysis was expanded in several directions during the present study. First, the Seasat imagery collected was examined over their entire coverage region, not just the JASIN area, and this data set was expanded to include all imagery collected over this region. And second, a theoretical analysis was conducted to determine the hydrodynamic mechanisms responsible for the formation of these deep water surface patterns. This latter analysis is discussed in Chapter 5.

The same procedures used in past analyses were implemented in this study (see Kasischke, et al., 1982). The JASIN data set previously examined was expanded to include Seasat Revs. 590, 785, 1149, 1307 and 1359. The results of this expanded analysis are summarized in Tables 6 and 7. From these tables, it can be seen that 67 percent of the deep water features had an associated internal wave pattern, 28 percent an associated frontal boundary, and 82 percent had either an internal wave and/or a frontal boundary. These results are consistent with the previous year's analysis. A more complete discussion of this data set is presented in the paper by Kasischke, et al. (1983a) which is included in Appendix C to this report.

3.2 SIR-A SAR DATA

Part of the scientific payload onboard NASA's second Space Shuttle mission in November of 1981 was an L-band SAR, almost identical to the one carried by Seasat. This system was named the Shuttle Imaging Radar-A, or SIR-A for short. During the two and one-half day shuttle mission, SIR-A collected almost eight hours of data which contained approximately ten million square kilometers of imagery. Because the SAR signal histories were optically recorded onboard the shuttle, SIR-A did not have to be within sight of a ground receiving station, like Seasat, in order to record the SAR signal histories, and could collect data anywhere along its orbital track. Figure 10 presents the ground coverage collected by SIR-A. For a more complete description of the SIR-A mission, the reader is referred to Ford, et al. (1983).

A comparison of the SIR-A versus Seasat system parameters is presented in Table 8 (after Ford, et al., 1983). A major goal of the SIR-A mission was to collect spaceborne SAR imagery suitable for geologic applications. To meet the scientific goals of this experiment, an incidence angle of approximately 47° was used (compared to the 20° incidence angle used on Seasat). Figure 11 (after Guinard

41

TABLE 6
SUMMARY OF OCCURRENCES OF BOTTOM-RELATED SURFACE PATTERNS
ON SEASAT SAR IMAGERY COLLECTED OVER
THE NORTHEAST ATLANTIC

Bottom Feature Covered by Seasat SAR	SAR Revolution Number	SAR-Observed Pattern	
		Internal Wave	Frontal Boundary
Rockall Bank	547	X	
	556		X
	714	X	
	757	X	
	791	X	
	958	X	X
	1044		
	1087		X
Anton Dohrn Seamount	547	X	X
	556	X	
	599	X	
	791		
West Shetland Shelf	642	X	
	762	X	
	1359	X	
Malin Shelf	547		X
	633	X	
	791	X	
	834		
Hebrides Terrace Seamount	547	X	
	642	X	
	791		
Hebrides Shelf	590	X	
	599		
	633		
	642		
	719		
	762	X	
	834		X
	1006		X
	1049		
	1307		

TABLE 6
SUMMARY OF OCCURRENCES OF BOTTOM-RELATED SURFACE PATTERNS
ON SEASAT SAR IMAGERY COLLECTED OVER
THE NORTHEAST ATLANTIC (Continued)

Bottom Feature Covered by Seasat SAR	SAR Revolution Number	SAR-Observed Pattern	
		Internal Wave	Frontal Boundary
Iceland-Faeroe Rise	719	X	
	762	X	X
	958	X	
	1044	X	X
	1087	X	
	1149	X	
Bill Bailey's Bank	719	X	X
	757		
	1006		X
	1044		
	1049	X	X
	1087	X	
	1307		
Lousy Bank	633	X	X
	590	X	
	791		X
	834	X	
	958	X	
	1006		
	1044	X	X
	1049	X	X
	1087	X	
Hatton Bank	547		
	791		X
	958		X
	1044	X	
George Bligh Bank	547	X	
	791		X
	958	X	
	1044	X	
	1087	X	
Faeroe Bank	556		X
	719		X
	757	X	X
	762	X	X

43

TABLE 6
SUMMARY OF OCCURRENCES OF BOTTOM-RELATED SURFACE PATTERNS
ON SEASAT SAR IMAGERY COLLECTED OVER
THE NORTHEAST ATLANTIC (Continued)

Bottom Feature Covered by Seasat SAR	SAR Revolution Number	SAR-Observed Pattern	
		Internal Wave	Frontal Boundary
Faeroe Shelf	556		X
	599	X	X
	642	X	X
	714	X	
	757		
	762	X	X
	1149	X	
Wyville-Thomson Ridge	556	X	
	599	X	
	642		X
	719	X	
	757		
	762	X	X
Ymir Ridge	556	X	
	599	X	
	642	X	
	719	X	
	757	X	
	1049	X	
North Feni Ridge	547	X	X
	556		X
	590	X	
	633		
	757		
	791	X	X
	834		
	1006	X	X
	1049		X
South Feni Ridge	556	X	
Rosemary Bank	556	X	
	599	X	
	633	X	X
	757		
	834	X	
	1006	X	X
	1049	X	
	1307		

44

TABLE 6
SUMMARY OF OCCURRENCES OF BOTTOM-RELATED SURFACE PATTERNS
ON SEASAT SAR IMAGERY COLLECTED OVER
THE NORTHEAST ATLANTIC (Concluded)

Bottom Feature Covered by Seasat SAR	SAR Revolution Number	SAR-Observed Pattern	
		Internal Wave	Frontal Boundary
Iceland Continental Shelf	547		
	590	X	
	633	X	
	719	X	
	762	X	
	791	X	
	834		
Norway Continental Shelf	556	X	
	599		
	757	X	
Ormonde Seamount	785	X	
Gettysburg Seamount	785	X	
Agadir Seamount	785		
Coral Patch Seamount	785	X	
Porcupine Bank	599	X	
	642	X	
North Atlantic Ridge	556	X	
	599	X	
	642	X	
	714	X	
	757	X	

45

TABLE 7
SUMMARY OF DETECTIONS OF DEEP WATER TOPOGRAPHIC FEATURES
BY SEASAT SAR IMAGERY USING DATA COLLECTED OVER
THE NORTHEAST ATLANTIC

Seasat Revolution	Total Number of Deep-Water Bottom Features Covered	Total Number of Occurrences of Internal Waves Over Features	Total Number of Occurrences of Frontal Boundaries Over Features
547	8	6	3
556	11	7	4
590	4	4	0
599	9	6	1
633	6	4	2
642	8	6	3
714	3	3	0
719	7	5	2
757	10	5	1
762	7	7	4
785	4	2	0
791	9	5	4
834	6	3	0
958	5	4	2
1006	5	2	4
1044	6	4	2
1049	6	4	2
1087	5	4	1
1149	2	2	0
1307	3	0	0
1359	1	1	0
Total	125	84	35
Percent		67%	28%

Figure 10. Ground Coverage of SIR-A SAR During November 1981

TABLE 8
COMPARISON OF SEASAT AND SIR-A SAR SYSTEM PARAMETERS

Parameter	Seasat SAR	SIR-A
ORBIT		
Altitude, km	795	259
Inclintion, deg.	108	38
RADAR		
Frequency, GHz	1.275	1.278
Wavelength, cm	23.5	23.5
System Bandwidth, MHz	19	6
Transmit Pulse Length, µs	33.4	30.4
Pulse Repetition Frequency, Hz	1463 to 1640	1464 to 1824
Transmitted Peak Power, W	1000	1000
Time-Bandwidth Product	634	182
Polarization	HH	HH
ANTENNA:		
Dimensions, m	10.74 x 2.16	9.4 x 2.16
Look Angle, deg.	20 ± 3	47 ± 3
INCIDENCE ANGLE, deg.	23 ± 3	50 ± 3
SWATH WIDTH, km	100	50
RESOLUTION, m	25 x 25	40 x 40
DATA RECORDING	Ground Station; Digital	Onboard; Optical
SIGNAL CORRELATION	Optical and Digital	Optical
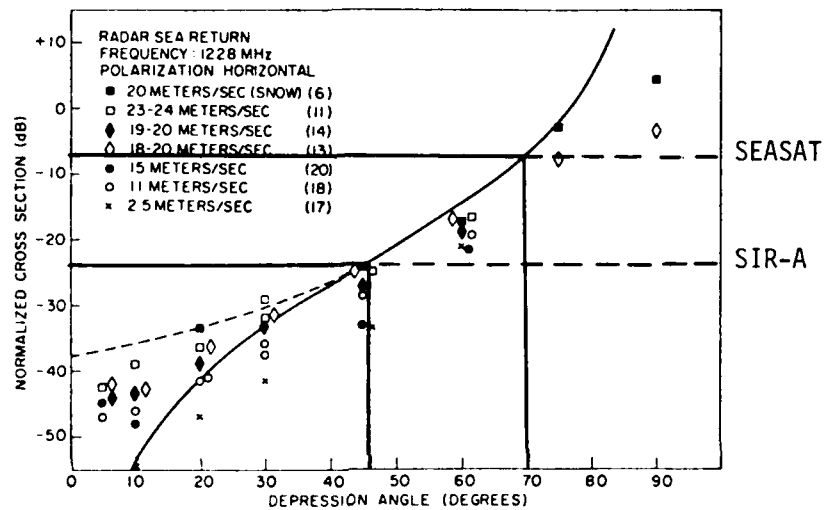
Figure 11. Relationship Between Radar Cross Section and
Depression Angle for L-Band SAR Data (After
Guinard and Daily, 1971)

49

and Daley, 1971) illustrates the effect of depression angle (which equals 90° minus the incidence angle) on L-band radar return from a water surface. It can be seen that for the SIR-A incidence angle, the radar backscatter from a water surface is approximately 15 dB lower than for the Seasat incidence angle. In terms of visibility on a SAR image, this relationship indicates that a pattern detected on Seasat imagery would not be as visible on SIR-B imagery. Hence, it was initially felt that the SIR-A imagery collected over oceanic areas would contain very little information. In an overall comparison, the SIR-A imagery did not contain as much information over water areas as did Seasat imagery. However, our examination of the imagery did reveal several circumstances where bottom-related surface patterns could be detected.

SIR-A was originally scheduled to operate over a four-day period. However, due to technical difficulties, the second Shuttle mission was shortened to two and one-half days. This abbreviation was fortuitious for the present study in that more SAR imagery of oceanic regions was collected than was originally planned.

Because the SIR-A SAR was optimized to collect imagery over land areas (therefore resulting in a lower probability of detecting ocean surface patterns than the Seasat SAR), a much less stringent and exhaustive analysis was performed on the SIR-A imagery than was performed on the Seasat data set. All twenty passes (or Data Takes) of SIR-A imagery were examined . These Data Takes ranged from 248 to 2515 seconds in length. Given the shuttle velocity of 7 km/sec, this translates to ground surface lengths of approximately 1700 to 17,600 km.

For the SIR-A data set, imagery from each pass was reviewed. All surface patterns believed to be bottom-related were noted and their geographic locations were determined. These patterns were then compared to bathymetric charts of the same region. A total of 16

bottom-related surface patterns were detected on the SIR-A data set. Table 9 presents a summary of the SIR-A observations. Presented in this table are the Data Take Number, Date, Time ON/OFF (GMT), length of pass in seconds, observed SAR surface patterns and corresponding bottom feature. From Table 9, it can be seen that there were fifteen examples of SIR-A-observed surface patterns related to a bottom feature. We will review five of these areas in the remainder of this section.

3.2.1 SOUTHEAST BAHAMAS

SIR-A imaged the southeastern portion of the Bahama Island group during Data Take 24BB on 13 November 1981 at approximately 22:20 GMT. In this section, we will present imagery collected over three island groupings: Crooked/Acklins Islands, Mayaguana Island and the Caicos Islands. At the time of the SIR-A overpass, the tide stage (after Kline, 1981) was approximately 1.5 hours after high water. Wind conditions for this image (from weather records in Miami, Florida and San Juan, Puerto Rico) were light (4-6 knots) from the west.

Figure 12 presents SIR-A imagery collected over Crooked and Acklins Islands. The smaller islands in the upper right-hand corner of this image are the Plana Cays. The corresponding bathymetry for this region is presented in Figure 13 (after DMA Chart No. 26280).

Of particular note on this image are the narrow white band which lies along the northern shores of the islands and the gravity wave pattern which can be detected. Measurement of this wave field from the SAR imagery indicates a swell with a wavelength of approximately 250 m, with a direction of propagation towards 170°(T).

Figure 14 (after Kline, 1981) gives a clearer picture of the almost continuous reef which lies along the northern edge of Crooked and Acklins Islands. The white band on the SIR-A imagery is believed to be the surf zone where the waves are breaking on the

51

TABLE 9

SUMMARY OF SIR-A SAR OBSERVATIONS OF BOTTOM-RELATED SURFACE PATTERNS

Data Take	Date	Time On (GMT)	Time Off (GMT)	Length (Seconds)	Observed Surface Patterns*	Bottom Feature
7	11-13-81	05:53:19	06:22:27	1750	None	
16-17	11-13-81	01:54:49	02:15:42	1253	None	
18	11-13-81	13:27:04	13:31:57	293	BP	Tongue of The Ocean Tidal Bar Belts
21	11-13-81	15:00:25	15:11:15	665	DB	Breaking Waves on Reef Off of Cat Island Diamond Shoals, Cape Hatteras
22	11-13-81	17:31:55	17:41:25	660	DB	Emerged Reefs Off Eastern Australia
24A	11-13-81	19:39:49	19:52:12	743	DB	Diamond Shoals, Cape Hatteras
24B	11-13-81	21:14:19	21:30:57	998	None	
24BB	11-13-81	22:14:19	22:26:19	713	DB	Breaking Waves on Coral Reefs Off of Crooked Island, Playa Cays, Mayaguna Island and Caicos Islands
24C	11-13-81	22:48:49	23:14:27	1538	None	
25	11-14-81	01:03:04	01:07:12	248	None	
28	11-14-81	05:49:49	06:17:12	1643	None	
29-30	11-14-81	07:00:49	07:30:57	1808	None	
31	11-14-81	08:37:19	08:45:32	503	None	
32-33	11-14-81	08:54:04	09:35:42	2498	None	
34	11-14-81	10:12:49	10:19:27	503	None	
35-36	11-14-81	10:32:49	11:14:44	2515	DB	Coral Reefs Off Western Australia
					DB	Shoals and Reefs Off of P. Raijua and Sawu
					DB	Shoals Northeast of Sumba
					DB	Bank Off of Klepulauan Tengah
					IW	Internal Waves Off Coast of New Zealand and Panama, and in Andaman Sea
37A	11-14-81	12:06:19	12:26:12	1119	None	
38	11-14-81	13:39:49	14:02:57	1388	None	

*Key: DB: Change in Radar Image Tone
       IW: Internal Wave Pattern
       BP: Banded Pattern

ERIM

RADAR DIVISION

reef. The gaps in the reef (F6/F7) are clearly visible on the SAR image. Although not as clear, the reefs north of Plana Cays (L4 to N3) can also be detected.

Two areas of wave refraction, which indicate shoaling water, are also detected on this image. These areas include the northeast tip of Acklins Island (I5) and the eastern edge of the Plana Cays (N3).

Figure 15 presents the SIR-A imagery collected over Mayaguana Island. The corresponding area from the hydrographic chart for this region is shown in Figure 16 (after DMA Chart No. 26260). Again, the coral reefs along the northern edge of the island are indicated by a bright line (B2 to D1). Several other important observations can be made from this image. First, the island forms a wave shadow on the southern side of the island, where no waves can be seen on the SAR image. This indicates the waves are coming from the north. Second, the extensive reef at Abraham Bay (D4 to E3) is not detected on the SAR image. There are several possible reasons for this: (1) no waves are breaking on this reef (because of the island shadow), hence no breaker line; (2) there are no current-induced surface patterns because of low tidal current velocities; or (3) if tidal generated surface patterns are subtle, the SIR-A SAR is not sensitive enough to detect these surface patterns.

Figure 17 presents SIR-A imagery of the western portion of the Caicos Islands, while Figure 18 depicts a portion the hydrographic chart from this area (after DMA Chart No. 26260). On this image, the coral reefs on the western (D4 to D6) and northern portion (D3 to F1) of the islands are again detected. It is not known if the large gap in the imagery at location C6 is due to a gap in the reefs or no breaking waves. There is also a region of subtle changes in radar image intensity along the southern edge of the Caicos Bank (F7 to H6). These patterns occur quite near the southern edge of the Caicos Banks, and therefore may be bottom related. However, they
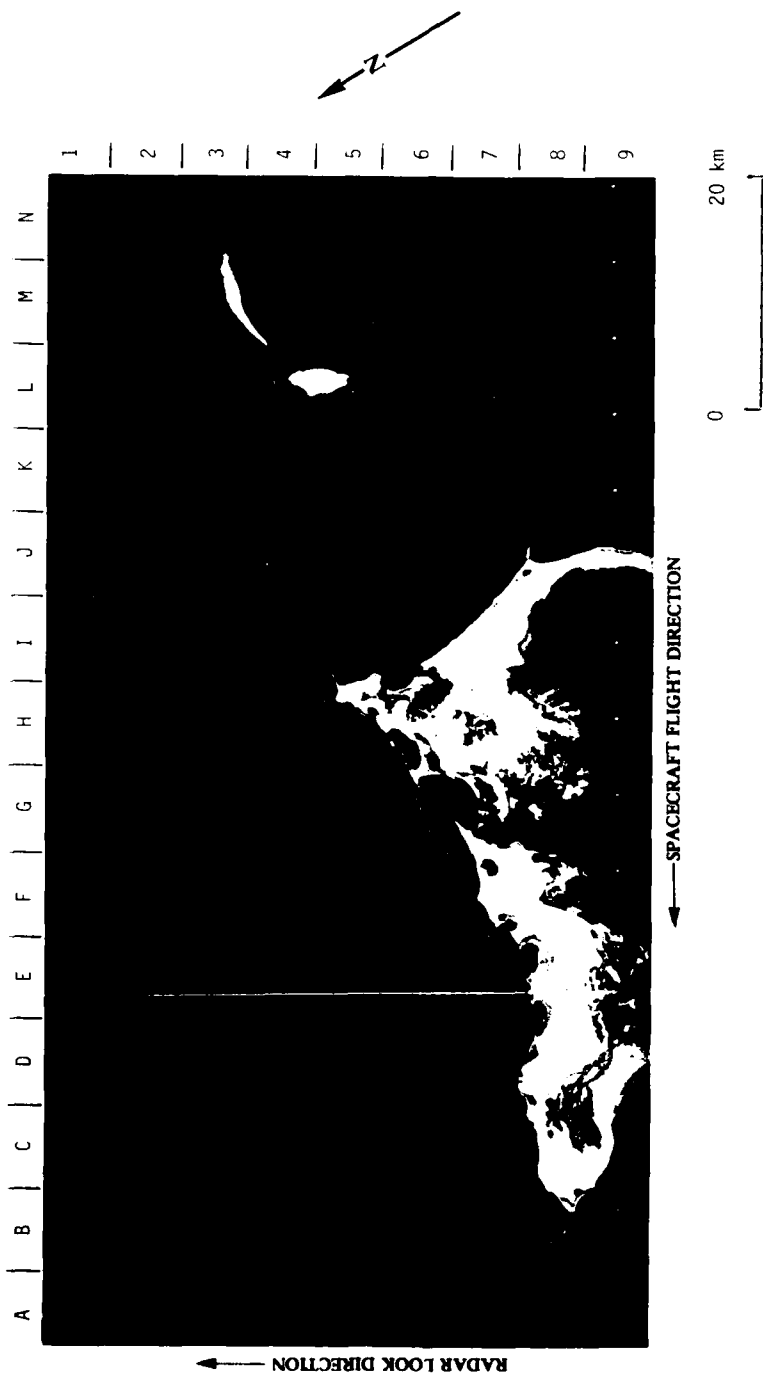
Figure 12. SIR-A SAR Imagery of Crooked Island, Acklins Island, and Plana Cays, Bahamas (Data Take 24 BB, 13 November 1981, Imagery Courtesy of NASA).
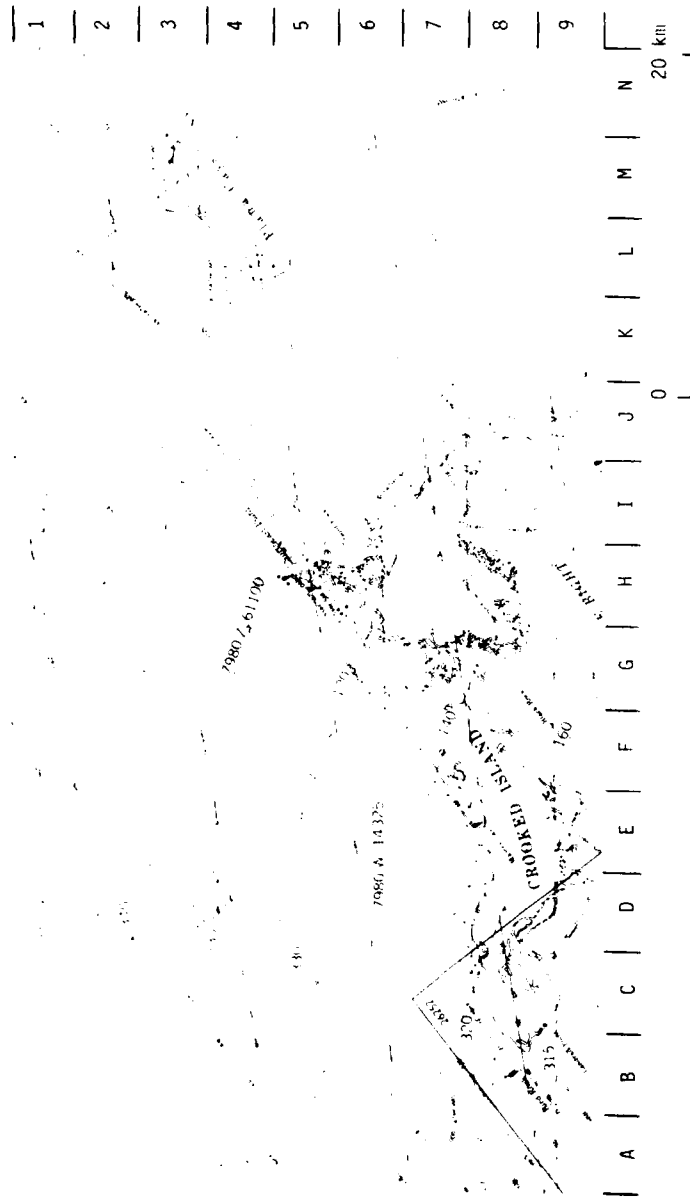
Figure 13. Hydrographic Chart of Crooked Island, Bahamas Region (After DMA Chart No. 26280, Depths in Fathoms and Feet)

55

Figure 14. Cruising Guide Chart to Crooked Island Bahamas (After Kline, 1981)
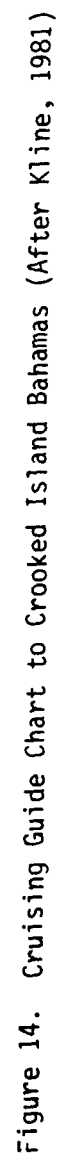
are quite similar in appearance to surface patterns associated with wind slicks or surface upwelling slicks (see Ford, et al., 1983), which may or may not be related to a bottom feature.

3.2.2 TONGUE OF THE OCEAN

SIR-A imaged the Tongue of the Ocean (TOTO) region of the Bahamas during Data Take 18 at approximately 13:30 GMT on 13 November 1981. The imagery from this overpass is presented in Figure 19, with the corresponding bathymetry shown in Figure 20. This particular region was extensively imaged by Seasat and has been analyzed during previous year's efforts (see Kasischke, et al., 1982). Although faint, surface patterns similar to those observed on Seasat SAR imagery are also present on the SIR-A imagery (D7).

Examination of the tide charts for this area (Kline, 1981) reveals that high water occured at 13:26 GMT, almost coincident with the SIR-A overpass. The current model developed for this region (Kasischke, et al., 1982) indicates little or no currents at high water. Since the presence of a current is believed to be necessary for the appearance of bottom-related surface patterns in this region (see Kasischke, et al., 1983), it is not surprising that SIR-A did not detect more distinct patterns over the TOTO region.

3.2.3 EASTERN AUSTRALIA

Figure 21 presents SAR imagery collected by SIR-A during Data Take 22 off the northeast coast of Australia on 13 November 1983 at approximately 17:35 GMT. By comparing the positions of the numerous ovate patterns in the SAR image to the bathymetric chart of this region in Figure 22, we can see that these patterns correspond to the numerous coral reefs in this area.

The tide tables for this region indicate that the tidal stage at the time of the Seasat overpass was approximately one hour before low water. Since the reefs in this region uncover at low water, it

N

A | B | C | D | E | F | G | H

1 2 3 4 5 6 7 8 9

RADAR LOOK DIRECTION →

← SPACECRAFT FLIGHT DIRECTION

0   20 km
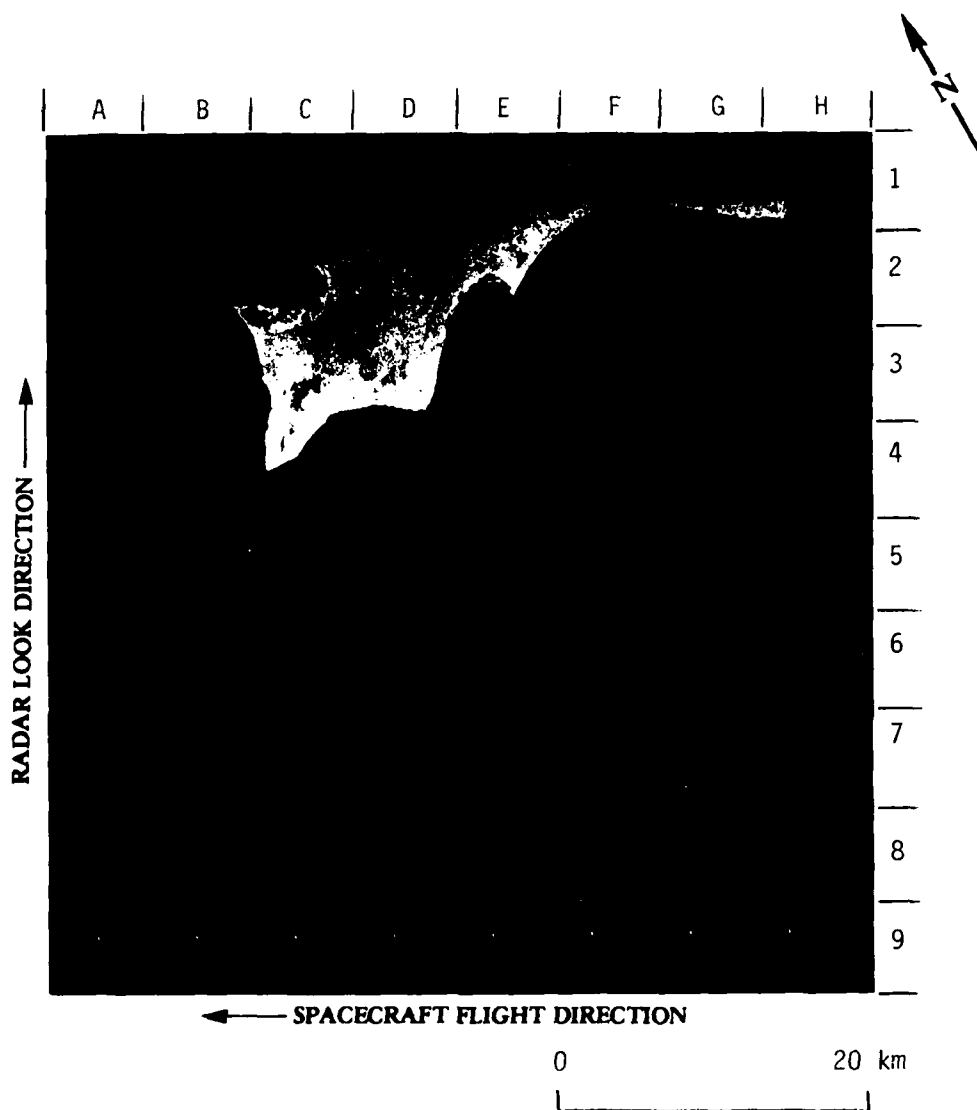
Figure 15.   SIR-A SAR Imagery of Mayaguana, Bahamas (Data Take 24 BB, 13 November 1981, Optically Processed Imagery Courtesy of NASA)
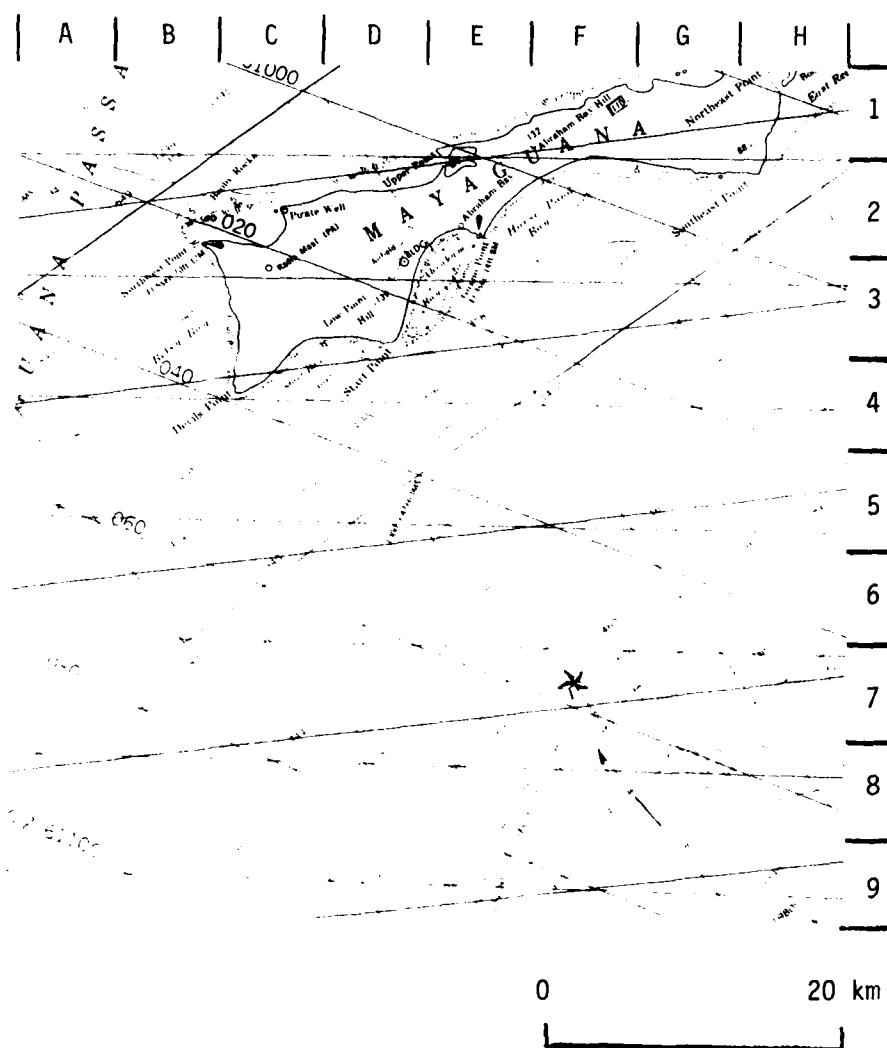
Figure 16.   Hydrographic Chart of Mayaguana, Bahamas (After
             DMA Chart No. 26260, Depth in Fathoms and Feet)
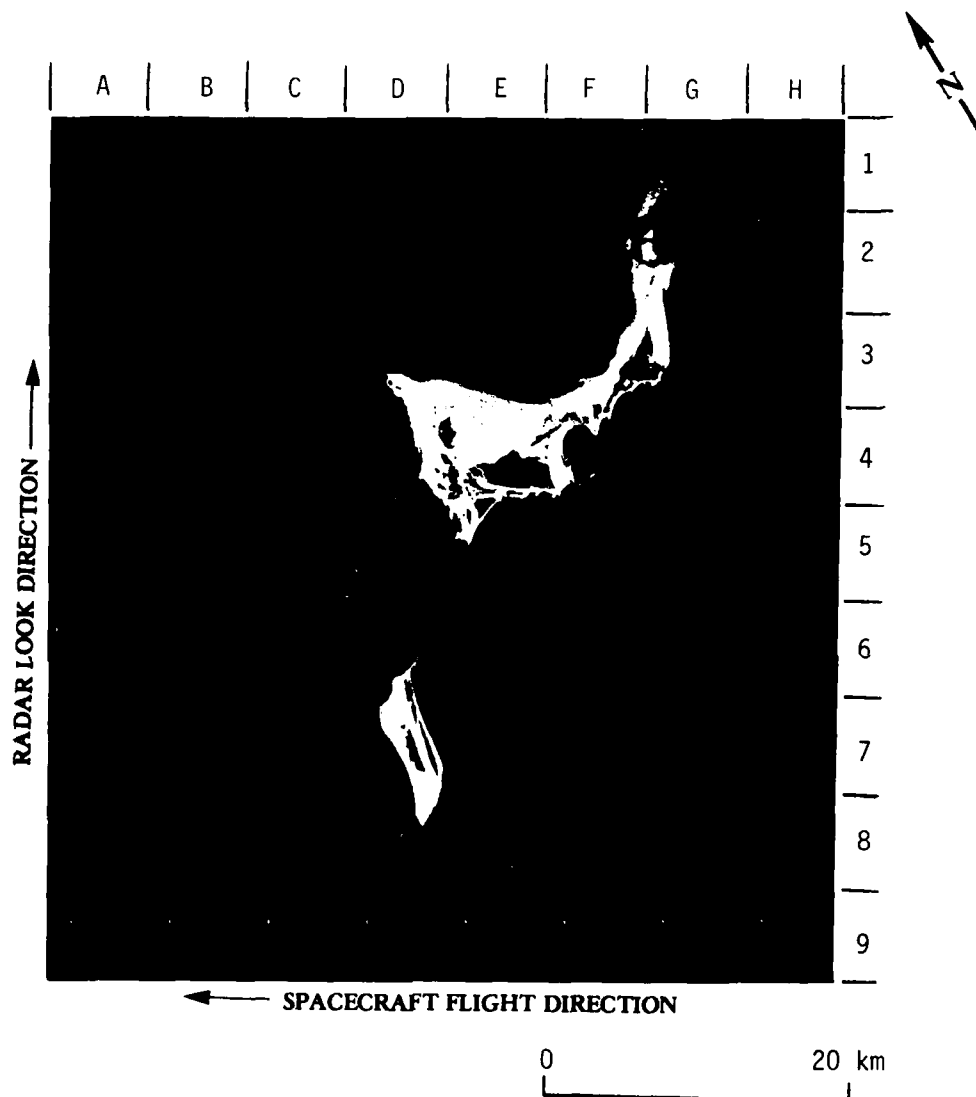
Figure 17. SIR-A SAR Image of Caicos Islands, Bahamas (SIR-A Data Take 24 BB, 13 November 1981, Optically Processed Imagery Courtesy of NASA)

60
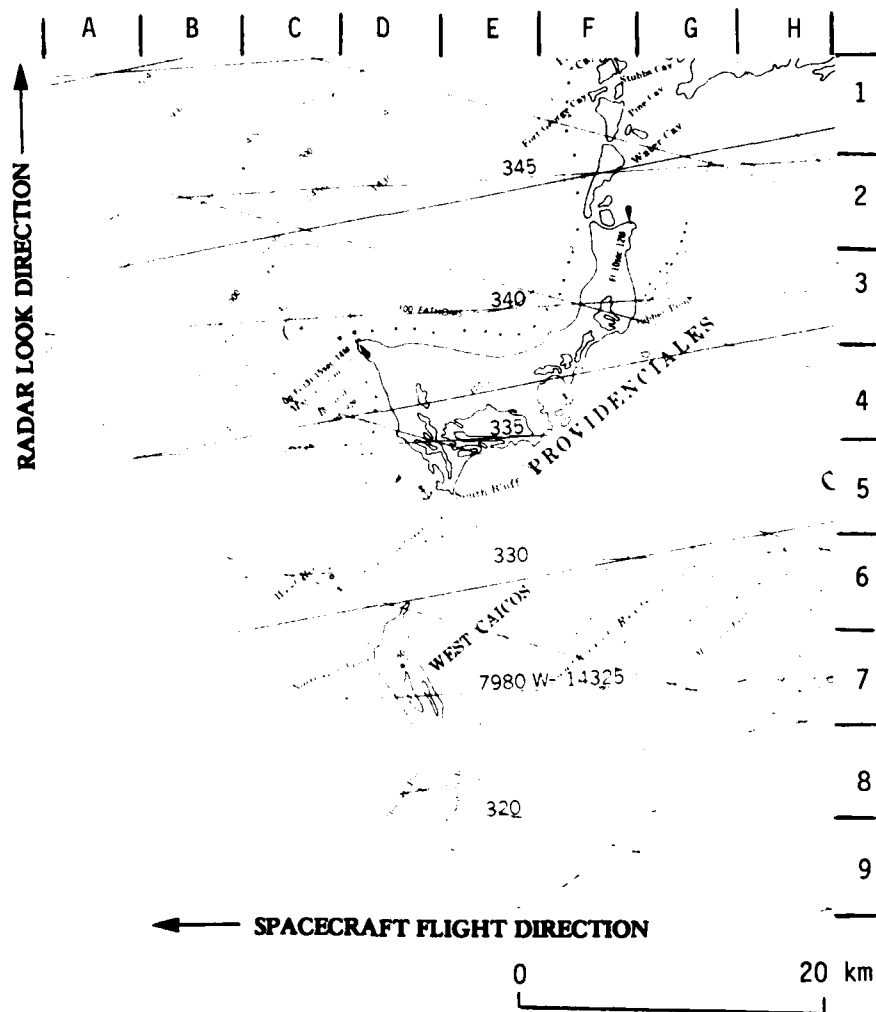
Figure 18.   Hydrographic Chart of Caicos Islands,
             Bahamas (After DMA Chart No. 26260,
             Depth in Feet and Fathoms)

61
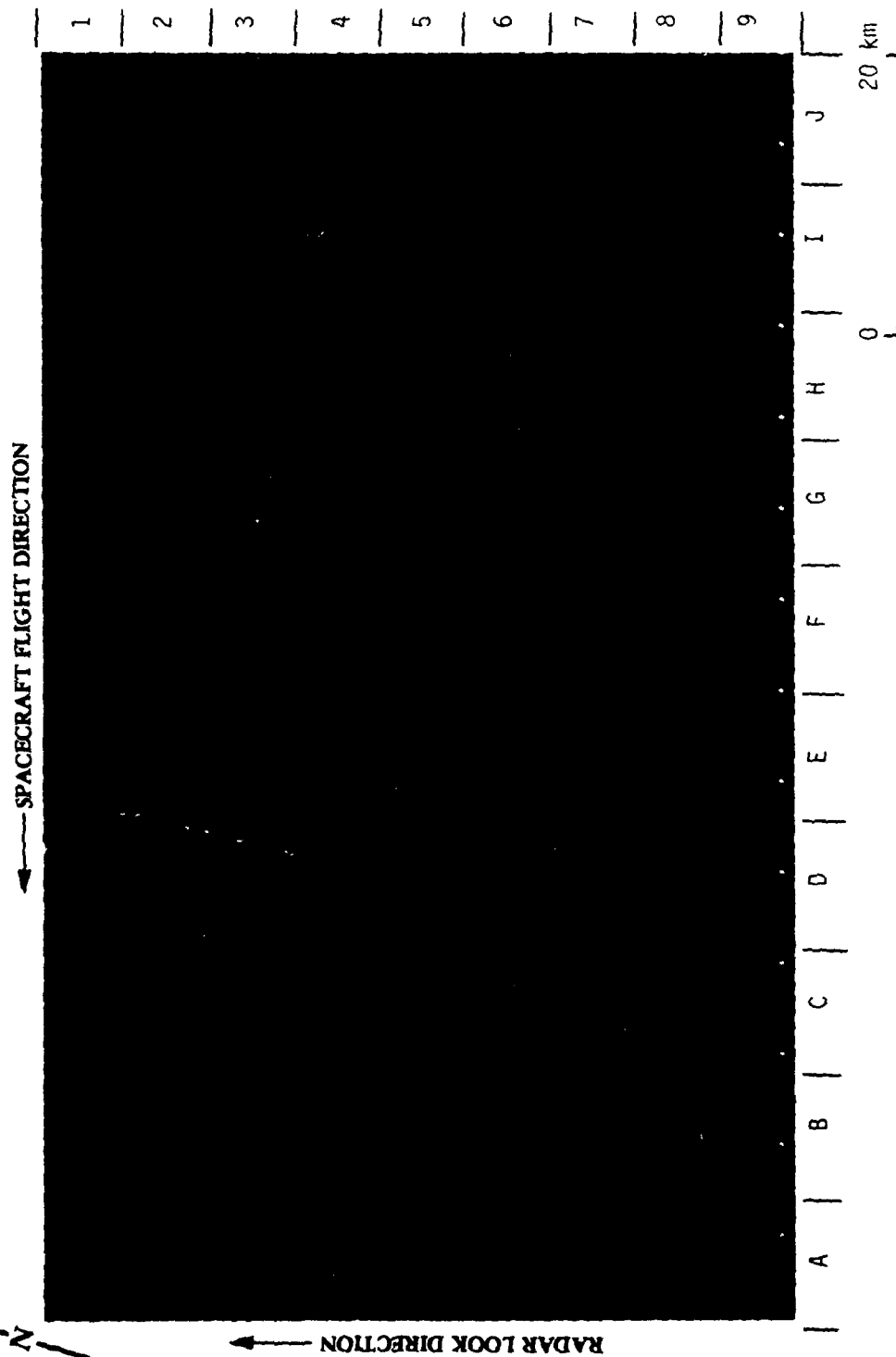
Figure 19. SIR-A SAR Image of Tongue of the Ocean (Data Take 18, 13 November 1981, Optically Processed Imagery Courtesy of NASA)
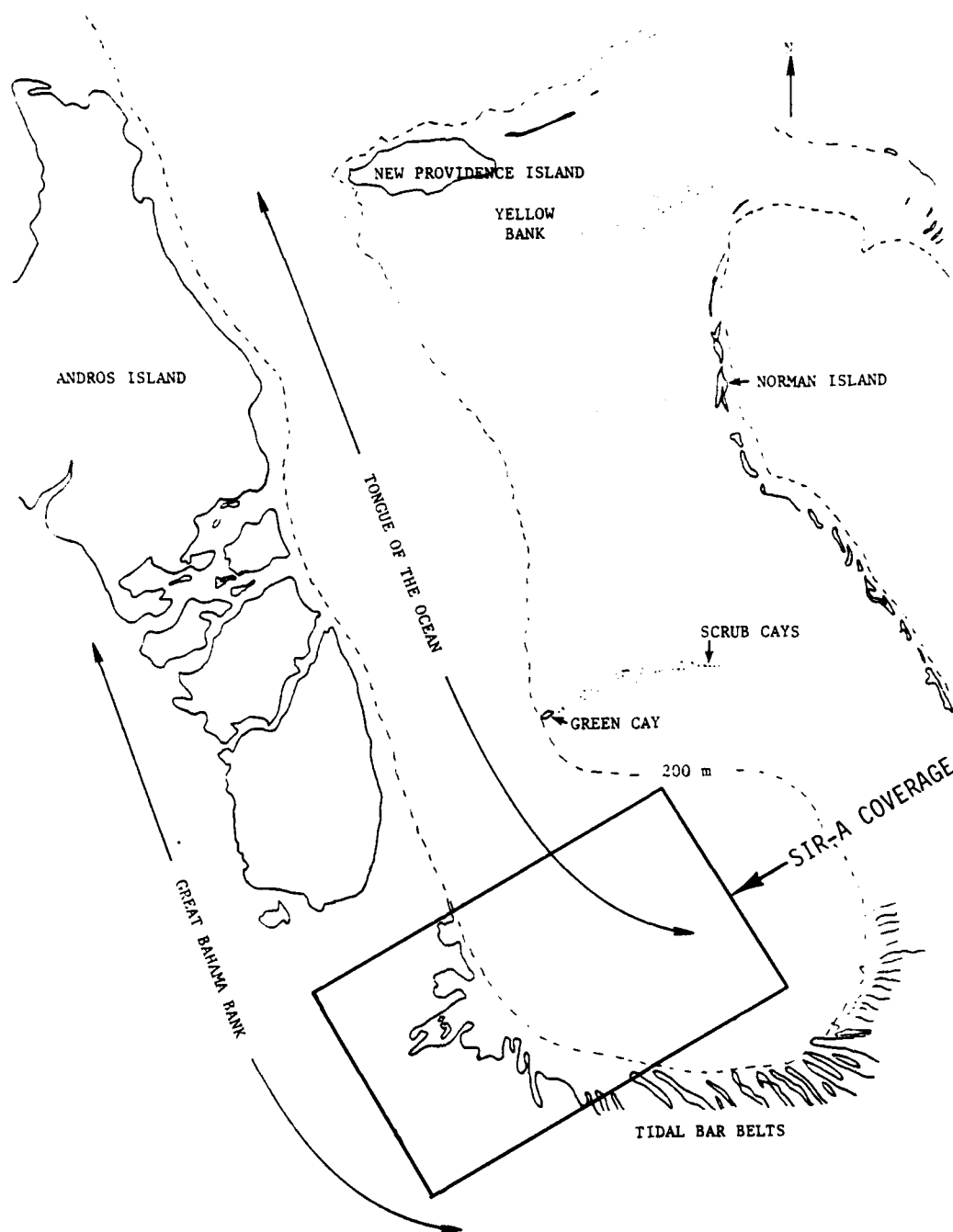
Figure 20. Ground Coverage of SIR-A Imagery in Figure 19

63
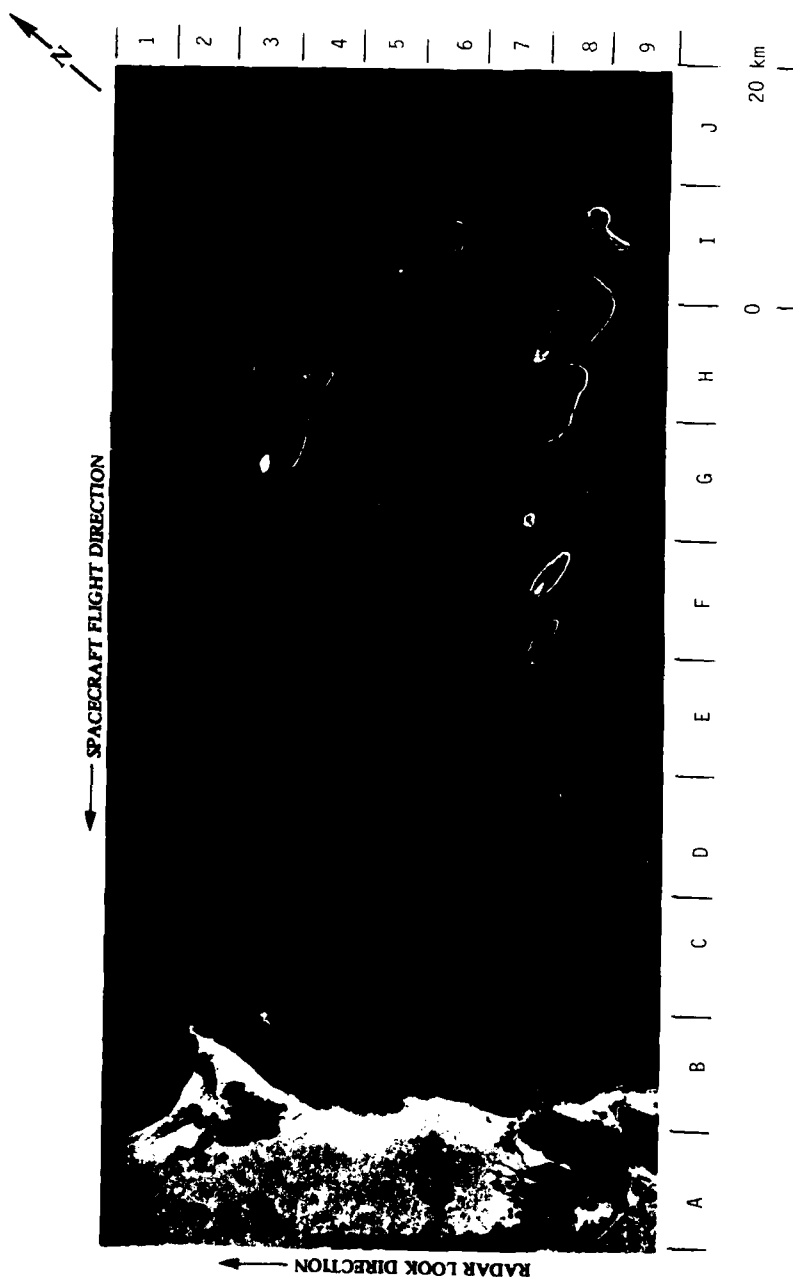
Figure 21. SIR-A SAR Image of Eastern Australian Reefs (Data Take 22, 13 November 1981, Optically Processed Imagery Courtesy of NASA
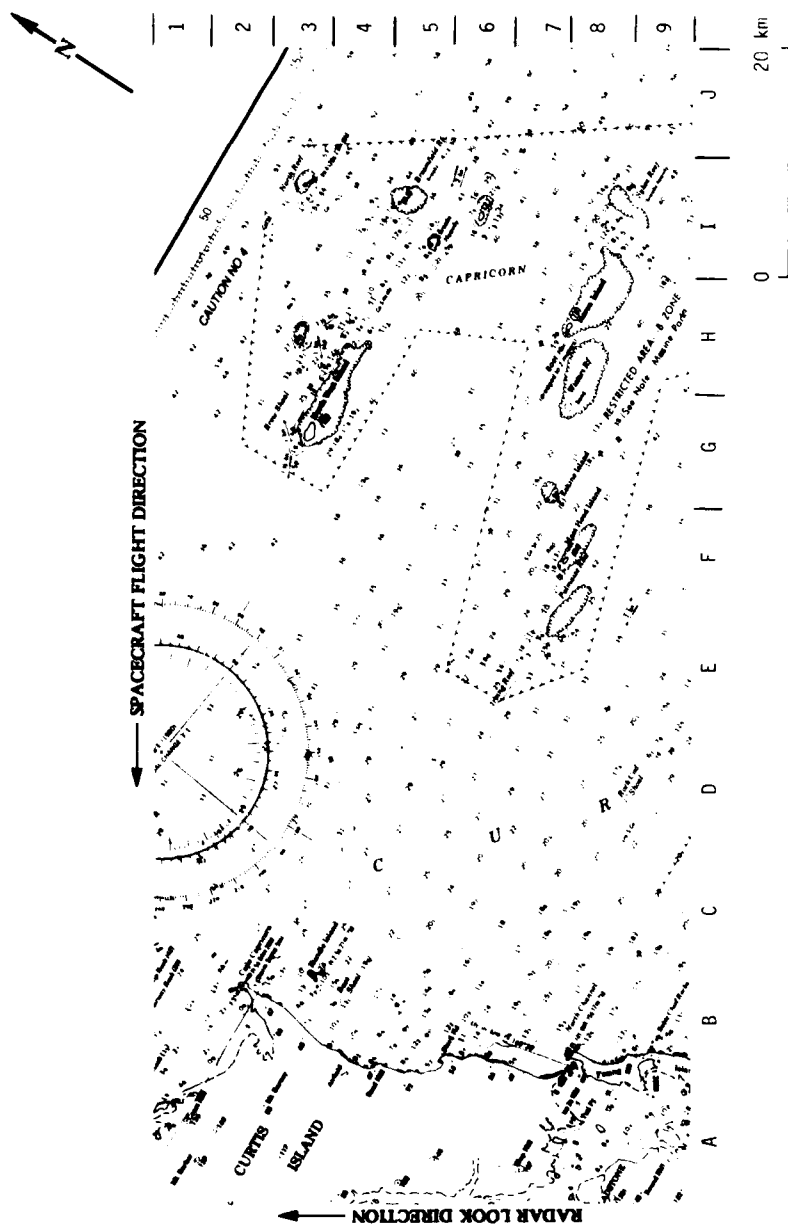
Figure 22. Hydrographic Chart of Northeastern Shore of Australia (After DMA Chart No. 74200, Depths in Fathoms)

65

is possible that the patterns in Figure 22 are the result of emergent reefs, although they may be surface patterns on the ocean due to the gravity waves breaking on the reefs.

3.2.4 DISCUSSION

Although the SIR-A SAR was not optimized to collect data over water, surface patterns did exist on its imagery which were correlated to bottom features. These examples serve to illustrate that a shuttle-based SAR can be used to collect useful SAR imagery for detection of navigation hazards.

The SIR-A images presented in this section also illustrate another method whereby SAR images can be used to detect a shallow-water bottom feature. The bright line where the gravity waves are breaking on the coral reefs clearly delineates the outer edge of the reef. No examples like these were found in the Seasat SAR data set. However, no gravity waves were detected on Seasat images in the regions of coral reefs either, probably because of the lack of a large enough ambient swell.

The above SIR-A images reinforce several important concepts concerning the use of SAR imagery (both SIR-A and Seasat) to detect bottom features. The gravity wave field present on the imagery is an important factor from several standpoints. First, the gravity wave pattern dictates what to look for, and second, it dictates where on the image to look. With a gravity wave field, we now know to look for three surface patterns: (1) refraction patterns; (2) changes in radar image intensity; and (3) bright lines which indicate regions of breaking waves. We can also determine the direction of the waves by looking at wave shadowing. This shadowing is important because we would not expect to find bottom-related surface patterns associated with gravity waves in those areas where gravity waves do not occur. Therefore, this is a clue to the hydrographer as to where to look. Finally, throughout the summer months in the Carribean, the

66

prevailing winds are from the southeast, and usually do not build up any significant longperiod swell. However, the storms in the fall/winter, which come from the north, usually produce a long period swell, which then propagate into the Carribean and can break on reefs. This illustrates the necessity of selecting imagery from different time periods to take advantage of differing environmental conditions, which are important in detecting certain bottom features.

3.3 APD-10 SAR DATA

During the past several years, two shallow-water coastal areas have been extensively imaged by the aircraft APD-10 SAR system. These two areas included the southeast coast of the North Sea, which was imaged during the fall of 1979 during the Maritime Remote Sensing (MARSEN) experiment, and the Nantucket Shoals area, which was imaged during the Naval Research Laboratory Remote Sensing Experiment in the summer of 1982.

The APD-10 system (built by Goodyear Aerospace) is a high resolution side-looking reconnaissance radar operating at X-band (3.2 cm) and carried aboard a U.S. Marine F-4. The APD-10 has six modes of operation, which provide a variety of standoff distances and also provide either fixed target imagery (FTI) along with moving target imagery (MTI). Imagery can be obtained from either side of the aircraft.

For the data presented in this paper, Mode 1 was used in which FTI is recorded on 24 cm (9.5 inch) film in four channels. Each channel is nominally 4.6 km (2.5 nmi) in width with an additional 0.46 km (0.25 nmi) overlap between adjacent channels. The nominal resolution of the APD-10 is approximately 3 m in both azimuth and slant range and is independent of altitude. The fixed slant-range distance to the near edge of the recorded data is 4.6 km (2.5 nmi). The nominal platform velocity of the APD-10 system is approximately

210 m/s. Table 10 lists the parameters of the UPD-10 system which are of interest.

In the remainder of this section, APD-10 SAR imagery from both the MARSEN and NRL Experiments test sites will be presented. This imagery contains numerous surface patterns which are demonstrated to be bottom related.

3.3.1 MARSEN DATA

The MARSEN experiment was conducted in the southern part of the North Sea during August and September of 1979 with the primary goal of further developing remote sensing techniques for the retrieval of oceanographic information (see Shuchman, et al., 1983). The data collected during this experiment included both remotely-sensed and in situ measurements.

As part of the MARSEN experiment, APD-10 SAR imagery was collected over two instrumented towers located in the North Sea. The Nordsee Tower was located in 30 m deep water approximately 80 km due west of the German island of Sylt, while the Noordwijk Tower was located in 10 m deep water approximately 10 km west of the Dutch Coast (see Figure 23). During each SAR data collection mission (called a "Line") a number of passes were flown over one of the two towers in order to image wind-generated gravity waves. During the lines over the Noordwijk Tower, a pass was also made over the south-eastern shore of the North Sea. SAR imagery collected during this pass on two separate dates forms the data set for the present analysis.

3.3.1.1 Methods

SAR imagery from Line 8 (collected on 25 September 1979 at 1330 GMT) and Line 6 (28 September 1979, 1320 GMT) were used in this analysis. Two test sites from each pass were selected; Borkum Island and Cuxhaven near the mouth of the Elbe River (see Figure 24).

TABLE 10
NOMINAL APD-10 RADAR PARAMETERS (MODE 1)

Vehicle Velocity	210 m/s
Along-Track Beamwidth	1.5°
Incident Angle	0 – 90°
Swath Width	18.5 km Slant Range (four 4.63 km subswaths)
Wavelength	0.032 m
Polarization	HH
Maximum Range	23.2 km
FM Rate	105 MHz/μsec
Pulse Width	0.95 μsec
Resolution	3 m Slant Range
	3 m Azimuth
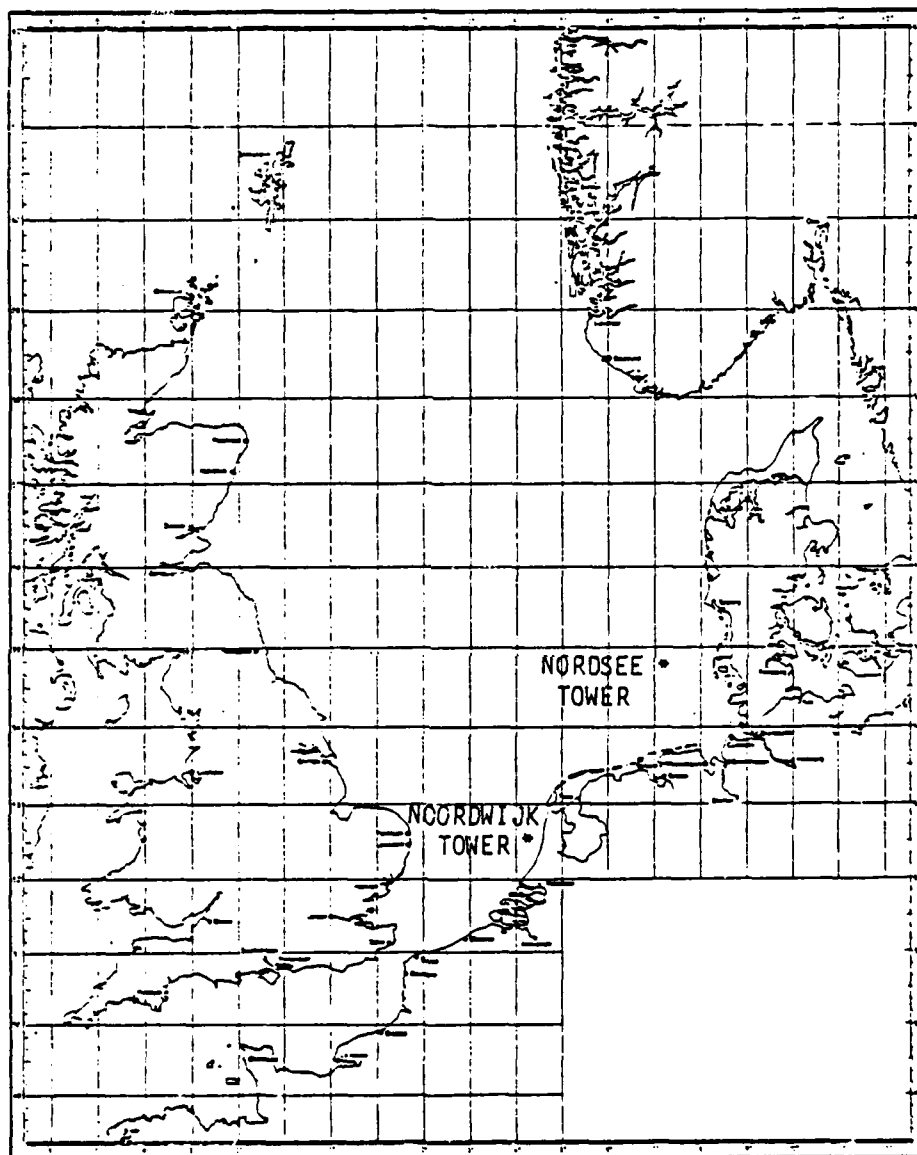
Figure 23. Map of Southeastern North Sea Showing Locations
of Noordwijk and Nordsee Test Towers
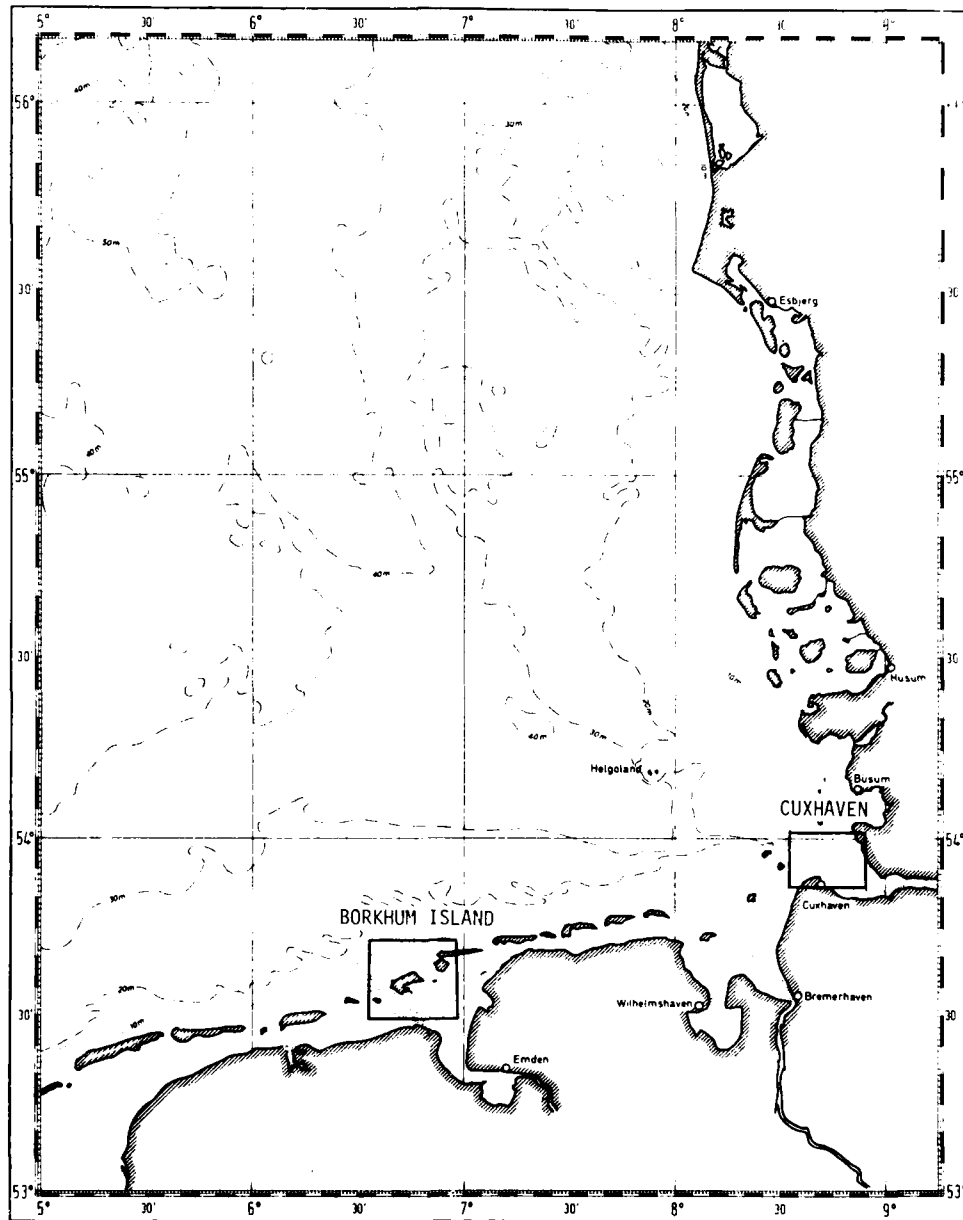
Figure 24. Location of MARSEN Test Sites

The APD-10 SAR data collected during MARSEN were precision opti-
cally processed and reviewed at ERIM. The data from two test sites
on the two different days were selected because they contained repre-
sentative examples of SAR observed surface patterns present on this
imagery and also because there were different tidal conditions pres-
ent at the time of the two overflights. Positive prints of the
imagery were obtained from all four channels of the data and mosaics
were produced. Clear cell overlays of the hydrographic charts to
the same scale as the SAR imagery (1:100,000) were generated. Cor-
relation between the SAR surface patterns and the bottom features in
the region were noted. Ancillary environmental data for each area
were obtained to better understand the hydrodynamic mechanisms re-
sponsible for the generation of the SAR-observed ocean surface
patterns.

3.3.1.2 Results

Figures 25 and 26 present APD-10 SAR imagery collected over the
Island of Borkum on 25 and 28 September, respectively. A portion of
the hydrographic chart for this area is presented in Figure 27.
Table 11 summarizes the ancillary environmental data available for
these dates.

One observation which is immediately apparent from a comparison
of the two images is that the tidal height (above the chart datum)
was higher on 25 September than it was on 28 September. The evidence
for this observation is that there is more exposed, dry land on
Figure 26 than on Figure 25 (compare Memmert, Borkum, and
Rottumeroog and Lutje Horn Islands). The tide tables for these dates
indicate just the opposite (see summary in Table 11), i.e., the pre-
dicted tide height was greater on 28 September. One possible ex-
planation for this difference is that the offshore wind on 25
September reduced the rising tide while the on-shore wind on 28
September added to the rising tide. Thus, it appears the tide
stages are not accurately reflected by the tables.

72

RADAR LOOK DIRECTION ⟶

FLIGHT DIRECTION ⟶

N

0   2 km

Figure 25. APD-10 X-Band SAR Imagery Collected Over Borkum Island, Holland (Line 8, 25 September 1979)

Figure 26. APD-10 X-Band SAR Imagery Collected Over Borkum Island (Line 6, 28 September 1979)

Figure 27. Hydrographic Chart of Borkum Island (After Dutch Hydrographic Service, 1982, Depths in Meters)

TABLE 11

SUMMARY OF ENVIRONMENTAL CONDITIONS DURING MARSEN EXPERIMENTS

| | | Wave Parameters | | | Wind Conditions | | Tide Conditions | | | |
| | | | Propagation* | | | | Borkum | | Cuxhaven | |
Line	Date	Period (sec)	Direction (°True)	Height	Speed (ms⁻¹)	Direction** (°True)	Stage	Height***	Stage	Height***
8	25 September	5.0	055	0.7	5.0	235	1.5 hours after high water	-2.2 m	1 hour after high water	-3.0 m
6	28 September	8.0	150	1.0	3.5	330	at high water	-2.4 m	1.7 hours before high water	-2.4 m

*Direction waves are propagating towards
**Direction wind is coming from
***Water level above chart datum.

It is clear from the APD-10 SAR images that most of the mud- and sand-flats of this region are underwater at the times of the SAR overpasses, and the land-water boundaries are distinct in the SAR images. A portion of the hydrographic chart for this region (see Figure 27) does not give an accurate portrayal of the shapes of the islands of Memmert, Borkum, Juist, Lujte Horn, and Rottumeroog.

At first inspection, there does appear to be bottom information on the APD-10 SAR imagery. For instance, on Figure 26, the channel between Borkum and Juist (H5 to L7), is visible on the SAR image as a region of darker radar return. The shoal region to the north of this channel appears as a series of bright streaks. The shoal regions to the west of Borkum and Memmert (D4 and K4), to the west of Juist (L4) and to the west of Lujte Horn (L7) also appear as bright streaks on both the images. However, there is no real consistent correlation between all the shallow water features and the SAR imagery in this area (for example, the channels south of Borkum).

Figure 28 presents APD-10 SAR imagery collected on 25 September 1979 near Cuxhaven, West Germany, while Figure 29 presents imagery collected over the same region on 28 September. Figure 30 presents a portion of the hydrographic chart for this region. Figure 28 contains some patterns which are related to bottom features. The shoal areas north of Cuxhaven (C6 to C8) and at the southwest edge of Gelb Sand (A1 to B3) appear as bright streaks on the imagery. Similar patterns are visible on Figure 29, as well as numerous other patterns.

Although there appears to be a greater number of patterns in Figure 29 which are bottom related, it is difficult to consistently correlate these patterns to any identifiable features on the map. The channel at position F5 to H6 is clearly present as a dark radar return, whereas the channel at position F3 appears as a series of bright streaks. Many of the other patterns cannot be so readily matched.

Recent analysis of MARSEN SAR data collected over deep-water areas has indicated that breaking waves result in the bright azimuth-oriented streaks present throughout much of the APD-10 SAR imagery collected over the North Sea (Lyzenga and Shuchman, 1983). In the deep-water MARSEN data, these azimuth streaks appear throughout the imagery, whereas in the shallow water data, there appears to be a concentration of these streaks over shallow water features in certain cases. Whether these streaks are due to wave breaking or current effects is not known at this time.

In summary, the APD-10 X-band SAR images collected during MARSEN present a very complex situation. Not only are there numerous shoals, a complex bottom topography and tidal channels within the region, but additionally there appears to be an azimuth streaking phenomena which confuses interpretation of the data further.

3.3.2 NRL REMOTE SENSING EXPERIMENT DATA

Seasat SAR imagery collected over the Nantucket Shoals during Rev. 880 (see Figure 31) generated considerable interest in both the SAR and oceanography scientific communities because of the many surface patterns which were found to be correlated to bottom features (as documented in previous DMA/NRL studies; see Kasischke, et al., 1980; 1982; and Shuchman, 1982). A workshop was held at Woods Hole Oceanographic Institute in August of 1980 to define and plan an experiment to further study the SAR-observed patterns in the Nantucket Shoals region (Valenzuela and Chen, 1983). The purpose of this experiment was to gain a better understanding of both the hydrodynamic and electromagnetic mechanisms responsible for bottom-related surface patterns on SAR imagery. This goal was to be achieved by collecting aircraft SAR imagery simultaneously with meteorologic and oceanic measurements over a sand bank in the Nantucket Shoals region. An experiment was subsequently planned and carried out by the Naval
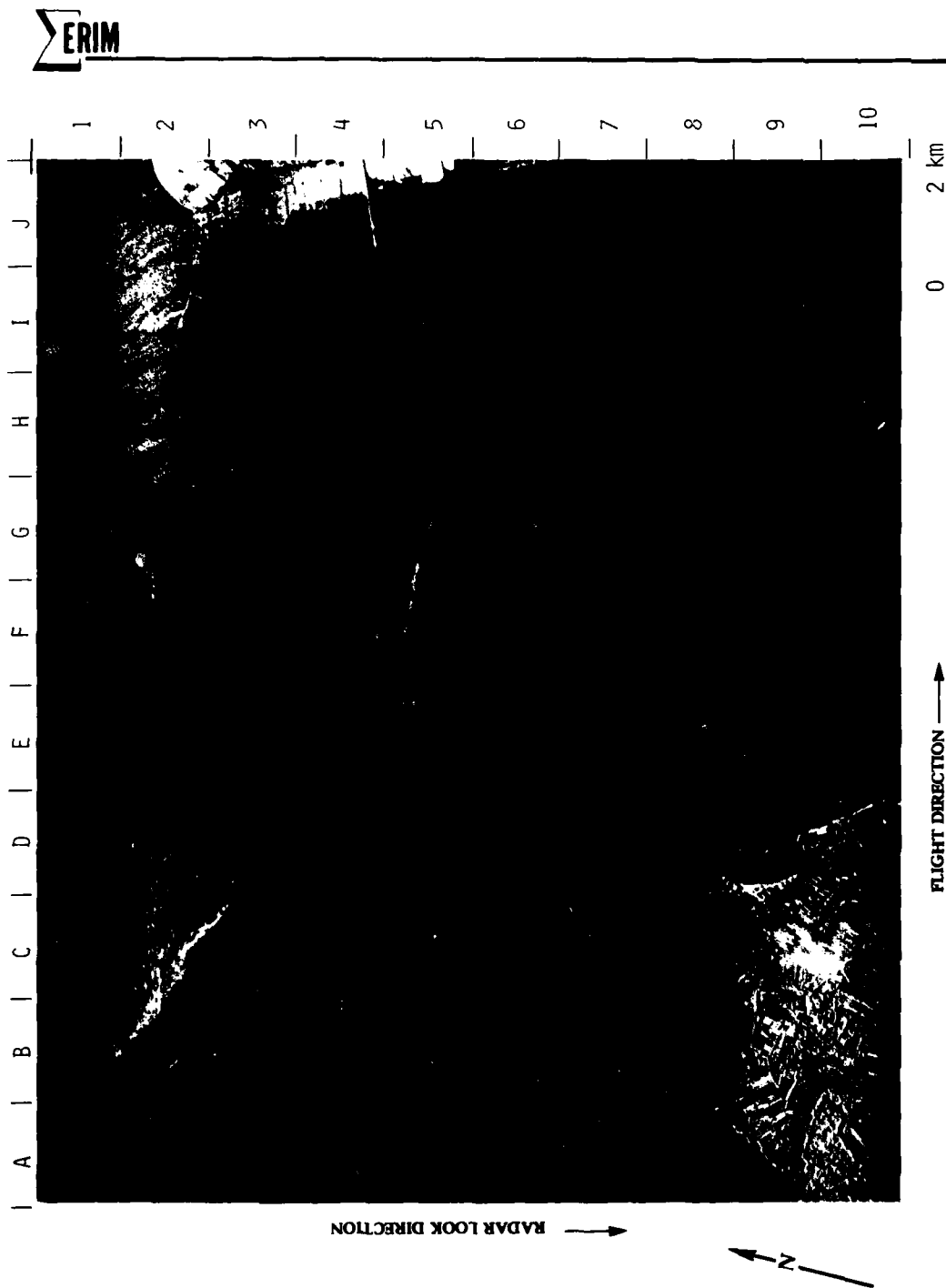
Figure 28. APD-10 X-Band SAR Imagery Collected Over Cuxhaven, West Germany (Line 8, 25 September 1979)

FLIGHT DIRECTION →

RADAR LOOK DIRECTION →

N

0   2 km

79

Figure 29. APD-10 X-Band SAR Imagery Collected Over Cuxhaven, West Germany (Line 6, 28 September 1979)

Figure 30. Hydrographic Chart of Cuxhaven, West Germany Area (After DMA Chart No. 37226, Depths in Meters)

81

Figure 31.   Seasat SAR Image of Nantucket Shoals   (Rev. 880, 27 August
1978; Digitally Processed Imagery Courtesy of JPL)

Research Laboratory (NRL). Based on results from the present investigation, we will discuss the correlation between the surface patterns imagery present on the data collected during NRL Remote Sensing Experiment and the bottom features in the area.

The NRL Remote Sensing Experiment took place during July of 1982 off Nantucket Island, Massachusetts. Although the primary study site was the Phelps Bank, aircraft SAR imagery was collected over the entire Nantucket Shoals region. The extent of the test site is indicated by the solid line on Figure 32. SAR data was collected by two U.S. Marine Corps RF-4 reconnaissance aircraft (identified as Aircrafts 10 and 23 or AC10 and AC23). The USNS Hayes was stationed near the Phelps Banks and performed extensive measurements of the surface wind, current and wave conditions, in addition to other environmental observations. A single mission for four days (11-14 July 1982) was scheduled for each aircraft.

Seven flight lines were planned for each mission. Because of weather conditions and equipment failures, one mission was flown by each aircraft on 11 July and one mission was flown by a single aircraft on 13 July. Because of the fuel consumption, only 6 out of 7 planned flight lines were collected during each mission. These lines are presented in Figure 33. The flight lines for the 13 July mission were modified from the original experiment plan. Figure 34 presents these modified flight lines. Table 12 summarizes important aircraft parameters for each mission, while Table 13 summarizes the ground track locations of each mission.

3.3.2.1 Analysis Methods

The analysis of the NRL Experiment SAR data set consisted of two phases: (1) correlation of the SAR-observed surface patterns to local bathymetric features, and (2) correlation of a subset of all SAR-observed surface patterns to the ancillary environmental data.

83
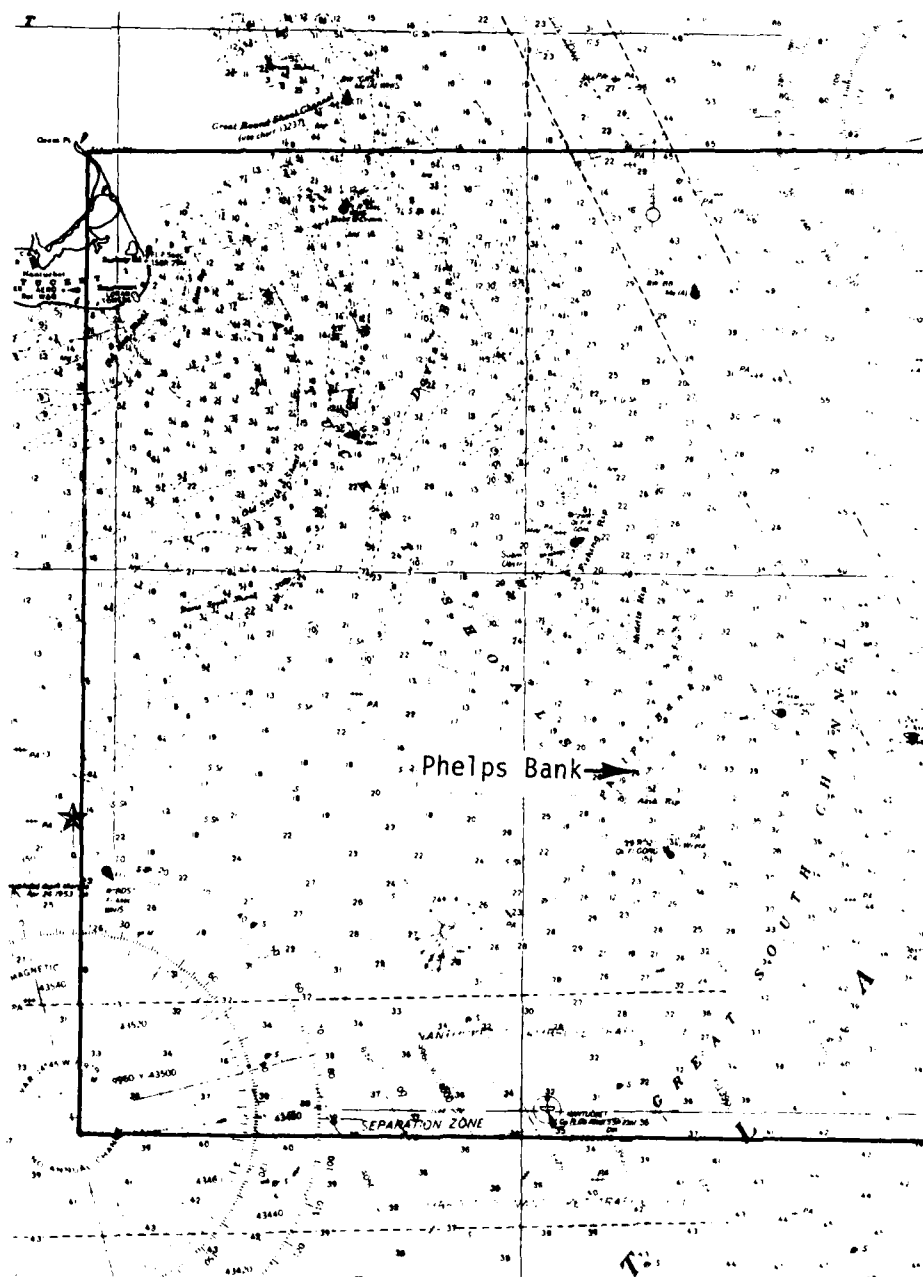
Figure 32.   Location of NRL Remote Sensing Experiment Test Site
              (After NOS Chart No. 13200. Depth in Fathoms)

84
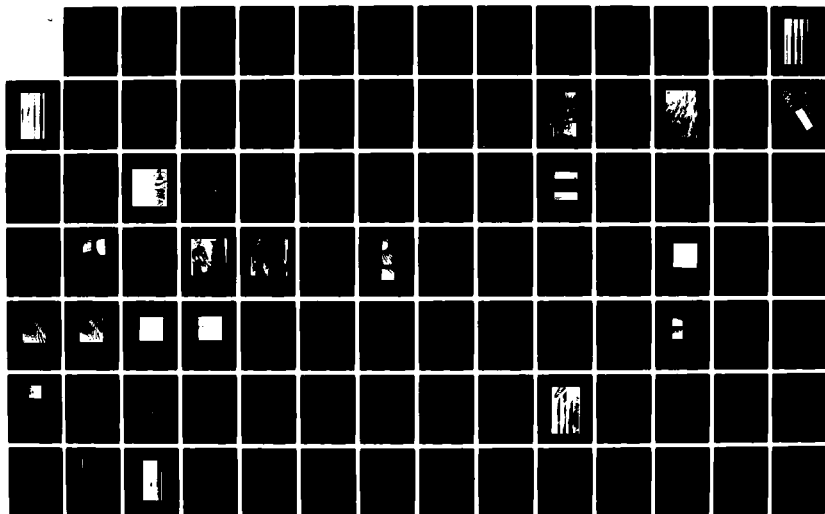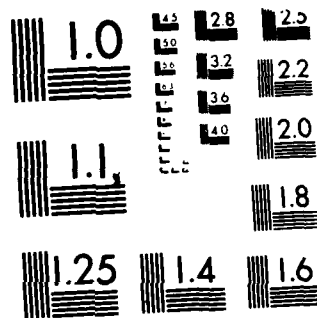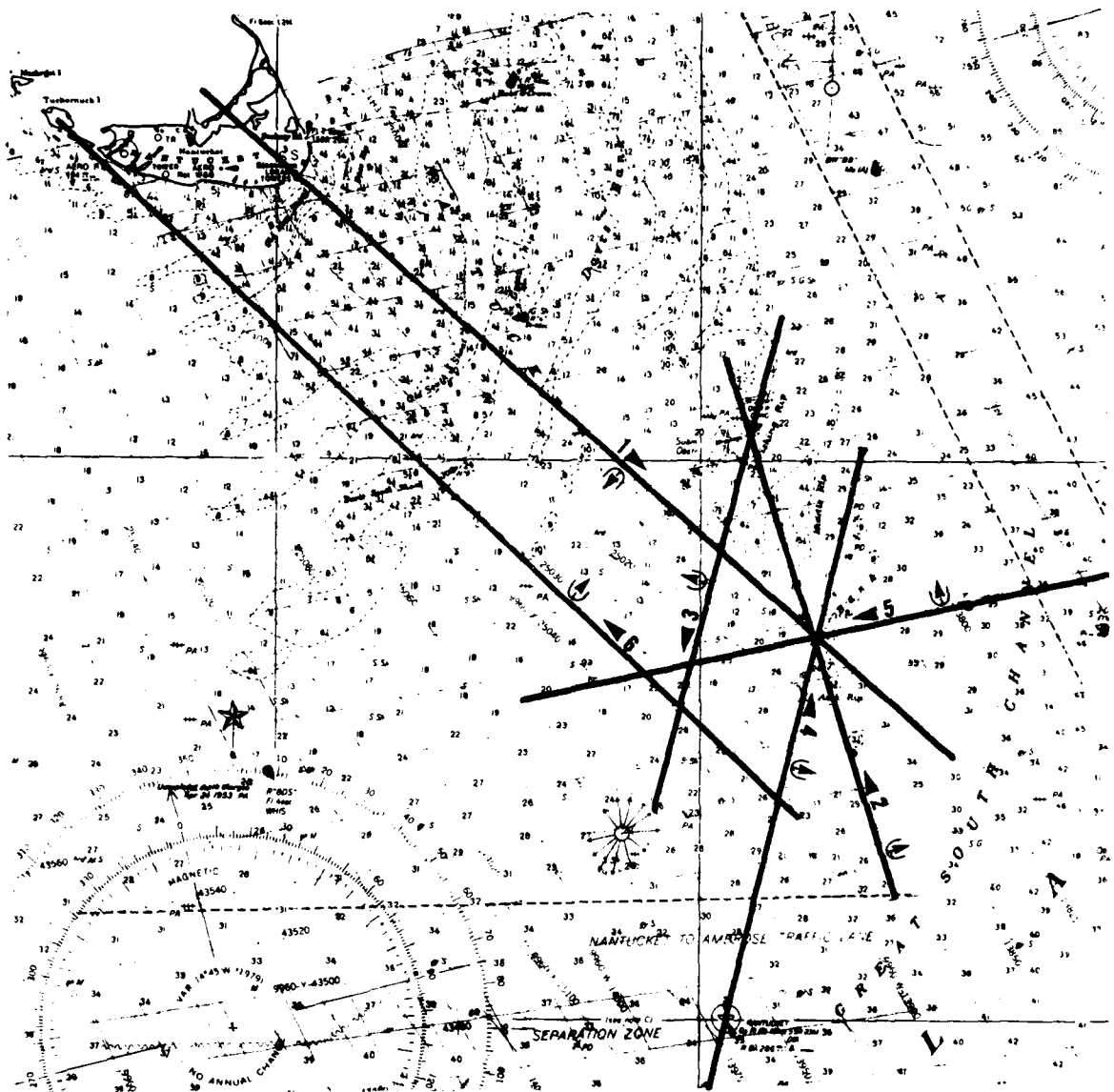
Figure 33.   Proposed Flight Lines for APD-10 SARs During the NRL Remote Sensing
Experiment

Figure 34.   Modified Flight Lines for APD-10 SARs During the
NRL Remote Sensing Experiment

TABLE 12
SUMMARY OF FLIGHT PARAMETERS
FOR APD-10 SAR FLIGHTS

Date	A/C No.	Pass No.	Time (EDST)	Ground Track (° True)	Radar Look Direction	Aircraft Altitude (ft.)
11 July 1982	10	4	1522-1528	13.6	R	11,000
11 July 1982	10	5	1532-1538	257.8	R	11,000
11 July 1982	10	2	1542-1546	342.9	R	11,000
11 July 1982	10	3	1550-1555	194.4	R	11,000
11 July 1982	10	6	1559-1608	312.6	R	11,000
11 July 1982	23	1	1435-1442	131.2	R	11,500
11 July 1982	23	2	1448-1453	343.2	R	11,300
11 July 1982	23	3	1457-1502	194.2	R	11,400
11 July 1982	23	4	1508-1512	15.4	R	11,400
11 July 1982	23	5	1517-1522	258.1	R	11,400
13 July 1982	10	2+	1411-1416	162.0	L	11,000
13 July 1982	10	3*	1453-1457	194.0	R	11,000
13 July 1982	10	4*	1420-1427	13.0	L	11,000
13 July 1982	10	5*	1430-1436	258.0	R	11,000

+Pass flown in reverse direction
*Flight lines modified

TABLE 13
GROUND COORDINATES FOR APD-10 SAR PASSES

Pass No.	Start Position				End Position			
	Near Edge		Far Edge		Near Edge		Far Edge	
	Latitude	Longitude	Latitude	Longitude	Latitude	Longitude	Latitude	Longitude
1	41°21.3'N	70°02.4'W	41°13.4'N	70°11.9'W	40°46.0'N	69°10.0'W	40°38.1'N	69°19.5'W
2	40°35.9'N	69°19.3'W	40°39.0'N	69°05.8'W	41°04.5'N	69°30.9'W	41°07.6'N	69°17.4'W
3	41°06.7'N	69°20.9'W	41°09.4'N	69°34.6'W	40°40.8'N	69°29.7'W	40°43.5'N	69°43.4'W
4	40°27.1'N	69°32.6'W	40°24.6'N	69°18.9'W	41°01.3'N	69°21.7'W	40°58.8'N	69°08.0'W
5	40°51.3'N	68°59.4'W	41°01.7'N	69°02.4'W	40°44.4'N	69°41.6'W	40°54.8'N	69°44.6'W
6	40°39.0'N	69°25.3'W	40°46.8'N	69°15.7'W	41°15.7'N	70°18.2'W	41°23.5'N	70°08.6'W
3 Modified	41°06.7'N	69°25.2'W	41°09.3'N	69°38.9'W	40°40.8'N	69°33.7'W	40°43.5'N	69°47.6'W
4 Modified	40°27.9'N	69°37.0'W	40°30.4'N	69°50.7'W	41°02.1'N	69°26.1'W	41°04.6'N	69°39.8'W
5 Modified	40°52.4'N	68°59.4'W	41°02.8'N	69°02.4'W	40°45.5'N	69°41.6'W	40°55.9'N	69°44.6'W

88

The APD-10 SAR data collected during the NRL Experiment was survey-optically processed at El Toro NAS, California using a Goodyear ES-83A correlator/processor. The signal films and survey-processed imagery were then forwarded to ERIM for further analysis and precision processing.

Upon examination of the survey-processed imagery, numerous areas were noted where the image intensity dramatically decreased. An analysis of the phase histories recorded on the signal film revealed numerous shifts in the Doppler spectrum, believed to be caused by aircraft attitude changes during data collection. Because the Goodyear ES-83A processors operate on the assumption that the Doppler spectrum position remains fixed during an entire pass, it generates unfocused imagery with reduced intensity when Doppler spectrum shifts are encountered. The ERIM precision optical processor has the versatility to track the Doppler spectrum as it shifts and can produce focused imagery which is more representative of the surface than that produced by the ES-83A processor. Selected portions of APD-10 SAR data set collected during SEBEX were optically-processed at ERIM. Although additional analysis and precision processing could produce higher quality imagery, the imagery produced at ERIM was of higher quality than the Marine survey-processed imagery. Imagery at a scale of 1:100,000 was produced.

For the correlation of the SAR-observed surface patterns to bathymetric features, the following procedure was used. First, the positions of all surface patterns present on the SAR imagery, as well as all land, buoys and ships, were marked onto clear cell overlays. These were then placed over a composite hydrographic chart of the area. This chart was generated by enlarging or reducing a set of nautical and bathymetric charts from the Nantucket Shoals region to the same scale [1:100,000] as the SAR imagery. These charts included Coastal and Geodetic Survey Chart No. 0708N-52 and National Ocean Survey Chart Nos. 13203 and 13237. All sand banks and shoals within

the coverage area of each pass were noted, as well as any SAR surface patterns which occurred over these features. Also noted were the occasions when a pattern on the SAR imagery did not occur over a bottom feature which was present in the coverage area.

The following rating categories were used:

Strong – A clear, distinct pattern was present on the SAR imagery over the bottom feature.

Subtle – A pattern was present on the SAR image which did not give a clear indication as to the extent of the bottom feature.

Mixed – A surface pattern was present on the SAR imagery which was partially strong and partially subtle.

None – No surface pattern was present on the SAR imagery.

Finally, an in-depth correlation of the SAR imagery collected over Middle and Fishing Rips with sea truth collected in these areas was performed. This particular area was selected because detailed ship-based current, wind and wave measurements were collected near these areas at the times of the SAR overflights.

This analysis was performed by compiling ancillary environmental data for those times that the SAR imaged the region and comparing these data to the SAR images. Wind and wave measurements were taken from the USNS Hayes and provided to ERIM in summary form for the entire experiment data collection period (Valenzuela and Chen, 1982). Three sets of current measurements were obtained. Eularian current measurements were collected to the east of Phelps Bank, and summarized by Greenewalt, et al. (1983). Langrangian current measurements were collected west of Phelps Bank and summarized by Greenewalt and Gordon (1982). The third set of current estimates were obtained from NOAA Tidal Current Tables (NOAA, 1981).

3.3.2.2 Results

Figure 35 presents the location of the total ground coverage of the APD-10 SAR overflights over the NRL Experiment test site. Also presented in Figure 35 are the locations of the 62 individual sand banks identified by number for the present analysis. Table 14 lists these individual sand banks along with the estimated water depths over and adjacent to these
sand banks.

Figures 36 and 37 present APD-10 SAR imagery collected during Pass 2 on two separate missions conducted during the NRL Experiment. Both images were collected over nearly the same surface area with the radar illuminating the swath from west to east. Figure 36 was collected by AC10 at 1540 EDT on 11 July, and Figure 37 was collected by AC10 at 1415 EDT on 13 July. Presented in Figure 38 is the hydrographic chart of this region. The APD-10 images illustrate the types of surface patterns present on the SAR imagery collected during this experiment. It was observed that the surface patterns associated with the bottom features ranged from very subtle to quite dramatic. For example, the patterns over the Old Man and Fishing Rips in Figure 37 (K1 to N3, G2 to J3, I1) are quite distinct and clearly give an interpreter a strong clue as to the shape and location of a bottom feature. The other surface patterns on this SAR imagery (e.g., D3 to E4, H5, B1) require more careful interpretation and do not give as much information about the bottom features in this region.

Table 15 summarizes the occurrences of surface patterns present on the APD-10 SAR imagery over the bottom features within the region. The 62 bottom features in this region were imaged a total of 295 times. Surface patterns were detected over these features 45 percent of the time (36 strong patterns occurred, 88 subtle patterns and 9 mixed patterns).
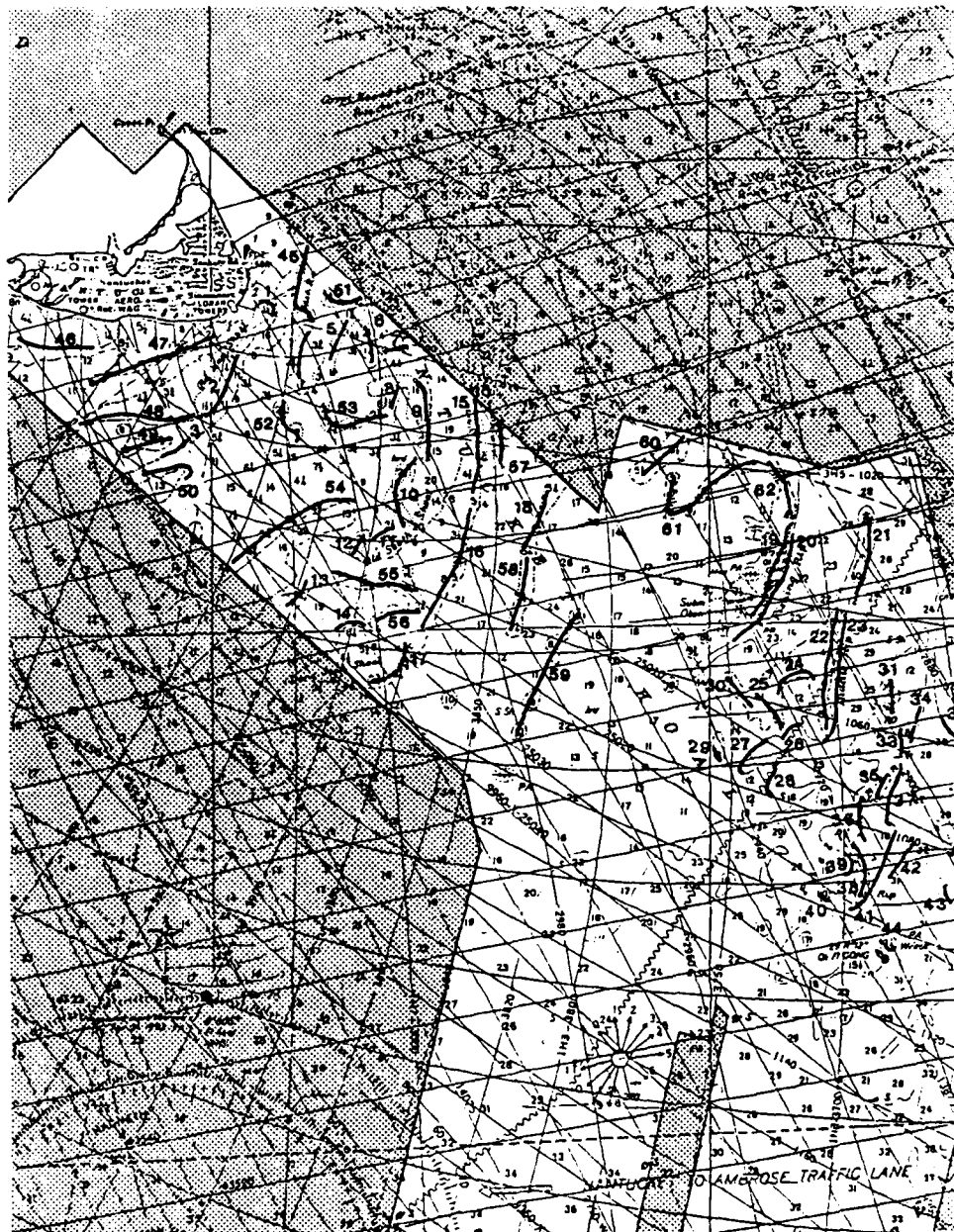
Figure 35.   APD-10 SAR Coverage Over NRL Test Area and Location
              of Shoals

TABLE 14
SUMMARY OF SAND BANKS LOCATED
WITHIN NRL TEST AREA

Feature	Feature Name	Depth Over Feature (m)	Depth Adjacent To Feature (m)
1	Old Man Shoal – N	3	17
2	Old Man Shoal – SE	3	20
3	Old South Shoal – SW Finger – NW	13	23
4	Bass Rip – W	7	3
5	Bass Rip – E	3	7
6	Old South Shoal – N Finger – NE	5	8
7	Old South Shoal – N Finger – NE	3	8
8	Old South Shoal – N Finger – E	4	8
9	Old South Shoal – N Finger – E	3	28
10	Old South Shoal – S Finger – NE	3	36
11	Old South Shoal – S. Finger – NE	6	36
12	Old South Shoal – S Finger – NW	5	18
13	Old South Shoal – S Finger – NE	11	20
14	Davis South Shoal – N	15	28
15	Old South Shoal – NE Finger – E	5	18
16	Old South Shoal – E	8	28
17	Davis South Shoal – NE	5	44
18	Davis Bank – SW	10	31
19	Fishing Rip Bank – S Finger – E	8	37
20	Fishing Rip	37	18
21	Middle Rip – NW	22	37
22	Middle Rip Bank – E Finger	7	37
23	Middle Rip	37	18
24	Middle Rip Bank – Center	18	22
25	Middle Rip Bank – SW Finger	15	22

TABLE 14
SUMMARY OF SAND BANKS LOCATED
WITHIN NRL TEST AREA (Continued)

Feature	Feature Name	Depth Over Feature (m)	Depth Adjacent To Feature (m)
26	Middle Rip – W	37	22
27	Middle Rip – SW	37	26
28	Middle Rip – SW	37	22
29	Middle Rip Sand Bar – SW	15	26
30	Middle Rip Bank – NW Finger	15	26
31	Phelps Bank – NE	17	22
32	Great South Channel – W	55	50
33	Phelps Bank – NW	15	37
34	Phelps Bank – NE	37	50
35	Phelps Bank – NE	17	37
36	Phelps Bank – E	13	30
37	Asia Rip – N	37	30
38	Phelps Bank – S	10	37
39	Phelps Bank – W	13	44
40	Phelps Bank – SW	18	30
41	Asia Rip	37	55
42	Asia Rip – NE	55	59
43	Great South Channel – W	55	39
44	Sand Bar – S	6	37
45	Bass Rip – N	3	14
46	Old Man Shoal – NW Finger	10	20
47	Old Man Shoal – W Finger	14	21
48	Old Man Shoal – SW	6	24
49	Sand Bar	16	24
50	Old Man Shoal – SW Finger – NE	11	24
51	Bass Rip – NE	4	7

TABLE 14
SUMMARY OF SAND BANKS LOCATED
WITHIN NRL TEST AREA (Concluded)

Feature	Feature Name	Depth Over Feature (m)	Depth Adjacent To Feat⸱ (m)
52	Bass Rip – SW	4	24
53	Old South Shoal – N Finger – NW	5	24
54	Old South Shoal – SW Finger – NE	10	27
55	Old South Shoal – S	6	37
56	Davis South Shoal – N	5	37
57	Old South Shoal – NE Finger – NE	4	22
58	Davis Bank – S	11	37
59	Sand Bars	16	20
60	Fishing Rip Bank – NW Finger – S	10	25
61	Fishing Rip Bank – W Finger – S	16	31
62	Fishing Rip Bank – S Finger – NW	7	29
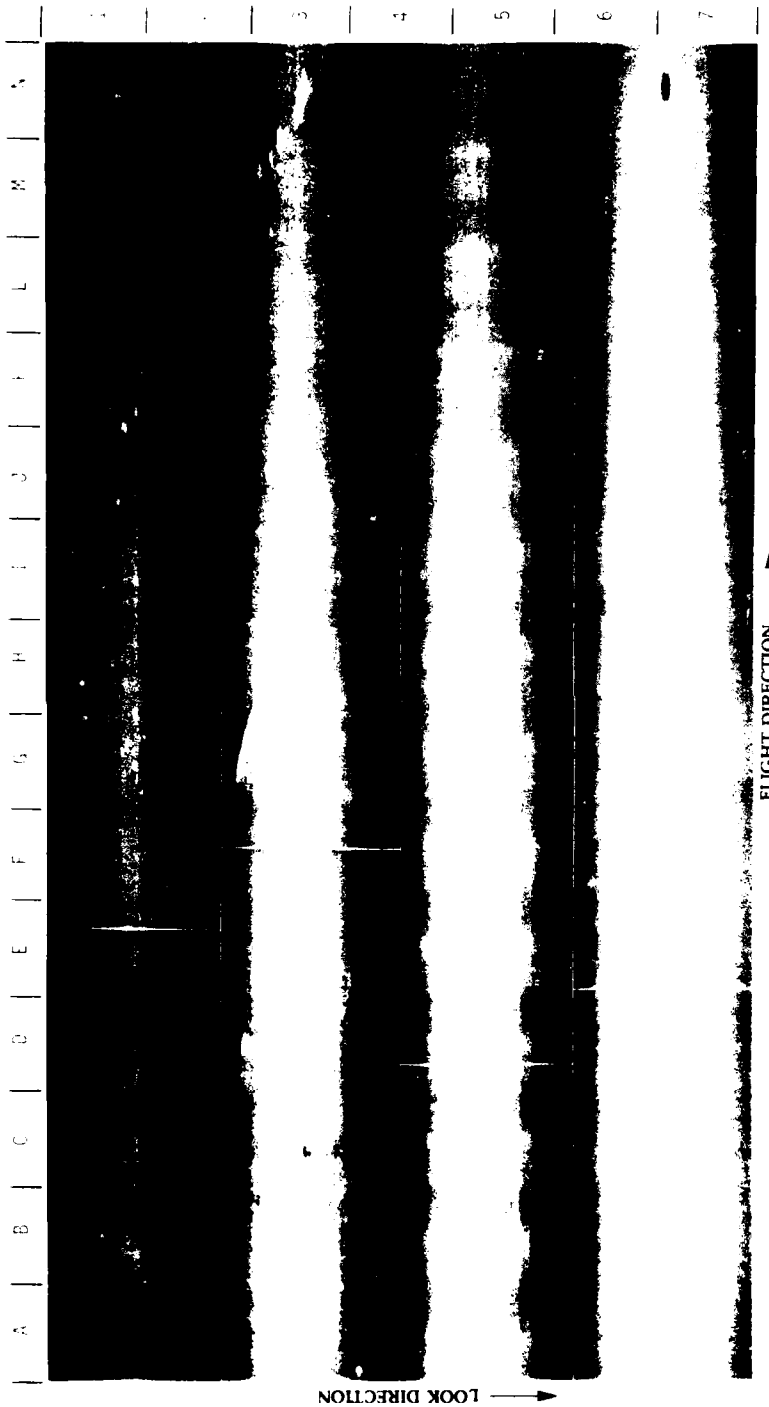
Figure 36. APD-10 X-Band SAR Imagery Collected Over Middle and Fishing Rips (11 July 1982, APD-10 Data Courtesy of NRL)
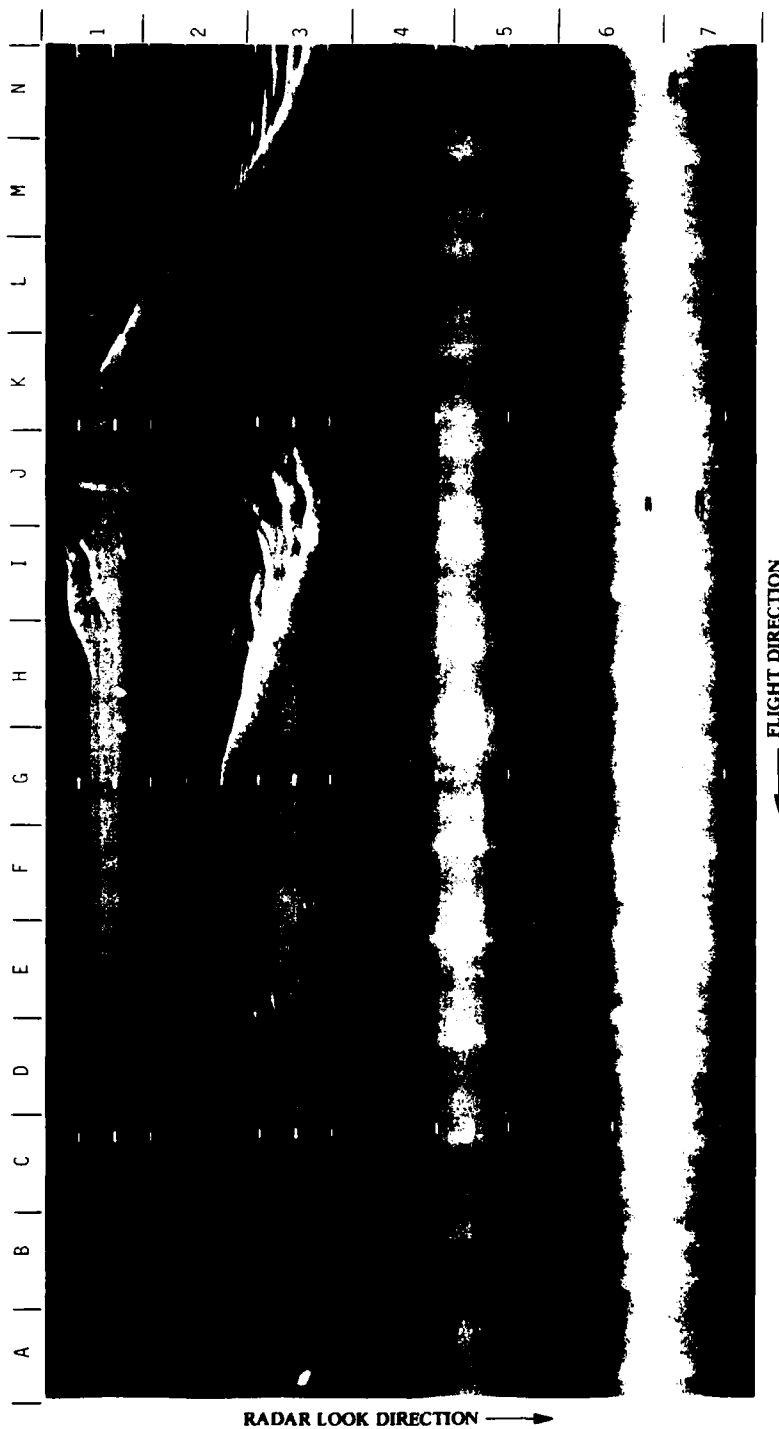
Figure 37. APD-10 X-Band SAR Imagery Collected Over Middle and Fishing Rips (13 July 1982, APD-10 Data Courtesy of HRL)

TABLE 15

SUMMARY OF BOTTOM RELATED SURFACE PATTERNS
ON APD-10 X-BAND SAR IMAGERY**

Date	11 July	11 July	11 July	11 July	11 July	11 July	11 July	11 July	11 July	11 July	13 July	13 July	13 July	13 July
Aircraft No.	23	23	23	23	23	23	23	23	23	23	10	10	10	10
Pass No.	1	2	3	4	5	4	10	2	3	6	2	4+	5+	3+
Time (GMT)	1435-1442	1448-1453	1457-1502	1508-1512	1517-1522	1522-1528	1532-1538	1542-1546	1550-1555	1559-1608	1411-1416	1420-1427	1430-1436	1453-1457
Bottom Features														
1. Old Man Shoal - N	o													
2. Old Man Shoal - SE	o	o												
3. Old Man Shoal - SW		o												
4. Finger - NW	o													
5. Bass Rip - W	x													
6. Bass Rip - E	x									|*				
7. Old South Shoal - N	x									o				
8. Finger - NE										o				
9. Old South Shoal - N	x									o				
10. Finger - NE										o				
11. Old South Shoal - S	x									o				
12. Finger - NE										o				
13. Old South Shoal - S	x													
14. Davis South Shoal - N	x		x						|	x				
15. Old South Shoal - NE			x						|					
16. Finger - NE				o	o	x								
17. Old South Shoal - E	o			o		x				|				
18. Davis South Shoal - NE	o													
19. Davis Bank - SW	|	|	|		o			|		|	x	•		x
Fishing Rip Bank	|	|		o				|		|	x	•		x
S Finger - E	|		|					|						
20. Fishing Rip	o	o					|	|			|x	|	|	|
21. Middle Rip - NW														
22. Middle Rip Bank E Finger														

Legend
o
x
\|*

+Modified flight line

TABLE 15
SUMMARY OF BOTTOM RELATED SURFACE PATTERNS
ON APD-10 X-BAND SAR IMAGERY

Date	11 July	11 July	11 July	11 July	11 July	11 July	11 July	11 July	11 July	11 July	13 July	13 July	13 July	13 July
Aircraft No.	23	23	23	23	23	23	23	23	23	10	10	10	10	10
Pass No.	1	2	3	4	5	4	5	2	3	6	2	4*	5+	3*
Time (GMT)	1435-1442	1448-1453	1457-1502	1508-1512	1517-1527	1522-1528	1532-1538	1542-1546	1550-1555	1559-1608	1411-1416	1420-1427	1430-1436	1453-1457
Bottom Features														
23. Middle Rip	x	•		o	o	x					x			
24. Center of Middle	o													
25. Rip Bank														
Middle Rip Bank														
SW Finger	o		o		o		o						x	
26. Middle Rip – W	o		o		o		o		o	o	x			
27. Middle Rip – SW	o	o	o		o		o	o	o	o	o			
28. Middle Rip – SW	o		o		o		o		o	o				
29. Middle Rip Sand Bar – SW					o		o			o				
30. Middle Rip Bank			o		o		o			o				
NW Finger														
31. Phelps Bank – NE	o	x		o									x	
32. Great South Channel – W		x		o	o	x	o	o	o		o		o	
33. Phelps Bank – NW		x	o	o			o	o					o	
34. Phelps Bank – NE	o	o	o	o		x	o			o	o		o	
35. Phelps Bank – NE	o	o	o	o	x	x			o	o	o		o	
36. Phelps Bank – E	o	o	o	o	o	x		o		o				
37. Asia Rip – N	o	o	o	o	o			o	o	o	o		o	
38. Phelps Bank – S	o	o	o	o	o			o		o	o			
39. Phelps Bank – W	o	o	o	o	o		o	o		o	o			
40. Phelps Bank – SW	o	o	o	o	o	x	o	o		o	o		o	
41. Asia Rip		o												
42. Asia Rip – NE	o	o	o			o	o			o	o		o	
43. Great South Channel – W	o	c		o		o				o	o		o	
44. Sand Bar – S	o													
45. Bass Rip – N									o	o				
46. Old Man Shoal	o									o				
NW Finger										o				
47. Old Man Shoal	o									o				
W Finger	o									c				
48. Old Man Shoal – SW	o													
49. Sand Bar	o									o				
50. Old Man Shoal – NE														
SW Finger – NE	o									o				

*Modified flight line

99

TABLE 15

SUMMARY OF BOTTOM RELATED SURFACE PATTERNS
ON APD-10 X-BAND SAR IMAGERY

Date	11 July	11 July	11 July	11 July	11 July	11 July	11 July	11 July	11 July	11 July	13 July	13 July	13 July	13 July
Aircraft No.	23	23	23	23	23	10	10	10	10	10	10	10	10	10
Pass No.	1	2	3	4	5	4	5	2	3	6	2	4+	5+	3+
Time (GMT)	1435-1442	1448-1453	1457-1502	1508-1512	1517-1522	1522-1528	1532-1538	1542-1546	1550-1555	1559-1608	1411-1416	1420-1427	1430-1436	1453-1457
Bottom Features														
51. Bass Rip - NE	o													
52. Bass Rip - SW	o													
53. Old South Shoal	o								o					
54. N Finger - NW	o									o				
Old South Shoal	o													
SW Finger - NE														
55. Old South Shoal - S	o									o				
56. Davis South Shoal - N	o									o				
57. Old South Shoal -														
58. NE Finger - NE	o									o	*			
59. Davis Bank - S	o												o	
60. Sand Bars	o		o									o	o	o
61. Fishing Rip Bank		*	o						o		*			
NW Finger - S														
Fishing Rip Bank														
62. W Finger - S		*	o					o	o		*			
Fishing Rip Bank														
S Finger - NW		o												

Legend:
X - Strong
- - Subtle
o - Part strong, part subtle
0 - No visibility
Blank - No coverage

*Modified flight line

100

Direction of Wind and Waves at Points A, B, and C.

11 July   13 July

Wind (100°)   Wind (250°)

Waves (280°)   Waves (040°)

0   1 Knot
Current Magnitudes

Figure 38.   Hydrographic Chart of Fishing and Middle Rips and Summary
             of Environmental Conditions (After NOS Chart No. 13200,
             Depth in Fathoms)

101

The tidal regime within the Nantucket Shoals is extremely complex. The tidal currents are of the rotary type and vary over the entire region. The formation of the sand banks and ridges in this region are strongly influenced by the tidal current flow, and in turn, themselves influence the currents. Therefore, the peak tidal current flow at a given sand bank can differ dramatically from nearby banks, and the optimum period for detection of bottom-related surface patterns on the aircraft SAR may not be co-incident between banks.

The ancillary environmental data collected coincident with the SAR data presented in Figures 36 and 37 were collected are summarized in Table 16 and graphically presented on Figure 38. We can see that the currents on both dates were in the same general direction, with the magnitude of the current being somewhat less on 11 July.

The bathymetric-related features in the imagery collected on July 11 and 13 (Figures 36 and 37) are similar in appearance, having sharp edges on the left side and more diffuse boundaries on the right side of each feature. The distinct left edges seem to be in roughly the same position on the two images, and to be aligned with the eastern edges of the corresponding bottom features. Since the currents were flowing in an easterly direction on both days, this corresponds to the lee edge of the features, where the current speed is decreasing (in the direction of the current). The current speeds on the two days were somewhat different, but the component of the current perpendicular to the bottom features axes were roughly the same (see Table 16 and Figure 38).

The wind and wave directions were both from the east on July 11 and from the west to northwest on July 13. Thus, in this case, the general shape of the bottom-related image features and the location of these features relative to the bottom seem to be determined by the current direction rather than by the wind or wave direction.

TABLE 16
SUMMARY OF WAVE,
WIND AND CURRENT INFORMATION

Wave and Wind Data

| | Wave | | Wind | |
Date	Height (m)	Direction* (° True)	Speed (knots)	Direction** (° True)
11 July 1982	<1	280°	10	100
13 July 1982	<1	040°	5	250

*Direction waves are traveling
**Direction wind comes from

Current Data

| | Type | Position | 11 July | | 13 July | |
			Speed (Knots)	Direction (° True)	Speed (knots)	Direction (° True)
A	Tide Table	41°02'N 69°41'W	0.8	105	1.5	044
B	Eulerian*	40°50.07'N 69°19.81'W	1.0	089	1.0	052
C	Lagrangian*	40°47'N 69°25'W	1.1	085	1.5	027

*Eulerian and Lagrangian current measurements were obtained onboard the USNS Hayes during the NRL Remote Sensing Experiment.

There are several theories which have been formulated which attempt to explain the appearance of bottom-related surface patterns on SAR imagery. One theory, based upon examination of Seasat imagery (see Shuchman, 1982; Kasischke, et al., 1983; or Lyzenga, et al., 1983) is based upon the modulation of the Bragg waves by the current as it flows over the bottom features. Another theory was formed using the NRL data by Gordon, et al. (1983). This theory states that there is a selective blocking of the short period waves by the current as its speed increases flowing over the shoal. This theory is schematically illustrated on Figure 39 (after Gordon, et al., 1983). In Figure 39, the short and long wavelength wind-driven surface waves are propagating towards the bank. The increased upstream current velocity is high enough to selectively block or trap the short wavelength surface waves at the banks edge. Figure 40 (also after Gordon, et al., 1983) presents a photograph of the water surface taken over Phelps Bank on which is illustrated in the different roughness characteristics caused wave trapping as currents flow over the bank.

The intensity and width of the features imaged by the APD-10 SAR are greater on the July 13 image than on the July 11 image. This difference may be due to the difference in the wind and wave directions mentioned above, or to the difference in wind speed shown in Table 16. The fact that the wind and waves were in the same direction as the current on July 13 would seem to imply that the phenomenon of wave blocking (Gordon, et al., 1983) was less important on that day than on July 11, when the wind and waves were in the opposite direction to the current. Thus, the difference in wind speed would seem to be the controlling factor.

A decreasing visibility of bottom-related image features with increasing wind speed was also observed in Seasat images of the English Channel (Shuchman, 1982). This behavior is also predicted by hydrodynamic/electromagnetic models which incorporate the effect

104
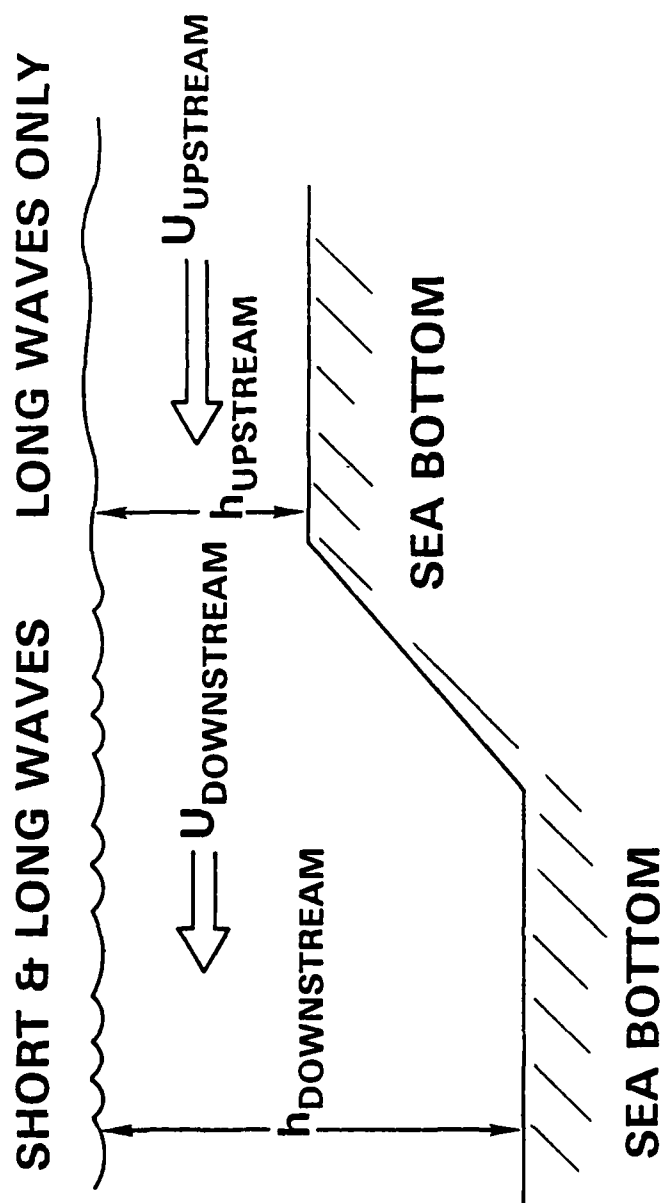
Figure 39. Schematic Diagram of Short Wave Trapping By a Current Flowing Over a Bottom Feature (After Gordon, et. al., 1983)

Figure 40. NRL Photograph of Sea Surface Near Asia Rip, Phelps Bank; The Smooth Surface is Over The Bank, While Rough Surface Is at Edge of Bank (After Gordon et al., 1983)

of the wind speed on the relaxation rate or lifetime of the Bragg waves (Shuchman, 1982; Lyzenga, et al., 1983). Intuitively, this dependence is due to the fact that when the wind speed is high, the waves are maintained in a nearly "saturated" state (Phillips, 1981) regardless of the hydrodynamic forces acting on them.

3.3.2.3 Comparison of Seasat and APD-10 SAR Data

Figure 41 presents an enlargement of a portion of the Seasat SAR image (Rev. 974) showing surface patterns located southeast of Nantucket Island. Presented in Figure 42 is a portion of the hydrographic chart of this region. Comparison of these two figures shows that there is a correlation between the SAR observed patterns and the charted shoals in this region.

Figure 43 presents APD-10 SAR imagery collected on 11 July superimposed onto the Seasat imagery. When the Seasat SAR image was collected, the currents were traveling in a southerly direction. When the APD-10 SAR data was collected, the currents were traveling in a easterly direction (see Table 16).

The superimposition of the L-band Seasat image of the Nantucket Shoals area with the X-band APD-10 image shows similar surface expressions, with a reversal of tone of the bottom-related surface features due to the difference in current directions (i.e., the bright lines in the APD-10 image correspond to dark areas on the Seasat SAR image). The X-band features also appear to be narrower than the L-band features. This difference is explainable, at least qualitatively, by the expected differences in the relaxation rate or lifetime of the corresponding X-band and L-band Bragg waves.

In summary, several aspects of the APD-10 SAR data sets seem to be consistent with a Bragg scattering explanation for the verification in reflectivity across the bottom-related image features. Wave blocking does not appear to be a primary factor, since this phenomenon is not expected to be significant in the data set showing

107

Figure 41. Seasat SAR Image of Nantucket Shoals (Rev. 880 27 August 1978; Digitally Processed Image Courtesy of JPL)
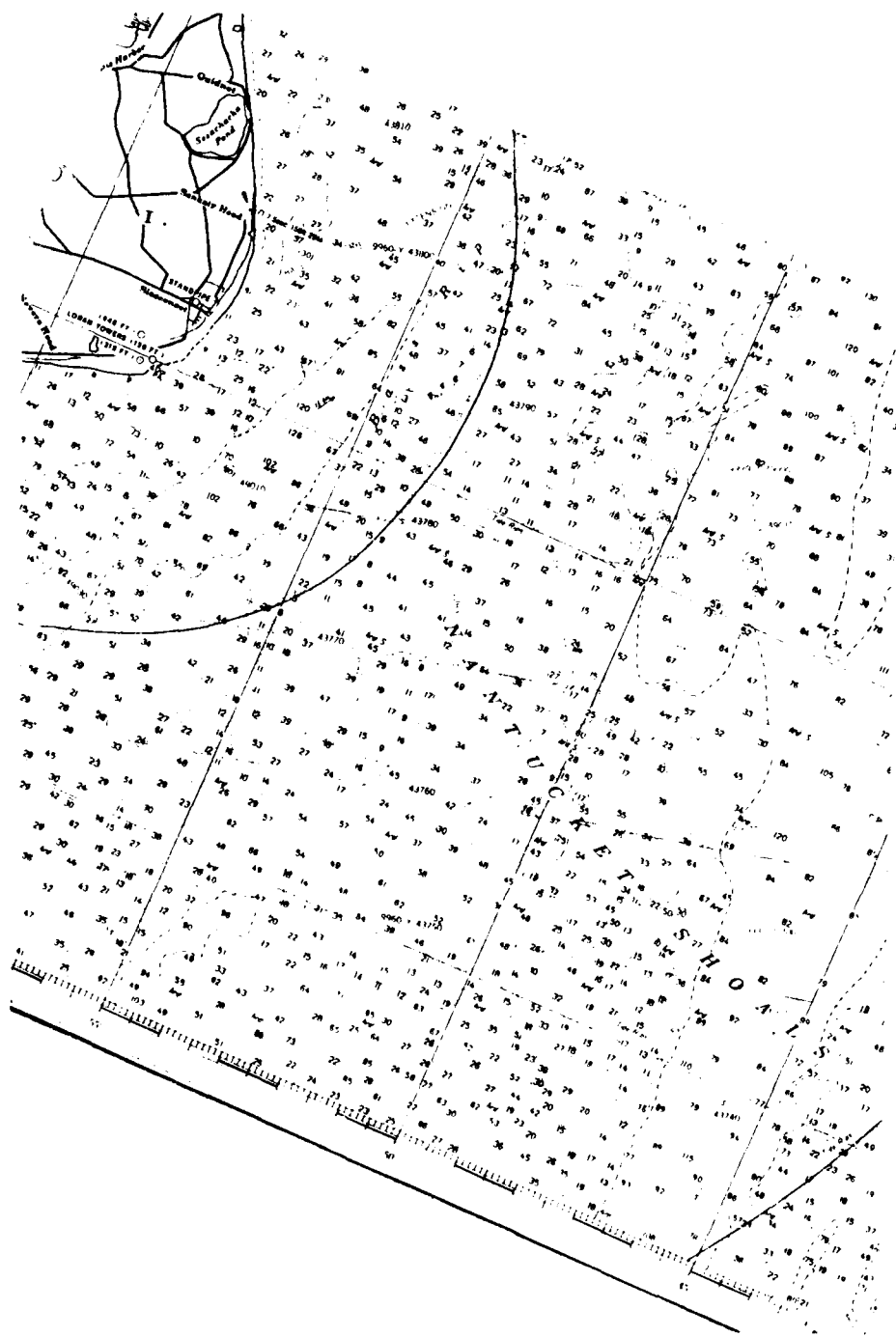
Figure 42. Hydrographic Chart of Nantucket Shoals Region (After NOS Chart No. 13237, Depth in Feet)

Figure 43. Seasat and APD-10 SAR Image of Nantucket Shoals

the highest contrast. The possibility of wave breaking as a con-
tributor to the X-band modulations is suggested by the streaked
appearance of the images (Lyzenga and Shuchman, 1983). However, the
difference in the width of the features at X-band and L-band, and
the apparent dependence of the contrast on wind speed, suggest that
Bragg scattering is the dominant mechanism.

3.3.3 DISCUSSION

The analyses presented in this section have demonstrated that
X-band SAR data collected with the APD-10 system do contain surface
patterns which can be correlated to bottom features. Data collected
during the MARSEN Experiment did exhibit a certain number of patterns
which were correlated to bottom features, but also displayed patterns
which were not correlated. However, extremely complex surface con-
ditions existed during data collection, including breaking waves,
high wind and complex tidal current patterns. A previous analysis
of MARSEN data indicates that the breaking waves may be responsible
for much of the azimuth streaking on the imagery (Lyzenga and
Shuchman, 1983), and may also be the cause of the bottom-related sur-
face patterns.

The NRL data showed numerous patterns which occurred over the
sand banks within the region, however not all bottom features had an
associated SAR-observed surface pattern. Since the SAR imagery was
collected over the same areas under different current wave and wind
conditions exhibited different surface patterns, this data set offers
an opportunity to further examine the mechanisms responsible for the
detection of bottom-related surface patterns on SAR imagery.

4
DIGITAL ANALYSIS OF SAR DATA

In this chapter, the results of three separate analyses of dig-
ital Seasat SAR data are presented. The first analysis involves
comparison of Seasat data collected over Cook Inlet, Alaska with
digital depth data from the region. The second analysis involves
comparison of two separate scenes of Seasat SAR data collected over
the Tongue of the Ocean with a Landsat scene collected five weeks
after the Seasat data. The third analysis presents the results of
an evaluation of the utility of speckle reduction routines for in-
creasing the interpretability of Seasat SAR imagery for ocean surface
patterns.

4.1 COOK INLET DATA ANALYSIS

Studies of Seasat SAR data collected over the Nantucket Shoals
region showed a high degree of cross-correlation (0.86) between water
depth and SAR image intensity variations for selected regions within
the data set (see Kasischke, et al., 1982). Correlations between
image intensity and depth were further investigated using Seasat SAR
data collected over Cook Inlet, Alaska during Rev. 289. This partic-
ular data set was selected because of: (1) previous qualitative
comparisons revealed that many of the SAR surface patterns occurred
over or near bottom features in the area, (2) the availability of
digital SAR data for this date, and (3) the availability of digital
depth data.

4.1.1 DATA SETS

Seasat Rev. 289 imaged the Cook Inlet region on 17 July 1978 at
approximately 05:48 GMT. Digital SAR data used in this study were
generated by the JPL digital Seasat processor and were provided to
ERIM in CCT format. Figure 44 presents an image generated from the

113
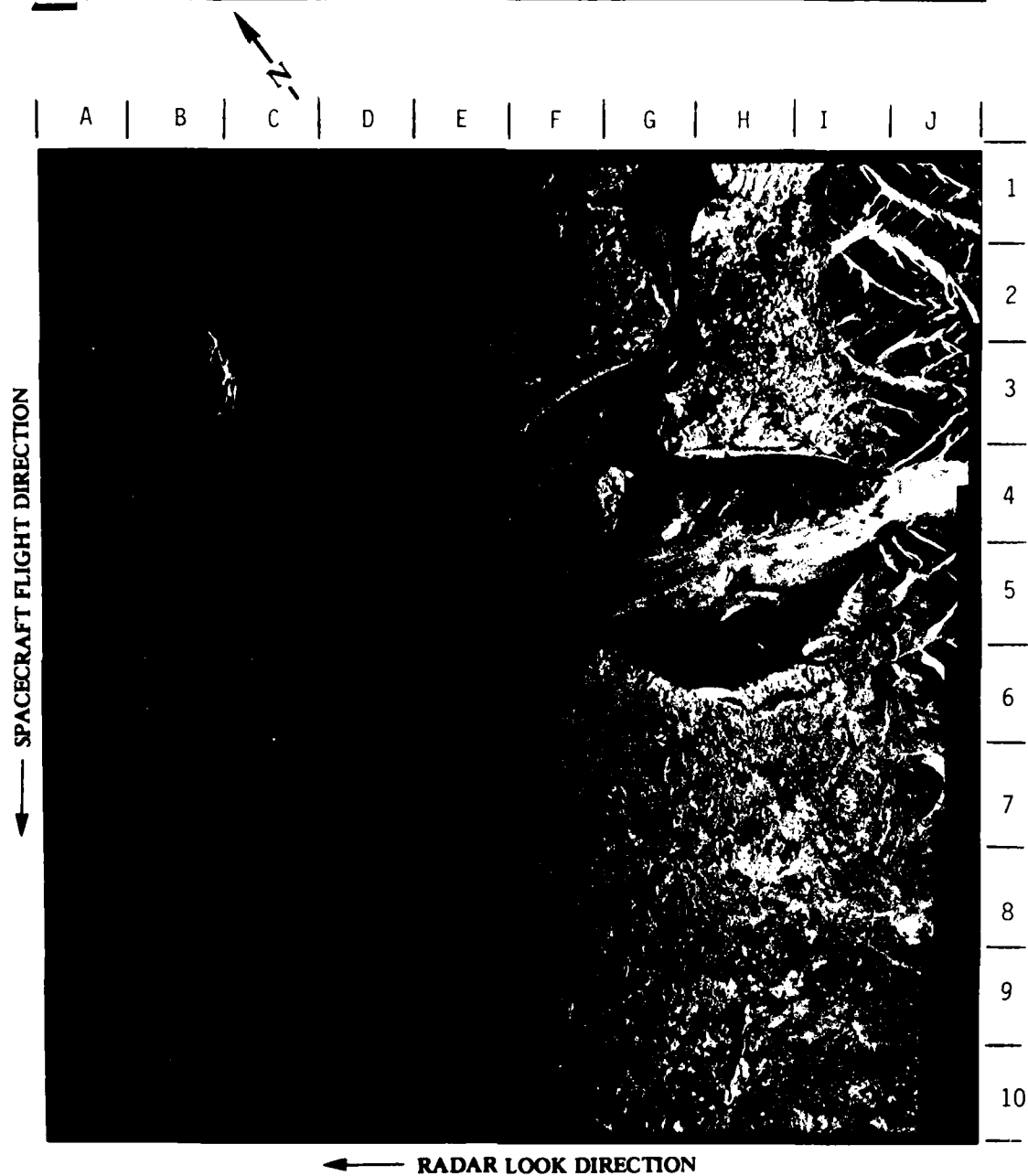
Figure 44. Seasat SAR Image of Cook Inlet, Alaska (Rev. 289, 17 July
1978. JPL Digitally Processed Data)
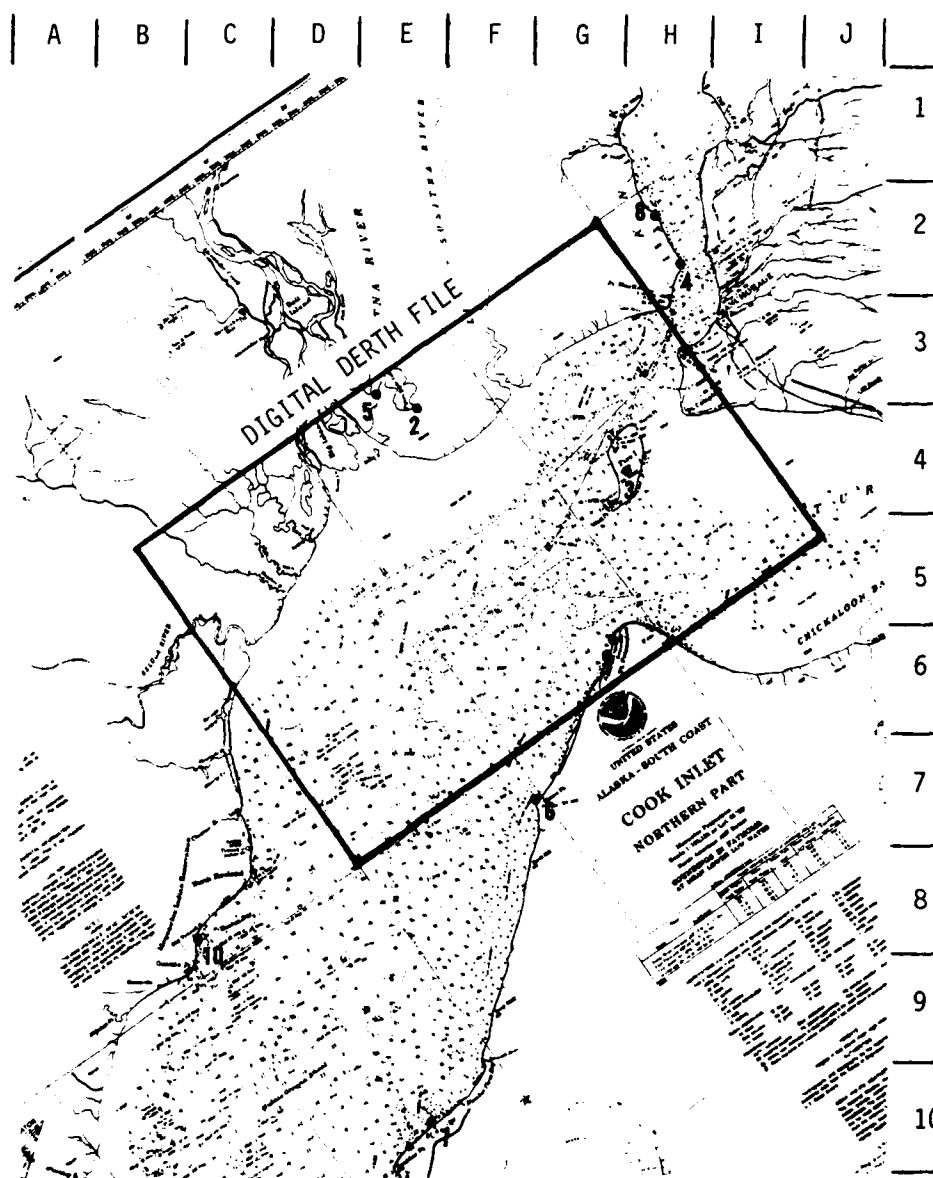
Figure 45. Hydrographic Chart of Cook Inlet (After National Ocean Survey Chart No. 16660, Depth in Fathoms)

115

digital SAR data. Figure 45 presents the hydrographic data for this region. Of particular interest to this study is the shoal running west of Fire Island (D6 to F4).

Water depth data were obtained in the form of digital depth soundings, collected by the National Ocean Survey and obtained from NOAA's Environmental Data and Information Service in CCT format. The area included on this CCT was from 61°N to 61°20'N and 150°W to 151°20'W. The position of the area covered by the digital depth files is marked on Figure 45. Figure 46 presents a grey-map generated from the soundings in the digital depth file.

At the time of the Seasat overpass, the wind was from the south-southeast (160° True) with a velocity of 6 m/s (12 knots) with gusts up to 10 m/s (20 knots). The tide stage (from NOAA Tide Tables) was one-half hour before high water, with the water level around Fire Island 4.3 m above mean low water. We can assume that at this tide stage there were relatively small (<0.5 m/s) tidal currents present in this area.

4.1.2 METHODS

The Seasat SAR data were first radiometrically and geometrically rectified using algorithms described by Kasischke, et al. (1982). To reduce the coherent speckle present in the SAR data and to achieve a sample size more equivalent to the digital depth data (the depth data has a spacing of 15 seconds in both latitude and longitude which corresponds to ground distances of approximately 450 m and 225 m, respectively), the Seasat SAR data were smoothed using an 11 x 11 pixel window. The first step in the registration process was to locate suitable features on the SAR imagery for use as ground control points (GCP's). Ten such features were identified and their line and pixel numbers were identified from line printer grey maps. Next, the latitude and longitude of these features were obtained from NOAA
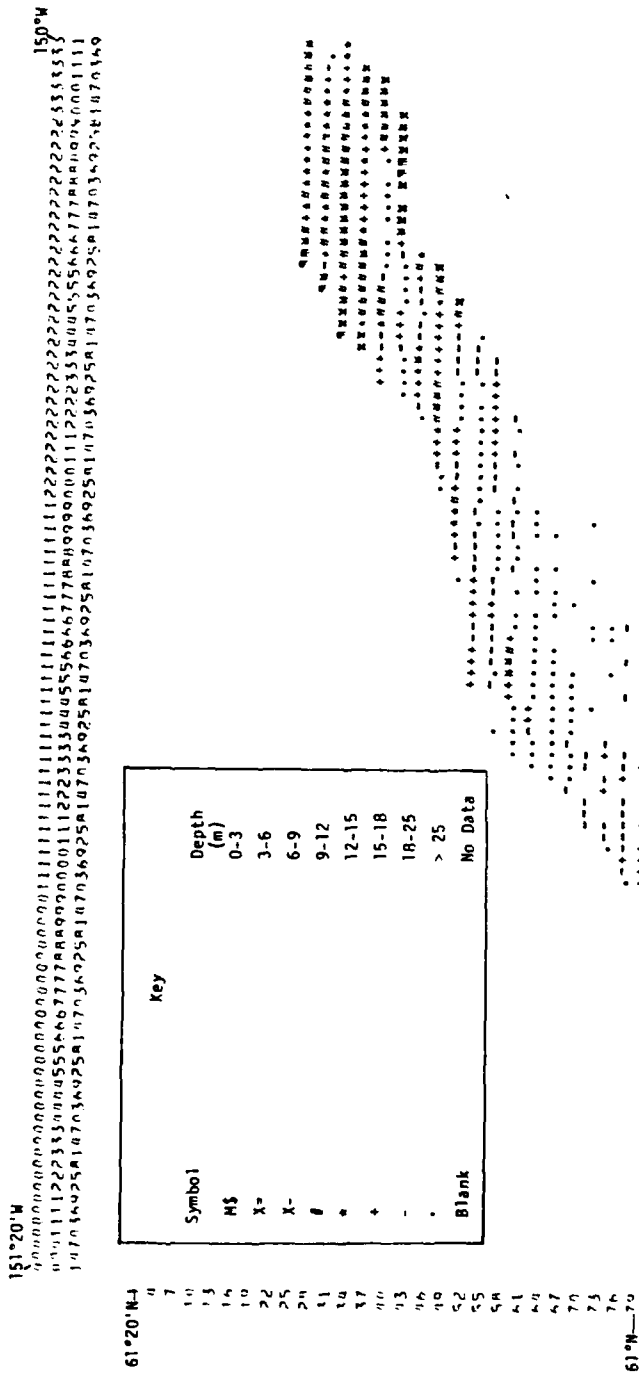
Figure 46. Digital Depth Data for Cook Inlet, Alaska

Chart No. 16660. These were transformed into equivalent line and point numbers in the digital depth data file using the following relationships:

$$\text{line} = \frac{61°20'N - \text{latitude}}{0.25'} + 0.5 \tag{1}$$

$$\text{point} = \frac{151°20'W - \text{longitude}}{0.25'} + 0.5 \tag{2}$$

These ground control points are summarized in Table 17 and their positions plotted on Figure 45. These points were then used as inputs into a registration program which merges the Seasat image intensities and digital depth file. The results of registering these data sets are summarized in Table 18. The rms error of 1.17 pixels correspond to a physical distance of about 300 m in both range and azimuth dimensions. This is still less than the sample spacing of the depth data, and thus, was judged precise enough for this analysis. Black and white level sliced images generated from the co-registered SAR and depth data sets are presented in Figure 47. The bright areas on the SAR image correspond to areas of higher radar return. The bright areas on the water depth image correspond to shallow water areas, with deeper water designated by a darker tone. Qualitative examination of these images indicates that areas of high radar backscatter correlate to shallow water regions.

To quantitatively examine the relationship between the registered SAR and water depth data, a computer program was written which allowed the cross-correlation of the two data sets to be calculated for a single pixel over a specified line range, or for a single line over a specified pixel range. The cross-correlation function can be used to study the interactions between two processes (in this study, water depth and SAR image intensity) with different scales of measurement or different variances and is defined as

$$\rho_{12} = \frac{\gamma_{12}(u)}{\sigma_1 \sigma_2} \tag{3}$$

TABLE 17
GROUND CONTROL POINTS FOR SEASAT SAR
TO WATER DEPTH REGISTRATION

GCP	SAR Image Location Line	SAR Image Location Point	Geographic Location Lat.	Geographic Location Long.	Line	Point	Description
1	415.4	272.3	61°14.7'N	150°57.3'W	22.3	91.9	Bridge on Beluga
2	308.4	153.6	61°18.9'N	150°26.8'W	5.5	210.8	Pt. on Fig. Eight Lake
3	192.7	199.1	61°08.6'N	150°13.0'W	46.6	268.9	Radar Dome on Fire Island
4	161.1	88.6	61°15.6'N	149°55.5'W	18.6	339.1	Pt. NE of Pt. MacKenzie
5	326.2	150.6	61°20.4'N	150°30.2'W	-0.7	200.0	Pt. near Fig. Eight Lake
6	250.9	378.8	60°57.3'N	150°42.3'W	91.8	151.9	Moose Pt.
7	312.3	547.6	60°46.6'N	150°09.6'W	134.6	42.4	Near Boulder Pt.
8	172.2	69.3	61°17.9'N	149°55.4'W	9.4	339.2	Lake near Pt. MacKenzie
9	203.7	283.2	61°02.3'N	150°23.9'W	72.0	225.5	Pt. Possession
10	436.4	442.0	61°01.8'N	151°18.5'W	73.8	7.0	Old Tyonek

119

TABLE 18.
SUMMARY OF LEAST SQUARES REGISTRATION OF DIGITAL
SEASAT DATA AND DIGITAL WATER DEPTH DATA

GCP#	DATA SET 1		DATA SET 2 (OBSERVED)		DATA SET 2 (PREDICTED)		DEVIATION	
	LINES	POINTS	LINES	POINTS	LINES	POINTS	LINES	POINTS
1	22.5	91.9	415.4	272.3	414.4	273.6	0.92	-1.33
2	5.5	210.8	308.0	153.6	308.0	153.3	0.38	0.22
3	46.6	268.9	192.7	199.1	193.3	198.9	-0.58	0.14
4	15.6	339.1	161.1	88.6	159.8	89.6	1.26	-0.95
5	-0.7	240.0	326.2	150.6	328.0	147.9	-1.80	2.78
6	91.8	151.9	250.9	378.8	253.2	378.1	-2.26	0.69
7	134.6	42.4	312.3	547.6	310.9	546.7	1.40	0.82
8	9.8	339.2	172.2	69.3	171.5	69.9	0.70	-0.66
9	72.0	225.5	203.7	283.2	204.0	283.6	-0.24	-0.46
10	73.8	7.0	436.4	442.0	436.1	443.3	0.25	-1.25

Seasat SAR Data
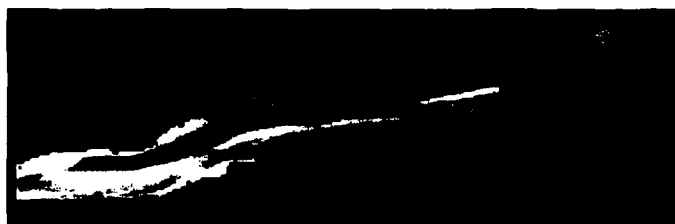
Digital Depth Data

Figure 47. Co-registered Seasat SAR Data and Digital Depth File

where

$$\gamma_{12}(u) = \frac{1}{N} \sum_{t=1}^{N} (X_1(t) - \bar{X}_1)(X_2(t + u) - \bar{X}_2) \tag{4}$$

where σ_1 and σ_2 are the standard deviations of the two samples, $\bar{X}_1$ and $\bar{X}_2$ are the means of the two samples, t is the sample number, u is the lag, and N is the total number of points in each sample. The computer program was designed to produce correlations for lag values ranging from -5 to 5. This allows the relative offset of the high radar backscatter areas from the shallow water areas to be calculated. Any offset could possibly be due to a tidal current in the area. The computer program which performed these calculations also produced a plot of the correlation as a function of lag. Thirteen areas on the shoal west of Fire Island were selected for cross correlation analysis.

4.1.3 RESULTS

Figure 48 presents a one-dimensional scan of co-registered relative SAR image intensities and water depth. The cross-correlation plot for these data is presented in Figure 49. From this plot, we can see that a maximum cross-correlation of 0.64 occurred when a lag of near zero was used. Table 19 summarizes the cross-correlation for the thirteen areas selected for analysis. The average cross-correlation achieved was 0.50 with an average lag of -0.4 pixels. In general, these correlations are not as high as those achieved in the previous analysis of this type performed are Seasat SAR data collected over the Nantucket Shoals (see Kasischke, et al., 1982).

4.1.4 DISCUSSION

This analysis has shown there is some statistical correlation between water depths and the Seasat SAR image intensity from Rev.

LINE 181

Relative SAR Intensity

Depth (m)

Distance (km)
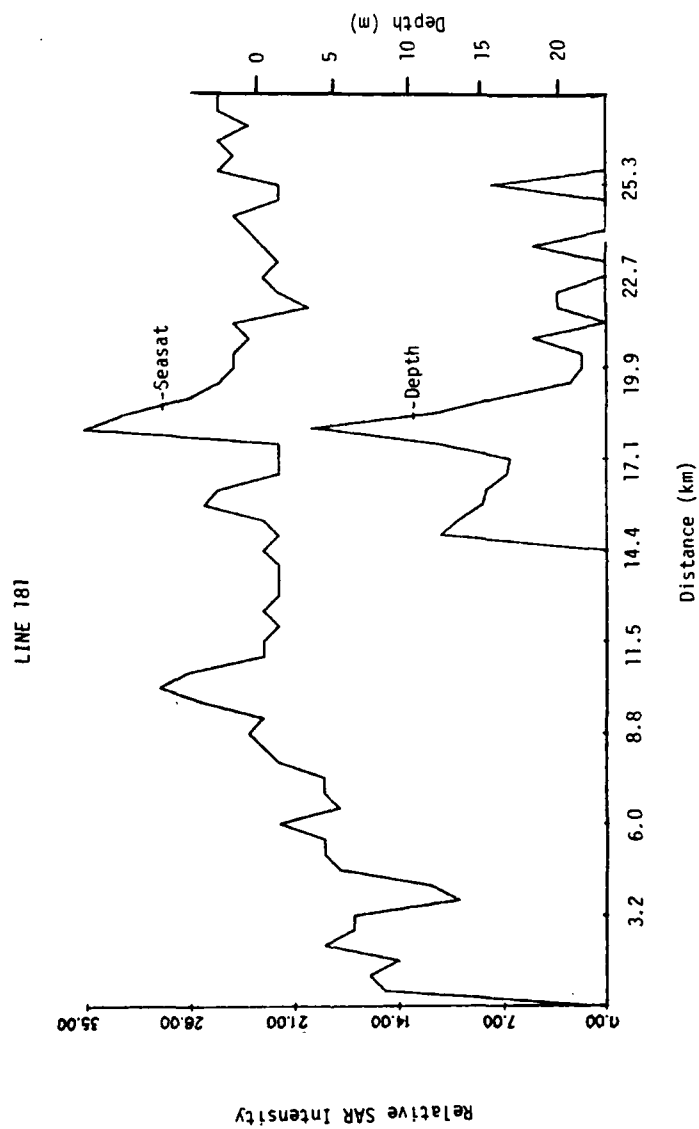
Figure 48. One-Dimensional Digital Depth Versus Seasat SAR Image Intensity
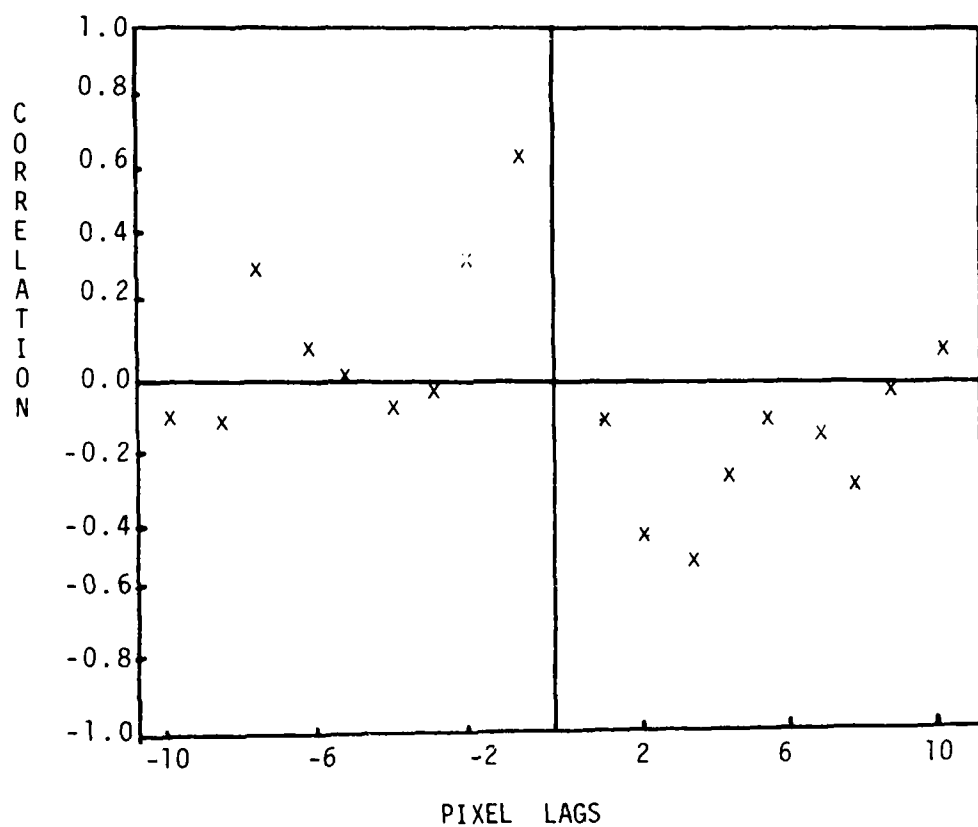
Figure 49. Cross-Correlation Plot of Data from Line 181

TABLE 19
RESULTS OF SAR/WATER DEPTH CORRELATION
FOR COOK INLET DATA

Line(s)	Pixel(s)	Maximum Correlation	Lag
51–66	161	0.59	−1
49–62	181	0.64	0
49–59	191	0.43	−2
48–60	201	0.27	−2
46–60	211	0.65	−2
35–57	241	0.21	0
23–42	291	0.60	−2
23–42	301	0.50	+2
23–40	311	0.54	0
26	265–321	0.36	0
46	205–275	0.50	+3
46	205–250	0.74	−1
61	130–165	0.51	0
	All Points	0.50	−0.4

125

289, but not as high as those found during past studies. As discussed in Section 4.1.1, the Seasat data were collected when the tide stage was near high water, when currents in the region were generally low. Also, as indicated by the weather records, wind speeds were possibly high at this time. A past study (Shuchman, 1982) indicated that the environmental conditions present when the Cook Inlet Seasat SAR data were collected were the least optimal for the generation of bottom-related surface patterns. Therefore, the low correlation was not surprising.

4.2 TONGUE OF THE OCEAN DATA ANALYSIS

Figure 50 presents Seasat SAR imagery collected over the Tongue of the Ocean (TOTO) region of the Bahamas on two separate dates. An analysis of these data (see Chapter 5) indicates that the banded patterns are a direct result of tidal currents flowing over the tidal bar belts, sand bars, and the edge of the Great Bahama Bank in this area. The two Seasat data sets, which are available in digital CCTs, present an interesting analysis in that there is a tonal reversal in the surface patterns over the bottom features, e.g., the dark bands in Figure 50(a) correspond to light bands in Figure 50(b) and vice versa.

Comparison of the digital Seasat SAR data to the depth readings in this area presents a challenge because many of the bathymetric readings are sparse and outdated (the charts for this region are based largely on British surveys made between 1836 and 1890). Techniques have recently been developed to extract water depth information from Landsat data (Lyzenga and Polycyn, 1979). Although the absolute accuracy of these techniques has yet to be determined, they do generate a good relative depth profile for water areas with low turbidity, such as those found in the Bahamas. In the present analysis, a Landsat-generated depth map is compared to the two digital Seasat SAR data sets.

126
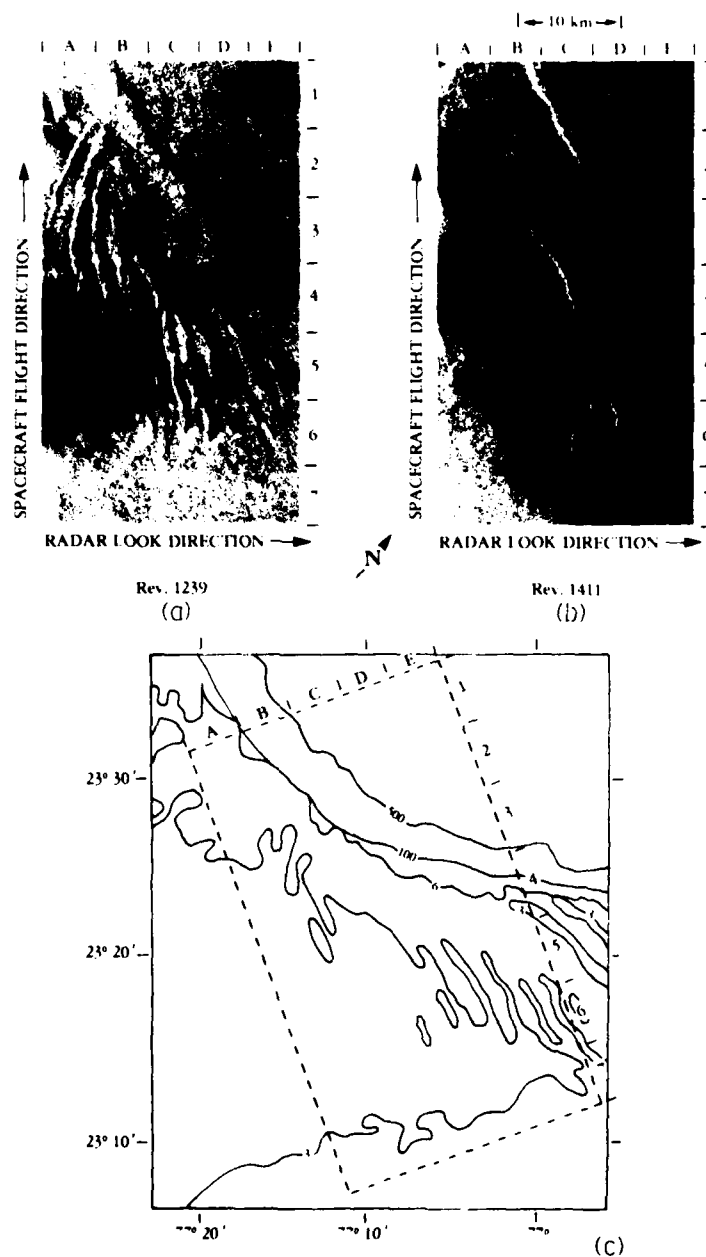
Figure 50. Seasat SAR Imagery and Hydrographic Chart of the Tongue of the Ocean: (a) Seasat Revolution 1239 (21 September 1978), (b) Seasat Revolution 1411 (8 October 1978), and (c) Hydrographic Chart of Area. (Seasat Digitally Processed Imagery Courtesy of the Jet Propulsion Laboratory; Chart Reproduced From DMA Chart Nos. 26300 and 27040, Depths in Fathoms.)

127

4.2.1 METHODS

The Seasat SAR data used in this analysis were collected during Revs. 1239 (21 September 1978) and 1411 (8 October 1978). The data were digitally processed at JPL and geometrically and radiometrically corrected at ERIM using the techniques described by Kasischke, et al. (1982). Figures 51 and 52 present images generated from the corrected data.

The Landsat data selected for this study was scene number E30240-14563 (31 October 1978). This particular data set was selected because it had a minimum amount of cloud cover and was collected near the time of the Seasat overpasses.

Both the Landsat and Seasat data were registered to match DMA Chart No. 26300 (Andros Island to San Salvador). The Landsat data were processed at ERIM's Earth Resources Data Center using standard Landsat registration algorithms (Wilson, 1979). The data were restored to a 50 x 50 m pixel size. A subset of the Landsat scene which contained the tidal bar belts at the southwestern corner of the TOTO was extracted and used in a water depth calculation algorithm. This algorithm uses Landsat bands 4, 5 and 6 for depth calculations (Lyzenga and Polcyn, 1979) and results in a single channel with a predicted depth for each pixel.

The Seasat data were also registered to DMA Chart No. 23600 using techniques similar to those outlined in Section 4.1.2. Both Seasat data sets were smoothed using a three by three boxcar averaging filter and resampled to 50 by 50 m pixels. Cross-correlation statistics were then generated for areas of the registered Landsat and Seasat data sets.

Figure 51.   Seasat SAR Image of Tongue of the Ocean Region
             (Rev. 1239, 21 September 1978; JPL Digitally
             Processed Data; Geometrically and Radiometrically
             Corrected at ERIM)

129

Figure 52. Seasat SAR Image of the Tongue of the Ocean
(Rev. 1411, 8 October 1978; JPL Digitally
Processed Data; Geometrically and Radiometrically
Corrected at ERIM)

130

4.2.2 RESULTS

Figure 53 presents images from the co-registered Seasat and Landsat data files. In the Landsat depth image, bright returns correspond to a shallower depth, while darker returns correspond to a deeper depth. The extremely dark patches in the Landsat bathymetry file corresponds to cloud cover. Figure 54 is an enlargement of DMA Chart No. 23600 from this region. It can be seen that the level of detail concerning the extent and location tidal bar belts is greater in the Landsat depth file, and that the Seasat images are similar to the depth profile. Due to the lack of depth calibration data, the Landsat imagery was processed to yield only relative depths, which are sufficient for the present analysis.

The co-registered Seasat and Landsat files were smoothed using a 5 x 5 pixel window and one-dimensional plots of water depth and radar image intensities were generated for every 50 lines (i.e., lines 50, 100, 150, 200, and 250). Figure 55 presents the plots generated for line 100 between pixels 50 and 215. Comparing the Rev. 1411 plot with the Rev. 1239 plot in Figure 55 reveals that for every "peak" in the Rev. 1411 data, there is a "valley" in the Rev. 1239 data, and for every valley in the Rev. 1411 data, there is a peak in the Rev. 1239 data. It can also be seen that the increase and decrease in radar image intensity closely correlate with the Landsat depth data presented in Figure 55.

This relationship supports the hydrodynamic model developed by Kasischke, et al. (1982; 1983, see Chapter 5) for this area. This theory states that a current flowing over a shallow-water bottom feature will result in both an increase and decrease in radar image tone. The juxtaposition of the radar intensity modulations will be dependent on the current direction. For the cases presented here, the current was flowing from right-to-left during Rev. 1239 and left-to-right during Rev. 1411. Therefore, one would expect a reversal in the position of the image intensities for the two different situations, as is the case.

131
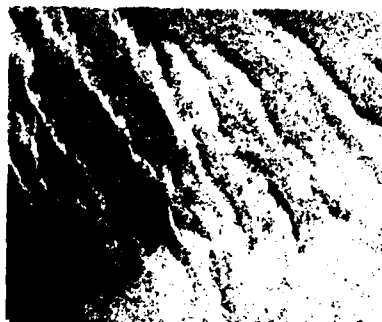
Rev. 1239
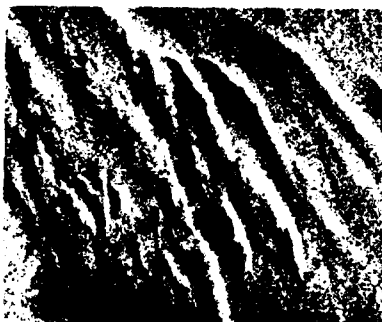
Rev. 1411
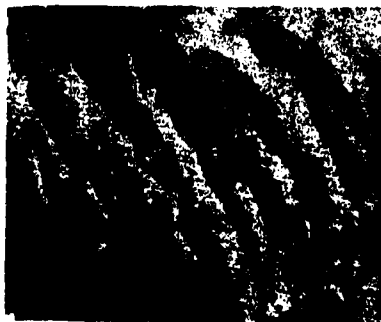
Landsat Bathymetry

Figure 53.   Co-Registered Seasat SAR Images and Landsat Bathymetric
Profile From Tongue of the Ocean Region
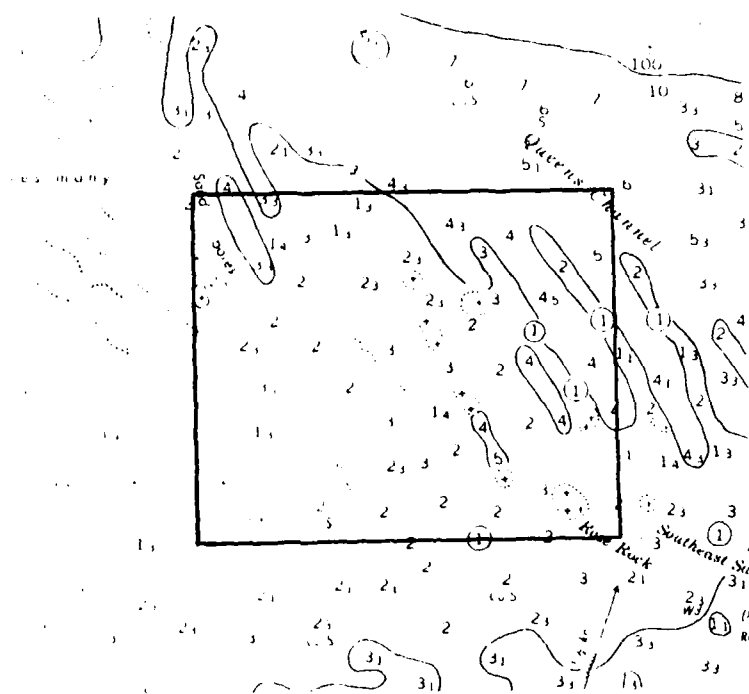
Figure 54. Bathymetric Chart of Area of Co-Registered
Seasat and Landsat Data (DMA Chart No.
27040, Depth in Fathoms and Feet)
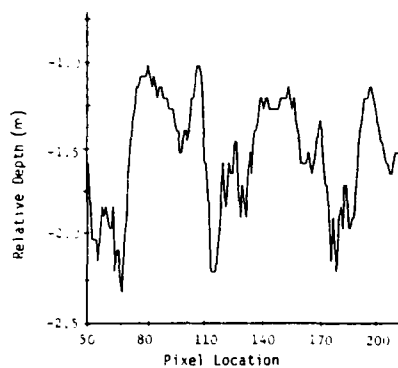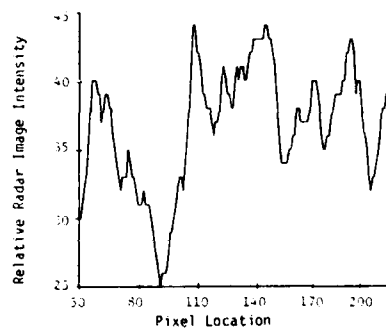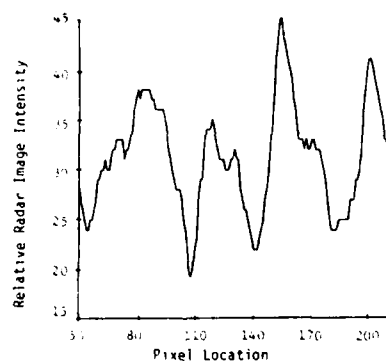
Figure 55. Comparison of Landsat Depth
File and Seasat SAR Image
Intensities for Line 100

134

The cross-correlation between the Line 100 Rev. 1239 and Line 100 Rev. 1411 data was -0.80 (pixels 115 to 215). The correlation between Landsat depth and Seasat image intensity was -0.45 for Rev. 1839 and -0.60 for Rev. 1411, somewhat lower than anticipated. However, an extremely complex situation is involved in this data set, with the following factors possibly playing a role in the changes in radar image intensity: (1) wind speed; (2) differences in water depths and currents; and (3) the closeness of the bottom features to one another creating a complex hydrodynamic situation.

If we reduce the area where the two data sets are compared, much higher correlations can be achieved. For example, between pixels 160 to 210 on Line 100, the correlation between depth and Seasat image intensity is 0.74 for Rev. 1239 and -0.84 for Rev. 1411. Similar correlations were achieved for specific areas within this data set.

4.2.3 DISCUSSION

This analysis supports the first order hydrodynamic model developed for situations similar to the TOTO tidal bar belts (see Chapter 5) in that it illustrates the tonal reversal expected during opposite current flow direction conditions. High correlations were achieved between SAR image intensity and a Landsat depth profile for limited cases. However, the hydrodynamic situation between the closely spaced tidal bar belts is probably extremely complex, and correlations over large areas are not as high as for the limited cases. This further demonstrates the need to develop more sophisticated analysis techniques when relating SAR image intensity to water depth.

4.3 DIGITAL IMAGE ENHANCEMENT

Up until this point, we have discussed digital processing of SAR data in terms of geometric and radiometric correction and merging of

Seasat data with other data sets. We should not lose sight of one
of the mostly widely practiced forms of digital processing: image
enhancement. With the development of high-speed computers and digi-
tally recorded remote sensing data, much research has been directed
towards development of routines which enhance the resultant imagery
for the visual interpretation.   These image enhancement routines
involve algorithms which smooth, contrast stretch, level slice and
filter the data. In this section, we will evaluate several smoothing
routines on Seasat SAR imagery of oceanic features.

4.3.1 METHODS

For this analysis, digital Seasat SAR data from Rev. 1239 were
used. From Figure 51, it can be seen there are several subtle fea-
tures just west of the tidal bar belts in the lower left quadrant of
the image. These features include both large scale, E-W oriented
striations, as well as numerous N-S oriented small scale, wave-like
features. A 1024 by 1024 pixel subset of this region was extracted
from the full Seasat scene, and is presented in a non-smoothed format
in Figure 56. With the 16 m pixel spacing, this image is approxi-
mately 16.4 km by 16.4 km. The features of interest are located at
grid locations A6 to C6, A5 and C5, A4, and A2 to C2.   In this
figure, we can also see the distinctive N-S patterns which occur
over the tidal bar belts.

A fundamental property of any coherent imaging system such as
SAR is that the imagery is characterized by speckle which results in
an image intensity that fluctuates widely from pixel to pixel even
if the surface is uniform in a statistical or geophysical sense.
Speckle occurs because the image is strongly influenced by interfer-
ence effects between scattering centers within each resolution
element.

136
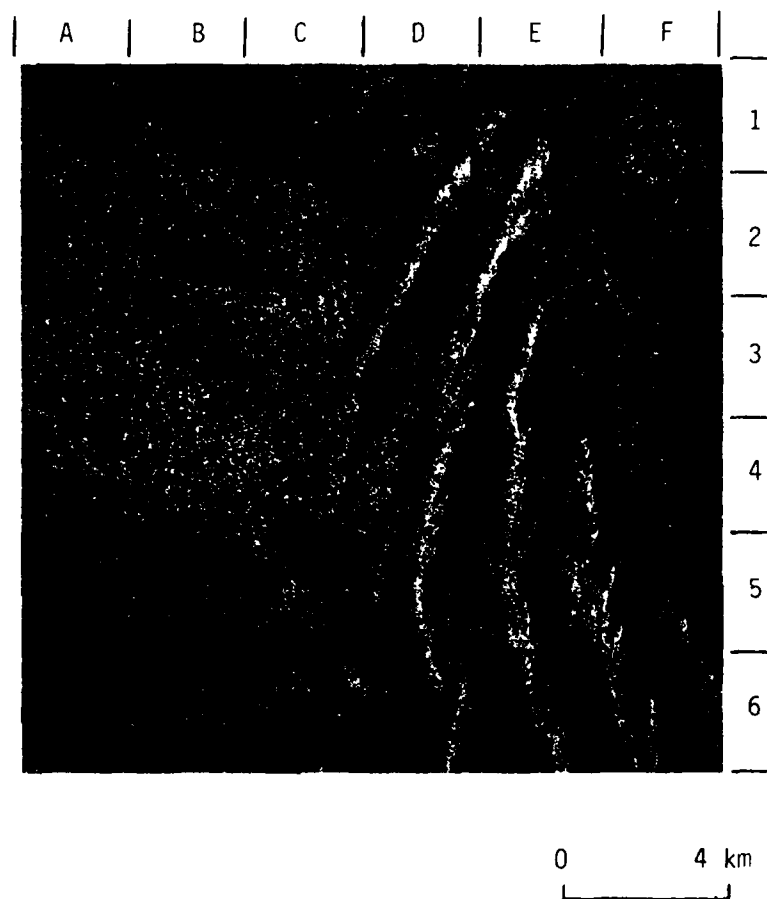
Figure 56.   Non-Smoothed Digital Seasat SAR Data (Rev. 1239)

In this section, we will discuss the results of four image proc-
essing algorithms which reduce image speckle. These routines in-
clude: (1) image averaging, (2) median filtering, (3) variance fil-
tering, and (4) convex hull filtering.

The simplest way to reduce speckle in SAR imagery is to apply an
average or "boxcar" filter to the data. In this smoothing algorithm,
the operator selects the number of pixels to use, which are referred
to as a window. In boxcar filtering, the central pixel of the window
is replaced by the average of all the pixels in the window. In the
present analysis, a 5 by 5 pixel window was used.

A median filter works along the same manner as an average filter,
with the exception that the center pixel is replaced by the median
of the pixels in the window (where median is defined as the middle
value in a set of observations ordered by size). For the median
filter used in this analysis, a 5 by 5 pixel window was selected.

The shortcomings of the average and median smoothing routines is
that they are insensitive to edges and sometimes smooth out the pat-
terns of interest within the image if the window size is too large.
There are several techniques which can be used to overcome this
shortcoming.

A variance filter smooths digital data by replacing the center
pixel by the statistical standard deviation of all pixels within the
window. Thus, this filter is more sensitive to sharp changes in
image intensity which are associated with edges of patterns. In this
analysis, a 5 x 5 pixel window for the variance filter was used.

The final smoothing routine evaluated was a convex hull filter.
The convex hull filter is a sophisticated geometric filter which
operates in three-dimensional space (Crimmins, 1983). It is an
iterative filter which evaluates the amplitudes of neighboring pixels
in its smoothing operation. It essentially smooths out small-scale
intensity variations such as speckle while retaining the larger-scale

features within the imagery. In the present analysis, ten iterations were used for the convex hull filter.

Finally, all images generated from the above smoothing routines were linearly contrast stretched to utilize the full dynamic range of the image display device.

4.3.2 RESULTS

Figures 57 through 60 present the four smoothed images which were compared to the raw data presented in Figure 56. Figure 57 presents imagery from the average smooth, Figure 58 the median smooth, Figure 59 the variance filter and Figure 60 the convex hull filter.

The average filtered image (Figure 57) shows about the same level of detail as the non-filtered image. The tidal bar belts (D1 to F6) show up just as well on either image, as do the small scale, wavelike patterns (e.g., A6 to C6). The larger scale patterns on the left side of the image (A4 to C6) appear to be a little more distinct on the average filtered
image.

The median-filtered image (Figure 58) displays a little more detail than the unsmoothed image. Both the large (D1 to F6 and A4 to C6) and small scale features (e.g., A6 to C6) on the left-hand side of the image are a little more distinct.

The variance-filtered image (Figure 59) displays less detail than the unsmoothed data. The small scale patterns (e.g., A6 to C6) are less distinct as are the larger scale, patterns (A4 to C6).

The convex hull filtered image (Figure 60) appears to enhance the larger patterns at the expense of the small scale patterns. Of particular interest in Figure 60 are the linear feature at A1 to B2, which is not visible on the unsmoothed image, the V-shaped pattern at C5 which, is highlighted on the convex hull image, and the large scale patterns at C4 to A6 which are distinct on this image.
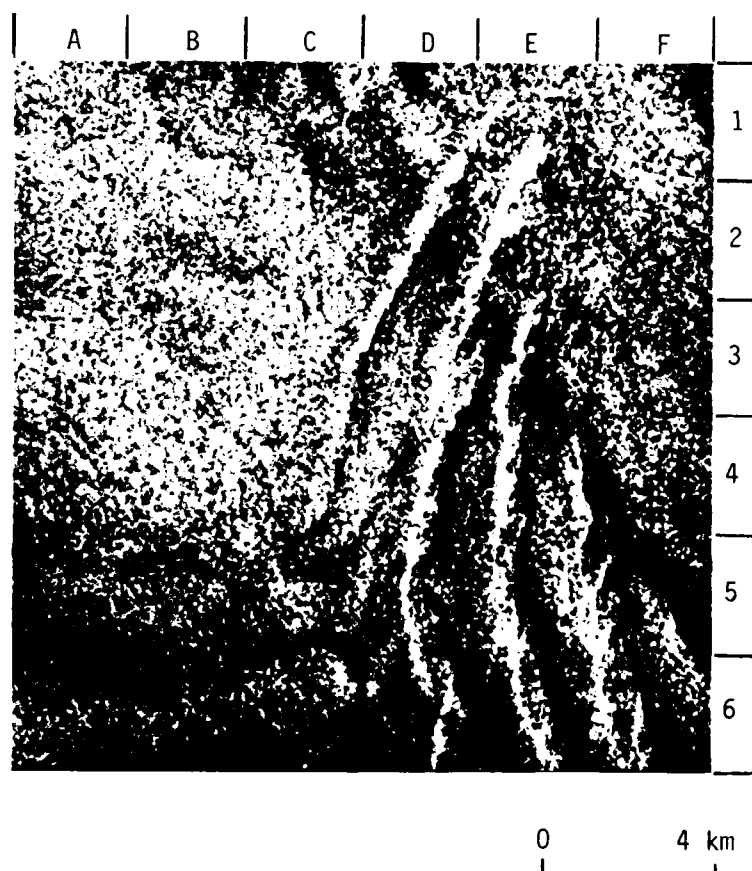
Figure 57. Seasat SAR Image Smoothed Using an Average
Filter (Rev. 1239, 5 × 5 Pixel Window)
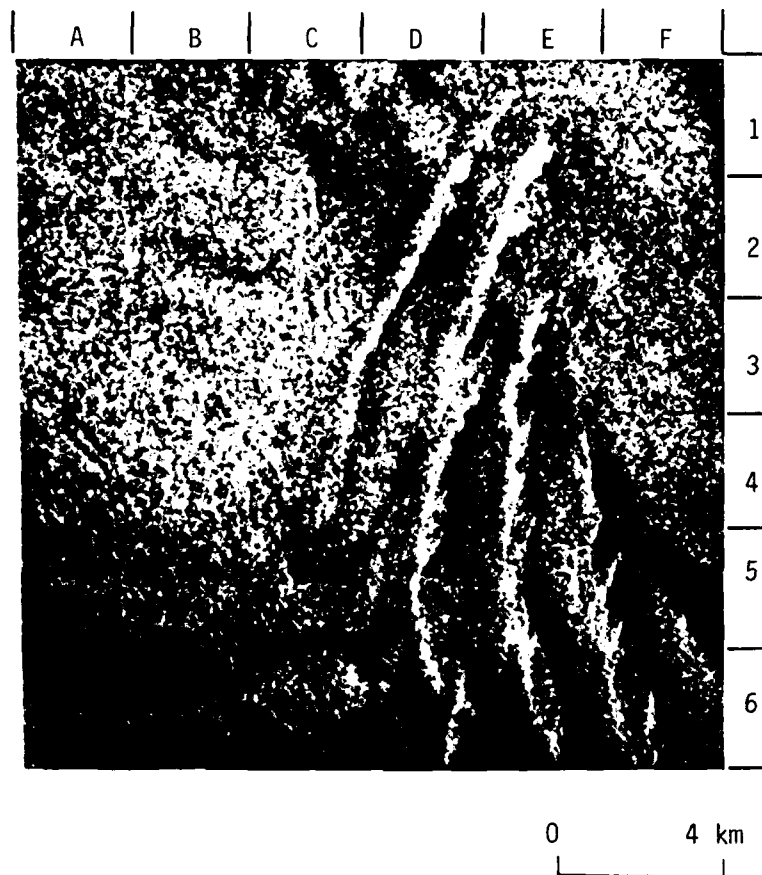
Figure 58. Seasat SAR Image Smoothed Using a Median
Filter (Rev. 1239, 5 × 5 Pixel Window)

141
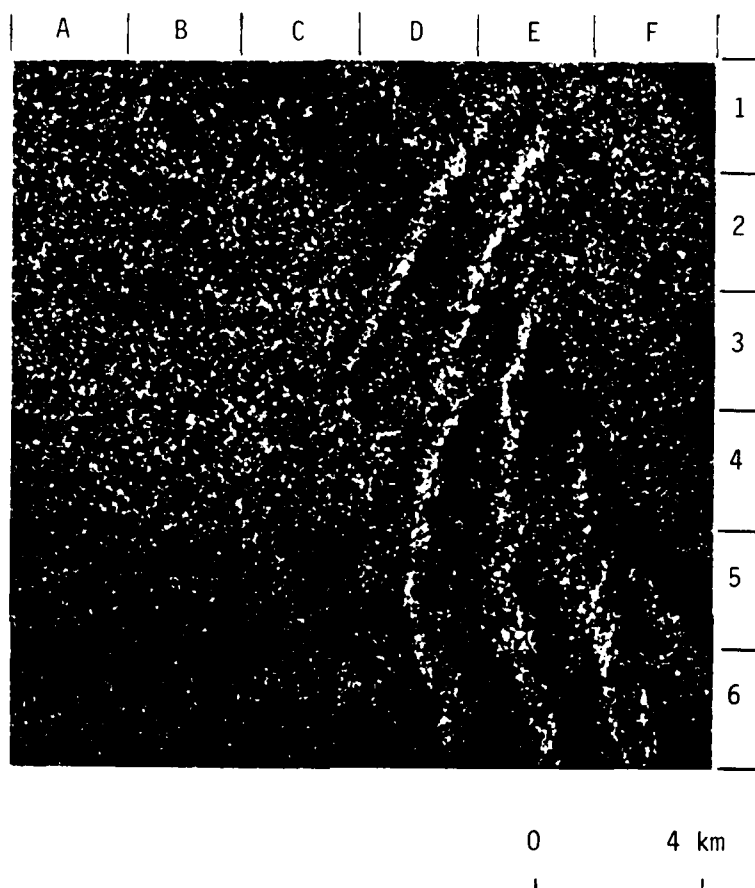
Figure 59. Seasat SAR Image Smoothed Using a
Variance Filter (Rev. 1239, 5 × 5
Pixel Window)
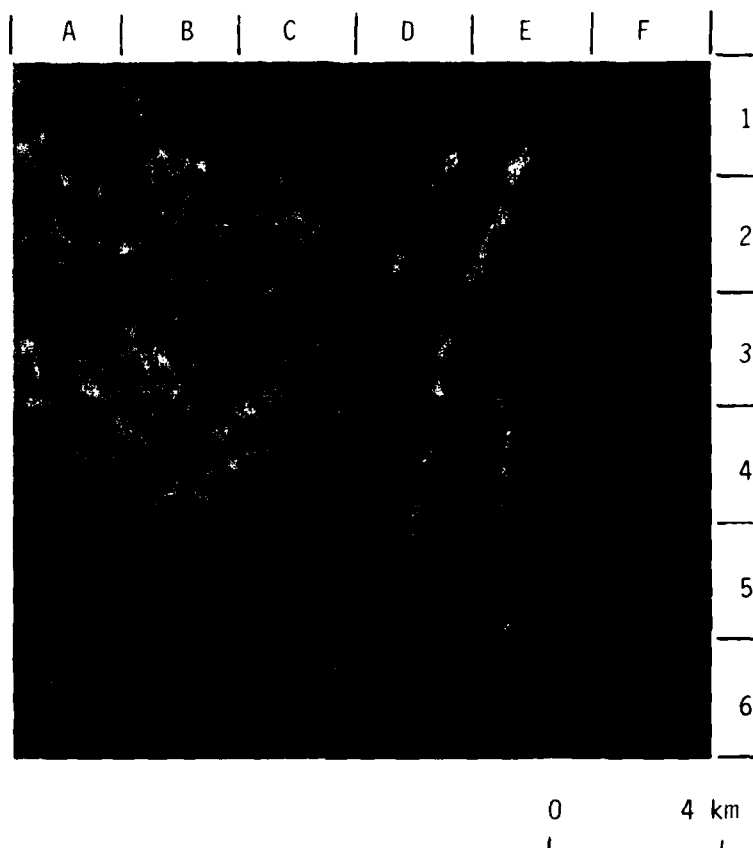
Figure 60.   Seasat SAR Data Smoothed Using a
             Convex Hull Filter (Rev. 1239)

4.3.3 DISCUSSION

It is difficult to quantitatively analyze the significance of the results of the smoothing routines in absolute terms of improving SAR imagery for detection of bottom-related surface patterns because of the lack of accurate bathymetric charts for the test site. The above examples do illustrate, however, that ocean surface patterns present on Seasat SAR imagery can be enhanced using smoothing algorithms.

If digital SAR data are available, it appears that a median filter is best suited as an all-round smoothing algorithm. However, for detection of larger scale patterns, the convex hull type filter may give better results.

In this analysis, we have addressed only one type of image enhancement by discussing several smoothing algorithms. Other digital *processing techniques which also may be used* include level slicing, directional filtering and frequency filtering.

5
MECHANISMS FOR THE DETECTION OF BOTTOM FEATURES ON SAR IMAGERY

In this chapter, the hydrodynamic mechanisms responsible for the appearance of bottom-related surface patterns on SAR imagery are discussed. Although several of these mechanisms were specifically analyzed under the present investigation, some were identified under previous efforts. The general theory of SAR detection of the ocean surface has been reported on elsewhere (see e.g., Shuchman, et al., 1981a). For completeness, a brief discussion is presented here.

The principle in imaging any ocean surface with a radar is that the backscatter of microwave energy (echo) received by the radar contains information on the roughness characteristics (shapes, dimensions and orientations) of the reflecting area. Parameters that influence the SAR image of the ocean surface include the motion of the scattering surfaces, coherent speckle, system resolution, noncoherent integration as well as the surface roughness. In addition, the orientation of ocean waves and of bottom topographic features with respect to the radar "look" direction are influencing parameters.

Several scattering models exist that attempt to explain ocean surface image formation with synthetic aperture radars. These models are of two types: static models that depend on instantaneous surface features, and dynamic models that employ surface scatterer velocities.

Three static models have been suggested to describe the radar scattering of energy from large areas on the ocean surface. These three scattering models are: (1) the tangent model which is most appropriate for small incident angles, (2) the Bragg-Rice scattering model, which correlates well with experimental data for incident angles larger than 10°, and (3) a Rayleigh scattering model which is

often used in terrestrial earth scattering calculations. There is general consensus within the radio-oceanography scientific community that a Bragg-Rice scattering theory best explains the SAR observed backscatter values obtained from the ocean surface for incidence angles between 20° and 60° (Shuchman, et al., 1981b). The Bragg-Rice scattering model is based on a well known phenomena in the study of crystals, grating, and periodic structures. If one considers the random ocean surface to be represented by a combination (i.e., spectrum) of periodic surfaces, then the spectrum region which satisfies the backscatter phase matching condition will be the main contributor to the backscatter cross section. Sometimes in the literature, this phase matching of the small ocean Bragg waves with the incident radar electromagnetic energy is termed a resonance phenomenon; more correctly stated, it should be termed a constructive interference between the electromagnetic and ocean waves.

Pioneering theoretical and experimental work by Wright (1966) at the NRL demonstrated the general validity of a Bragg scattering model for an ocean surface imaged by radar. In a series of wave tank measurements using 3 and 25 cm wavelength continuous wave (CW) Doppler radars, Wright demonstrated that Bragg scattering, that is, transmitted radar energy with wave number K, interacts in a resonant or interference fashion with ocean surface waves with wave number K_w, such that

$$K_w = 2K \sin \theta,$$ (5)

where $K_w = 2\pi/L$ and $K = 2\pi/\lambda$, (L and λ are the wavelengths of the surface waves and the radar, respectively), and θ is the incidence angle. Shuchman, et al. (1981b) showed that a Bragg scattering equation satisfactorily explained the radar backscatter return from SAR using data collected during the Marineland experiment (for a discussion of the Marineland experiment, see Shemdin, 1980). It should be noted that radar data of large ocean areas (1 x 1 km) were averaged in that analysis. Thus based on the above, the principal radar

reflectivity mechanism of imaging ocean surfaces is via the capillary and small gravity waves which produce Bragg scattering (Raney and Shuchman, 1978).

Synthetic aperture radars are also sensitive to the motion of scatterers present in the imaged scene (Raney, 1971). Effects of scatterer motion on SAR imagery may include: (1) image displacement, smearing and loss of focus in the azimuth direction, and (2) loss of focus in the range direction. Some of these effects can be removed during processing of the SAR signal histories by making appropriate adjustments to the processor (Shuchman, 1981). Effects which cannot be removed during processing may reduce the detectability of gravity waves, but are not expected to have a large influence on the depth-related image features.

Loss of focus in the range direction is due to a rotation of the phase history of the target (i.e., migration through range cells). This loss of focus is proportional to the range velocity and the integration time, and can be corrected by a rotation of the lenses in the optical processor, assuming the range velocity is constant during the integration time.

Loss of focus in the azimuth direction can be caused by a constant velocity in the azimuth direction or a changing velocity (i.e., an acceleration) in the range direction. These effects can be corrected by a change in the azimuth focus setting of the processor, assuming that the azimuth velocity and radial acceleration are constant. Since they are both inversely proportional to the platform velocity, these effects are less important for spaceborne than for aircraft SAR systems.

A variety of processes can alter the surface Bragg waves, resulting in a distinct pattern on SAR imagery. These include oceanic processes (currents, surface waves, internal waves, slicks, local water depth variations, water temperature and salinity) variations,

147

climatic processes (wind, rain and air temperature) and man-made phenomena (ships, buoys and oil spills). It is the hydrodynamic interaction between several oceanic processes and a distinct bottom feature which allows that feature to be detected on SAR imagery. Examples of these bottom-induced surface patterns will be presented below. For examples of other surface patterns on Seasat SAR imagery, see Shuchman, et al., (1981); Gower (1981); Beal, et al. (1981); or Fu and Holt (1982).

There are two dominant oceanic processes, which when they interact with a bottom feature, can result in a SAR-observed surface pattern: gravity waves and currents. These result in a set of six SAR-observed patterns which can be used as an indicator of the presence of a bottom feature. These six patterns are summarized in Table 1. The remainder of this chapter discusses the hydrodynamic mechanisms responsible for the appearance of these patterns on SAR imagery.

5.1 REFRACTION OF SURFACE GRAVITY WAVES IN COASTAL WATERS

The first method for detection of submerged features on SAR imagery is the monitoring of wave refraction in shallow water, provided the size of the shoaling bottom is large compared to the wavelength of the gravity wave. Figure 61 illustrates the theoretical refraction of a gravity wave as it enters a shoaling coastal region. This wave refraction diagram assumes that the bottom depth contours are straight and parallel with respect to the shoreline. As a wave propagates shoreward, it will begin to respond to the shoaling ocean-bottom at the point where the ratio of the water depth (h) to the deep-water wavelength (L_0) approximately equals one-half (i.e., $h/L_0 = 0.5$). If the angle (α) between the wavefront and the bottom contour is not equal to zero, the shoreward portion of the wave will feel the bottom first, resulting in a decrease in the wave velocity (celerity), and thus the angle of the shoreward portion of the wave will decrease relative to the seaward portion of the wave.
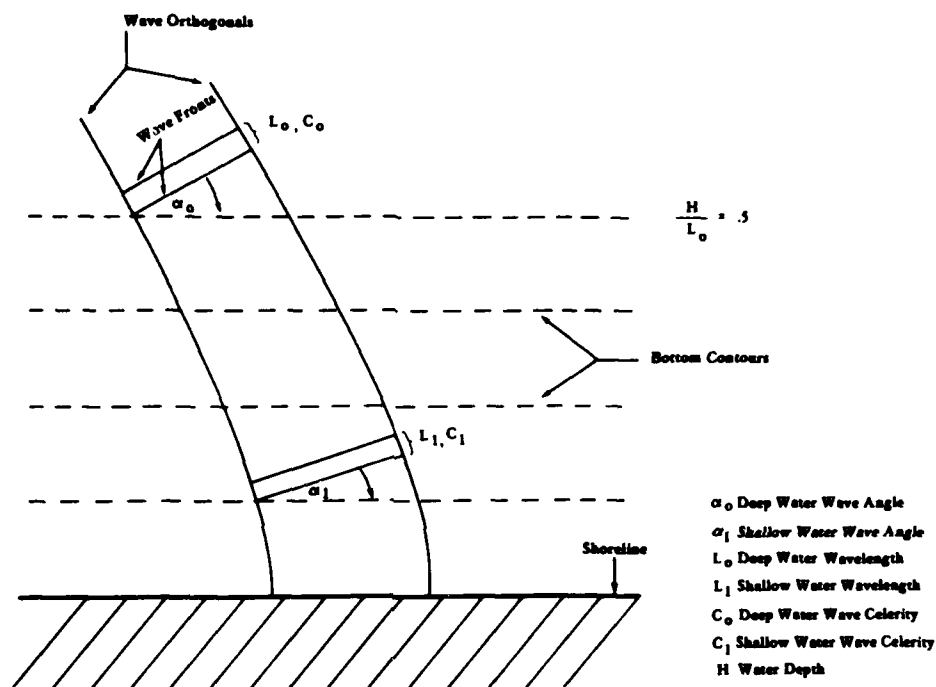
Figure 61.   Theoretical Refraction of Waves in Shoaling Water

149

The decrease in velocity will also cause a decrease in the wavelength between two successive waves, independent of the wave angle. In summary, as a wave propagates shoreward, its wavelength (L) and direction (α) will both decrease.

For the case presented in Figure 61, the shallow-water wavelength (L_1) is given by

$$L_1 = L_0 \tanh \frac{2\pi h}{L_1} , \qquad (6)$$

and the shallow-water direction of propagation (α_1) is given by

$$\sin \alpha_1 = \sin \alpha_0 \tanh \frac{2\pi h}{L_1} . \qquad (7)$$

Therefore, if L_1, L_0, α_1, and α_0 can be measured, then the water depth (h) can be calculated by inverting either Eq. (6) or Eq. (7).

As illustrated in Figure 12 (see Section 3.2.1), shoal areas can be delineated by correctly interpreting refracting gravity wave patterns. It has also been shown that accurate estimates of dominant gravity wavelength (L) and direction of propagation (α) can be estimated from SAR data through the use of two-dimensional Fourier transforms (see Kasischke, 1980; Shuchman, et al., 1982). Figure 62 presents two examples of Seasat SAR imagery (collected during Rev. 974 on 3 September 1978) of gravity waves off Cape Hatteras, North Carolina, and their resultant two-dimensional fast Fourier transforms (FFTs). The distance between their peaks in the FFT spectra are inversely proportional to the dominant wavelength, and the orientation of the peaks can be used to estimate the dominant direction of propagation. Figure 62(a) is from a deep water (h ~ 100 m) area, while Figure 62(b) is from a shallow-water (h = 20 m) area. It is evident from both the SAR imagery as well as the FFTs that the wavelength and direction have changed.
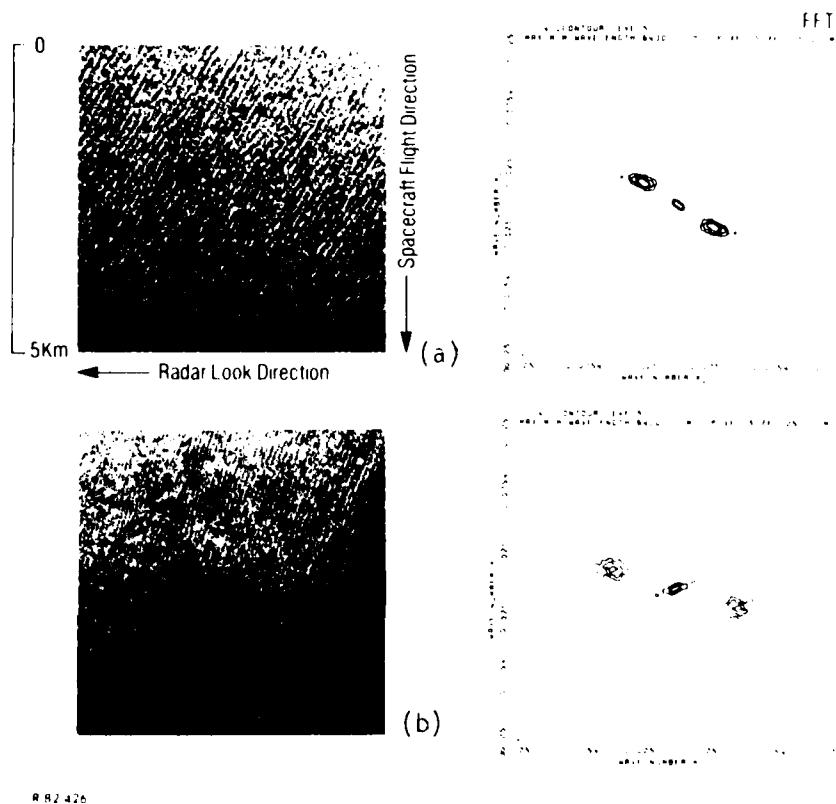
Figure 62. Seasat SAR Images Illustrating Change in Wavelength
and Direction Due to Wave Refraction in Shoaling Water;
(a) is in Deep Water (200 m); (b) is in Shallow Water
(20 m) (Rev. 974, Cape Hatteras, N.C., 3 September 1978).

151

Studies have shown that by using SAR estimates of dominant wavelength in Eq. (6), estimates of water depths can be generated (Shuchman, et al., 1979; Kasischke, et al., 1981; Meadows, et al., 1983). Figure 63 shows a scatterplot of water depths estimated using Eq. (6) versus hydrographic survey water depths.

5.2 NON-LINEAR INTERACTIONS OF GRAVITY WAVES

The above discussed wave refraction case assumes a bottom morphology with a gradual (compared to the surface wavelength) change in depth which results in a linear gravity wave interaction with the bottom. When the shoaling is more abrupt, such as at a shoal, reef or sill around an island, non-linear gravity wave/bottom interactions can occur, resulting in surface patterns which are detected on SAR imagery. Two distinct cases are discussed here: non-breaking and breaking waves.

5.2.1 NON-BREAKING WAVES

The SAR image in Figure 64 was collected during Revolution 762 (19 August 1978) as Seasat passed over North Rona Rock, an island located approximately 75 km off the northeast tip of Scotland. Detected on this SAR image is a distinct change in radar backscatter in the shoal region (designated by the 50 m line) surrounding North Rona Rock. The gravity wave field present on this date is also clearly evident on the SAR imagery. Surface measurements made concurrently with the Seasat overpass about 300 kilometers west of North Rona Rock indicate a swell with a dominant wavelength of 206 m, a significant wave height $(H_{1/3})$ of 4.3 m and a direction of propagation towards 60° (T) was present in the northeast Atlantic Ocean at this time. A wind from 186° (True) with a surface velocity of 12 m/s was also present. The diffraction of the waves as they pass North Rona Rock can also be seen on the image.
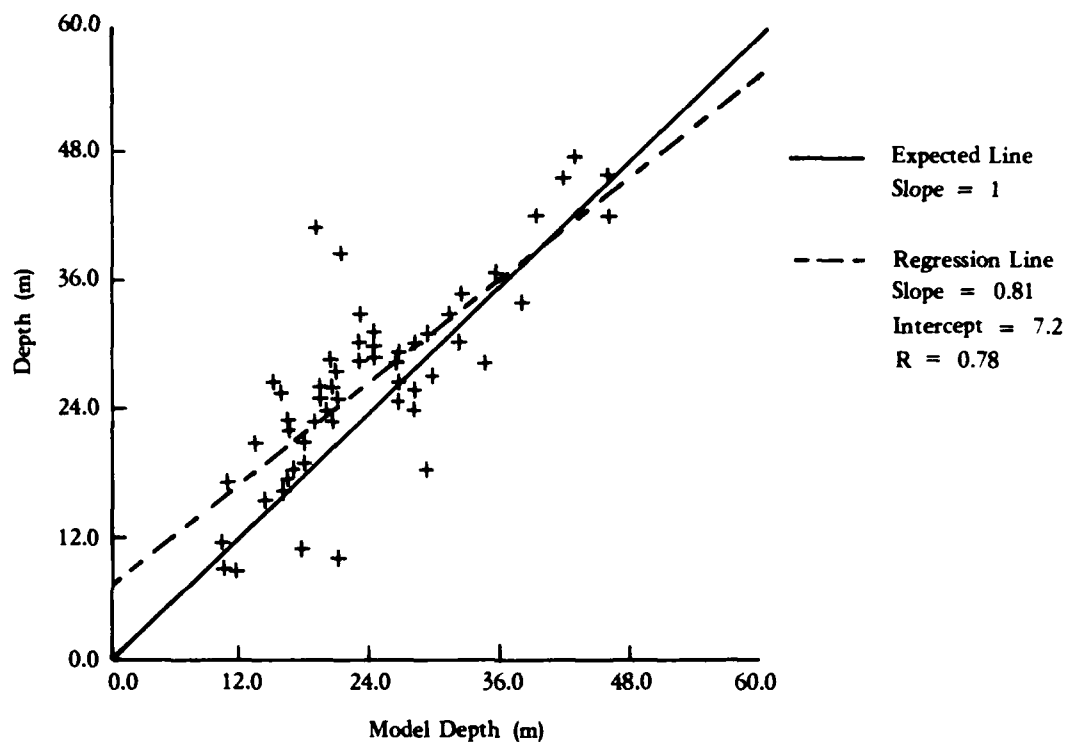
Figure 63. Plot of Water Depths Calculated Using Inverted
Airy Wave Theory (Eq. (6)) with Changes of
Wavelength Extracted from Seasat SAR Imagery
Versus Depths Obtained from National Ocean Surveys
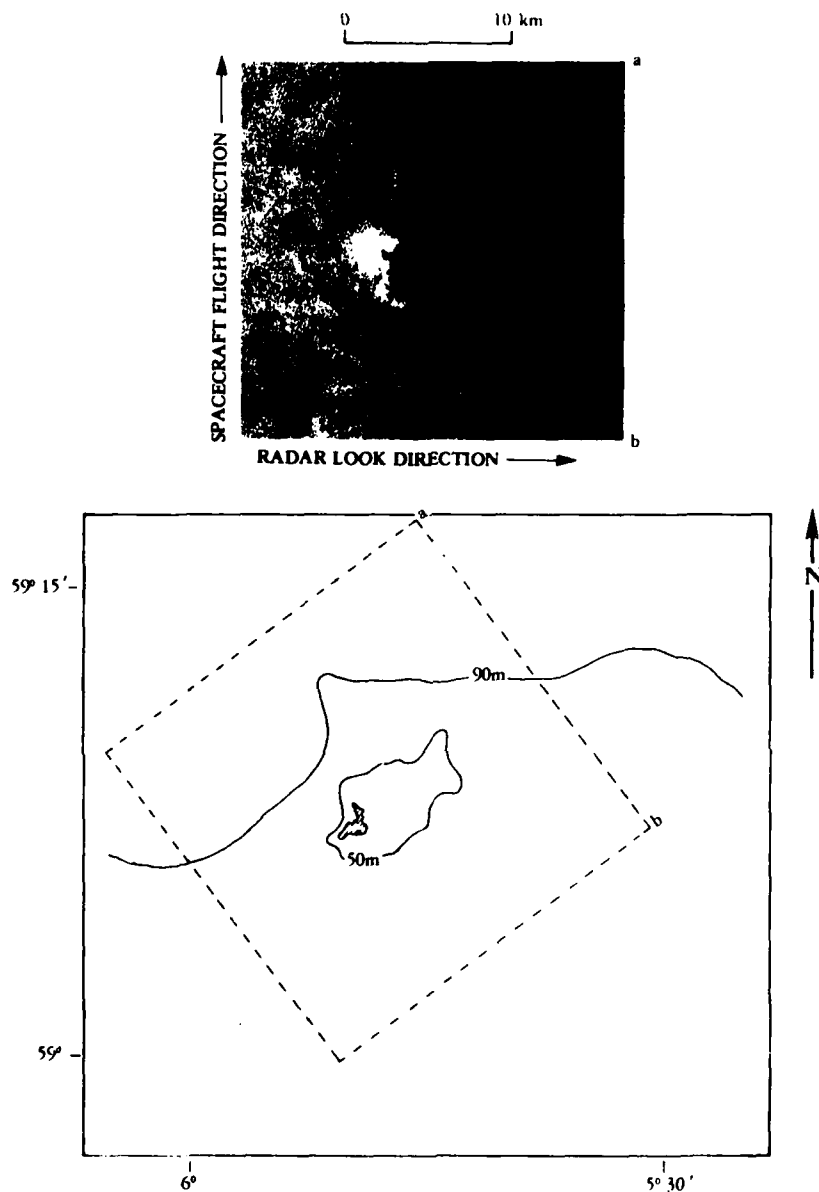
Figure 64.   Seasat SAR Imagery and Hydrographic Chart of North Rona Rock
(Collected During Revolution 762, 19 August 1978) Illustrating
Change in Image Tone (Radar Backscatter) Associated With the
Shoal Region Around the Island. (Seasat SAR Data Collected By
the European Space Agency and Optically Processed at ERIM.
Chart Reproduced From DMA Chart No. 35200.)

154

The example presented in Figure 64 was selected for a more in-
depth hydrodynamic analysis by Dynamics Technology under sub-contract
to ERIM (Liu, 1983). A complete copy of Dynamics Technology's final
report for this sub-contract is presented in Appendix B. A summary
of their analysis of the North Rona Rock Seasat example is presented
below.

The processes that generate the variations in Bragg scattering
observed in the Seasat SAR image presented in Figure 64 most likely
involved a combination of modifications of Bragg scattering waves
due to tidal flow over topography and currents generated by the im-
pingement and refraction of swell and long waves on the shoal. It
has been shown by Longuet-Higgins (1967) that islands can trap long-
wave energy and this phenomenon was observed at Macquarie Island in
the Southern Ocean. The probable existence of such "edge waves" or
topographically-trapped waves in the shoal region surrounding North
Rona Rock may cause the change in radar backscatter. Some light can
be thrown on the phenomenon of wave trapping by considering the sim-
plest possible case: that of long free waves around a circular sill
in shallow water, as shown in Figure 65(a). The solution of the
wave- field is illustrated in Figure 65(b), which shows the plan
view of the wave crests. Two systems of waves propagate along
trajectories inside and outside the sill. In general, the trapping
of the energy is essentially due to the waves being reflected
internally at the edge of the sill, when their angle of incidence is
greater than a critical angle. A mathematical analysis of this
special case is presented in Appendix B. This theory is a possible
explanation of the the SAR-observed pattern in Figure 64.

In general, a more exotic wave-wave interaction could generate
higher harmonic waves which could be trapped around an island. Wave/
current interaction could produce wave breaking caused by the block-
age phenomenon (Phillips, 1977). A recent paper of Larsen (1980)
suggests that wavelets may be trapped in the current field over
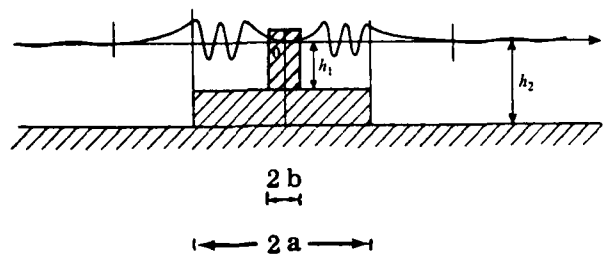
(a) Radial Cross Section
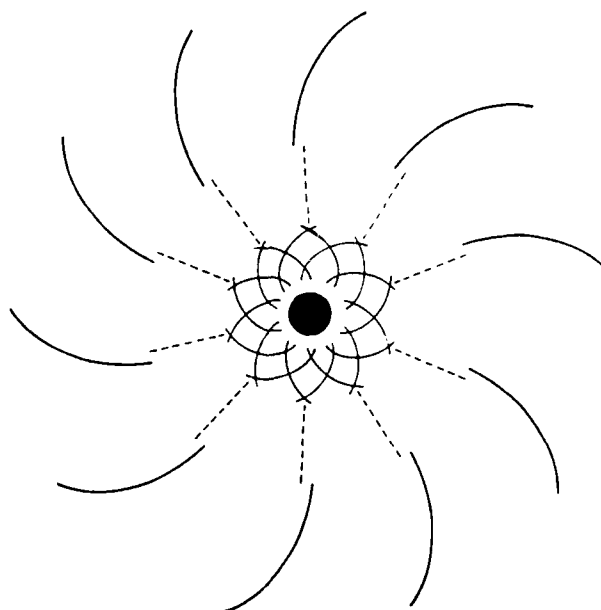
(b) Plan View of the Wave Crests
(After Longuet-Higgins, 1967)

Figure 65. Illustration of Long Wave Trapping by a Sill
Around an Island

topography, even when the wave group velocity does not match current speed (non-resonant condition). These mechanisms, if they occur, would enhance the trapping phenomenon and, in turn, change the radar backscatter. The additional energy associated with the trapped wave energy most likely alters the surface capillary wave structure sufficiently to be detected on the SAR imagery.

5.2.2 BREAKING WAVES

When a gravity wave propagates onto a very abrupt shoal or reef, it can break. These breaking waves can then be detected on SAR imagery as an area of high radar backscatter, thus delineating the edge of the shoal or reef. Figures 12, 15 and 17 present examples of this breaking wave phenomena which were observed in SIR-A SAR imagery. This imagery was all collected during the same pass.

The gravity wave field is clearly evident on the SIR-A imagery presented in Figures 12, 15 and 17. The dominant wavelength of these waves is approximately 250 m. Because of the shadowing on the south side of the island in Figure 15, it can be assumed that the waves are propagating towards the south.

The bright lines off the north and west sides of the islands in the imagery clearly outline the edges of the barrier reefs and are believed to be due to the breaking of the gravity waves. The concept of being able to detect breaking waves on SAR imagery is straightforward to understand. In the highly agitated breaking wave surf, there is an increase in both Bragg scattering (Alpers, et al., 1981) as well as increased specular and wedge scattering (Lyzenga, et al., 1983). Therefore, breaking waves result in an increase in radar backscatter which can easily be distinguished against a background of non- breaking waves.

157

5.3 TIDAL CURRENTS FLOWING OVER SHALLOW WATER FEATURES

The case where a tidal current flows over a shallow-water shoal, the edge of a bank, or a coral reef is perhaps the most graphic illustration of a bottom-related surface pattern as well as the most well understood. In this section, we will present an example which utilizes Seasat SAR imagery collected over the Tongue of the Ocean, which was presented in Chapter 4. This presentation is a summary of a previous year's efforts (Kasischke, et al., 1982; 1983).

Figure 50 presented two examples of Seasat SAR images collected at the edge of the Great Bahama Bank, over a series of tidal bar belts in the southern end of the Tongue of the Ocean (TOTO). It is postulated that the patterns present on the Seasat imagery in Figure 50 were the result of an interaction between a tidal current flowing over the distinct bottom features in this area. Although the tidal range between high and low water is only about one meter in the Bahamas, tidal currents in the tidal bar belts region of the TOTO have been reported to be between 1 and 1.5 m/s (2 to 3 knots).

The strong tidal-driven flow of water over the tidal bar belts and off the edge of Great Bahama Bank into the TOTO sufficiently disturbs the small scale surface roughness structure (i.e., the capillary and ultra-gravity waves) to cause a corresponding change in radar backscatter. It should be further noted that although the surface patterns occur in the same locations in the two Seasat images in Figure 50, their appearance is different. These differences can be explained through the use of the hydrodynamic/electromagnetic model developed by Shuchman (1982), a qualitative synopsis of which is given in the following paragraphs.

There are three major environmental factors influencing the ocean surface roughness sensed by the SAR over sand banks such as those located at the TOTO. These factors are: (1) the current speed; (2) depth of water; and (3) the wind speed and direction. In regions

where the depth (and therefore the current speed) is changing rapidly, the roughness is influenced primarily by the rate of change of the current speed. A changing current tends to increase or decrease the amplitude of the small capillary and ultra-gravity waves on the surface and make the surface rougher or smoother, depending on the direction of the current relative to the waves.

In general, where the depth is decreasing in the direction towards which the current is flowing, the surface velocity of the water will increase, resulting in a decrease in the amplitude of the surface capillary waves traveling with the current. In areas where the depth in increasing, the surface velocity will decrease, resulting in an increase in the amplitude of the surface capillary waves traveling with the current. This alternating increase and decrease of the water velocity results in the banded patterns imaged by the Seasat SAR over the sand banks.

In areas where the depth and the current are nearly constant, the surface roughness is governed primarily by the wind. The wind can be thought of as a restoring force which tends to bring the wave height, or surface roughness into an equilibrium value which depends primarily on the wind speed. Thus, if current variations cause the wave height to be decreased, the wind, given sufficient time, will return the wave height to its original value. These general statements are applied to the two particular cases illustrated in Figure 50 in the following paragraphs.

The bottom topography for the southern edge of the TOTO may be modeled and divided into seven zones as illustrated in Figure 66. The pattern of surface roughness variations depends on the current direction. For simplicity, in both of these cases the waves are assumed to be propagating in the same direction as the current. Essentially the same qualitative descriptions hold if the waves are propagating in the opposite direction to the current except that the

159

a) Falling Tide:

| Radar Image Tone | Gray | Dark | Bright | Gray | Bright | Gray |

Surface Roughness

Current Magnitude

| Zone | 1 | 2 | 3 | 4 | 5 | 6 | 7 |

Bottom

b) Rising Tide:

| Radar Image Tone | Gray | Bright | Gray | Dark | Gray | Dark | Gray |

Surface Roughness

Current Magnitude

| Zone | 1 | 2 | 3 | 4 | 5 | 6 | 7 |
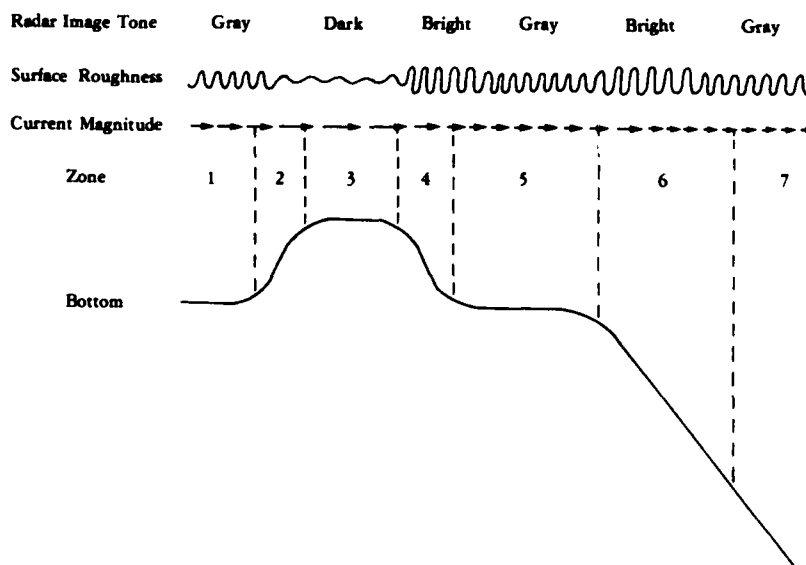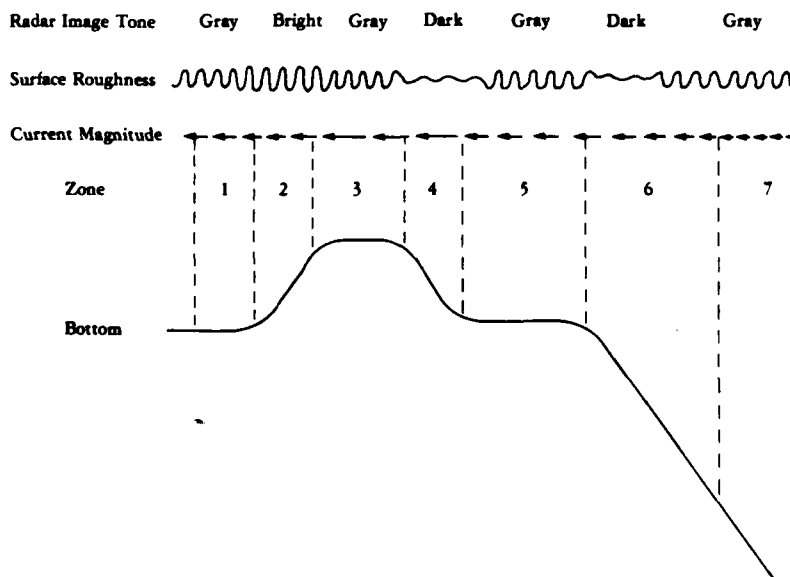
Bottom

Figure 66.   Schematic Diagram of Interactions of Current, Bottom
and Capillary Waves and the Resultant SAR Image
Intensity Variation

160

phenomenon of wave blockage can occur if the current velocity changes from less than the group velocity of the waves to larger than this velocity. For a falling tide (Figure 66a) the following interactions occur:

Zone 1: The depth is assumed to be uniform over a large enough area so that the wave height (surface roughness) has reached an equilibrium value for the existing wind speed and current conditions.

Zone 2: Decreasing depth causes an increasing water current which in turn causes a progressive smoothing out of the surface roughness pattern (i.e., a decrease in the amplitude of the capillary and ultra gravity waves).

Zone 3: The current remains constant while the wave height (surface roughness) is brought back into equilibrium by the action of the wind.

Zone 4: Increasing depth causes a decreasing current, thus a compression of the surface waves, and a corresponding progressive roughening of the surface.

Zone 5: Depth and current remain constant while the wave height readjusts into equilibrium with the wind.

Zone 6: Similar to region 4, i.e., a decreasing current causes an increasing surface roughness.

Zone 7: Similar to region 5, i.e., a gradual return to equilibrium with the given wind conditions.

The above model appears to adequately describe the patterns in Figure 50 for Revolution 1411, when an ebb tidal flow was present. Note in the SAR image collected over the southern portion of the TOTO, there exists a series of ridges, each of which has the banded appearance as described in regions 1 through 5 above.

For a rising (flood) tide (i.e., a current flowing onto the bank), the following interactions occur, as illustrated in Figure 66b:

Region 7: The depth is assumed to be uniform over a large enough area so that the wave heights (i.e., surface roughness) has reached an equilibrium with the existing wind speed and current conditions, resulting in an area of uniform radar backscatter.

Zone 6: A decreasing water depth causes an increasing current which in turn causes a smoothing out (damping) of the surface capillary and ultra-gravity waves.

Zone 5: Gradual return to equilibrium.

Zone 4: Same as Region 6.

Zone 3: Gradual return to equilibrium.

Zone 2: An increasing water depth causes a decreasing current which in turn causes a compression of the surface waves and a progressive roughening of the surface with respect to the incident radar waves.

Zone 1: Gradual return to equilibrium.

This model appears to adequately describe the patterns present on Revolution 1239 (Figure 50) during a flood tide.

5.4 COASTAL INTERNAL WAVES

It is now widely accepted that internal baroclinic tides propagating onto a continental shelf, at a time when a stratified water column exists, result in internal wave fields which can be detected on satellite imagery. Figure 67 shows Seasat SAR imagery collected over the New York Bight during Rev. 974 on 3 September 1978. Figure 68 consists of line drawings of the internal wave positions observed on Figure 67 super-imposed on the bottom topography (after Liu, 1983). Periodic striations of four sequential wave pockets are clearly visible in the middle of the SAR image, apparently radiating from the edge of the continental shelf. The dotted area near the top right corner of Figure 68 represents an area of low radar return

Figure 67. Seasat SAR Imagery of Internal Waves Collected Over New York Bight (Rev. 974, 3 September 1978, JPL Optically Processed Imagery)
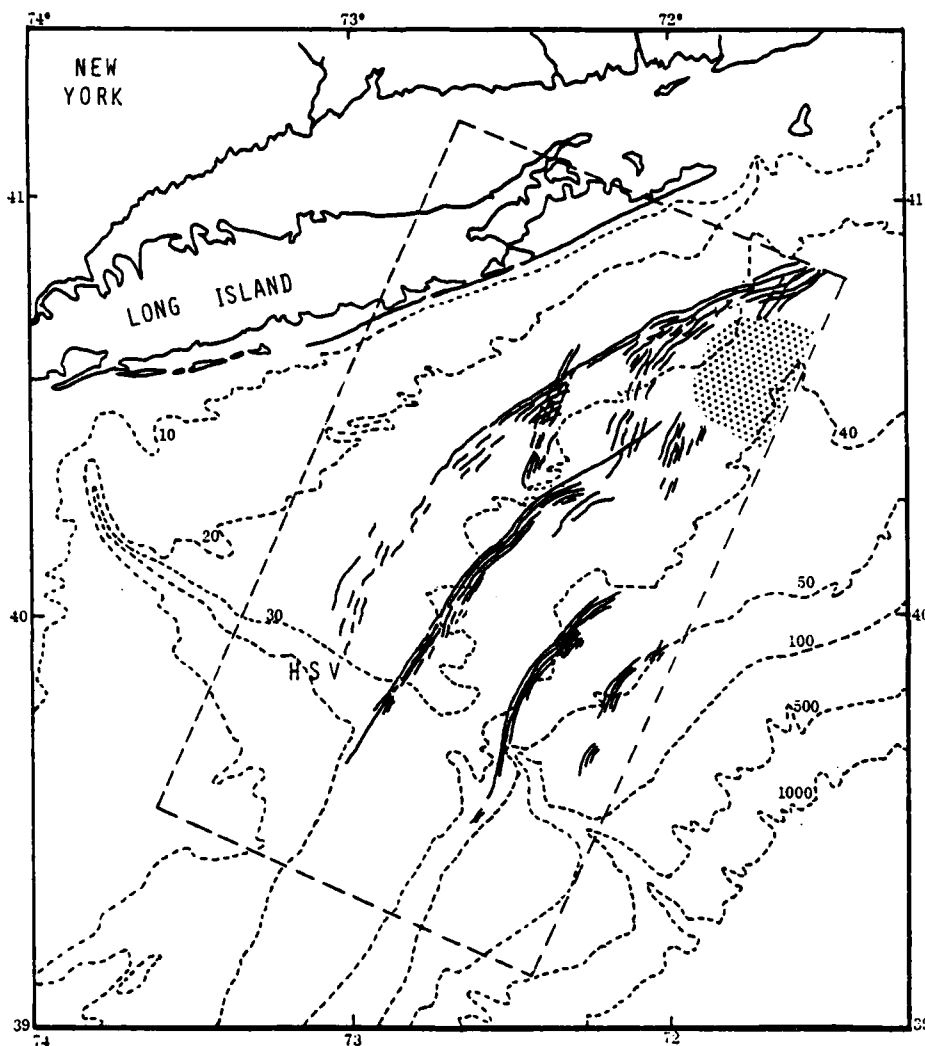
$\sum$**ERIM**

Figure 68. Schematic Line Drawing of the Internal
Wavefield Observed in Rev. 974
Superimposed on the Bottom Topography

164

on the Rev. 974 SAR image which was most likely caused by low surface winds.

Long-term current and temperature observations on the Middle Atlantic Shelf were reported by Mayer, et al. (1979) during two years, 1975 and 1976. They reported that a mixed layer of 30 m depth was present for the summer months of June 1975 and September 1976. Although the SAR image of Figure 67 was taken on 3 September 1978, the seasonal characteristics of the shelf water mass are expected to be similar. In general, stratification builds to a maximum in August in this region.

The following mechanism explains the generation process of the internal waves. First, the scattering of the barotropic tidal energy into an internal baroclinic tide occurs at the edge of the continental shelf for a few hours during the peak tide current. This baroclinic current distribution then generates internal waves by shear flow instability on the bottom of the mixed layer (Tsai and Apel, 1979). As the tidal currents rotate through the tidal ellipse, the instability starts up and shuts down every 12.5 hours. Thus a packet of waves is created at the shelf edge and launched once each semi-diurnal-tidal cycle as shown schematically in Figure 69: it typically contains about 10 waves. Then the wave packet propagates up onto the shelf until the mixed layer intersects the bottom, whereupon the waves break and deposit their energy into turbulence and bottom sediment transport.

A hydrodynamic analysis of the Rev. 974 internal waves was performed by Dynamics Technology (Liu, 1983). This analysis is summarized below and presented in detail in Appendix B.

The model developed by Liu (1983) is based on a two-layer solitary wave theory, with the wavelengths and amplitudes within a packet monotonically decreasing from front to rear. Each wave within a packet has a surface current, which in turn, perturbs the surface capillary waves.
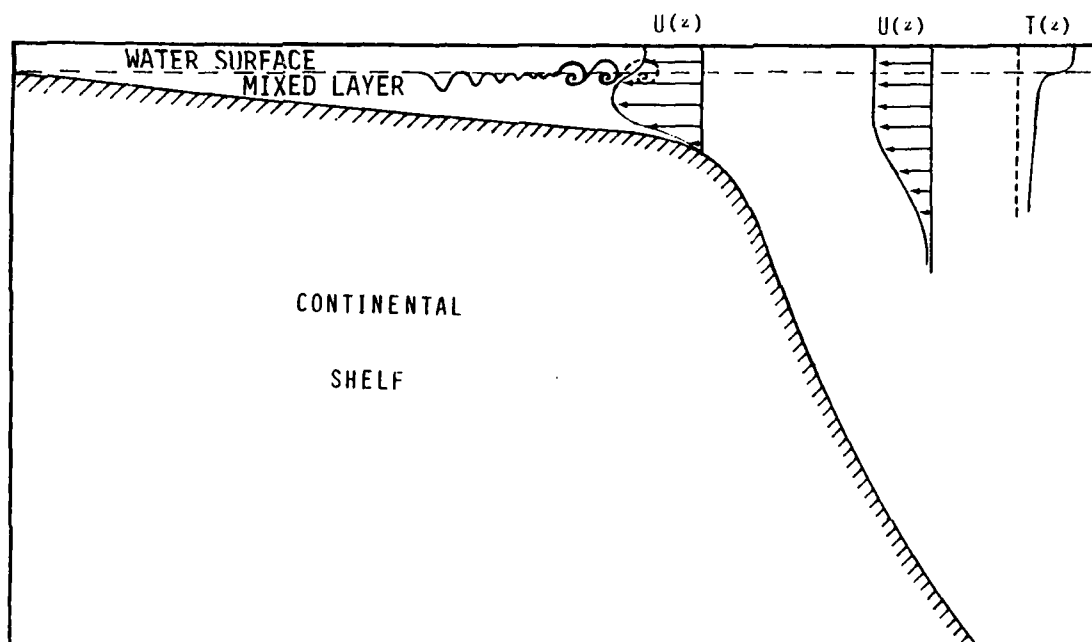
Figure 69.   Schematic Diagram of Generation of an Internal Wave
              Packet on the Edge of a Continental Shelf

Figure 70(a) presents the surface currents for an internal wave field for the estimated conditions for Rev. 974. Figure 70(b) presents the surface strain rate of the capillary waves induced by the surface currents. Figure 71 presents a simulated SAR negative image of the internal wave packet. This negative indicates that an internal wave crest consists of a light band followed by a dark band, which is consistent with the internal waves imaged during Rev. 974.

5.5 DEEP WATER INTERNAL WAVES

Tidal currents flowing over deep water bottom features can generate internal waves as well as frontal boundaries (which are discussed in the next section). Figure 72 shows Seasat SAR imagery of deep water features over the Wyville-Thomson Ridge collected during Revolution 762 on 19 August 1978. Figure 73(a) presents the corresponding bathymetric chart for this region. Figure 73(b) combines line drawings of internal waves and a frontal boundary observed in Figure 72 with the corresponding bathymetric chart for this area. From Figures 72 and 73, it can be seen that there are numerous internal wave signatures. The internal waves in the middle of the image (F5 to J8) appear to be generated over the Wyville-Thomson Ridge. Near the lower right corner of the image, three wave packets are visible along the edge of the continental shelf (D4 to F4). It is to be noted that no waves are generated on the north side of the Wyville-Thomson, as will be discussed below.

Figure 74 presents a cross-section of the Wyville-Thomson ridge through the points C, O, D, F and G on Figure 73(b). It's dominant bottom features are a broad, saddle-like valley on the east side of the ridge near the Faeroe Bank, and a 90° sector of deep water perpendicular to the ridge, as shown in Figure 75. The ridge has the characteristic scales of approximately 10 km in both the longitudinal and transverse directions.

167
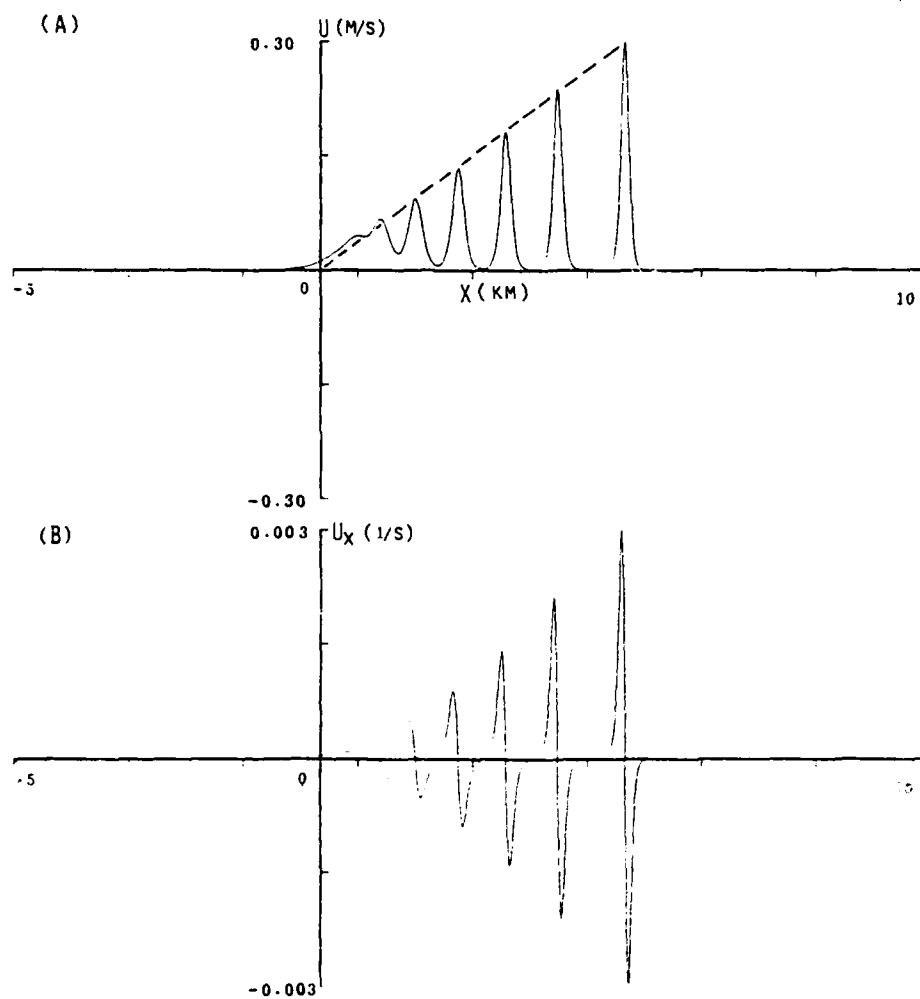
Figure 70. Surface Current (A) and Surface Strain Rate
Induced (B) By an Internal Wave Packet

10 KM (Azimuth)

5 KM (Range)
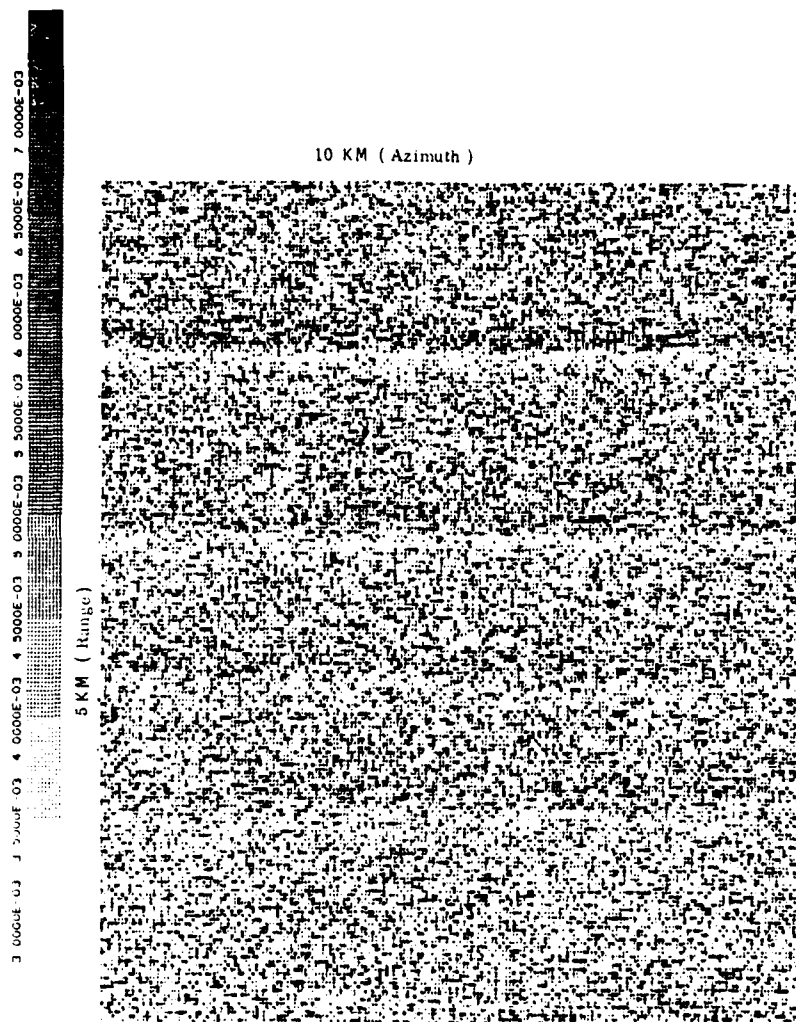
Figure 71. Simulated Seasat SAR Negative Image for Rev. 974
Showing Good Visibility of Internal Waves

169
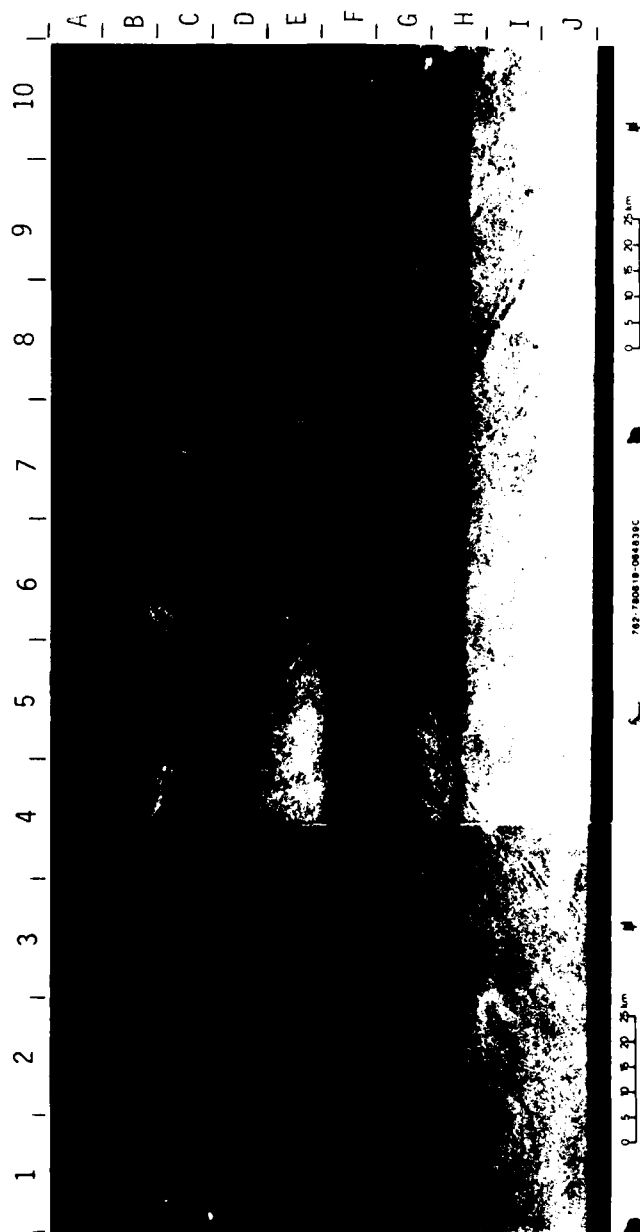
Figure 72. Seasat SAR Imagery Collected Over Wyville-Thomson Ridge Illustrating Internal Wave and Frontal Boundary Patterns (Seasat Rev. 762, 19 August 1978, JPL Optically Processed Imagery)

170
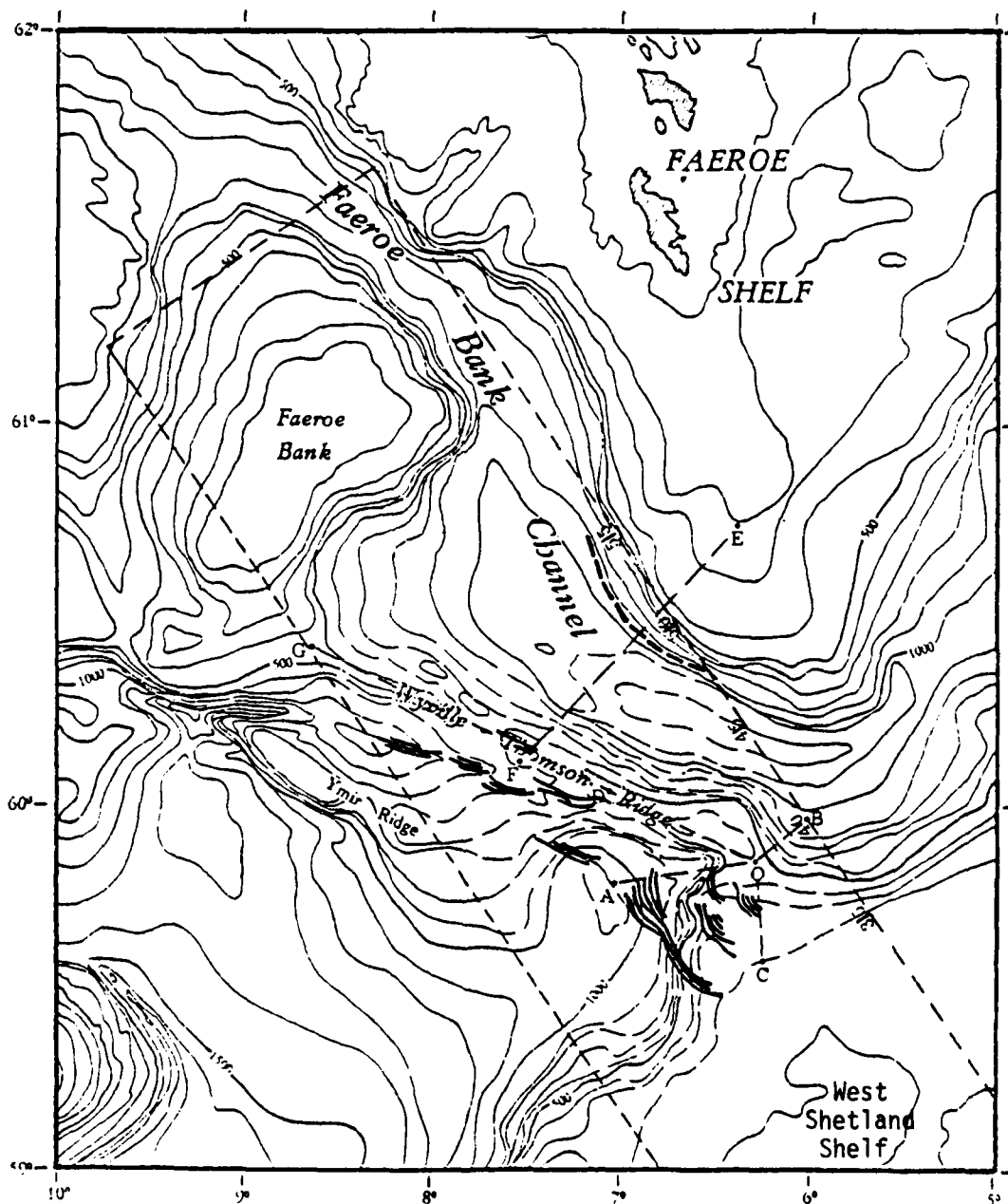
Figure 73a. Line Drawings of Internal Waves and a Frontal Boundary Observed in Seasat Rev. 762 Superimposed on the Hydrographic Chart of the Northeast Atlantic Ocean

171
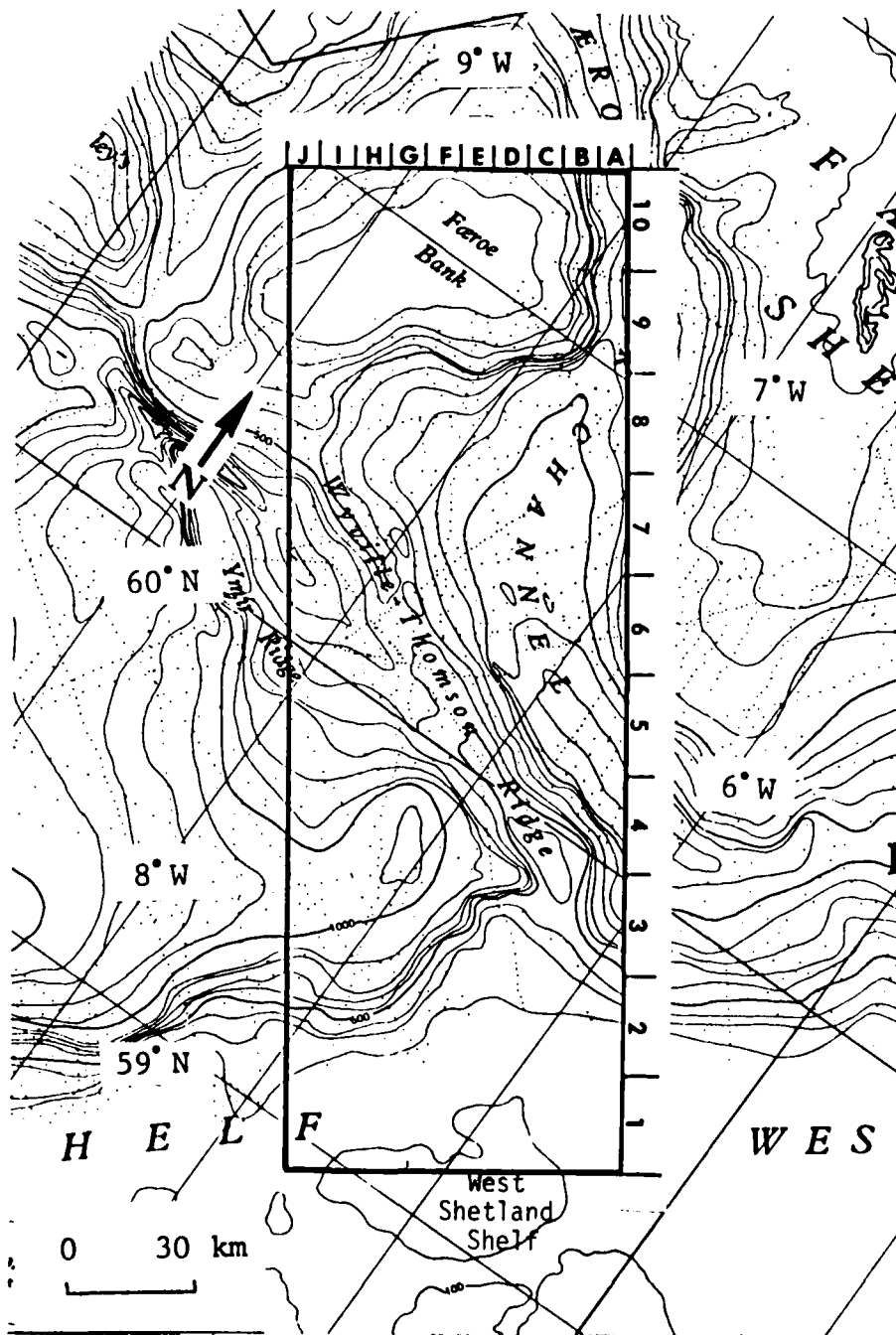
Figure 73b. Ground Coverage of Rev. 762 Over Wyville-Thomson Ridge (After IOS Chart No. C6567, Depth Contours in Meters)
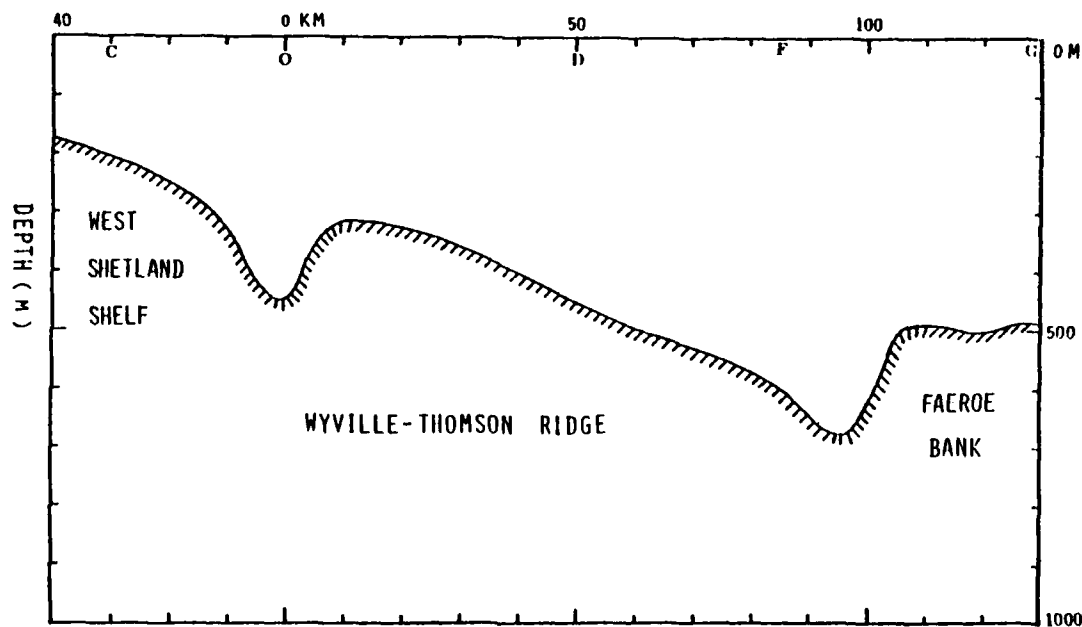
Figure 74. Cross-Section Diagram of Bottom Topography of the Wyville-Thomson Ridge
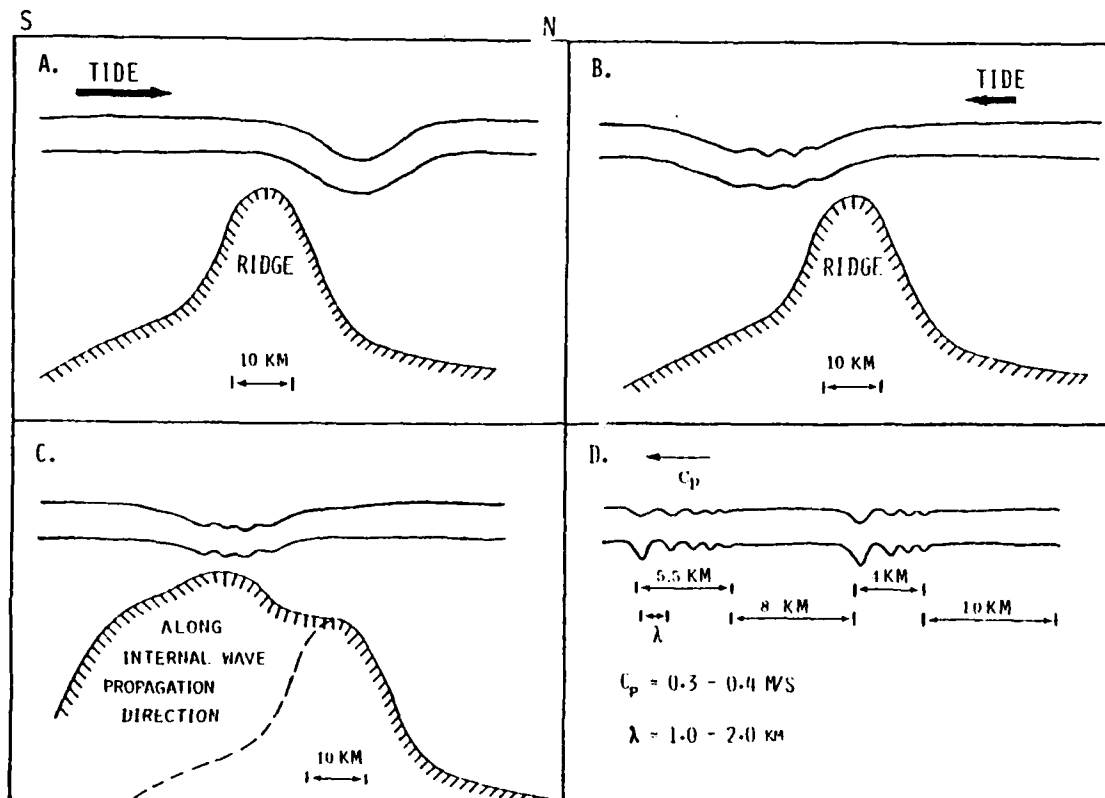
Figure 75. Schematic Diagram Summarizing the Generation and
Evolution of an Internal Wave Packet Over the
Wyville-Thomson Ridge

Based on the bathymetry of the area, it seems that the wave packets observed on the Rev. 762 Seasat imagery are produced by lee wave formation—a mechanism similar to the undulation of the jet stream as it passes over a mountain ridge. Figure 75 schematically illustrates the stages that are hypothesized during the production of solitary internal wave packets. As the strong semidiurnal tidal current flows north into the Faeroe Bank Channel, an internal lee wave forms on the northern edge of the ridge, as illustrated in Figure 75a. As the tidal flow goes to zero six hours later, the lee wave, trying to maintain its group velocity relative to the current, escapes south over the ridge barrier back into the deep water, emerging as a packet of solitary waves (Figure 75b). This phenomenon has previously been studied by Holbrook, et al. (1983) in the Sulu Sea. The initial waveform then can be viewed as a localized source that immediately begins to propagate, and evolves into a series of solitary waves while undergoing radial spreading, encountering variable topography and slowly losing energy through dissipation (Figure 75c). The absence of internal waves on the north side of the ridge is probably because there is no strong tidal current flowing south across the ridge; most of the tidal current may flow along the Faeroe Bank Channel.

These deep-water internal waves appear on SAR imagery for the same reasons as the Continental Shelf internal wave patterns discussed in the previous section.

5.6 DEEP WATER FRONTAL BOUNDARIES

The cold front that forms the boundary between the two layer system on the off-shore side and the vertically-mixed water inshore has been observed on Seasat SAR images of the Faeroe Bank Channel. The curved, dark line beginning at A9 and continuing to A6, as indicated in Figure 72, is believed to be a surface pattern caused by a frontal boundary. Its location appears to be over the edge of the Faeroe

Shelf, and closely matches the 900 meter bottom contour as illustrated in Figure 73(b).

The relationship of the front to local upwelling topographic mixing may be described by the following process. Figure 76 shows the cross-section diagrams of bottom topography of the Wyville-Thomson Ridge, through points C, O, D and A, O, B in Figure 73(b). It appears that the tidal current flowing over the ridge through another saddle-like valley on the west side of the ridge forces the deep water isotherms up toward the surface. To illustrate this mechanism for frontal boundary generation, a schematic diagram of deep water upwelling over the Faeroe Bank Channel is shown in Figure 77. Therefore, the frontal boundary seems to represent simply a surface intersection of the seasonal thermocline. The combination of frontal slope and current shear could yield information on density contrast across the front. The formulation of this upwelling problem is given in Appendix B for reference.

In summary, the frontal boundary pattern in Figure 72 appears to be the direct result of an interaction between a deep ocean tidal current and the Faeroe Shelf which results in deep water upwelling in this area. It is theorized that other frontal boundary patterns observed on Seasat SAR imagery collected over the eastern North Atlantic were similarly formed.
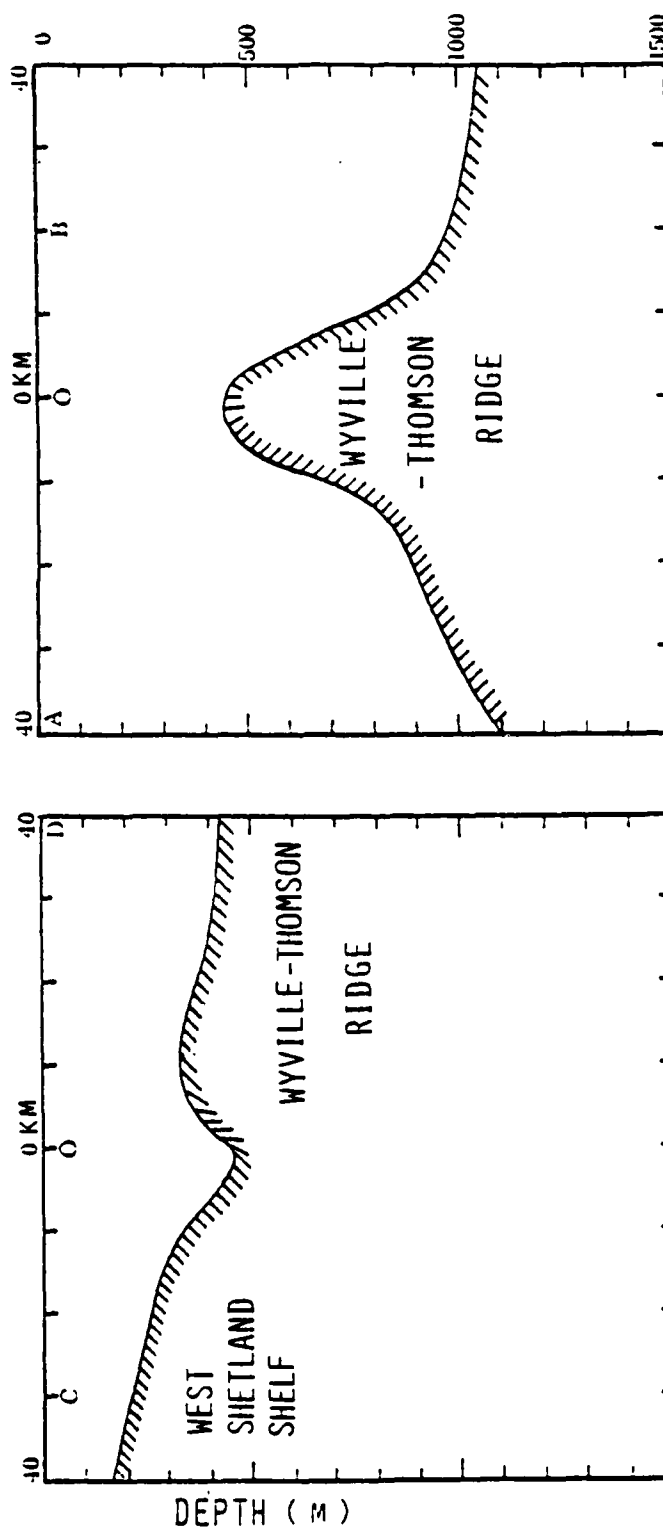
Figure 76. Longitudinal and Transverse Bathymetric Profiles Across Ridge, with a Saddle-Like Valley at 0 (Locations of Letters A, B, C, D and 0 are Indicated in Figure 73)

177
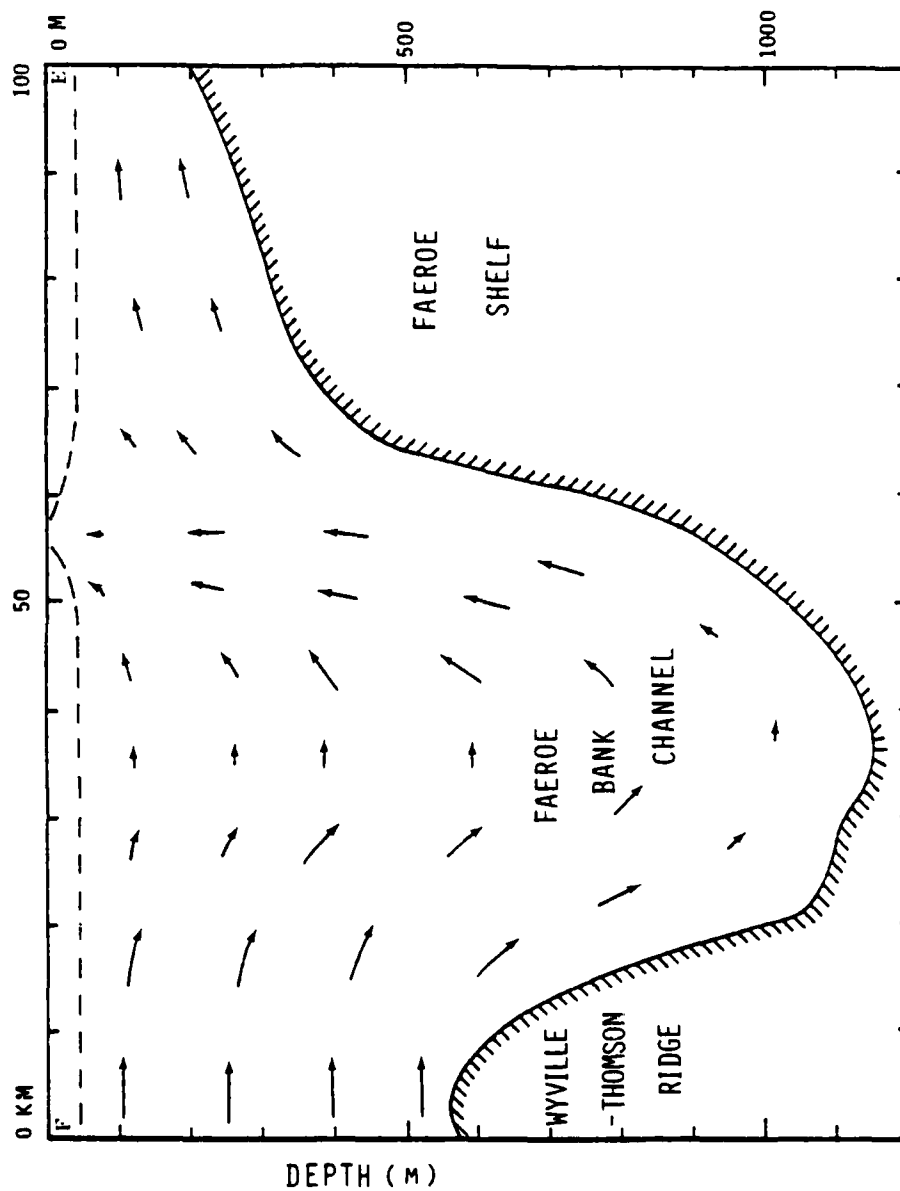
Figure 77. Schematic Diagram Illustrating Deep Water Upwelling Over the
Faeroe Bank Channel

6
CONCLUSIONS AND RECOMMENDATIONS

The significant results and findings of the analyses conducted for NRL throughout the past year have been summarized in Chapter 2 (Executive Summary). In this chapter, we would like to re-state the overall goals of the NRL/DMA sponsored program, discuss SAR's ability to address these goals (based upon the past four years' studies) and present recommendations for future demonstration projects and research topics which may be pursued to more fully define the potential of airborne and spaceborne SARs to detect and chart submerged navigation hazards.

The goals of using remote sensing in updating nautical charts are, in order of priority:

1. To detect uncharted or mispositioned submerged features which are potentially hazardous to surface and subsurface navigation,

2. To define the boundary and location of these hazards in either an absolute or relative sense, and

3. To extract accurate, detailed and complete water depth information.

The studies have demonstrated there is a distinct set of patterns on SAR imagery which correlates to submerged bottom features. These patterns appear in both deep and shallow water. Some of these patterns, however, are similar in appearance to non-depth related patterns on the ocean surface, and must be carefully interpreted to avoid false alarms. This interpretation requires a basic understanding of the SAR imaging mechanism of the ocean surface and of ocean dynamics. When interpreting SAR imagery, it is also helpful to define the ocean conditions present at the time the data were collected.

179

There are several types of surface patterns on SAR imagery which give a strong clue as to the actual shape and location of a bottom feature. These include current-induced banded patterns over shallow water sand banks and shoals, striped patterns at the edges of banks, and wave-induced changes in radar image intensity over shoals and coral reefs. It has not been possible to precisely determine the position of the SAR-observed patterns relative to a specific bottom feature for several reasons, including the lack of accurate, up-to-date, high-density hydrographic data to compare with the SAR data.

There are several approaches to overcome these shortcomings. Future collection of SAR imagery over areas where surface patterns have been previously observed could be beneficial if sufficient ground truth (i.e., depth measurements) were obtained and if specific, known points on the feature were bench-marked so as to appear on the SAR imagery. Another approach would be through further development of electromagnetic/hydrodynamic models, which can predict the positions of the SAR-observed surface patterns relative to the bottom features. These models would have to be validated using actual data, but would have the advantage of being able to predict surface patterns under a variety of SAR-configurations and ambient environmental conditions. A third approach would be to survey the positions of bottom-features which are stationary and compare these positions to already existing SAR imagery. An example of a stationary bottom feature is a barrier coral reef in the Bahamas.

Several comparisons of digital Seasat SAR data to depth data of the same region have shown strong statistical correlations between these parameters. These analyses have shown that radar image intensity is also dependent on the direction and magnitude of the currents and the strength of the wind. Therefore, although the potential exists to extract depth data from SAR imagery, further research is needed to fulfill this potential. This research should include both the modeling and model verification as described above.

In summary, SAR data can be used to assist hydrographers to up-date nautical charts. However, further basic and applied research is needed to fully evaluate SAR's potential. Recommendations based on the conclusions from this series of studies include programs to demonstrate SAR's potential to DMA hydrographers as well as basic research.

Specific recommendations for programs which will demonstrate the usefulness of SAR imagery to DMA hydrographers include:

1. Generation of a user's manual on the techniques for inter-preting bottom-related surface patterns on SAR imagery. This manual should include sections on basic SAR theory, avail-ability and sources of past, present and future SAR imagery, the theory of SAR imaging of the ocean surface, examples of SAR observed patterns on the ocean surface, test-cases which illustrate examples of the different kinds of bottom-related surface patterns on SAR imagery and discussions as to how these patterns occur, digital processing of SAR data, and advanced SAR interpretation techniques.

2. Utilization of the 1984 Shuttle Imaging Radar-B (SIR-B) experiment as a hands-on demonstration of the use of SAR systems for the detection of bottom-related surface patterns. In this recommended demonstration program, a SAR image inter-preter with oceanographic experience would assist DMA hydrographers in reviewing the proposed SIR-B coverage areas, select test sites (if possible those which have questionable or outdated surveys, and will be covered by SIR-B), obtain and process the imagery from these test sites, and interpret the SIR-B data for bottom-related surface patterns, including analysis of the ambient environmental conditions.

Further basic research in conjunction with field data collection programs are needed to determine the position of SAR observed surface

AD-A141 658   THE USE OF SATELLITE AND AIRCRAFT SAR TO DETECT AND
                CHART HAZARDS TO NAVI..(U) ENVIRONMENTAL RESEARCH INST
                OF MICHIGAN ANN ARBOR RADAR DIV E S KASISCHKE ET AL.

UNCLASSIFIED   AUG 83 ERIM-163000-2-F N00014-82-C-2308   F/G 8/3   NL

3/4
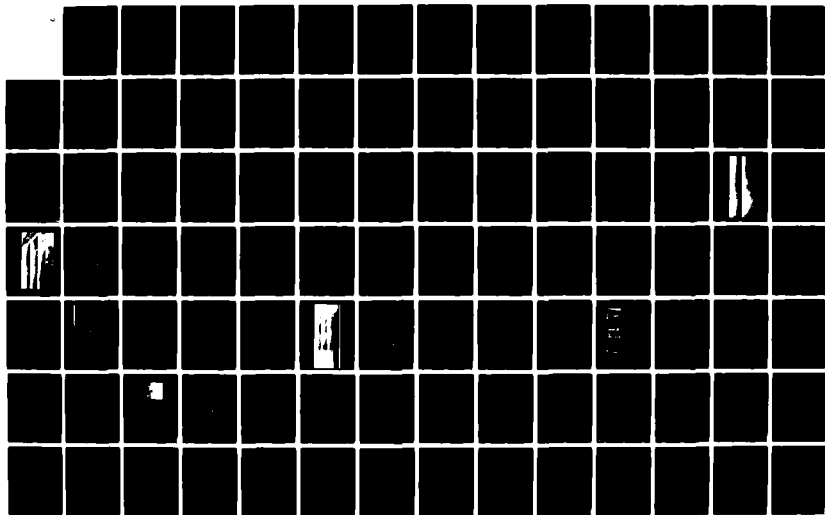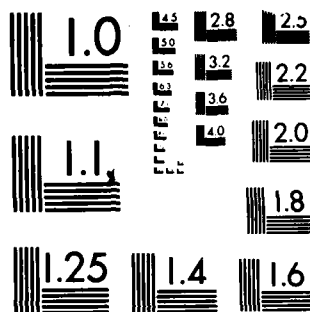
MICROCOPY RESOLUTION TEST CHART
NATIONAL BUREAU OF STANDARDS-1963-A

patterns relative to bottom features and to further define the correlations between SAR image intensity and water depth. To address these areas, the following research programs are recommended:

1. Further development of electromagnetic/hydrodynamic models which predict radar backscatter as a function of SAR system parameters, water depth and the ambient environmental conditions (waves, wind, and currents). Such models, when verified, can further define the potential for extracting water depths from SAR images and for predicting the position of a bottom feature relative to SAR observed pattern.

2. In conjunction with the SIR-B Experiment, conduct a field data collection program to gather the necessary water depth and ambient environmental data to validate hydrodynamic/electromagnetic models which have been formulated to date. The SIR-B experiment could include the collection of sea-truth information over a region where bottom-related surface patterns are likely to occur. A candidate test site is the Nantucket Shoals, which has a high probability of being imaged during the SIR-B Experiment.

REFERENCES

Alpers, W.E., D.B. Ross, and C.L. Rufenach, On the Detectability of Ocean Surface Waves by Real and Synthetic Aperture Radar, J. Geophys. Res., 86, 6481-6498, 1981.

Beal, R.C., P.S. DeLeonibus and I. Katz (eds.), Spaceborne Synthetic Aperture Radar for Oceanography, Johns Hopkins Univ. Press, Baltimore, MD, 215 pp., 1981.

Crimmins, T.R., Geometric Filter for Speckle Reduction, Internal ERIM Report, 38 pp., 1983.

Curlander, J.C. and W.E. Brown, Jr., A Pixel Location Algorithm for Spaceborne SAR Imagery, 1981 International Geoscience and Remote Sensing Symposium Digest (IGARSS '81), pp. 843-850, 1981.

Ford, J.P., J.B. Cimino, and C. Elachi, Space Shuttle Columbia Views the World with Imaging Radar: The SIR-A Experiment, JPL Publication 82-95, Pasadena, CA, 166 pp., 1983.

Fu, L. and B. Holt, Seasat Views Oceans and Sea Ice with Synthetic Aperture Radar, JPL Publication No. 81-120, 200 pp., 1982.

Gordon, C., D. Greenewalt, and J. Witting, Asia Rip: Surface Wave Expression of Bathymetry, NRL Report 5027, Washington, DC, 40 pp., 1983.

Gower, J.F.R. (ed.), Oceanography from Space, Plenum Press, New York, NY, 977 pp., 1981.

Greenewalt, D., C. Gordon, and J. McGrath, Eularian Current Measurements at Phelphs Banks, NRL Memorandum Report 5047, Washington, D.C., 51 pp., 1983.

Greenewalt, D. and C. Gordon, Lagrangian Current Measurements at Phelphs Banks, NRL Memorandum Report 4695, Washington, D.C., 1982.

Guinard, N.W. and J.C. Daley, An Experimental Study of a Sea Clutter Model, Proceedings of the IEEE, 50, pp. 543-550, 1970.

Holbrook, J.R., J.R. Apel, and J. Tsai, The Sulu Sea Internal Soliton Experiment, Part B: Observations and Analysis, J. Phys. Oceanogr. (in press), 1983.

Kasischke, E.S., Extraction of Gravity Wave Information from Synthetic Aperture Radar Data, Univ. of Mich. M.S. Thesis, 108 pp., 1980.

Kasischke, E.S., R.A. Shuchman and J.D. Lyden, Detection of Bathymetric Features Using SEASAT Synthetic Aperture Radar - A Feasibility Study, ERIM Final Report No. 135900-2-F$_2$, 77 pp., 1980.

Kasischke, E.S., R.A. Shuchman, G.A. Meadows, P.L. Jackson, Y. Tseng, J.D. Lyden, Further Seasat Coastal Ocean Wave Analysis, ERIM Final Report No. 138600-6-F, Ann Arbor, MI, 189 pp., 1981.

Kasischke, E.S., D.R. Lyzenga, R.A. Shuchman, Y.S. Tseng, B.S. Termaat, B.A. Burns, and G.A. Meadows, The Use of Synthetic Aperture Radar to Detect and Chart Submerged Navigation Hazards, ERIM Final Report No. 155200-1-F, Ann Arbor, MI, 232 pp., 1982.

Kasischke, E.S. and D.R. Lyzenga, Remote Sensing of Oceanic Phenomena Pertinent to Hydrocarbon Resource Development, Proceedings of the International Symposium on Remote Sensing of Environment, Second Thematic Conference: Remote Sensing for Exploration Geology, Ann Arbor, MI, 1983.

Kasischke, E.S., R.A. Shuchman, D.R. Lyzenga, and G.A. Meadows, Detection of Bottom Features on Seasat Synthetic Aperture Radar Imagery, Photogrametric Engineering and Remote Sensing, 49, pp. 1341-1353, 1983.

Kasischke, E.S., Y.C. Tseng, and G.A. Meadows, Observations of Internal Waves and Frontal Boundaries on Seasat SAR Imagery Collected Over the Eastern North Atlantic Ocean, Proceedings of the Seventeenth International Symposium on Remote Sensing of Environment (in press), Ann Arbor, MI, 1983a.

Kenyon, N.H., Bedforms of Shelf Seas Viewed with SEASAT Synthetic Aperture Radar, in Advances in Hydrographic Surveying, ed. M.J. Wright, Society for Underwater Technology, London, pp. 67-73, 1981.

Kenyon, N.H., Tidal Current Bedforms Investigated by Seasat, in Satellite Microwave Remote Sensing, ed. by T.D. Allan, Ellis Horwood Ltd., Chichester, England, pp. 261-270, 1983.

Kline, H., Yachtsman's Guide to the Bahamas, 28th Edition, Tropic Isle Publishers, North Miami, FL, 1978.

Kline, H., Yachtsman's Guide to the Bahamas, 31st Edition, Tropic Isle Publishers, North Miami, Florida, 1981.

Larsen, L.H., Modulation Solitons in Inhomogeneous Media, Physics of Fluids, 1980.

Liu, A. K., Detection of Bottom Features on Seasat Synthetic Aperture Radar Imagery, Dynatech Report No. DT-8312-01, Torrance, CA, 45 pp., 1983.

Lodge, D.W.S., Expression of Bathymetry on Seasat Synthetic Radar Imagery, in Satellite Microwave Remote Sensing, ed. by T.D. Allan, Ellis Horwood Ltd., Chichester, England, pp. 261-270, 1983.

Longuet-Higgins, M.S., On the Trapping of Wave Energy Around Islands, J. Fluid Mech., 29, pp. 781-821, 1977.

Lyzenga, D.R., Remote Bathymetry Using Active and Passive Techniques, 1981 International Geoscience and Remote Sensing Symposium Digest, Washington, D.C., pp. 777-786, 1981.

Lyzenga, D.R. and F.C. Polcyn, Techniques for the Extraction of Water Depth Information from Landsat Digital Data, ERIM Final Report No. 129900-1-F, Ann Arbor, MI, 57 pp., 1979.

Lyzenga, D.R. and R.A. Shuchman, Analysis of Motion Artifacts in MARSEN X-Band SAR Imagery, J. Geophys. Res., 88, pp. 9769-9775, 1983.

Lyzenga, D.R., R.A. Shuchman, E.S. Kasischke, and G.A. Meadows, Modeling of Bottom-Related Surface Patterns Imaged by Synthetic Aperture Radar, International Geoscience and Remote Sensing Symposium (IGARSS '83) Digest, pp. FA-6-7.1-7.10, 1983.

Mayer, D.A., D.V. Hansen, and D.A. Ortman, Long-Term Current and Temperature Observations on the Middle Atlantic Shelf, J. Geophys. Res., 84, pp. 1776-1792, 1979.

Meadows, G.A., R.A. Shuchman, Y.S. Tseng, and E.S. Kasischke, The Observation of Gravity Wave - Current Interactions Using Seasat Synthetic Aperture Radar, J. Geophys. Res., 88, pp. 4393-4406, 1983.

Mollo-Christensen, E., Surface Signs of Internal Ocean Dynamics, in Spaceborne Synthetic Aperture Radar for Oceanography, ed. by R.C. Beal, P.S. DeLeonibus, and I. Katz, Johns Hopkins University Press, Baltimore, pp. 140-145, 1981.

NOAA, Tidal Current Tables, 1981, Atlantic Coast of North America, U.S. Department of Commerce, Washington, D.C., 1981.

Phillips, O.M., The Dynamics of the Upper Ocean, Second Ed., Cambridge Univ. Press, 1977.

Phillips, O.M., The Structure of Short Gravity Waves on the Ocean Surface, in Spaceborne Synthetic Aperture Radar for Oceanography, ed. by R.C. Beal, P.S. DeLeonibus, and I. Katz, Johns Hopkins Univ. Press, Baltimore, MD, pp. 24-31, 1981.

Raney, R.K. and R.A. Shuchman, SAR Mechanism for Imaging Waves, Proc. Fifth Canadian Symp. on Remote Sensing, Victoria, B.C., 1978.

Shemdin, O.H., The Marineland Experiment: An Overview, Trans. Amer. Geophys. Union, 61, No. 38, pp. 625-626, 1980.

Shuchman, R.A., Processing Synthetic Aperture Radar Data of Ocean Waves, Oceanography from Space, ed. by J.F.R. Gower, Plenum Press, New York, pp. 477-496, 1981.

Shuchman, R.A., E.S. Kasischke, G.A. Meadows, J.D. Lyden, D.R. Lyzenga, P.L. Jackson, A.L. Maffett, and A. Klooster, Jr. The Utility of SAR to Monitor Ocean Processes, ERIM Final Report 124300-11-F, 133 pp., 1981a.

Shuchman, R.A., A.L. Maffett, and A. Klooster, Static Modeling of a SAR Imaged Ocean Scene, IEEE J. Oceanic Eng., OE-6, pp. 41-49, 1981b.

Shuchman, R.A., Quantification of SAR Signatures of Shallow Water Ocean Topography, Univ. of Mich. PhD Dissertation, Ann Arbor, MI, 130 pp., 1982.

Shuchman, R.A. and E.S. Kasischke, The Detection of Oceanic Bottom Topographic Features Using SEASAT Synthetic Aperture Radar Imagery, Proc. Thirteenth Int. Symp. Remote Sens. Environ., pp. 1277-1292, 1979.

Shuchman, R.A., E.S. Kasischke, A. Klooster and P.L. Jackson, SAR Coastal Ocean Wave Analysis - A Wave Refraction and Diffraction Study, ERIM Final Report No. 138600-2-F, Ann Arbor, MI, 78 pp., 1979.

Shuchman, R.A. and E.S. Kasischke, Refraction of Coastal Ocean Waves, in Spaceborne Synthetic Aperture Radar for Oceanography, ed. by R.C. Beal, P.S. DeLeonibus and I. Katz, Johns Hopkins Univ. Press, Baltimore, MD, pp. 128-135, 1981.

Shuchman, R.A., E.S. Kasischke, J.D. Lyden and G.A. Meadows, The Use of Synthetic Aperture Radar (SAR) to Measure Ocean Gravity Waves, Measuring Ocean Waves - Proceedings of a Symposium and Workshop on Wave-Measurement Technology, National Academy Press, Washington, D.C., pp. 95-111, 1982.

Shuchman, R.A., E.S. Kasischke, G.A. Meadows, and K.H. Amble, SEASAT SAR English Channel Data, ERIM Report No. 155200-T-1, 53 pp., 1981.

Shuchman, R.A., E.S. Kasischke, G.A. Meadows, J.D. Lyden, D.R. Lyzenga, P.L. Jackson, A.L. Maffett, and A. Klooster, Jr., The Utility of SAR to Monitor Ocean Processes, ERIM Final Report 124300-11-F, 133 pp., 1981a.

Shuchman, R.A., W. Rosenthal, J.D. Lyden, D.R. Lyzenga, E.S. Kasischke, H. Gunther, and H. Linne, Analysis of MARSEN X-Band SAR Ocean Wave Data, J. Geophys. Res., 88, pp. 9757-1968, 1983.

Tsai, J. and J.R. Apel, Tidally Induced Shear Flow Instability as a Source of Internal Waves on the Continental Shelf, NOAA Pacific Marine Env. Lab. Contrib. No. 415, 1979.

U.S. Naval Oceanographic Office, Oceanographic Office of the North Atlantic, Section I - Tides and Currents, Washington, D.C., 1977.

Valenzuela, G.R. and D.T. Chen, Personnel Communication, 1982.

Valenzuela, G.R. and D.T. Chen, Plan for a Remote Sensing Experiment in the Nantucket Shoals (SEBEX) (December 1, 1980), NRL Report 8659, 31 pp., 1983.

Wilson, C.L., Image Mapping Software at ERIM, presented at the Second Annual International User's Conference on Computer Mapping Hardware, Software, and Data Bases, Cambridge, MA, 20 pp., 1979.

Wright, J.W., Backscattering from Capillary Waves with Application to Sea Clutter, IEEE Trans. Antenna Propagat., AP-14, pp. 749-754, 1966.

APPENDIX A
SUMMARY OF SEASAT SAR OBSERVED BOTTOM RELATED
SURFACE PATTERNS

This appendix consists of a summary table listing all occurrences of bottom related surface patterns on Seasat SAR imagery. This table consists of the following information:

REVOLUTION: Seasat revolution

DATE: Date, relative to Greenwich Mean Time, data were collected

TIME: Approximate time (GMT) of the center of the Seasat revolution

LOCATION: Location of the bottom features imaged during the Seasat revolution

BOTTOM FEATURE TYPE: The type of bottom feature using the following key:

BE	Edge of large bank in Carribean
CR	Coral Reef
CS	Continental Shelf
DWB	Deep water bank
DWS	Deep water shelf
DWSM	Deep water seamount
FA	False alarm, no bottom feature
SWSB	Shallow water sand bank
SWSI	Shallow water shoal surrounding an island

SAR PATTERN: The type of surface pattern observed on the Seasat imagery, using the following key (see also Figure 1):

BP	Banded pattern
DB	Change in radar image intensity
FB	Frontal boundary pattern

A-1

IW   Internal wave pattern

NP   No pattern

SP   Striped Pattern

COMMENTS: Observations concerning the SAR data which affect image interpretation:

Weather – Low wind in the area of interest resulting in an area of no radar return

Processing – Processing or radar artifacts make data uninterpretable

Both – Imagery contains both WEATHER and PROCESSING problems.

TABLE A1.

SUMMARY OF SEASAT SAR OBSERVED BOTTOM RELATED SURFACE PATTERNS

REVOLUTION	DATE	TIME (GMT)	LOCATION	BOTTOM FEATURE TYPE*	SAR PATTERN*	COMMENTS*
107	7-04-78	12:10	U.S. WEST COAST	CS	IW	
150	7-07-78	13:15	U.S. WEST COAST	CS	IW	PROCESSING
			GULF OF CALIFORNIA	CS	IW	
			STRAIT OF GEORGIA	SWSH	NP	
			CANADIAN WEST COAST	CS	IW	PROCESSING
163	7-08-78	10:15	TONGUE OF THE OCEAN	SWSB	NP	
			GRAND BAHAMA BANK-EAST	BE	NP	
			TONGUE OF THE OCEAN-SOUTH	BE	NP	
			TONGUE OF THE OCEAN-EAST	BE	NP	
			TONGUE OF THE OCEAN-NORTH	BE	SP	
			LITTLE BAHAMA BANK-WEST	CS	IW	
			FLORIDA COAST			
193	7-10-78	12:25	GULF OF CALIFORNIA	CS	IW	
221	7-12-78	11:20	GULF OF MEXICO	CS	NP	
230	7-13-78	02:55	U.S. WEST COAST	CS	IW	WEATHER
			STRAIT OF GEORGIA	SWSH	NP	WEATHER
			HARO STRAITS	SWSH	DB	
			HEIN BANK	SWSH	DB	
			CONSTANCE BANK	SWSH	DB	
232	7-13-78	06:10	KUSKOKWIM RIVER	MB	DB	
			KUSKOKWIM RIVER	SWSB	BP	
			ALASKA COAST	CS	IW	
236	7-13-78	12:30	GULF OF CALIFORNIA	CS	IW	
242	7-13-78	23:10	CUBAN SOUTH COAST	BE	DB	
			CUBAN WEST COAST	BE	SP	
			GRAND BAHAMA BANK-EAST	BE	NP	
263	7-15-78	09:50	U.S EAST COAST	CS	IW	
273	7-16-78	03:05	U.S WEST COAST	CS	IW	
289	7-17-78	05:13	COOK INLET	MB	DB	
			FIRE ISLAND SOUTH SHOAL	SWSB	SP	
			FIRE ISLAND WEST SHOAL	SWSB	SP	
			MIDDLE GROUND SHOAL	SWSB	SP	
			ISE POINT SHOAL	SWSB	SP	
308	7-18-78	13:15	CORTEZ BANK	SWSH	NP	
			U.S. WEST COAST	CS	IW	
323	7-19-78	14:25	ALASKA COAST	CS	NP	

*SEE PAGE A-1 FOR KEY TO BOTTOM FEATURE TYPE, SAR PATTERN AND COMMENTS

A-3

TABLE A1.

SUMMARY OF SEASAT SAR OBSERVED BOTTOM RELATED SURFACE PATTERNS (CONTINUED)

REVOLUTION	DATE	TIME (GMT)	LOCATION	BOTTOM FEATURE TYPE*	SAR PATTERN*	COMMENTS*
335	7-20-78	10:30	U.S. EAST COAST	CS	NP	
			MOUCHOIR BANK	BE	NP	
			MOUCHOIR BANK	CR	NP	
			TURKS ISLANDS	BE	NP	
			CAICOS BANK	BE	NP	
			CAICOS BANK	CR	DB	
337	7-20-78	14:05	ALASKA COAST	CS	IW	
351	7-21-78	13:25	U.S. WEST COAST	CS	IW	
			TRIANGLE ISLAND	SWSH	DB	
			SARTINE ISLAND	SWSH	DB	
			LANZ ISLAND	SWSI	DB	
			COX ISLAND	SWSI	DB	
378	7-23-78	10:40	U.S. EAST COAST	CS	NP	
380	7-23-78	14:10	ALASKA COAST	MB	DB	
			ALASKA COAST	CS	IW	
387	7-24-78	02:20	U.S. WEST COAST	CS	NP	
			GULF OF CALIFORNIA	CS	IW	
388	7-24-78	03:55	SENTRY SHOAL	SWSH	NP	
			CANADIAN WEST COAST	CS	NP	
393	7-24-78	03:55	MISSISSIPPI RIVER DELTA	FA	BP	
			GULF OF MEXICO	CS	NP	
			COMPECHE BANK	BE	SP	
			MIRA POR VOS CAYS	BE	SP	
			FALSE CAPE BANK	BE	SP	
			MIKITO CAY	BE	DB	
			VIVARIO CAY	BE	NP	
			CARATASCA CAYS	BE	NP	
			EDNIBURGH REEF	CR	DB	
			NEE REEF	CR	NP	
			PIDGEON CAYS	BE	SP	
			ISLA DE SAN ANDROS	BE	SP	
			COURTOWN CAYS	BE	SP	
394	7-24-78	13:30	U.S. WEST COAST	CS	IW	
			STRAIT OF GEORGIA	SWSH	NP	
			CANADIAN WEST COAST	CS	NP	
400	7-24-78	00:05	MISTERIOSA BANK	BE	SP	
			U.S. EAST COAST	CS	IW	
			DIAMOND SHOALS	SWSH	NP	
			SWAN ISLAND	BE	SP	
			CUBAN SOUTH COAST	BE	SP	
			FLORIDA COAST	BE	NP	
			CUBAN NORTH COAST	CR	NP	
			ISLA DE JUVENTUD	BE	DB	

A-4

*SEE PAGE A-1 FOR KEY TO BOTTOM FEATURE TYPE, SAR PATTERN AND COMMENTS

SUMMARY OF SEASAT SAR OBSERVED BOTTOM RELATED SURFACE PATTERNS (CONTINUED)

TABLE A1

REVOLUTION	DATE	TIME (GMT)	LOCATION	BOTTOM FEATURE TYPE*	SAR PATTERN*	COMMENTS*
400	7-24-78	00:05	CAYO CANTILLES	BE	NP	
			GULFO DE BATABANO	BE	DB	
407	7-25-78	11:20	U.S. EAST COAST	CS	IW	
			CUBAN WEST COAST	BE	DB	
			CUBAN NORTH COAST	CR	NP	
			GRAND BAHAMA BANK-WEST	BE	SP	
			GRAND BAHAMA BANK-EAST	BE	SP	WEATHER
			LITTLE BAHAMA BANK-WEST	BE	SP	
416	7-26-78	02:55	CORTEZ BANK	SWSH	NP	
			U.S. WEST COAST	CS	IW	
422	7-26-78	12:25	GULF OF MEXICO	CS	NP	
			GULF OF MEXICO	FA	SP	
430	7-27-78	02:30	U.S. WEST COAST	CS	IW	
443	7-27-78	00:15	VIVARIO CAY	BE	SP	
			CARATASCA CAYS	BE	SP	
			CAXONES/HOBBIES ISLANDS	BE	SP	
			CORAL LEDGE	BE	NP	
447	7-28-78	06:45	ALASKA COAST	CS	IW	
			NONECK, ALASKA	SWSH	DB	
			ALASKA PENINSULA	SWSI	DB	
			MCKENZIE RIVER DELTA	MB	DB	
450	7-28-78	11:25	TONGUE OF THE OCEAN	SWSB	BP	
			U.S. EAST COAST	CS	NP	
			HAITI	FA	SP	
			ABACO ISLAND	CR	DB	
			ELEUTHRA ISLAND	CR	NP	
			CUBAN NORTH COAST	CR	DB	
			COLUMBUS REEF	CR	NP	
			COCHINAS BANK	BE	DB	
			CAY ST. DOMINGO	BE	NP	
			TONGUE OF THE OCEAN-SOUTH	BE	SP	
			TONGUE OF THE OCEAN-EAST	BE	SP	
			TONGUE OF THE OCEAN-NORTH	BE	SP	
			LITTLE BAHAMA BANK-WEST	BE	SP	
			LITTLE BAHAMA BANK-NORTH	BE	SP	
			GREEN CAY	CR	NP	
			MIDDLE BANK	CR	NP	
			YELLOW BANK	CR	NP	
465	7-29-78	12:35	GULF OF MEXICO	CS	NP	WEATHER
472	7-30-78	00:50	GULF OF MEXICO	CS	IW	
473	7-30-78	02:30	U.S. WEST COAST	CS	NP	
			CLARION ISLAND	SWSI	DB	

A-5

*SEE PAGE A-1 FOR KEY TO BOTTOM FEATURE TYPE, SAR PATTERN AND COMMENTS

TABLE A1
SUMMARY OF SEASAT SAR OBSERVED BOTTOM RELATED SURFACE PATTERNS (CONTINUED)

REVOLUTION	DATE	TIME (GMT)	LOCATION	BOTTOM FEATURE TYPE*	SAR PATTERN*	COMMENTS*
400	7-24-78	00:05	CAYO CANTILLES	BE	NP	
			GULFO DE BATABAND	BE	DB	
407	7-25-78	11:20	U.S. EAST COAST	CS	IW	
			CUBAN WEST COAST	BE	DB	
			CUBAN NORTH COAST	CR	NP	
			GRAND BAHAMA BANK-WEST	BE	SP	
			GRAND BAHAMA BANK-EAST	BE	SP	WEATHER
			LITTLE BAHAMA BANK-WEST	BE	SP	
416	7-26-78	02:55	CORTEZ BANK	SWSH	NP	
			U.S. WEST COAST	CS	IW	
422	7-26-78	12:25	GULF OF MEXICO	CS	NP	
			GULF OF MEXICO	FA	SP	
430	7-27-78	02:30	U.S. WEST COAST	CS	IW	
443	7-27-78	00:15	VIVARIO CAY	BE	SP	
			CARATASCA CAYS	BE	SP	
			CAXONES/HOBBIES ISLANDS	BE	SP	
			CORAL LEDGE	BE	NP	
447	7-28-78	06:45	ALASKA COAST	CS	IW	
			NONECK, ALASKA	SWSH	DB	
			ALASKA PENINSULA	SWSI	DB	
			MCKENZIE RIVER DELTA	MB	DB	
450	7-28-78	11:25	TONGUE OF THE OCEAN	SWSB	BP	
			U.S. EAST COAST	CS	NP	
			HAITI	FA	SP	
			ABACO ISLAND	CR	DB	
			ELEUTHRA ISLAND	CR	NP	
			CUBAN NORTH COAST	CR	DB	
			COLUMBUS REEF	BE	NP	
			COCHINAS BANK	BE	DB	
			CAY ST. DOMINGO	BE	NP	
			TONGUE OF THE OCEAN-SOUTH	BE	SP	
			TONGUE OF THE OCEAN-EAST	BE	SP	
			TONGUE OF THE OCEAN-NORTH	BE	SP	
			LITTLE BAHAMA BANK-WEST	BE	SP	
			LITTLE BAHAMA BANK-NORTH	BE	SP	
			GREEN CAY	CR	NP	
			MIDDLE BANK		NP	
			YELLOW BANK		NP	
465	7-29-78	12 35	GULF OF MEXICO		NP	WEATHER
472	7-30-78	00:50	GULF OF MEXICO	CS	IW	
473	7-30-78	02:30	U.S. WEST COAST	CS	NP	
			CLARION ISLAND	SWSI	DB	

*SEE PAGE A-1 FOR KEY TO BOTTOM FEATURE TYPE, SAR PATTERN AND COMMENTS

A-5

TABLE A1

SUMMARY OF SEASAT SAR OBSERVED BOTTOM RELATED SURFACE PATTERNS (CONTINUED)

REVOLUTION	DATE	TIME (GMT)	LOCATION	BOTTOM FEATURE TYPE*	SAR PATTERN*	COMMENTS*
474	7-30-78		U.S. WEST COAST	CS	IW	
			STRAIT OF GEORGIA	SWSH	NP	
			CONSTANCE BANK	SWSH	NP	
			ALDEN BANK	SWSH	DB	
480	7-30-78	13:45	U.S. WEST COAST	CS	IW	WEATHER
			STRAIT OF GEORGIA	SWSH	NP	
			ALDEN BANK	SWSH	DB	
488	7-31-78	03:40	U.S. WEST COAST	CS	NP	
493	7-31-78	11:30	U.S. EAST COAST	CS	IW	
			ROCHELOIS BANK	SWSH	DB.SB	
			CAT ISLAND	CR	NP	
			CROOKED ISLAND	CR	NP	
			ABACO ISLAND	CR	DB	
			LONG ISLAND	CR	NP	
			RUM CAY	CR	NP	
			SAN SALVADOR	CR	NP	
			GREAT INAGUA	CR	NP	
502	8-01-78	03:05	U.S. WEST COAST	CS	IW	
508	8-01-78	12:40	GULF OF MEXICO	CS	NP	
509	8-01-78	14:25	U.S. WEST COAST	CS	IW	
517	8-02-78	04:20	U.S. WEST COAST	CS	IW	
			HEIN BANK	SWSH	NP	
			PARTRIDGE BANK	SWSH	NP	
522	8-02-78	12:10	GULF OF MEXICO	CS	IW	
			DRY TORTUGAS	SWSH	DB	
			FLORIDA COAST	BE	SP	
523	8-02-78	13:55	U.S. WEST COAST	CS	NP	WEATHER
529	8-02-78	00:30	TONGUE OF THE OCEAN	SWSB	BP	
			ELEUTHRA ISLAND	CR	NP	
			CUBAN NORTH COAST	CR	DB	
			TONGUE OF THE OCEAN-SOUTH	BE	NP	
			TONGUE OF THE OCEAN-EAST	BE	NP	
			TONGUE OF THE OCEAN-NORTH	BE	NP	
			GRAND BAHAMA BANK-NORTH	BE	SP	
			GREEN CAY	CR	NP	
			MIDDLE BANK	CR	NP	
531	8-03-78	03:50	U.S. WEST COAST	CS	IW	
536	8-03-78	11:10	U.S. EAST COAST	CS	IW	

A-6

*SEE PAGE A-1 FOR KEY TO BOTTOM FEATURE TYPE, SAR PATTERN AND COMMENTS

TABLE A1

SUMMARY OF SEASAT SAR OBSERVED BOTTOM RELATED SURFACE PATTERNS (CONTINUED)

REVOLUTION	DATE	TIME (GMT)	LOCATION	BOTTOM FEATURE TYPE*	SAR PATTERN*	COMMENTS*
545	8-04-78	03:15	U.S. WEST COAST	CS	IW	
			COLORADO RIVER	SWSB	BP	
547	8-04-78	06:15	HATTON BANK	DWB	NP	
			GEORGE BLIGH BANK	DWB	IW	
			ROCKALL BANK	DWB	IW	
			ANTON DOHRN SEAMOUNT	DWSM	IW,FB	
			MALIN SHELF	CS	IW,FB	
			HEBRIDES TERRACE SEAMOUNT	DWSM	IW	
			NORTH FENI RIDGE	DWR	IW,FB	
			ICELAND COAST	CS	NP	
			IRISH SEA	SWSB	BP	
			LES SEPT ISLES	SWSI	DB	
			LES HAUX	SWSI	DB	
			ROCHES DOUVRES	SWSI	DB	
			THE SMALL	SWSI	DB	
552	8-04-78	14:40	CORTEZ BANK	SWSH	NP	
			U.S. WEST COAST	CS	IW	
556	8-04-78	21:35	FAEROE BANK	DWB	FB	
			ROCKALL BANK	DWB	FB	
			ANTON DOHRN SEAMOUNT	DWSM	IW	
			FAEROE SHELF	DWS	FB	
			WYVILLE-THOMSON RIDGE	DWR	IW	
			YMIR RIDGE	DWR	IW	
			NORTH FENI RIDGE	DWR	FB	
			ROSEMARY BANK	DWB	IW	
			NORWAY COAST	CS	IW	
			SOUTH FENI RIDGE	DWR	IW	
			NORTH ATLANTIC RIDGE	DWR	IW	
558	8-05-78	01:05	U.S. EAST COAST	CS	NP	
			GULF OF MEXICO	CS	NP	
			LIGHT HOUSE REEF	BE	SP	
			GLOVER REEF	BE	SP	
565	8-05-78	12:15	CAY SAL BANK	BE	SP	
			FLORIDA COAST	BE	NP	
574	8-06-78	03:55	U.S. WEST COAST	CS	IW	
590	8-07-78	06:20	LOUSY BANK	DWB	IW	
			ANTON DOHRN SEAMOUNT	DWSM	IW	
			HEBRIDES SHELF	CS	IW	
			NORTH FENI RIDGE	DWR	IW	
			ICELAND COAST	CS	IW	
			BRISTOL CHANNEL	SWSB	BP	
			ALDERNAY ISLAND	SWSI	DB	
			PORTLAND ISLAND	SWSI	DB	
			ROCHES DOUVRES	SWSI	DB	
			CASQUET BANKS	SWSB	BP	

*SEE PAGE A-1 FOR KEY TO BOTTOM FEATURE TYPE, SAR PATTERN AND COMMENTS

SUMMARY OF SEASAT SAR OBSERVED BOTTOM RELATED SURFACE PATTERNS (CONTINUED)

REVOLUTION	DATE	TIME (GMT)	LOCATION	BOTTOM FEATURE TYPE*	SAR PATTERN*	COMMENTS*
590	8-07-78	06:20	GURNSEY ISLANDS	SWSI	DB	
			MANQUERS	SWSH	DB	
			ISLE CHAUSSEY	SWSI	DB	
			ISLE CHAUSSEY	SWSH	DB	
			JERSEY ISLAND	SWSI	DB	
595	8-07-78	14:35	U.S. WEST COAST	CS	IW	WEATHER
			VANCOUVER ISLAND AREA	SWSI	NP	
			ISLAND OF CERROS	SWSI	SP	
			CANADIAN WEST COAST	CS	IW	
599	8-07-78	21:45	ANTON DOHRN SEAMOUNT	DWSM	IW	
			HEBRIDES SHELF	CS	NP	
			FAEROE SHELF	DWS	IW,FB	
			WYVILLE-THOMSON RIDGE	DWR	IW	
			YMIR RIDGE	DWR	IW	
			ROSEMARY BANK	DWB	IW	
			NORWAY COAST	CS	NP	
			NORTH ATLANTIC RIDGE	DWR	IW	
			PORCUPINE BANK	DWB	IW	
605	8-08-78	07:45	ALASKA COAST	CS	NP	
608	8-08-78	12:25	CAY SAL BANK	BE	NP	
			FLORIDA COAST	BE	NP	
			GRAND BAHAMA BANK-EAST	BE	NP	
617	8-09-78	04:00	U.S. WEST COAST	CS	IW	
623	8-09-78	13:30	GULF OF MEXICO	CS	NP	WEATHER
631	8-10-78	03:30	U.S. WEST COAST	CS	IW	
			GULF OF CALIFORNIA	CS	IW	
633	8-10-78	06:30	LOUSY BANK	DWB	IW,FB	
			HEBRIDES SHELF	CS	NP	
			MALIN SHELF	CS	IW	
			NORTH FENI RIDGE	DWR	NP	
			ROSEMARY BANK	DWB	IW,FB	
			ICELAND COAST	CS	IW	
			BRISTOL CHANNEL	MB	DB	
			PORTLAND ISLAND	SWSI	DB	
637.	8-10-78	13:00	GULF OF MEXICO	CS	NP	
638	8-10-78	14:45	U.S. WEST COAST	CS	IW	
			STRAIT OF GEORGIA	SWSH	NP	
			CANADIAN WEST COAST	CS	IW	WEATHER
642	8-10-78	21:50	HEBRIDES SHELF	CS	NP	
			WEST SHETLAND SHELF	CS	IW	
			HEBRIDES TERRACE SEAMOUNT	DWSM	IW	

A-8

*SEE PAGE A-1 FOR KEY TO BOTTOM FEATURE TYPE, SAR PATTERN AND COMMENTS

TABLE A1.
SUMMARY OF SEASAT SAR OBSERVED BOTTOM RELATED SURFACE PATTERNS (CONTINUED)

REVOLUTION	DATE	TIME (GMT)	LOCATION	BOTTOM FEATURE TYPE*	SAR PATTERN*	COMMENTS*
642	8-10-78	21:50	FAEROE SHELF	DWS	IW,FB	
			WYVILLE-THOMSON RIDGE	DWR	FB	
			YMIR RIDGE	DWR	IW	
			NORTH ATLANTIC RIDGE	DWR	IW	
			PORCUPINE BANK	DWB	IW	
648	8-11-78	07:50	ALASKA COAST	CS	IW	
			ALASKA COAST	SWSB	BP	
			MCKENZIE RIVER DELTA	MB	DB	
651	8-11-78	12:30	CUBAN WEST COAST	CR	SP	
			CUBAN NORTH COAST	CR	NP	
			GRAND BAHAMA BANK-WEST	BE	SP	
			GRAND BAHAMA BANK-EAST	BE	SP	
			LITTLE BAHAMA BANK-WEST	BE	SP	
659	8-12-78	02:30	GULF OF MEXICO	CS	IW	
660	8-12-78	04:05	U.S. WEST COAST	CS	NP	
674	8-13-78	03:40	U.S. WEST COAST	CS	IW	
			GULF OF CALIFORNIA	CS	IW	
681	8-13-78	14:50	GULF OF CALIFORNIA	CS	IW	
			COLORADO RIVER	SWSB	BP	
687	8-14-78	01:30	CUBAN NORTH COAST	CR	NP	
			VIVARIO CAY	BE	DB,SB	
			CAXONES/HOBBIES ISLANDS	BE	DB,SB	
			CORAL LEDGE	BE	NP	
691	8-14-78	08:00	ALASKA COAST	CS	NP	
			ALASKA COAST	SWSB	NP	
			MCKENZIE RIVER DELTA	MB	DB	
694	8-14-78	12:40	TONGUE OF THE OCEAN	SWSB	BP	
			U.S. EAST COAST	CS	NP	
			ABACO ISLAND	CR	DB	
			CUBAN NORTH COAST	CR	DB	
			TONGUE OF THE OCEAN-SOUTH	BE	SP	
			TONGUE OF THE OCEAN-EAST	BE	NP	
			TONGUE OF THE OCEAN-NORTH	BE	SP	
			LITTLE BAHAMA BANK-NORTH	BE	SP	
			GREEN CAY	CR	NP	
			MIDDLE BANK	CR	NP	
			YELLOW BANK	CR	NP	
714	8-15-78	22:35	ROCKALL BANK	DWB	IW	
			FAEROE SHELF	DWS	IW	
			NORTH ATLANTIC RIDGE	DWR	IW	
716	8-16-78	02:05	GULF OF MEXICO	CS	NP	

A-9

*SEE PAGE A 1 FOR KEY TO BOTTOM FEATURE TYPE, SAR PATTERN AND COMMENTS

REVOLUTION	DATE	TIME (GMT)	LOCATION	BOTTOM FEATURE TYPE*	SAR PATTERN*	COMMENTS*
719	8-16-78	06:40	ICELAND-FAEROE RISE	DWS	IW	
			BILL BAILEY'S BANK	DWB	IW,FB	
			FAEROE BANK	DWB	FB	
			HEBRIDES SHELF	CS	NP	
			WYVILLE-THOMSON RIDGE	DWR	IW	
			YMIR RIDGE	DWR	IW	
			ICELAND COAST	CS	IW	
720	8-16-78	08:35	KUSKOKWIN RIVER	MB	DB	
			KUSKOKWIN RIVER	SWSB	BP	
			ALASKA COAST	CS	IW	
723	8-16-78	13:15	GULF OF MEXICO	CS	NP	
			ROSILAND BANK	BE	NP	
724	8-16-78	14:55	GULF OF CALIFORNIA	CS	IW	
737	8-17-78	12:45	ROCHELOIS BANK	SWSH	DB	
			CAT ISLAND	CR	NP	
			CONCEPCION ISLAND	CR	NP	
			CROOKED ISLAND	CR	DB	
			CROOKED ISLAND	BE	SP	
			MIRA POR VOS CAYS	BE	DB	
			HAITI	FA	SP	
			CLARION ISLAND	BE	NP	
			LONG ISLAND	CR	NP	
			RUM CAY	CR	NP	
			SAN SALVADOR	CR	NP	
			GREAT INAGUA	CR	NP	
757	8-18-78	22:40	BILL BAILEY'S BANK	DWB	NP	
			FAEROE BANK	DWB	IW,FB	
			ROCKALL BANK	DWB	IW	
			FAEROE SHELF	DWS	NP	
			WYVILLE-THOMSON RIDGE	DWR	NP	
			YMIR RIDGE	DWR	IW	
			NORTH FENI RIDGE	DWR	NP	
			ROSEMARY BANK	DWB	NP	
			NORWAY COAST	CS	IW	
			NORTH ATLANTIC RIDGE	DWR	IW	
759	8-19-78	02:10	GULF OF MEXICO	CS	IW	
			ARROW BANK	BE	SP	
			COZUMAL ISLAND	SWSI	SP	
			AMBERGIS KEY	BE	SP	
			LAKE ST. PIERRE	SWSB		
761	8-19-78	05:30	U.S. WEST COAST	CS	IW	
762	8-19-78	06:45	NORTH RONA ROCK	SWSI	DB	
			SULA SGIER	SWSI	DB	
			ICELAND-FAEROE RISE	DWS	IW,FB	

A-10

*SEE PAGE A-1 FOR KEY TO BOTTOM FEATURE TYPE, SAR PATTERN AND COMMENTS

TABLE A1.

SUMMARY OF SEASAT SAR OBSERVED BOTTOM RELATED SURFACE PATTERNS (CONTINUED)

REVOLUTION	DATE	TIME (GMT)	LOCATION	BOTTOM FEATURE TYPE*	SAR PATTERN*	COMMENTS*
762	8-19-78	06:45	HEBRIDES SHELF	CS	IW	
			FAEROE BANK	DWB	IW,FB	
			FAEROE SHELF	DWS	IW,FB	
			WEST SHETLAND SHELF	CS	IW	
			WYVILLE-THOMSON RIDGE	DWR	IW,FB	
			ICELAND COAST	CS	IW	
			ENGLISH CHANNEL-SOUTH	SWSB	BP	
			ENGLISH CHANNEL-SOUTH	SWSB	BP	
			ENGLISH CHANNEL-SOUTH	SWSB	BP	
			ENGLISH CHANNEL-SOUTH	SWSB	BP	
			ENGLISH CHANNEL-SOUTH	MB	DB	
766	8-19-78	13:20	GULF OF MEXICO	FA	SP	
			GULF OF MEXICO	CS	IW	
			DRY TORTUGAS	SWSH	DB	
			PEDRO BANK	BE	NP	
			PICKLE BANK	BE	DB	
			BAJO NEUVO	BE	SP	
			ALICE SHOAL	BE	SP	
785	8-20-78	21:40	ORMONDE SEAMOUNT	DWSM	IW	
			GETTYSBURG SEAMOUNT	DWSM	IW	
			CORAL PATCH SEAMOUNT	DWSM	NP	
			AGADIR SEAMOUNT	DWSM	NP	
			LES SEPT ISLES	SWSI	DB	
			PLATEAU DES TROIS	SWSI	DB	
			GURNSEY ISLANDS	SWSI	DB	
			ALDERNAY ISLAND	SWSI	DB	
			PORTLAND ISLAND	SWSI	DB	
			ISLE OF WIGHT	SWSB	BP	
			CASQUET BANKS	SWSB	NP	
789	8-21-78	04:25	GULF OF CALIFORNIA	CS	IW	
			COLORADO RIVER	SWSB	BP	
791	8-21-78	07:25	LOUSY BANK	DWB	FB	
			HATTON BANK	DWB	FB	
			GEORGE BLIGH BANK	DWB	FB	
			ROCKALL BANK	DWB	IW	
			ANTON DOHRN SEAMOUNT	DWSM	IW	
			MALIN SHELF	CS	IW	
			HEBRIDES TERRACE SEAMOUNT	DWSM	NP	
			NORTH FENI RIDGE	DWR	IW,FB	
			ICELAND COAST	CS	IW	
			IRISH SEA	SWSB	BP	
			IRISH SEA	SWSB	BP	
			THE SMALL	SWSI	DB	
795	8-21-78	14:00	GULF OF MEXICO	CS	NP	
			BANCO CHINCORO	BE	SP	

*SEE PAGE A-1 FOR KEY TO BOTTOM FEATURE TYPE, SAR PATTERN AND COMMENTS

TABLE A1.

SUMMARY OF SEASAT SAR OBSERVED BOTTOM RELATED SURFACE PATTERNS (CONTINUED)

REVOLUTION	DATE	TIME (GMT)	LOCATION	BOTTOM FEATURE TYPE*	SAR PATTERN*	COMMENTS*
802	8-22-78	02:15	U.S. EAST COAST	CS	IW	
			DRY TORTUGAS	SWSH	DB	
			GULF OF MEXICO	CS	NP	WEATHER
806	8-22-78	08:45	ALASKA COAST	CS	NP	PROCESSING
809	8-22-78	13:25	CAY SAL BANK	BE	SP	
			PEDRO BANK	BE	DB	
			FLORIDA COAST	BE	SP	
811	8-22-78	16:55	ALASKA COAST	CS	IW	
834	8-24-78	07:30	LOUSY BANK	DWB	IW	
			HEBRIDES SHELF	CS	NP	
			MALIN SHELF	CS	NP	
			NORTH FENI RIDGE	DWR	NP	
			ROSEMARY BANK	DWB	IW	
			ICELAND COAST	CS	IW	
			BRISTOL CHANNEL	MB	DB	
838	8-24-78	14:05	GULF OF MEXICO	CS	IW	
845	8-25-78	02:20	U.S. EAST COAST	CS	IW	
852	8-25-78	13:30	DIAMOND SHOALS	SWSH	DB	
			U.S. EAST COAST	CS	IW	
			LITTLE BAHAMA BANK-WEST	BE	SP	
874	8-27-78	02:55	U.S. WEST COAST	CS	IW	
			GULF OF MEXICO	CS	NP	
			ARRECIFE ALACRAN	BE	SP	
			ARRECIFE ALACRAN	CR	DB	
880	8-27-78	12:25	U.S. EAST COAST	CS	IW	
			NANTUCKET SHOALS	SWSB	BP	
			LAKE ST. PIERRE	SWSB	DB	
882	8-27-78	15:55	GULF OF CALIFORNIA	CS	IW	
			COLORADO RIVER	SWSB	BP	
888	8-28-78	02:25	U.S. EAST COAST	CS	IW	
909	8-29-78	13:15	U.S. EAST COAST	CS	IW	
931	8-31-78	02:40	U.S. EAST COAST	CS	IW	
			DIAMOND SHOALS	SWSH	DB	
957	9-01-78	22:15	ENGLISH CHANNEL-SOUTH	SWSB	NP	
			ENGLISH CHANNEL-SOUTH	SWSB	NP	
			ENGLISH CHANNEL-SOUTH	SWSB	NP	
			ENGLISH CHANNEL-SOUTH	SWSB	BP	

*SEE PAGE A-1 FOR KEY TO BOTTOM FEATURE TYPE, SAR PATTERN AND COMMENTS

TABLE A1

SUMMARY OF SEASAT SAR OBSERVED BOTTOM RELATED SURFACE PATTERNS (CONTINUED)

REVOLUTION	DATE	TIME (GMT)	LOCATION	BOTTOM FEATURE TYPE*	SAR PATTERN*	COMMENTS*
958	9-01-78	23:53	ICELAND-FAEROE RISE	DWS	IW	
			LOUSY BANK	DWB	IW	
			GEORGE BLIGH BANK	DWB	IW	
			HATTON BANK	DWB	FB	
			ROCKALL BANK	DWB	IW,FB	
963	9-02-78	08:00	ENGLISH CHANNEL-CENTRAL	SWSB	BP	
			ISLE OF MANN	SWSB	BP	
974	9-03-78	02:50	U.S. EAST COAST	CS	IW	
			DIAMOND SHOALS	SWSH	DB	
991	9-04-78	07:22	CANADIAN WEST COAST	CS	NP	
1006	9-05-78	08:15	BILL BAILEY'S BANK	DWB	FB	
			LOUSY BANK	DWB	NP	
			HEBRIDES SHELF	CS	FB	
			NORTH FENI RIDGE	DWR	IW,FB	
			ROSEMARY BANK	DWB	IW,FB	
1017	9-06-78	03:03	U.S. EAST COAST	CS	IW	
1024	9-06-78	14:20	TONGUE OF THE OCEAN	SWSB	BP	
			ABACO ISLAND	CR	DB	
			TONGUE OF THE OCEAN-WEST	BE	NP	
			TONGUE OF THE OCEAN-SOUTH	BE	SP	
			TONGUE OF THE OCEAN-EAST	BE	SP	
			TONGUE OF THE OCEAN-NORTH	BE	SP	
			LITTLE BAHAMA BANK-WEST	BE	NP	
			LITTLE BAHAMA BANK-NORTH	BE	NP	
			GREEN CAY	CR	NP	
1038	9-07-78	13:50	U.S. EAST COAST	CS	IW	
1044	9-08-78	00:18	ICELAND-FAEROE RISE	DWS	IW,FB	
			BILL BAILEY'S BANK	DWB	NP	
			LOUSY BANK	DWB	IW,FB	
			HATTON BANK	DWB	IW	
			GEORGE BLIGH BANK	DWB	IW	
			ROCKALL BANK	DWB	NP	
1048	9-08-78	07:05	SENTRY SHOAL	SWSH	NP	
			GRANT REEF	SWSH	NP	
			EXITER SHOAL	SWSH	NP	
			CANADIAN WEST COAST	CS	NP	
1049	9-08-78	08:27	BILL BAILEY'S BANK	DWB	IW,FB	
			LOUSY BANK	DWB	IW,FB	
			HEBRIDES SHELF	CS	NP	
			YMIR RIDGE	DWR	IW	
			NORTH FENI RIDGE	DWR	FB	
			ROSEMARY BANK	DWB	IW	
			ST. KILDA	SWSI	DB	

A-13

*SEE PAGE A-1 FOR KEY TO BOTTOM FEATURE TYPE, SAR PATTERN AND COMMENTS

TABLE A1.

SUMMARY OF SEASAT SAR OBSERVED BOTTOM RELATED SURFACE PATTERNS (CONTINUED)

REVOLUTION	DATE	TIME (GMT)	LOCATION	BOTTOM FEATURE TYPE*	SAR PATTERN*	COMMENTS*
1087	9-10-78	00:30	ICELAND-FAEROE RISE	DWS	IW	
			BILL BAILEY'S BANK	DWB	IW	
			LOUSY BANK	DWB	IW	
			GEORGE BLIGH BANK	DWB	IW	
			ROCKALL BANK	DWB	FB	
1096	9-11-78	15:10	GULF OF MEXICO	CS	NP	BOTH
			ABACO ISLAND	BE	NP	
			LITTLE BAHAMA BANK-NORTH	BE	NP	
1110	9-12-78	14:45	TONGUE OF THE OCEAN	SWSB	BP	
			U.S. EAST COAST	CS	IW	
			ABACO ISLAND	CR	NP	
			GRAND BAHAMA BANK-EAST	BE	SP	
			TONGUE OF THE OCEAN-WEST	BE	SP	
			TONGUE OF THE OCEAN-SOUTH	BE	SP	
			TONGUE OF THE OCEAN-EAST	BE	SP	
			TONGUE OF THE OCEAN-NORTH	BE	NP	
			LITTLE BAHAMA BANK-NORTH	BE	SP	
			LITTLE BAHAMA BANK-NORTH	CR	NP	
			GREEN CAY	CR	NP	
			MIDDLE BANK	CR	NP	
			YELLOW BANK	CR	NP	
1126	9-13-78	17:45	ALASKA COAST	CS	NP	
			CONTROLLER BAY	MB	DB	
1139	9-14-78	15:25	GULF OF MEXICO	CS	NP	
1140	9-14-78	17:10	GULF OF CALIFORNIA	CS	IW	
			COLORADO RIVER	SWSB	BP	
1149	9-15-78	08:20	ICELAND-FAEROE RISE	DWS	IW	
			FAEROE SHELF	DWS	IW	
			FAIR ISLAND	SWSI	DB	
			SHOALA ISLAND	SWSI	DB	
			STRAIT OF MESSINA	SWSB	BP	
1153	9-15-78	14:55	TONGUE OF THE OCEAN	SWSB	BP	
			U.S. EAST COAST	CS	NP	
			ABACO ISLAND	CR	DB	
1153	9-15-78	14:55	GRAND BAHAMA BANK-EAST	BE	SP	
			TONGUE OF THE OCEAN-WEST	BE	SP	
			TONGUE OF THE OCEAN-SOUTH	BE	SP	
			TONGUE OF THE OCEAN-EAST	BE	SP	
			TONGUE OF THE OCEAN-NORTH	BE	SP	
			LITTLE BAHAMA BANK-WEST	BE	SP	
			LITTLE BAHAMA BANK-NORTH	BE	NP	
			GREEN CAY	CR	NP	
1177	9-17-78	07:43	STRAIT OF GEORGIA	SWSH	NP	PROCESSING
			CANADIAN WEST COAST	CS	NP	PROCESSING

A-14

*SEE PAGE A-1 FOR KEY TO BOTTOM FEATURE TYPE, SAR PATTERN AND COMMENTS

TABLE A1
SUMMARY OF SEASAT SAR OBSERVED BOTTOM RELATED SURFACE PATTERNS (CONTINUED)

REVOLUTION	DATE	TIME (GMT)	LOCATION	BOTTOM FEATURE TYPE*	SAR PATTERN*	COMMENTS*
1181	9-17-83	14:03	CANADIAN EAST COAST LAKE ST. PIERRE	CS SWSB	IW DB	
1182	9-17-83	15:40	GULF OF MEXICO	CS	NP	PROCESSING
1183	9-17-83	17:20	GULF OF CALIFORNIA COLORADO RIVER	CS SWSB	IW BP	
1193	9-18-78	10:30	MCKENZIE RIVER DELTA	MB	DB	
1196	9-18-78	15:10	TONGUE OF THE OCEAN	SWSB	NP	
			ABACO ISLAND	CR	NP	
			CUBAN NORTH COAST	CR	NP	
			GRAND BAHAMA BANK-EAST	BE	NP	
			TONGUE OF THE OCEAN-WEST	BL	SP	
			TONGUE OF THE OCEAN-SOUTH	BE	NP	
			TONGUE OF THE OCEAN-EAST	BE	NP	
			TONGUE OF THE OCEAN-NORTH	BE	NP	
			LITTLE BAHAMA BANK-NORTH	BE	NP	
			GREEN CAY	CR	NP	
1201	9-18-78	23:55	NORWAY COAST	CS	NP	
1204	9-19-78	05:05	GULF OF MEXICO	CS	IW	
1205	9-19-78	06:48	U.S WEST COAST	CS	NP	
1206	9-19-78	08:05	NORWAY COAST CANADIAN WEST COAST	CS CS	IW NP	PROCESSING
1209	9-19-78	13:05	U.S. EAST COAST	CS	NP	
1210	9-19-78	14:40	U.S. EAST COAST	CS	IW	
1211	9-19-78	16:15	U.S. WEST COAST GULF OF MEXICO	CS CS	IW NP	
1215	9-19-78	23:30	NORWAY COAST	CS	IW	
1225	9-20-78	15:50	GULF OF MEXICO	CS	NP	
1226	9-20-78	12:35	GULF OF CALIFORNIA COLORADO RIVER	CS SWSB	IW NP	
1232	9-21-78	06:30	U.S. EAST COAST DIAMOND SHOALS	CS SWSH	IW DB	
1235	9-21-78	09:05	CANADIAN WEST COAST	CS	NP	
1236	9-21-78	10:40	MCKENZIE RIVER DELTA	MB	DB	

A-15

*SEE PAGE A-1 FOR KEY TO BOTTOM FEATURE TYPE, SAR PATTERN AND COMMENTS

TABLE A1

SUMMARY OF SEASAT SAR OBSERVED BOTTOM RELATED SURFACE PATTERNS (CONTINUED)

REVOLUTION	DATE	TIME (GMT)	LOCATION	BOTTOM FEATURE TYPE*	SAR PATTERN*	COMMENTS*
1239	9-21-78	15:20	TONGUE OF THE OCEAN	SWSB	BP	
			ABACO ISLAND	CR	DB	
			CUBAN NORTH COAST	CR	NP	
			GRAND BAHAMA BANK-EAST	BE	NP	
			TONGUE OF THE OCEAN-WEST	BE	SP	
			TONGUE OF THE OCEAN-SOUTH	BE	SP	
			TONGUE OF THE OCEAN-EAST	BE	NP	
			TONGUE OF THE OCEAN-NORTH	BE	NP	
			LITTLE BAHAMA BANK-NORTH	BE	SP	
			GREEN CAY	CR	NP	
1249	9-22-78	08:35	CANADIAN WEST COAST	CS	IW	
1252	9-22-78	13:20	CANADIAN EAST COAST	CS	IW	
1253	9-22-78	14:50	U.S. EAST COAST	CS	IW	
1254	9-22-78	16:30	GULF OF MEXICO	CS	NP	
1258	9-22-78	23:42	NORTH SEA COAST	MB	DB	
			NORTH SEA COAST	SWSH	NP	
			ENGLISH CHANNEL-CENTRAL	SWSB	NP	
1259	9-23-78	01:22	ICELAND-FAEROE RISE	CS	IW	
			BILL BAILEY'S BANK	DWB	IW	
			LOUSY BANK	DWB	IW	
			HATTON BANK	DWB	IW	
			GEORGE BLIGH BANK	DWB	IW	
1263	9-23-78	08:08	SENTRY SHOAL	SWSH	NP	BOTH
			GRANT REEF	SWSH	NP	WEATHER
			EXITER SHOAL	SWSH	NP	
			CANADIAN WEST COAST	CS	IW	
1265	9-23-78	11:12	COAST OF GREENLAND	CS	NP	
1267	9-23-78	14:25	U.S. EAST COAST	CS	IW	
			BERMUDA	CR	DB	
1269	9-23-78	17:60	GULF OF CALIFORNIA	CS	IW	
			COLORADO RIVER	SWSB	NP	
1279	9-24-78	10:55	MCKENZIE RIVER DELTA	MB	DB	
1282	9-24-78	15:35	TONGUE OF THE OCEAN	SWSB	BP	
			ABACO ISLAND	CR	NP	
			GRAND BAHAMA BANK-EAST	BE	NP	WEATHER
			TONGUE OF THE OCEAN-WEST	BE	SP	
			TONGUE OF THE OCEAN-SOUTH	BE	SP	
			TONGUE OF THE OCEAN-EAST	BE	NP	
			TONGUE OF THE OCEAN-NORTH	BE	NP	
			LITTLE BAHAMA BANK-NORTH	BE	SP	
			GREEN CAY	CR	NP	

*SEE PAGE A-1 FOR KEY TO BOTTOM FEATURE TYPE, SAR PATTERN AND COMMENTS

TABLE A1

SUMMARY OF SEASAT SAR OBSERVED BOTTOM RELATED SURFACE PATTERNS (CONTINUED)

REVOLUTION	DATE	TIME (GMT)	LOCATION	BOTTOM FEATURE TYPE*	SAR PATTERN*	COMMENTS*
1287	9-24-78	00:22	COAST OF NORWAY	CS	NP	
1291	9-25-78	07:10	U.S. WEST COAST	CS	IW	
1292	9-25-78	08:50	ALASKA COAST	CS	NP	
			ALASKA PENINSULA	SWSI	DB	
1296	9-25-78	15:05	U.S. EAST COAST	CS	IW	
1306	9-26-78	08:20	STRAIT OF GEORGIA	SWSH	NP	BOTH
			CANADIAN WEST COAST	CS	NP	PROCESSING
1307	9-26-78	09:45	BILL BAILEY'S BANK	DWB	NP	
			LOUSY BANK	DWB	NP	
			HEBRIDES SHELF	CS	NP	
			ROSEMARY BANK	DWB	NP	
			ISLE OF MANN	SWSB	NP	
1312	9-26-78	17:55	GULF OF CALIFORNIA	CS	NP	
			COLORADO RIVER	SWSB	BP	
1318	9-27-78	04:30	U.S. EAST COAST	CS	IW	
1321	9-27-78	09:30	CANADIAN WEST COAST	CS	IW	
1322	9-27-78	11:05	MCKENZIE RIVER DELTA	MB	DB	
1324	9-27-78	14:10	CANADIAN EAST COAST	CS	IW	
1325	9-27-78	15:45	TONGUE OF THE OCEAN	SWSB	BP	
			U.S. EAST COAST	CS	NP	
			ABACO ISLAND	CR	DB	
			CUBAN NORTH COAST	CR	NP	
			GRAND BAHAMA BANK-EAST	BE	NP	
			TONGUE OF THE OCEAN-WEST	BE	SP	
			TONGUE OF THE OCEAN-SOUTH	BE	SP	
			TONGUE OF THE OCEAN-EAST	BE	NP	
			TONGUE OF THE OCEAN-NORTH	BE	NP	
			LITTLE BAHAMA BANK-WEST	BE	SP	
			LITTLE BAHAMA BANK-NORTH	BE	NP	
			GREEN CAY	CR	NP	
1333	9-28-78	05:42	GULF OF MEXICO	CS	NP	
1335	9-28-78	09:00	CANADIAN WEST COAST	CS	IW	
			QUEEN CHARLOTTE ISLAND	SWSH	DB	
1339	9-28-78	15:20	U.S. EAST COAST	CS	NP	
1344	9-28-78	00:08	NORTH SEA COAST	MB	DB	
			ENGLISH CHANNEL-CENTRAL	SWSB	BP	

A-17

*SEE PAGE A-1 FOR KEY TO BOTTOM FEATURE TYPE, SAR PATTERN AND COMMENTS

TABLE A1

SUMMARY OF SEASAT SAR OBSERVED BOTTOM RELATED SURFACE PATTERNS (CONTINUED)

REVOLUTION	DATE	TIME (GMT)	LOCATION	BOTTOM FEATURE TYPE*	SAR PATTERN*	COMMENTS*
1349	9-29-78	08:33	CANADIAN WEST COAST	CS	IW	
1352	9-29-78	13:15	CANADIAN EAST COAST	CS	IW	
1355	9-29-78	18:15	GULF OF CALIFORNIA	CS	IW	
			COLORADO RIVER	SWSB	BP	
1359	9-30-78	01:15	WEST SHETLAND SHELF	CS	IW	
1360	9-30-78	03:00	U.S. EAST COAST	CS	IW	
1365	9-30-78	11:20	MCKENZIE RIVER DELTA	MB	DB	
1367	9-30-78	14:23	CANADIAN EAST COAST	CS	IW	
1368	9-30-78	16:00	TONGUE OF THE OCEAN	SWSB	BP	
			ABACO ISLAND	CR	NP	WEATHER
			CUBAN NORTH COAST	CR	NP	
			TONGUE OF THE OCEAN-WEST	BE	SP	
			TONGUE OF THE OCEAN-SOUTH	BE	SP	
			TONGUE OF THE OCEAN-EAST	BE	SP	
			TONGUE OF THE OCEAN-NORTH	BE	NP	
			LITTLE BAHAMA BANK-NORTH	BE	NP	WEATHER
			GREEN CAY	CR	NP	
1377	10-01-78	07:40	U.S. WEST COAST	CS	NP	
1378	10-01-78	09:15	CANADIAN WEST COAST	CS	IW	
			QUEEN CHARLOTTE ISLAND	SWSH	DB	
1387	10-01-78	00:20	NORTH SEA COAST	MB	DB	
			ENGLISH CHANNEL-CENTRAL	SWSB	BP	
1391	10-02-78	07:10	GULF OF CALIFORNIA	CS	IW	WEATHER
1395	10-02-78	13:30	CANADIAN EAST COAST	CS	IW	
1397	10-02-78	16:40	MISTERIOSA BANK	BE	SP	
			GULF OF MEXICO	CS	NP	
			SWAN ISLAND	SWSI	DB	
			SWAN ISLAND	CR	DB	
			GORDA BANK	BE	SP	
1398	10-02-78	18:25	GULF OF CALIFORNIA	CS	IW	
			COLORADO RIVER	SWSB	BP	
1401	10-03-78	05:05	CAY SAL BANK	BE	SP	
			U.S EAST COAST	CS	IW	
			DIAMOND SHOALS	SWSH	NP	
			GRAND PAHAMA BANK-WEST	BE	SP	
			LITTLE BAHAMA BANK-WEST	BE	SP	

*SEE PAGE A-1 FOR KEY TO BOTTOM FEATURE TYPE, SAR PATTERN AND COMMENTS

A-18

SUMMARY OF SEASAT SAR OBSERVED BOTTOM RELATED SURFACE PATTERNS (CONTINUED)

REVOLUTION	DATE	TIME (GMT)	LOCATION	BOTTOM FEATURE TYPE*	SAR PATTERN*	COMMENTS*
1408	10-03-78	11:30	MCKENZIE RIVER DELTA	MB	DB	
1411	10-03-78	16:15	TONGUE OF THE OCEAN	SWSB	BP	
			U.S. EAST COAST	CS	NP	
			ABACO ISLAND	CR	DB	
			CUBAN NORTH COAST	CR	NP	
			GRAND BAHAMA BANK-EAST	BE	NP	
			TONGUE OF THE OCEAN-WEST	BE	SP	
			TONGUE OF THE OCEAN-SOUTH	BE	SP	
			TONGUE OF THE OCEAN-EAST	BE	SP	
			TONGUE OF THE OCEAN-NORTH	BE	SP	
			LITTLE BAHAMA BANK-WEST	BE	SP	
			LITTLE BAHAMA BANK-NORTH	BE	SP	
			GREEN CAY	CR	NP	
1420	10-04-78	07:50	U.S. WEST COAST	CS	NP	
1425	10-04-78	16:00	U.S. EAST COAST	CS	NP	
1428	10-04-78	20:55	ALASKA COAST	CS	NP	
1430	10-04-78	00:35	ENGLISH CHANNEL-SOUTH	SWSB	NP	
			ENGLISH CHANNEL-SOUTH	SWSB	NP	
			ENGLISH CHANNEL-SOUTH	SWSB	NP	
			ENGLISH CHANNEL-SOUTH	SWSB	BP	
1431	10-05-78	07:25	GULF OF CALIFORNIA	CS	IW	WE..HER
1438	10-05-78	13:40	CANADIAN EAST COAST	CS	IW	
1440	10-05-78	16:50	MISTERIOSA BANK	BE	SP	
			SWAN ISLAND	SWSI	DB	
			SWAN ISLAND	CR	DB	
1441	10-05-78	18:40	GULF OF CALIFORNIA	CS	IW	
			COLORADO RIVER	SWSB	BP	
1447	10-06-78	05:15	MISTERIOSA BANK	BE	NP	
			CAY SAL BANK	BE	NP	
			U.S. EAST COAST	CS	IW	WEATHER
			DIAMOND SHOALS	SWSH	NP	
			GRAND BAHAMA BANK-WEST	BE	SP	
			LITTLE BAHAMA BANK-WEST	BE	SP	
1449	10-06-78	08:30	U.S. WEST COAST	CS	IW	
1451	10-06-78	11:45	MCKENZIE RIVER DELTA	MB	DB	
1463	10-07-78	08:05	U.S. WEST COAST	CS	NP	WEATHER
1468	10-07-78	15:55	U.S. EAST COAST	CS	NP	

*SEE PAGE A-1 FOR KEY TO BOTTOM FEATURE TYPE, SAR PATTERN AND COMMENTS

TABLE A1

SUMMARY OF SEASAT SAR OBSERVED BOTTOM RELATED SURFACE PATTERNS (CONCLUDED)

REVOLUTION	DATE	TIME (GMT)	LOCATION	BOTTOM FEATURE TYPE*	SAR PATTERN*	COMMENTS*
1471	10-07-78	21:10	ALASKA COAST	CS	NP	
1473	10-08-78	00:45	ENGLISH CHANNEL-SOUTH	SWSB	NP	
			ENGLISH CHANNEL-SOUTH	SWSB	NP	
			ENGLISH CHANNEL-SOUTH	SWSB	BP	
			ENGLISH CHANNEL-SOUTH	SWSB	BP	
			ENGLISH CHANNEL-CENTRAL	SWSH	NP	
			NORTH SEA COAST	MB	DB	
			ENGLISH CHANNEL-CENTRAL	SWSB	BP	
1483	10-08-78	17:05	MISTERIOSA BANK	BE	SP	
			GULF OF MEXICO	CS	NP	
			SWAN ISLAND	SWSI	DB	
			SWAN ISLAND	CR	DB	
			GORDA BANK	BE	SP	
1484	10-08-78	18:50	GULF OF CALIFORNIA	CS	IW	WEATHER
			COLORADO RIVER	SWSB	NP	WEATHER
1490	10-09-78	05:20	MISTERIOSA BANK	BE	NP	
			CAY SAL BANK	BE	SP	
			GRAND BAHAMA BANK-WEST	BE	SP	
			LITTLE BAHAMA BANK-WEST	BE	NP	
			LITTLE BAHAMA BANK-NORTH	BE	NP	
1492	10-09-78	08:45	U.S. WEST COAST	CS	NP	
1493	10-09-78	10:03	NORTH SEA COAST	MB	DB	
			NORTH SEA COAST	SWSB	BP	
1494	10-09-78	11:55	MCKENZIE RIVER DELTA	MB	DB	
1497	10-09-78	16:38	U.S. EAST COAST	CS	NP	WEATHER
			ABACO ISLAND	CR	NP	WEATHER
			LITTLE BAHAMA BANK-WEST	BE	NP	WEATHER
			LITTLE BAHAMA BANK-NORTH	BF	NP	
1499	10-09-78	20:10	ALASKA COAST	CS	NP	
1502	10-10-78	01:25	COAST OF NORWAY	CS	NP	

*SEE PAGE A-1 FOR KEY TO BOTTOM FEATURE TYPE, SAR PATTERN AND COMMENTS

APPENDIX B.
"DETECTION OF BOTTOM FEATURES ON SEASAT SYNTHETIC APERTURE RADAR"

Report Prepared By:

Dynamics Technology Under ERIM Subcontract No. 163000-1

Dynamics Technology, Inc.

DT-8312-01

DETECTION STUDY OF BOTTOM FEATURES

ON

SEASAT SYNTHETIC APERTURE RADAR IMAGERY

March 1983

By: A. K. Liu

Dynamics Technology, Inc.
22939 Hawthorne Blvd., Suite 200
Torrance, California 90505
(213) 373-0666

This report has undergone an extensive internal review before release, both for technical and non-technical content, by the Division Manager and an independent internal review committee.

Division Manager:

Judith Soukup

Internal Review:

Stew R Borchardt

ABSTRACT

This report presents an analytical investigation of the oceanic processes involved in the bottom-related surface signatures observed on the Seasat SAR imagery. Two sets of data from Seasat orbits during Revolutions 974 and 762 were used to examine the relationship between the bottom features and surface patterns. Shallow water internal waves on the East Coast and New York Bight are studied and analyzed. Based on a two-layer solitary wave theory and the Seasat SAR image data (Rev. 974), the internal wave field has been formulated. The wind wave modulation induced by the internal waves is estimated, and a numerically simulated Seasat SAR image shows good visibility of the internal waves. Three selected features in the northeast Atlantic test site on the Seasat SAR imagery for Rev. 762 have been examined carefully. Deep water internal waves over the Wyville-Thomson Ridge appear to be produced by lee wave formation. A frontal boundary over the Faeroe Bank Channel seems to be generated by deep water upwelling. The change in backscatter around North Rona Rock is probably caused by the trapping of wave energy around the island. This study has demonstrated that these patterns can be used for inference about bathymetry and submerged features. The limitations of the theoretical model are discussed, along with recommendations for future efforts on further data analysis and numerical simulation.

TABLE OF CONTENTS

ACKNOWLEDGMENTS

LIST OF FIGURES

LIST OF FIGURES (Continued)

1. INTRODUCTION

It has become apparent in recent years that striking evidence of subsurface topography is often observed in microwave radar images of the ocean surface. Since microwave radiation does not penetrate to any significant depth below the sea surface, this phenomenon must be the surface manifestation of the wind wave-current interaction induced by bottom features. Analyses of Seasat SAR images reveal that this is a common phenomenon occurring in a large number of coastal, island and seamount regions. Numerical examples of these subsurface topographic effects in SAR imagery have been described, for example, by Shuchman (1982) and by Fu and Holt (1982). Several comprehensive documents collecting information on Seasat SAR are available (e.g., Apel, 1980; Beal, *et al.*, 1981; Vesecky and Stewart, 1982). Apparently, SAR imagery is rapidly becoming an important tool for investigation of oceanic processes.

For the Seasat SAR, backscatter from the ocean surface is produced predominantly by the Bragg resonant scattering mechanism. That is, the surface waves traveling in the radar range direction with a wavelength of $\lambda/2 \sin\phi)$, the Bragg waves, account for most of the backscattering, where λ is the radar wavelength and ϕ the incidence angle. Therefore, Seasat SAR imagery of the ocean is fundamentally a map of the radar scattering characteristics of wind waves with a wavelength of 34 cm. The capability of SAR to detect bottom features is a consequence of hydrodynamic interaction between the topographically induced surface current field and the wind-driven ocean surface waves. The resulting spatial variations of sea surface roughness are, in turn, imaged by the radar as variations in image brightness. Thus, the utility of SAR for providing bathymetric information requires understanding and analysis of these hydrodynamic processes.

A recent report by Kasischke *et al.* (1982) has discussed the utility of Seasat SAR data for the detection and charting of bottom features which might be hazardous to navigation. Their investigation supports the goals of the Defense Mapping Agency with respect to the utilization of remotely sensed data. The final goals of using remote sensing are to provide a rapid survey capability to detect and locate geographically submerged

features potentially hazardous to navigation, as well as to provide esti-
mates of water depth in order to aid in updating of nautical charts. SAR
imaging is a powerful technique for high spatial resolution observation
under all weather conditions of geographical regions of concern to the
DMA. The work at ERIM supported by DMA has already gone a considerable way
toward identifying the oceanic processes in SAR imagery. The present work
was sponsored by ERIM and supports ERIM's effort under sponsorship of the
DMA. Based on ERIM's preliminary investigation by Kasischke *et al.* (1982),
they suggested the data sets for further hydrodynamic analysis, and also
supplied DynaTech with copies of Seasat SAR imagery and hydrographic data.
In this report, the hydrodynamic processes are studied in detail for a
better understanding of the causes of surface signatures that map bottom
features.

Due to the limited scope of the investigation, efforts are concentrated on
the illustrative description and theoretical analysis of the hydrodynamic
processes underlying the subsurface topographic signatures in SAR imagery.
Four major oceanic processes that result in SAR observation of submerged
features are focused on. First, the shallow water internal waves on the
East Coast and New York Bight are studied in Section 2. The generation
mechanism is discussed and the internal wavefield is formulated based on a
two-layer shallow water solitary wave theory and SAR image data. The sur-
face roughness modulation of wind waves by the internal wave-induced sur-
face current is estimated by a spectral transport model. The Seasat SAR
image is simulated numerically to show the visibility of internal waves.
Then, in Section 3, the surface patterns in the northeast Atlantic test
site caused by the oceanic currents flowing over distinct bottom features
are studied; this includes the deep water internal waves over the Wyville-
Thomson Ridge, a frontal boundary over the Faeroe Bank Channel, and the
change in backscatter around North Rona Rock. The hydrodynamic processes
involved in the formation of these SAR observed phenomena are described and
formulated with the appropriate equations. Finally, this detection study
of bottom features on Seasat SAR imagery is summarized and discussed in
Section 4, along with recommendations for future efforts on further
detailed data analysis and theoretical/numerical modeling.

2.   SHALLOW WATER INTERNAL WAVES

2.1 Background

Peculiar striations more than one hundred kilometers long are visible on satellite photographs, and these surface striations are often interpreted as the surface roughness modulation induced by the passage of the under-lying nonlinear internal waves.   These nonlinear waves are apparently generated by a tidally driven flow over sills, continental shelf edges, or other major variations in underwater topography.   Surface signatures of these topographically generated internal waves have been observed with Landsat (Apel *et al.*, 1975, 1976) off the North American and African coasts, and Seasat (Apel, 1981) off the West Coast of Baja California, Mexico.   Recently, several studies of internal waves on Seasat SAR imagery were reported by Trask and Briscoe (1983), by Alpers and Salusti (1983) and by Hughes and Gower (1983).

The generation and propagation of nonlinear internal waves in a stable, stratified fluid has been a subject of considerable recent interest.   The existence of a class of nonlinear waves of permanent form in a stratified medium has been investigated by Benney (1966) and by Benjamin (1966) for a shallow water system.   The mechanism whereby these waves, usually known as solitary waves, retain their shapes and speed can be explained in terms of a balance between nonlinear and dispersive effects.   The results often demonstrate the existence of such a solitary wave solution.

The solitary wave theory which describes the generation and evolution of the nonlinear internal waves has been modeled and compared with field measurements.   A study of underwater current and temperature variations associated with such large internal waves in the Andaman Sea was reported by Osborne and Burch (1980).   They used a two-layer shallow water model (Korteweg-deVries or KdV equation) to describe the physics of these non-linear waves and their interactions with surface waves.   Their observations are in good overall agreement with the characteristics of internal solitary

waves predicted by the KdV equation. Recently, Apel and Holbrook (1983) and Holbrook *et al.* (1983) reported on what appeared to be very large internal waves visible on satellite images taken over the Sulu Sea. Then, Liu *et al.* (1983) reported on an analytical investigation of these internal solitary waves in the Sulu Sea based on the nonlinear finite-depth theory. The analytical results agree reasonably well with the Sulu Sea data and the numerical simulations demonstrate the generation and evolution of a series of solitons in a wave packet.

2.2 East Coast and New York Bight Observations

Continental shelf internal waves have been chosen by Apel *et al.* (1975, 1976) for interpretation and analysis because of their coherence and clearly defined characteristics when viewed from spacecraft. Figure 1 shows the Seasat SAR imagery of internal waves collected over the East Coast during Revolution 974 on 3 September 1978 at approximately 02:50 GMT. The scene dimensions are 170 km x 55 km; South end of the image lies approximately 250 km from Cape Hatteras. Figure 2 shows the interpretive line drawings of the internal waves observed on the east coast of Delaware and also shows the bottom topography with isobaths given in fathoms. As shown in Figure 2, the internal waves are generated near the edge of the continental shelf at the depth around 100 fm. A series of internal wave packets are visible along the coast on the continental shelf. Another Seasat SAR image of internal waves, collected over New York Bight during Revolution 974, is shown in Figure 3. The scene dimensions are 200 km x 110 km; it shows Long Island at the top corner. Figure 4 consists of line drawings of internal waves observed in Figure 3 superimposed on the bottom topography. Periodic striations of four sequential wave packets are clearly visible in the middle of the SAR image, apparently radiating from the edge of the continental shelf. The dotted area near the top right corner indicates a dark region, most likely due to low wind speed. The complicated pattern of wave-wave interaction of two wave packets can be observed at the top part of the image, near Long Island.

25 KM

Figure 1. Seasat SAR Imagery of Internal Waves Collected Over East Coast. Revolution 974, from ERIM.

-5-

B-13
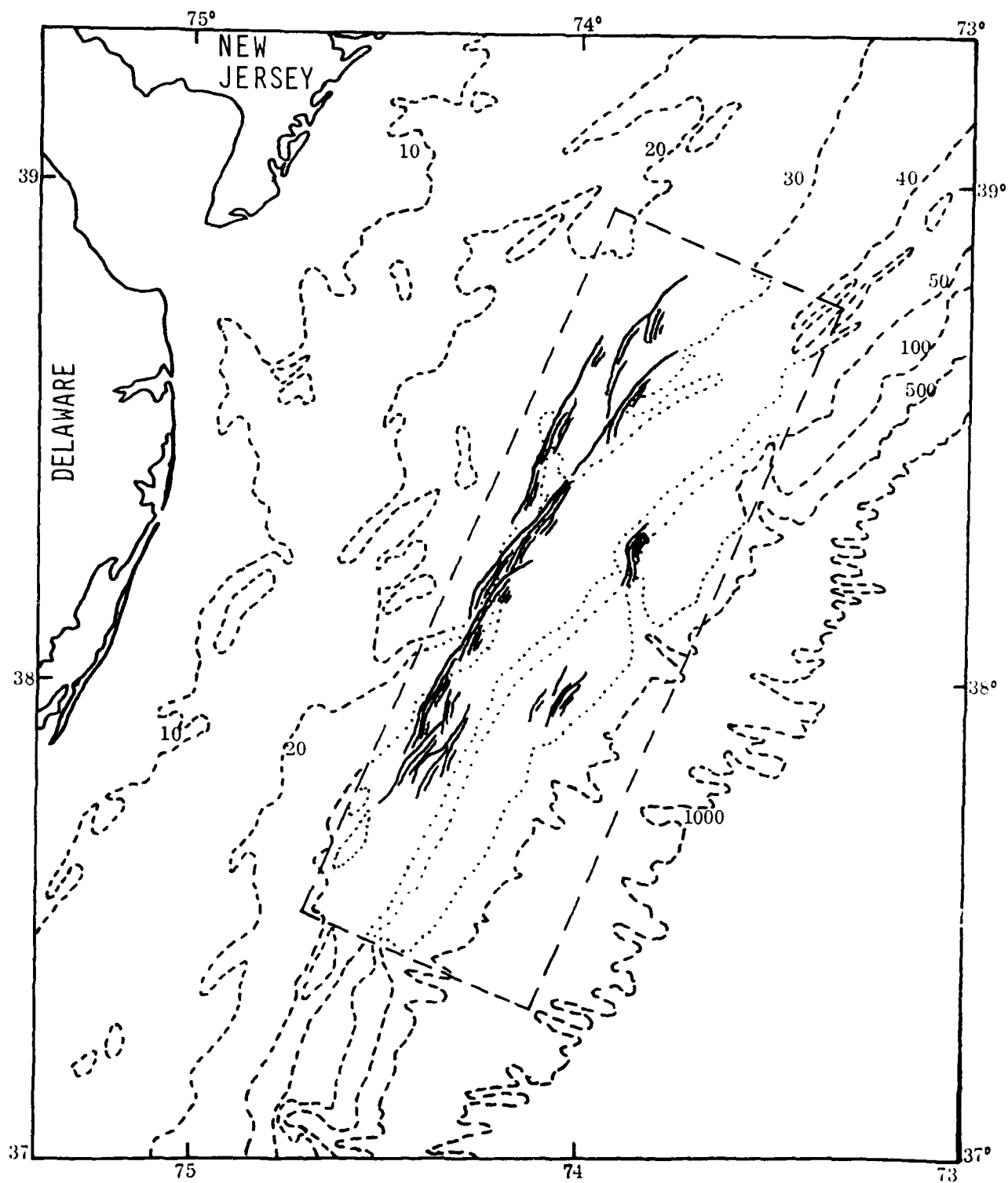
Figure 2.   Line Drawing of the Internal Wavefield Observed in Figure 1 Superimposed on the Bottom Topography.
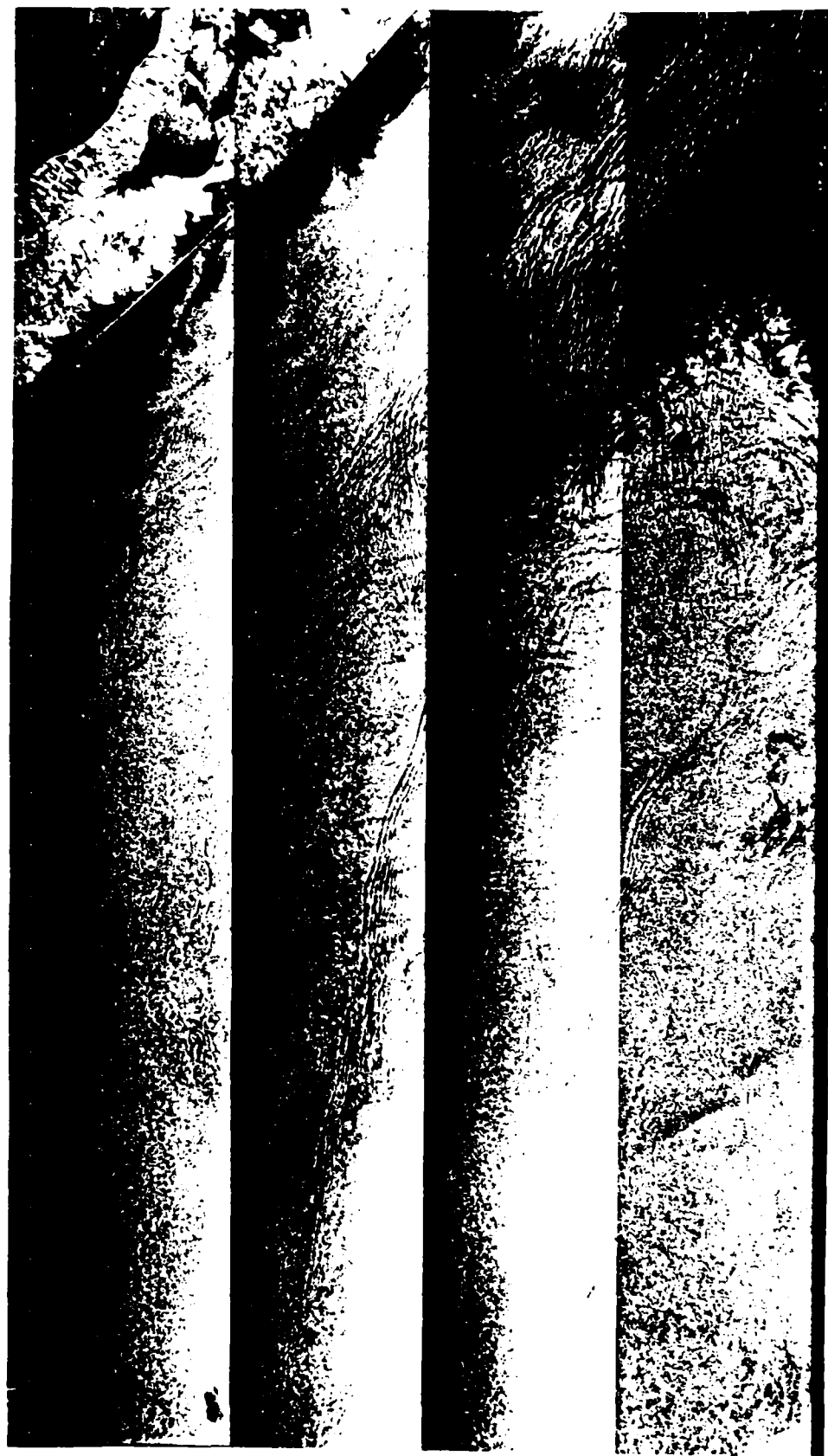
Figure 3. Seasat SAR Imagery of Internal Waves Collected Over New York Bight. Revolution 974, from ERIM.

25 KM
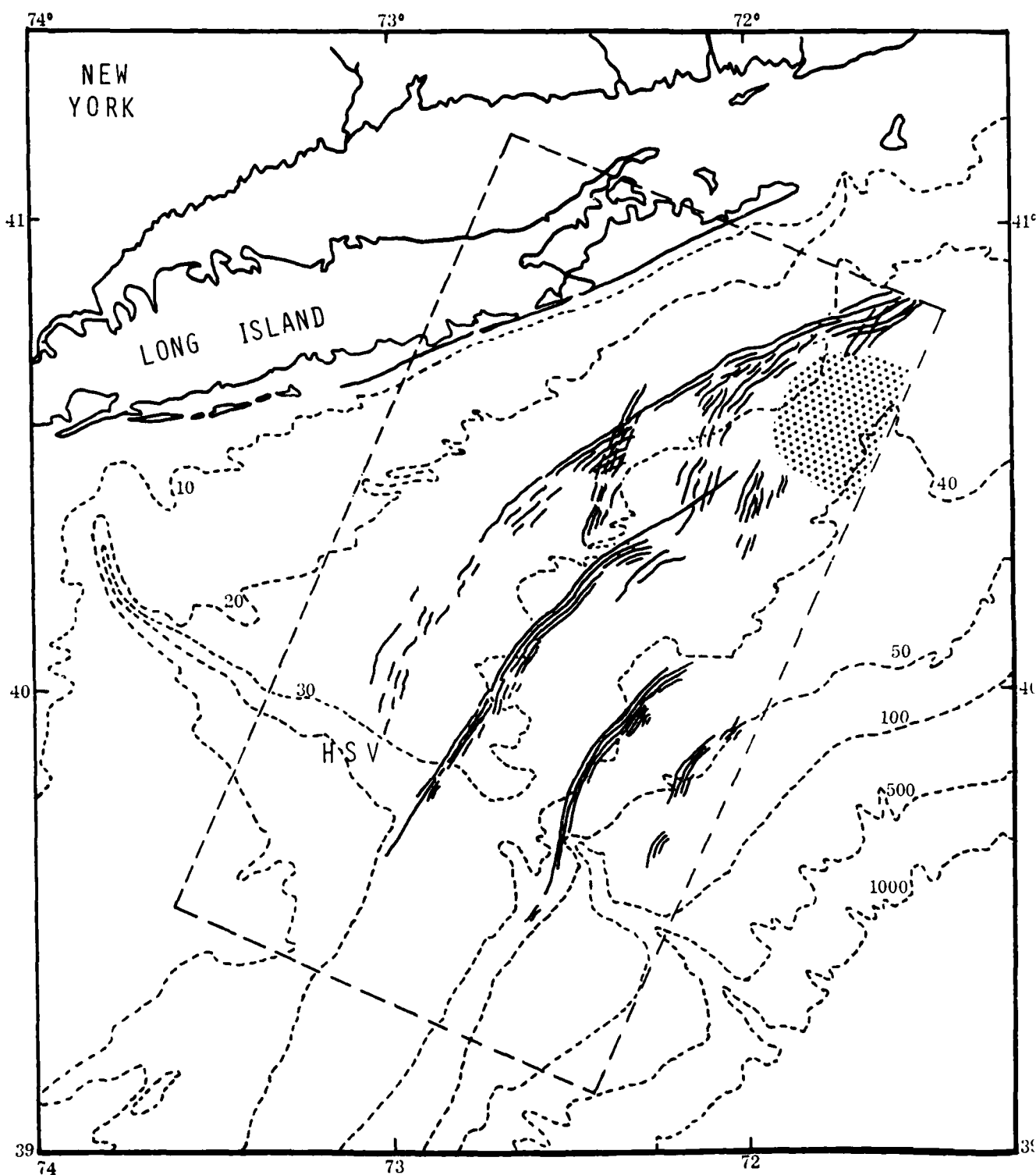
Figure 4. Line Drawing of the Internal Wavefield Observed in Figure 3 Superimposed
          on the Bottom Topography.

B-16

-3-

Long-term current and temperature observations on the Middle Atlantic Shelf were reported by Mayer *et al.* (1979) during two years, 1975 and 1976. Example contours of temperature and sigma t for the section of shelf just north of the Hudson Shelf Valley (HSV) are shown in Figure 5. A mixed layer of 30 m depth is evident for the summer months of June 1975 and September 1976. Although the SAR image of Figure 1 was taken on 3 September 1978, the seasonal characteristics of the shelf water mass are expected to be similar. In general, stratification builds to a maximum in August in this region.

While no sea truth is available, the identification with internal waves is reasonably certain. The following mechanism seems to explain the generation process. First, the scattering of the barotropic tidal energy into internal baroclinic tide occurs at the edge of the continental shelf for a few hours during the peak tidal current. This baroclinic current distribution then generates internal waves by shear flow instability on the bottom of the mixed layer (Tsai and Apel, 1979). As the tidal currents rotate through the tidal ellipse, the instability starts up and shuts down every 12.5 hours. Thus, a packet of waves is created at the shelf edge and launched once each semidiurnal-tidal cycle as shown schematically in Figure 6; it typically contains about ten waves. Then, the wave packet propagates up onto the shelf until the mixed layer intersects the bottom, whereupon the waves break and deposit their energy into turbulence and bottom sediment transport.

The observed important characteristics of the surface pattern induced by the internal waves on the continental shelf are summarized as follows:

1. The internal waves occur in packets, separated by distances that are on the order of 25 km.

2. Based on the assumption of a semidiurnal tidal origin, the wave speed is estimated to be 0.55 m/s.

3. The wave packets in this region contain about te: - ves with a packet width about 5 km.

4. Within a given wave packet, the wavelengths appear to be monotonically decreasing, front to rear, from 1200 m to 300 m.

-9-
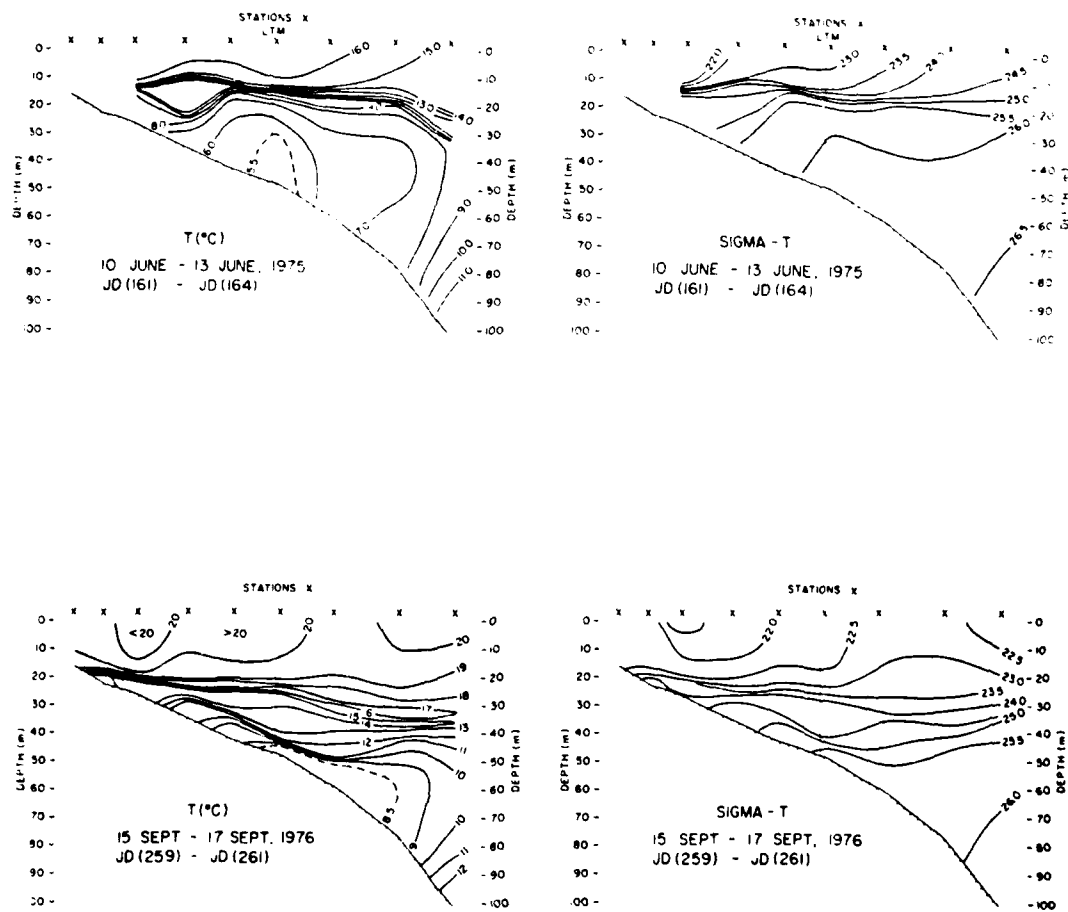
Figure 5.   Temperature and Sigma t Contours, Four Panels During June 1975
and September 1976, North of the Hudson Shelf Valley.
From Mayer, Hansen and Ortman (1979).
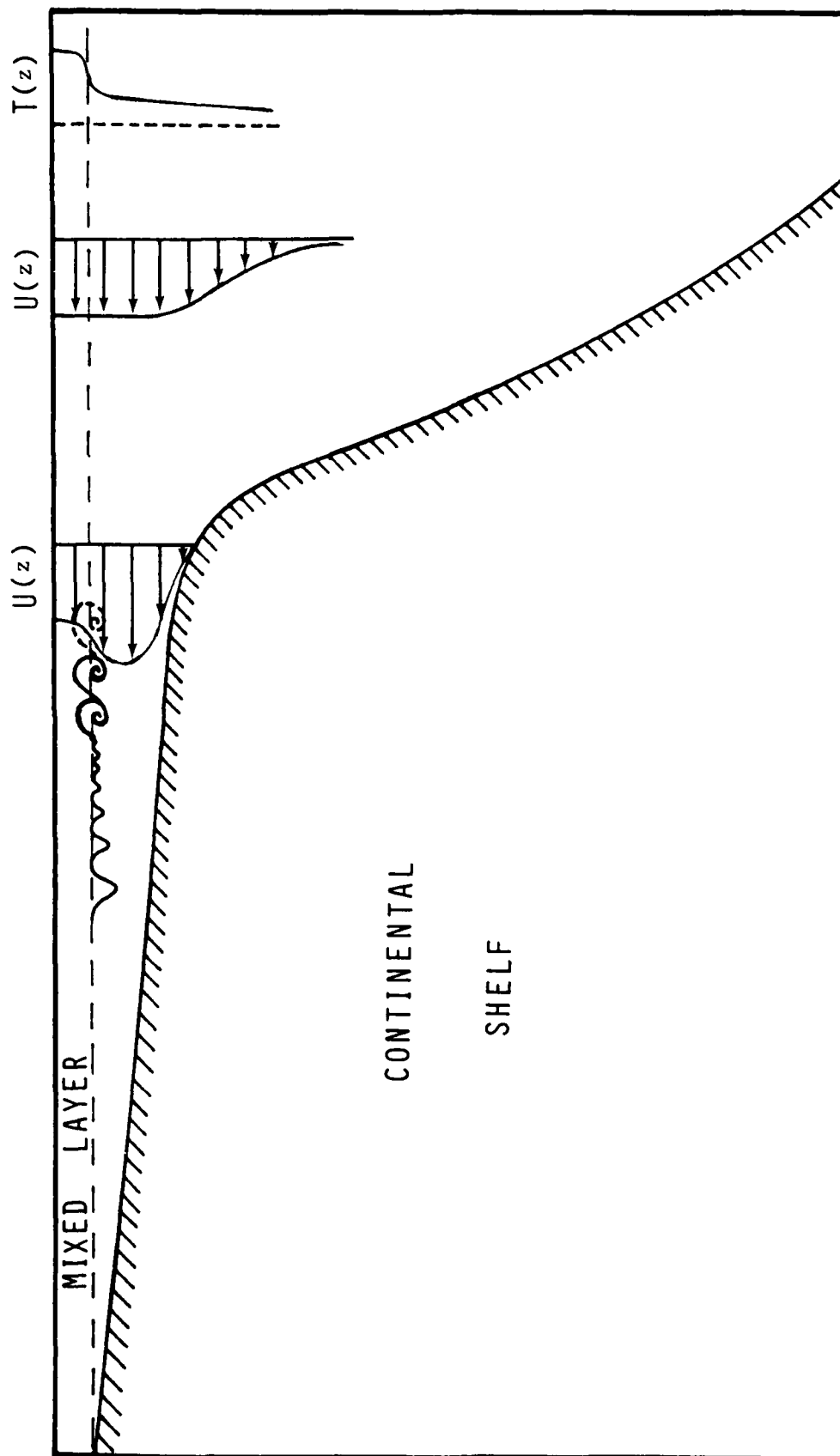
Figure 6. Schematic Diagram of Generation of an Internal Wave Packet on the Edge of Continental Shelf.

5. The surface pattern is always more observable at the front of the wave packet than at the rear.

6. Each wave is characterized by a bright band followed immediately by a dark band.

The above features suggest that these internal waves in each packet are probably the rank-ordered solitary waves with the largest, fastest and longest waves found out in front. The solitary wave theory which describes the evolution of the internal wave packet is reviewed in the next section.

2.3 Solitary Wave Theory

Since there is no *in situ* measurement of the density profile, a two-layer model is used based on the historical data described in the previous section. The system considered is a mixed layer of depth H_1 lying on top of a denser layer with thickness H_2 and density contrast $\Delta\rho/\rho$. Because the wavelength of the internal wave is much larger than the total water depth, the shallow water theory is adopted. Then, the evolution equation for the displacement of the interface $h(x,t)$ is given by the Korteweg-deVries equation

$$h_t + C_o h_x + \frac{3(H_1 - H_2)}{2 H_1 H_2} C_o h\, h_x + \frac{1}{6} C_o H_1 H_2\, h_{xxx} = 0 \quad , \qquad (2.1)$$

where subscripts t,x denote time and space derivatives, and the linear wave speed C_0 is

$$C_o = \left[\frac{\Delta\rho}{\rho}\, g\, \frac{H_1 H_2}{H_1 + H_2} \right]^{1/2} . \qquad (2.2)$$

It is easily seen from Equation (2.1) that the character of the solitary wave can be directly inferred from consideration of the depths of the water and interface. When $H_1 > H_2$, only waves of elevation can occur, whereas if $H_1 < H_2$, only waves of depression can occur. When $H_1 = H_2$, the nonlinear term in the evolution equation (2.1) vanishes.

-12-

The steady-state solution of Equation (2.1) is given (Whitham, 1974) by

$$h(x,t) = -A \, \text{sech}^2 \left[(x-Ct)/L \right] , \tag{2.3}$$

where A is the wave amplitude, the wave speed C is

$$C = C_0 \left[1 + \frac{A(H_2-H_1)}{2H_1 H_2} \right] , \tag{2.4}$$

and the half width L is

$$L = H_1 H_2 \left[\frac{4}{3A(H_2-H_1)} \right]^{1/2} . \tag{2.5}$$

In the New York Bight, the density contrast $\Delta\rho/\rho \simeq 10^{-3}$, and the mixed layer depth $H_1 \simeq 30$ m with $H_2 \simeq 60$ m. From Equation (2.2) the linear wave speed is estimated to be $C_0 \simeq 0.45$ m/s. As reported by Proni and Apel (1975), the wave amplitude $A \simeq 20$ m in this area, based on the XBT data and the towed thermistor data. Then, the wave speed C is calculated from Equation (2.4) to be 0.53 m/s, which is consistent with the wave speed of 0.55 m/s estimated from the SAR images. The width of the wave, 2L, is evaluated from Equation (2.5) to be 170 m. Thus, a packet of depression waves propagates up onto the shelf until $H_2 \simeq H_1$, whereupon the waves disintegrate into a dispersive wave train. As evident in Figure 4, the wave packet starts to disappear approximately at the water depth of 60 m near the 30-fathom contour.

The number of solitary waves N which emerge from an initial disturbance can be determined from the Schrödinger equation. For the specific case where the initial waveform is a $\text{sech}^2 x$ potential well, the amplitude A for each solitary wave of a wave packet can be written approximately in the form (Whitham, 1974)

$$A_n = A_1 \left[(N-n)/(N-1) \right]^2 , \tag{2.6}$$

where n is the number of a particular solitary wave in a packet, and A_1 is the amplitude of the first wave in the packet.

After the initial interaction, each solitary wave moves in the packet with velocity $C-C_0$, which is proportional to the wave amplitude. Then, for each solitary wave of a wave packet, the distance behind the first wave is approximately given by

$$R - R_n = R \{1 - [(N-n)/(N-1)]^2\} , \qquad (2.7)$$

where R is the packet width, which can be estimated from the SAR image.

Therefore, for a train of solitary waves in a packet, the internal wavefield can be approximately expressed by

$$h(\xi) = \sum_{n=1}^{N} -A_n \operatorname{sech}^2 \left[\frac{\xi-R_n}{L_n}\right] , \qquad (2.8)$$

where L_n is given by Equation (2.5), and $\xi = x - C_0 t$.

This simplified model of the internal wavefield can then be used to estimate the surface effects, which will be presented in the next section. It is to be noted that the present solitary wave theory is limited to a two-dimensional inviscid fluid without radial spreading and energy dissipation. Such a deduction is not expected to be highly accurate, of course, but it can provide order-of-magnitude estimates if the nonlinear effect is appreciable.

The total wave energy per unit crest length for a wave packet is given by

$$E \simeq \Delta\rho \, g \int_{-\infty}^{\infty} h^2(\xi) \, d\xi ,$$

$$= \sum_{n=1}^{N} \frac{4}{3} \Delta\rho \, g \, A_n^2 \, L_n . \qquad (2.9)$$

-14-

In general, larger internal wave energies will result in a clearer surface pattern under ideal conditions. For the sake of reference, an estimate of the total energy per unit crest length is 10^6 Joule/m in the New York Bight. Based on the SAR image of 100 km crest length, these waves could deliver energy to the coast at the rate of 10^{11} Joules per each wave period $T = 2L/C \simeq 5$ min. This estimate may account for a significant portion of the 10^{12} watt loss due to the dissipation of tidal energy by the sharp depth change at the edges of the continental shelves (Halpern, 1971). Evidently, this process is also important to the coastal seiche excitation by tide-generated internal waves, as reported by Giese *et al.* (1982).

2.4 Surface Effects

The essential element of the surface effects is the interaction between the internal wave-induced surface current field and the wind-driven ocean surface waves. This interaction has been studied, notably by Lewis, Lake and Ko (1974) and Hughes (1978). Basically, the analysis is based on a near-equilibrium spectral transport model to estimate the roughness modulation by a variable surface current. The effect of the surface current is to alter the spectrum from its equilibrium value, while the natural processes of wave energy input from the wind, wave breaking and other non-conservative processes act to restore the ambient equilibrium spectrum.

The surface current induced by the wave packet can be expressed as

$$U(x) = -\frac{C_o}{H_1} h(x) , \qquad (2.10)$$

where $h(x)$ is given by Equation (2.8).

Then the strain rate is defined by

$$U_x(x) = -\frac{C_o}{H_1} h_x(x) ,$$

$$= \sum_{n=1}^{N} \frac{2C_o A_n}{H_1 L_n} \operatorname{sech}^2 \left[\frac{x-R_n}{L_n}\right] \tanh \left[\frac{x-R_n}{L_n}\right] . \qquad (2.11)$$

-15-

The maximum and minimum values of the strain rate are located at $x = R_n \pm 0.66 L_n$.

A strictly horizontal surface current induced by the internal waves is assumed for a locally one-dimensional wave packet. Then, the surface wave spectral function $F(\underset{\sim}{k},x,t)$ is related to the distribution of the mean square surface displacement by the expression

$$\langle \eta^2(x,t) \rangle = \int F(\underset{\sim}{k},x,t) \, d\underset{\sim}{k} \quad , \tag{2.12}$$

where $\langle \ \rangle$ denotes ensemble average.

The variation of the wave action spectrum, $E(\underset{\sim}{k},\underset{\sim}{x},t) = (\omega_0/k)F(\underset{\sim}{k},\underset{\sim}{x},t)$ is described by a spectral transport equation:

$$\frac{\partial E}{\partial t} + \frac{dx}{dt}\frac{\partial E}{\partial x} + \frac{d\underset{\sim}{k}}{dt}\frac{\partial E}{\partial \underset{\sim}{k}} = BE \left[1 - \left(\frac{E}{E_e}\right)^2 \right] \quad , \tag{2.13}$$

where k is the wave number, ω_0 is the intrinsic frequency, B is the surface wave relaxation rate (Inoue, 1966), and F_e is the equilibrium spectrum (Pierson and Stacy, 1973). The equation for the characteristics are

$$\frac{dx}{dt} = \frac{\partial \omega}{\partial k_1} \quad , \qquad \frac{\partial k_1}{\partial t} = -\frac{\partial \omega}{\partial x} \quad , \qquad k_2 = \text{const.} \quad , \tag{2.14}$$

where the dispersion relation is

$$\omega = \omega_0 + [U(x) + C_0] k_1 \quad ,$$

$$= (gk + \gamma k^3)^{1/2} + [U(x) + C_0] k_1 \quad , \tag{2.15}$$

where γ is the coefficient of surface tension, and C_0 is the linear internal wave speed. The spectral perturbation function is defined by

$$f(\underset{\sim}{k},x,t) = F(\underset{\sim}{k},x,t)/F_e(\underset{\sim}{k}) - 1 \quad , \tag{2.16}$$

-16-

and is an indication of the surface roughness modulation, which is assumed to be smaller than unity.

By linearizing the spectral transport equation for f, it reduces to

$$\frac{df}{dt} + 2Bf = \{[\frac{k}{F_e} \frac{\partial F_e}{\partial k} + (\frac{kC_g}{\omega_0} - 1)] \sin^2\theta + \frac{1}{2} \frac{1}{F_e} \frac{\partial F_e}{\partial \theta} \sin2\theta\} \frac{\partial U}{\partial x} ,$$

$$\equiv S(k,\theta,t) \frac{\partial U}{\partial x} , \tag{2.17}$$

where θ is the radar look angle corresponding to the surface wave propagation direction, and C_g is the surface wave group velocity.

Equation (2.17) has the simple integral solution

$$f = \int_0^t e^{-2B(t-t')} S(k,\theta,t') \frac{\partial U}{\partial x} dt' . \tag{2.18}$$

When the current is relatively small compared with the group velocity of the surface waves, it can be neglected in the computation of the characteristics. In general, the surface current can be represented in terms of the Fourier integral $\hat{U}(\alpha)$. Then the final solution for the spectral function can be expressed as

$$f(x) = \frac{1}{2\pi} \int_{-\infty}^{\infty} \frac{i \alpha S \hat{U}(\alpha)}{2B + i\alpha(C_g\sin\theta + C_0)} e^{i\alpha x} d\alpha + O(e^{-2Bt}) . \tag{2.19}$$

As indicated, Equation (2.19) is valid for Bt >> 1, i.e., when the interaction time is much larger than the relaxation time, which is generally true for the short Bragg waves. Therefore, a quasi-steady state surface pattern will be established, as observed on the SAR image.

In the New York Bight, the surface current and strain rate are constructed, based on the Seasat SAR image and the solitary wave theory as shown in Figure 7(a) and (b). A wave packet consisting of ten rank-ordered solitary waves with packet width of 5 km covers the range of 15 km. The amplitude of the first wave is assumed to be 20 m. The maximum surface current and strain rate are 0.30 m/s and 0.003 1/s, respectively.

Figure 7(c) illustrates a scenario where a surface current induced by an internal wave packet is interacting with the wind waves. The resultant SAR image intensity variation is caused by the wind wave modulation. The surface pattern depends on the environmental conditions (wind) as well as the radar operating conditions (look direction). Figure 8(a) shows surface roughness modulation induced by the internal wave packet as given by Equation (2.19) for four different wind and look directions. Case 1 is the cross-track wind with along-track look direction relative to the track of internal wave propagation direction. Case 2 is the cross-track wind with down-track look direction. Case 3 corresponds to the along-track direction for both look and wind. Case 4 corresponds to the down-track direction for both look and wind. The wind speed is assumed to be 5 knots for all cases. The maximum surface roughness modulations are 0.34, 0.39, 0.13, and 0.14 for these four cases, respectively.

It is to be noted that surface roughness is a maximum ahead of the wave crest and is minimum immediately after the crest, which corresponds to a rough region followed immediately by a smooth region. This surface characteristic is consistent with the SAR image of internal waves, which shows a bright band followed immediately by a dark band. It is believed that once the surface roughness modulation is less than 10%, the surface pattern may not be observable by SAR. As demonstrated in Figure 8(b), a Seasat SAR negative image for Revolution 974 is simulated for Case 2 above, based on the models described in this report. Those surface roughness values are converted to reflectivities using a formula for Bragg scattering (Valenzuela, 1978). Exponential speckle noise is multiplied into the data to produce the final image. Using a Seasat SAR sized pixel of 25 m x 6.25 m, four azimuth resolution looks are incoherently averaged with a resulting

-18-
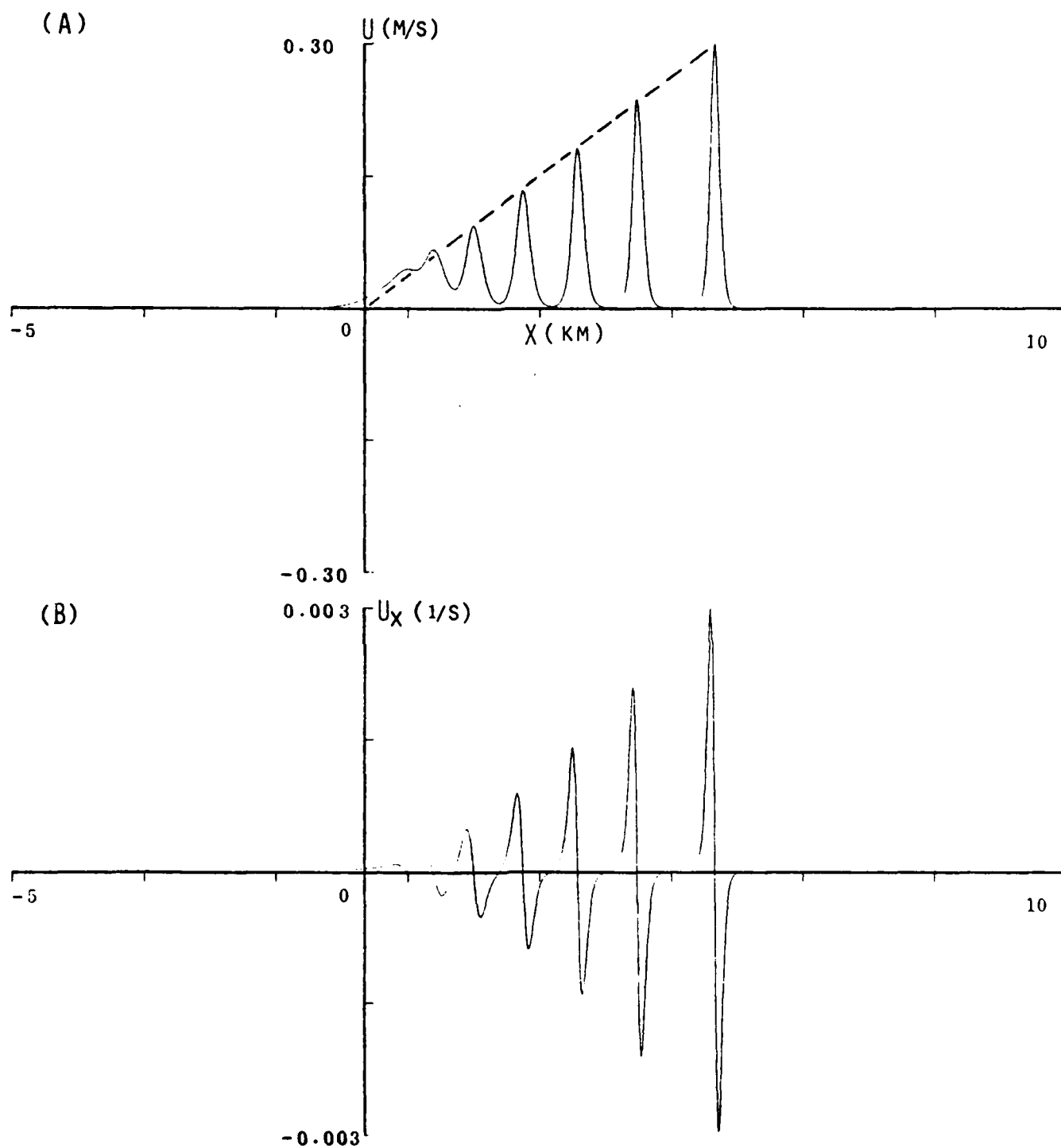
Figure 7. (a) Surface Current, and (b) Strain Rate Induced by an Internal Wave Packet.

B-27
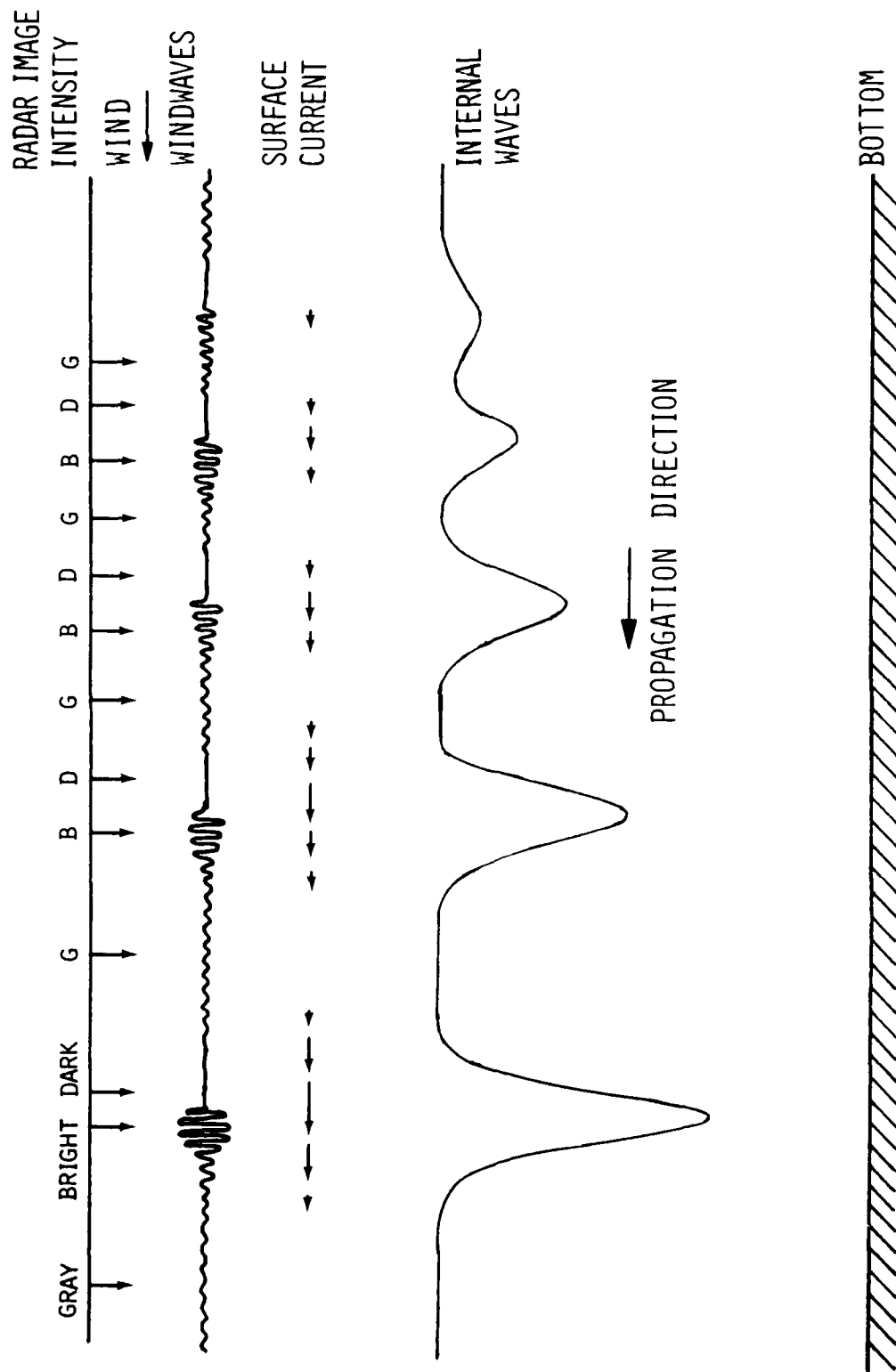
Figure 7. (c) Schematic Diagram of Interactions of Internal Waves, Surface Current Field, Wind Waves and the Resultant SAR Image Intensity Variation

VER[.] [S]CALE, I INCH [=] 0.[1]75
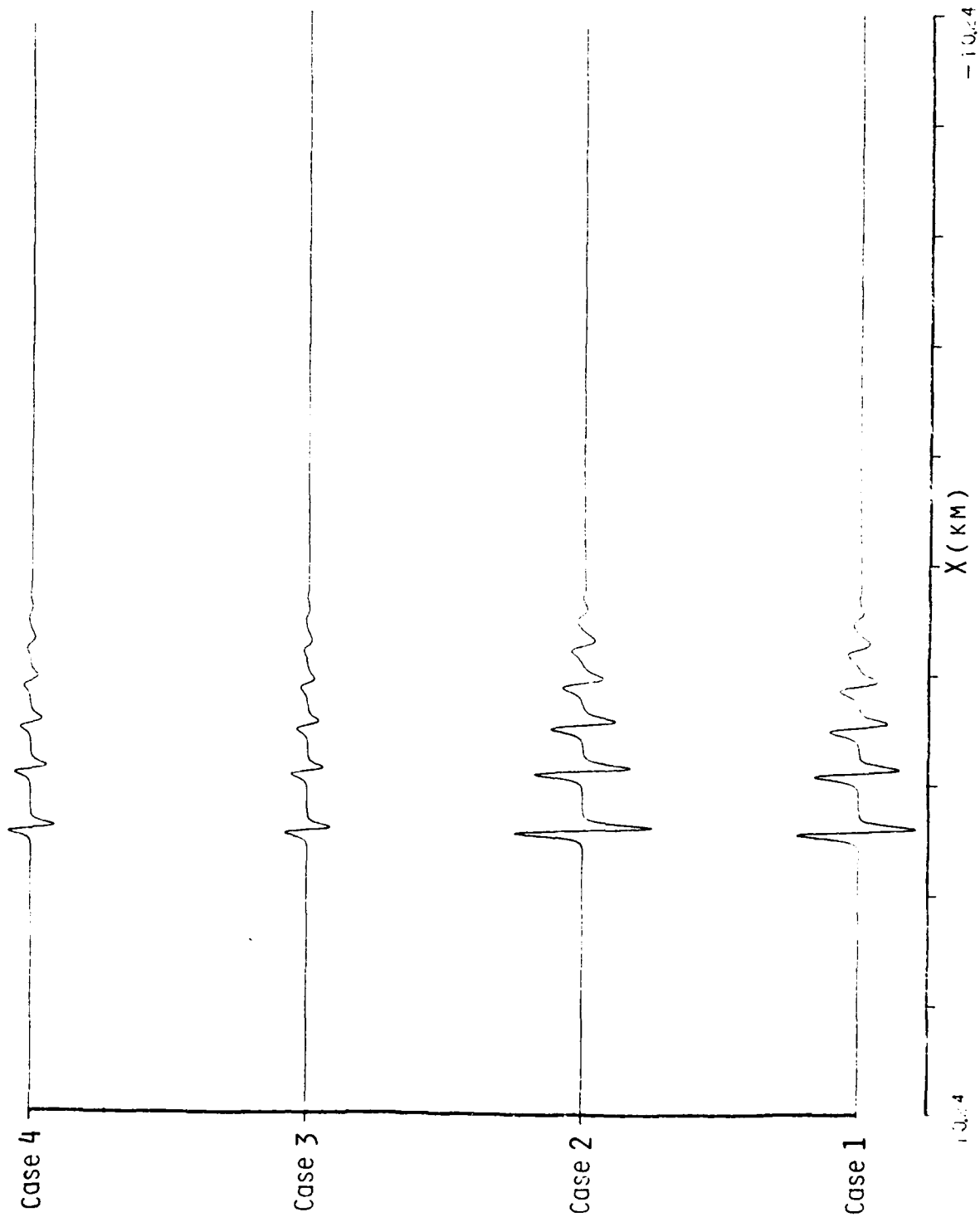
Figure 8. (a) Surface Roughness Modulation Induced by an Internal Wave Packet for Four Different Wind and Look Directions.

Case 4

Case 3

Case 2

Case 1

X (KM)

− 10.4

10.4

B-29

10 KM (Azimuth)
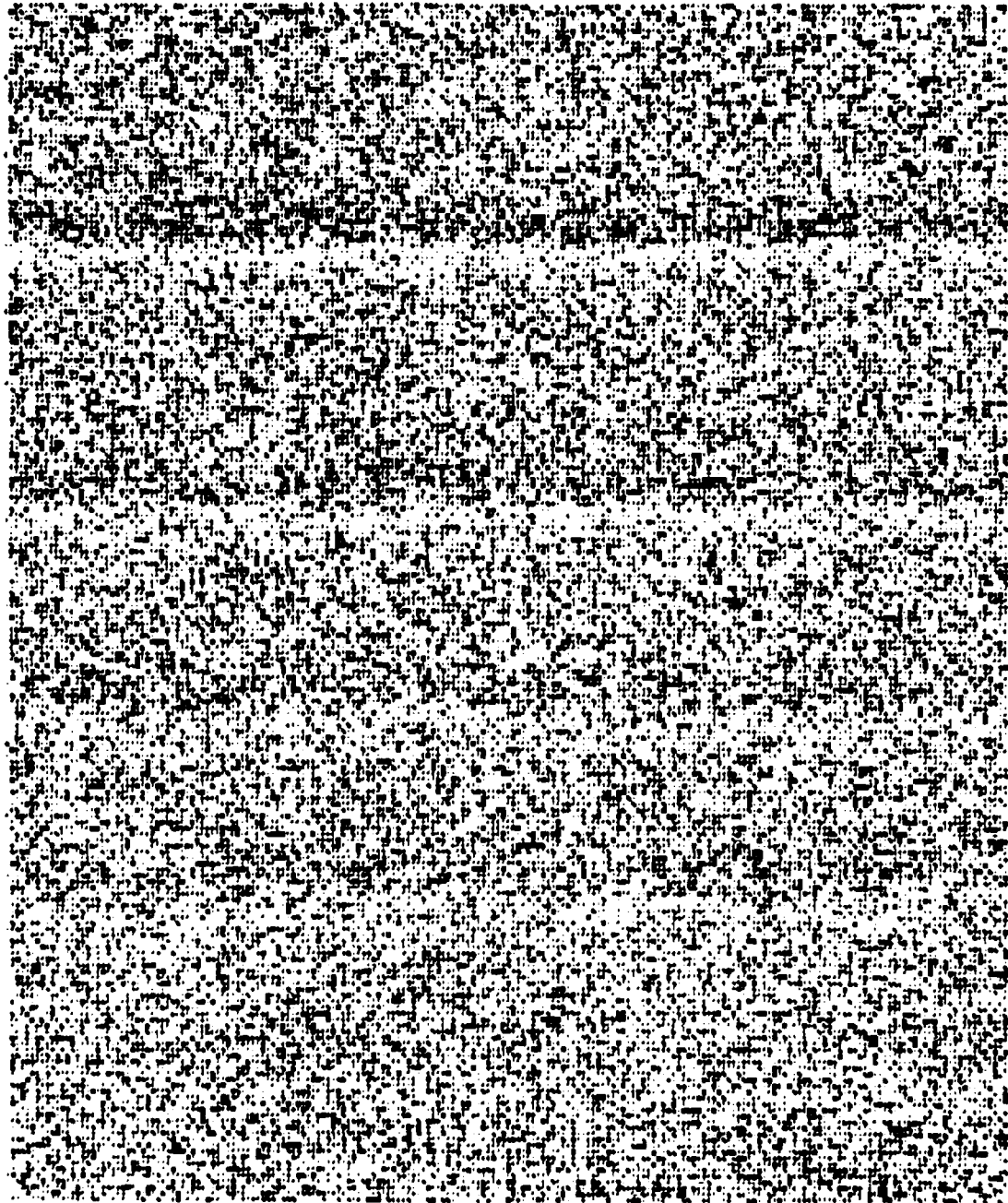
Figure 8. (b) Simulated Seasat SAR Negative Image for Rev. 974 Showing Good Visibility of Internal Waves.

25 m x 25 m pixel. Four internal waves are clearly visible in this simulated image. Similar reflectivity maps of South Falls were reported by Shuchman (1982) through extensive hydrodynamic and electromagnetic modeling efforts on the tidal flow over sand waves. As mentioned before, these order-of-magnitude estimates are based on simplified models and are not expected to be highly accurate. However, the hydrodynamic transfer function model can be refined through comparison with satellite data and *in situ* field measurements. Further study on this is recommended in the last section.

Dynamics Technology

3. SELECTED FEATURES IN NORTHEAST ATLANTIC TEST SITE

3.1 Background

Bottom-related surface patterns exist in deep water as well as shallow-water regions. An extensive data survey was reported by Kasischke *et al.* (1982) on 35 Seasat orbits to examine nine test sites. The northeast Atlantic test site actually contained 17 distinct bottom features such as seamounts, submarine ridges, banks, and the edges of continental shelves. Several types of surface patterns observed on Seasat SAR imagery are believed to be the result of an interaction between tidal currents and such bottom topography. ERIM suggested the data sets to DynaTech for further hydrodynamic analyses in order to have a better understanding of the causes of these selected surface signatures.

In this report, a careful examination is conducted of Seasat SAR imagery collected during Revolution 762, to further study the relationship between bottom topography and surface signatures in the northeast Atlantic test site. Three surface patterns are focused on in this study: (1) internal waves over the Wyville-Thomson Ridge; (2) a frontal boundary over the Faeroe Bank Channel; and (3) change in backscatter around North Rona Rock. The first two are deep-water features, the third is a shallow-water feature. The hydrodynamic processes involved in the formation of the above-mentioned SAR observed phenomena are described with the appropriate equations in the following sections.

Deep water internal waves have been studied by Apel *et al.* (1983), and they conclude that the solitary waves in the Sulu Sea are generated as a result of intense tidal flow over sharp, narrow bathymetric features. Surface signatures of these waves have been observed in images from the DMSP, Landsat, Nimbus-7 and SIR-A satellites. Legeckis (1978) has reported a survey of satellite images that show temperature fronts associated with ocean currents and upwelling at a wide variety of locations around the world. When the long surface wave field crosses an abrupt change in water depth, the wave energy can be trapped due to wave-wave interaction, as shown by Longuet-Higgins (1967). The occurrence of such "edge waves" in the shoal region was observed at Macquarie Island in the Southern Ocean.

3.2 Internal Waves Over the Wyville-Thomson Ridge

Figure 9 shows the Seasat SAR imagery of deep water features over the Wyville-Thomson Ridge collected during Revolution 762 on 19 August 1978 at approximately 06:45 GMT. Figure 10 combines line drawings of internal waves and a frontal boundary observed in Figure 9 with the corresponding bathymetric chart for this area. From Figure 10, it can be seen that there are numerous internal wave signatures. The internal waves in the middle of the image appear to be generated over the Wyville-Thomson Ridge. Near the lower right corner of the image, three wave packets are visible. It is to be noted that no waves were generated on the north side of the ridge.

The dominant bottom features are a broad, saddle-like valley on the East side of the ridge, and a 90° sector of deep water extending out from the ridge, as shown in Figure 11. The ridge has the characteristic scales of approximately 10 km in both the longitudinal and transverse direction. The minimax of the bathymetric saddle is at a depth of about 450 m.

Based on the bathymetry, it seems that the wave packets are produced by lee wave formation--a mechanism similar to the undulation of the jet stream as it passes over a mountain ridge. Figure 12 schematically illustrates the stages that are hypothesized during the production of solitary internal wave packets. As the strong semidiurnal tidal current flows north into the Faeroe Bank Channel, an internal lee wave forms on the northern edge of the ridge. As the tidal flow goes to zero six hours later, the lee wave, trying to maintain its group velocity relative to the current, escapes south over the ridge barrier back into the deep water, emerging as a packet of solitary waves. This phenomenon has previously been studied by Holbrook et al. (1983) in the Sulu Sea. The initial waveform then can be viewed as a localized source that immediately begins to propagate, and evolves into a series of solitary waves while undergoing radial spreading, encountering variable topography and slowly losing energy through dissipation. The disappearance of internal waves on the north side of the ridge is probably because there is no strong tidal current flowing south across the ridge; most of the tidal current may flow along the Faeroe Bank Channel.

Figure 9. Seasat SAR Imagery of Deep Water Features Over the Wyville-Thomson Ridge. Revolution 762, from ERIM.

B-34
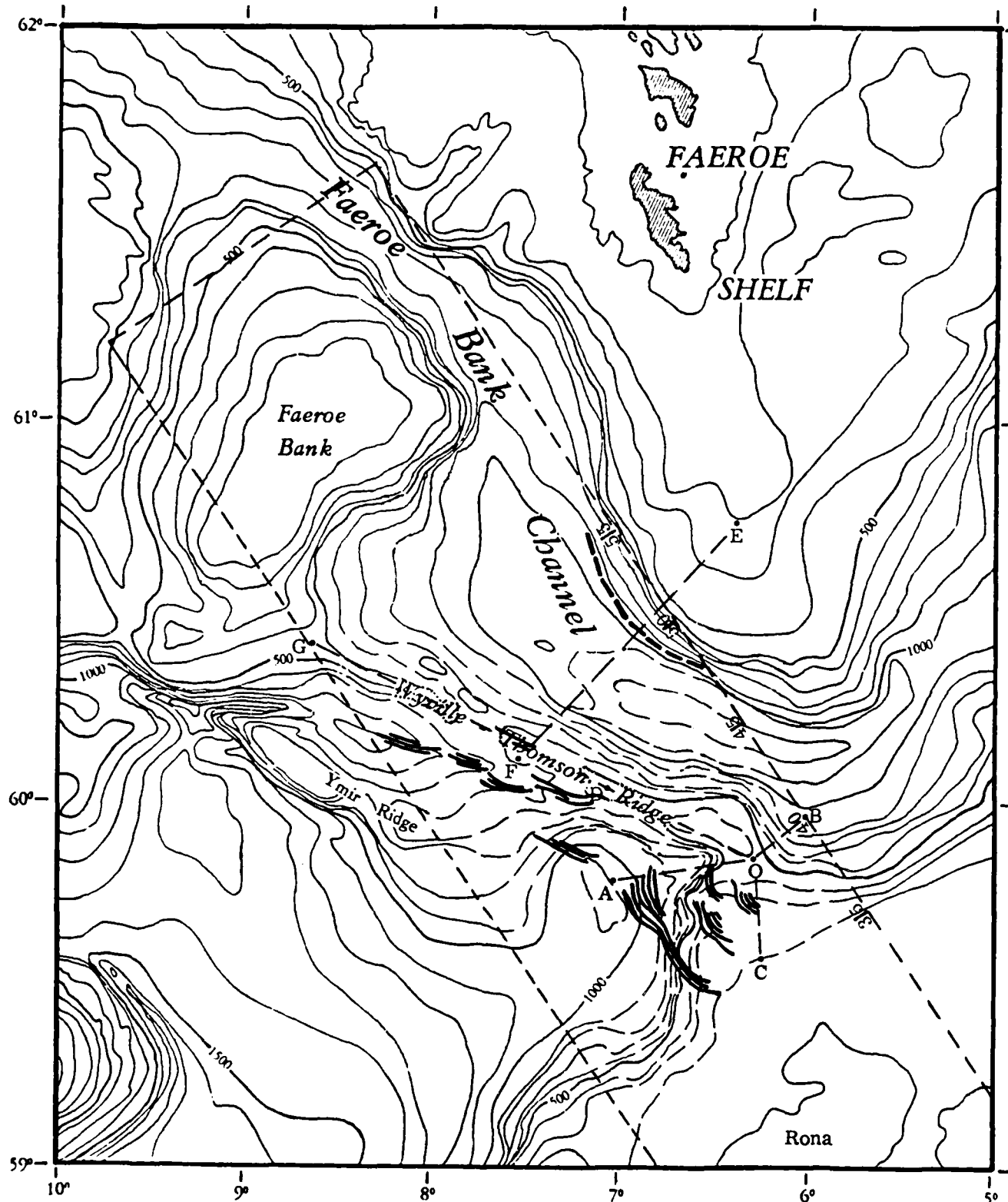
Figure 10. Line Drawings of Internal Waves and a Frontal Boundary Observed in Figure 9 Superimposed on the Hydrographic Chart of the Northeast Atlantic Ocean.
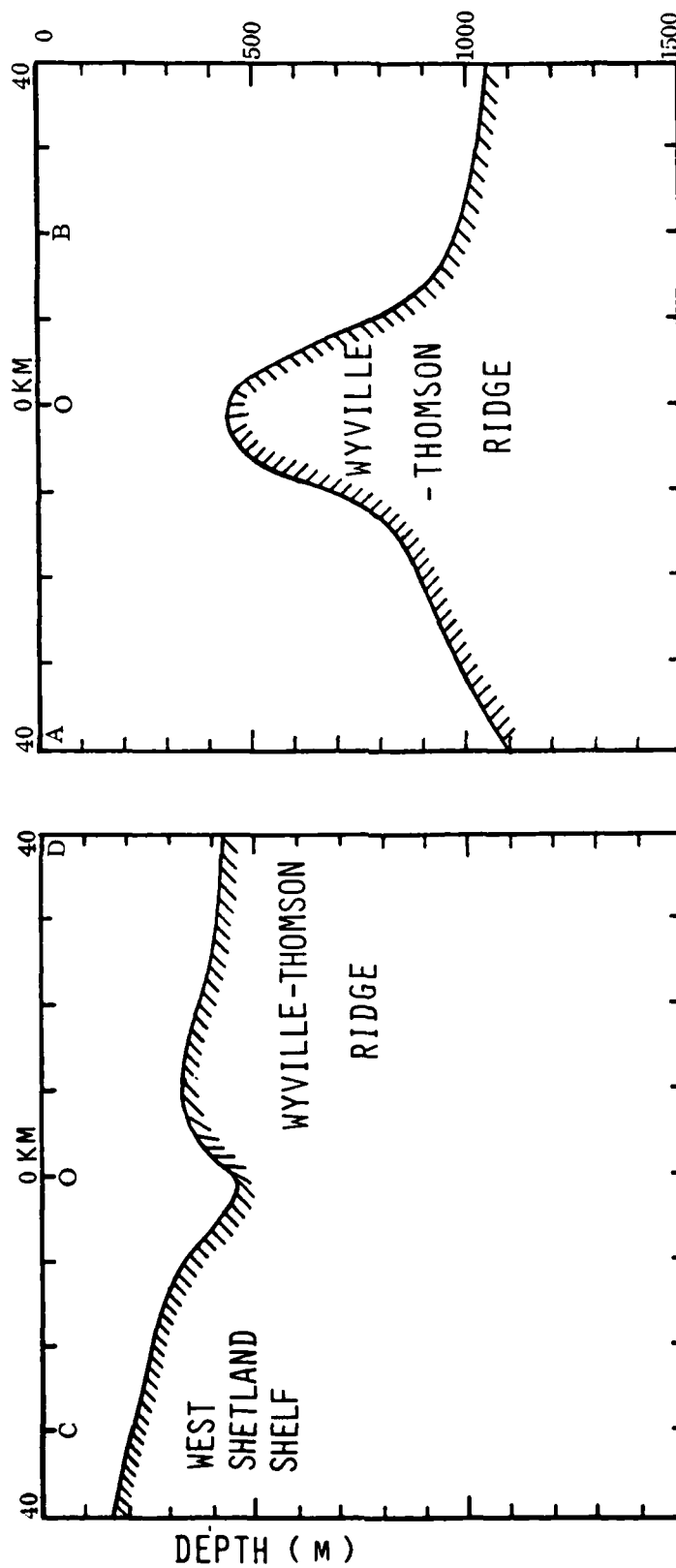
-27-

Figure 11. Longitudinal and Transverse Bathymetric Profiles Across Ridge, with a Saddle-like Valley at 0. Locations 1f Letters A, B, C, D and 0 are Indicated in Figure 10.
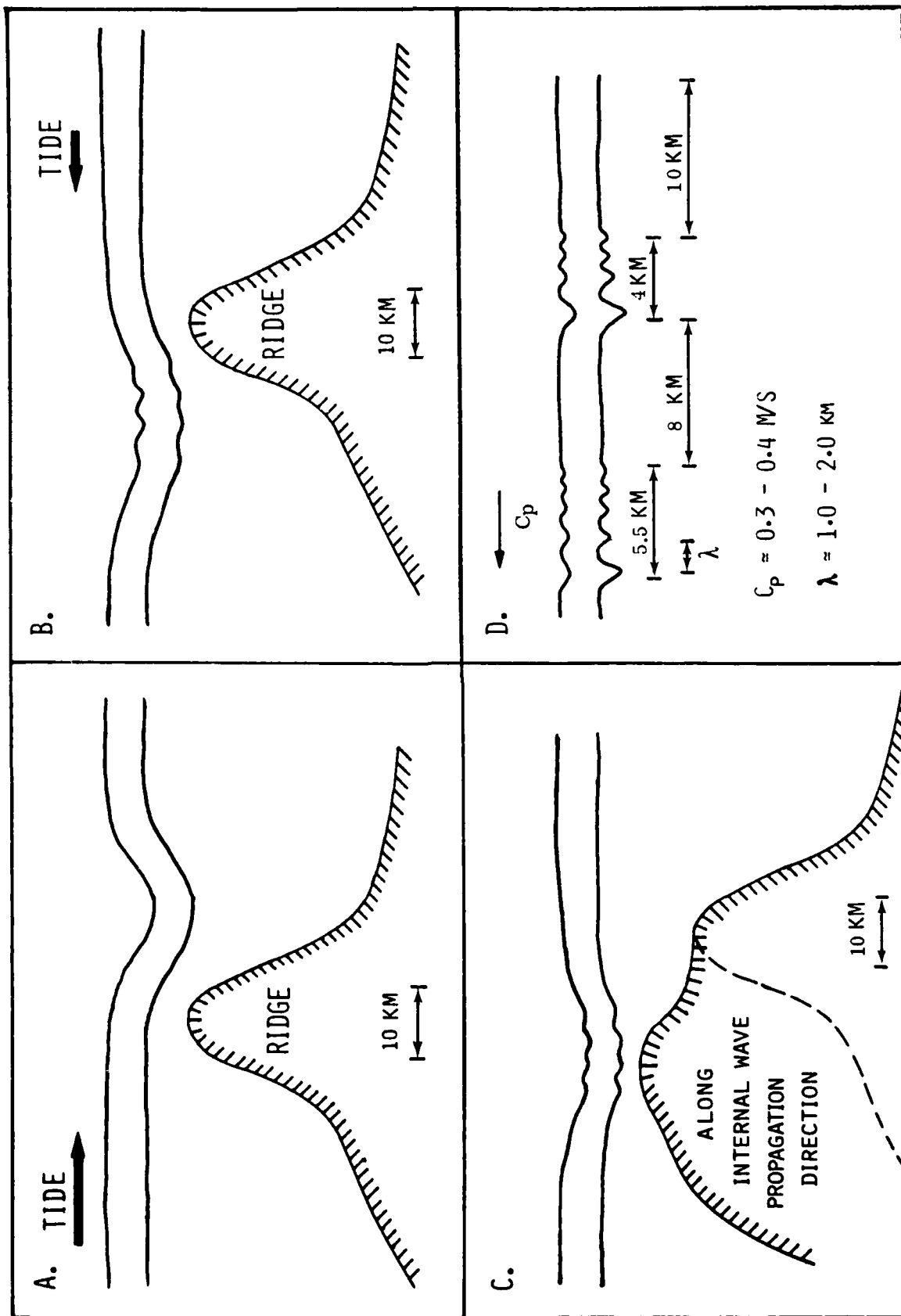
Figure 12. Schematic Diagram Summarizing the Generation and Evolution of an Internal Wave Packet Over the Wyville-Thomson Ridge.

Based on the Seasat SAR image, wave packets in deep water over the Wyville-Thomson Ridge have the following properties:

1. Wave packets are separated by distances of the order of 14 km.

2. Wave speed is estimated to be 0.31 m/s based on the assumption of a semidiurnal tidal origin.

3. Wave packets in this region contain about five waves with packet width about 5 km.

4. Wavelengths are between 500 m and 1000 m.

5. The crests are curved in a horizontal plane with their convex sides pointed in the direction of propagation.

Although no *in situ* measurements are available, it is believed this area is dominated by tidal currents with velocities of less than 0.5 m/s at the surface. Figure 13 shows the profiles of potential temperature, salinity and sigma theta generated from data collected over the Iceland-Faeroe Rise during the Atlantic Expedition in August 1972 (Bainbridge, 1980). Station 19 is expected to be the measurement closest to the Wyville-Thomson Ridge area. As evident from Figure 13, a mixed layer of 40 m is dominant in this area during the summer. Based on the two-layer finite depth model, the linear wave speed is given by

$$C_o \simeq \left[\frac{\Delta\rho}{\rho} \frac{g}{k} \frac{1}{\coth kH_1 + \coth kH_2} \right]^{1/2} . \tag{3.1}$$

Near the Wyville-Thomson Ridge, $\Delta\rho/\rho \simeq 0.6 \times 10^{-3}$, $H_1 \simeq 40$ m, $H_2 \simeq 260$ m, $2\pi/k \simeq 500$ m, and thus the wave speed is approximately 0.40 m/s, depending on the water depths. This value is consistent with the estimated wave speed of 0.31 m/s from the SAR image. Based on the wavelength, the wave amplitude is estimated to be between 10 to 15 m. Note that the effect of shear is important in this case, since the wave speed is slow compared with the background current. Also, the bottom topography near the Shelf West is
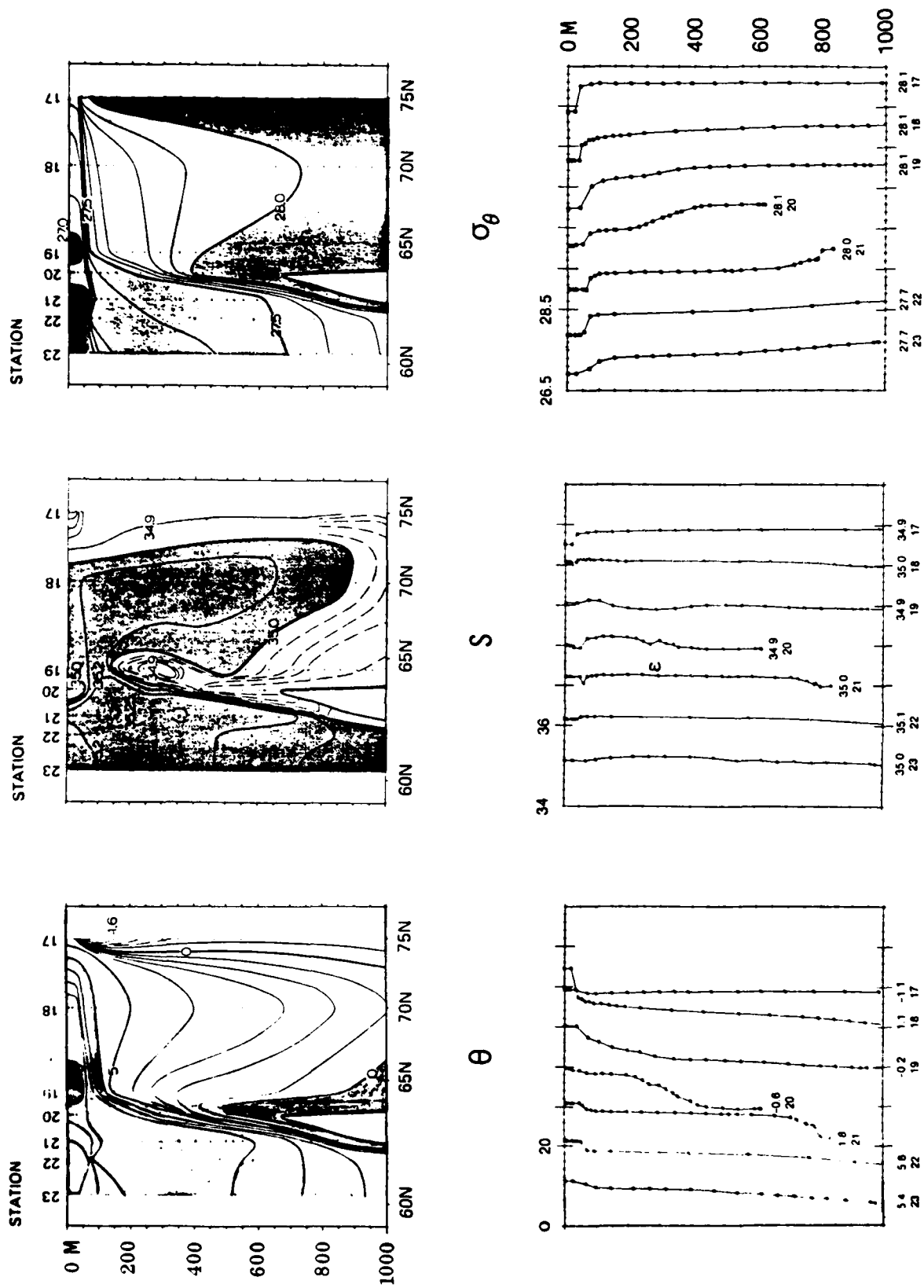
Figure 13. Profiles of Potential Temperature, Salinity and Sigma Theta from Data Collected Over the Icelandic-Faeroe Rise. From Bainbridge (1980).

complex, which influences the evolution of wave packets, as shown in Figure 10. A similar solitary wave theory developed by Liu *et al.* (1983) can be applied here. However, due to the limited scope of this investigation, the detailed analysis and calculations will have to wait until sea-truth data are available.

To understand the surface pattern caused by the internal wavefield, the essential physics element is the interaction between the internal wave-induced surface current field and the wind-driven ocean surface gravity and capillary waves. As discussed in Section 2, the wind wave modulation can be estimated by a spectral transport model. Such surface effects result in a SAR-detected surface pattern similar to that produced by the shallow-water internal waves.

3.3 Frontal Boundary Over the Faeroe Bank Channel

The cold front that forms the boundary between the two layer system on the off-shore side and the vertically-mixed water inshore has been observed on Seasat SAR images of the Faeroe Bank Channel. The curved, dark line beginning at 48 and continuing to 55, as indicated in Figure 10, is believed to be a surface pattern caused by a frontal boundary. Its location appears to be over the edge of the Faeroe Shelf, and closely matches the 900 meter bottom contour.

As shown in Figure 13, the deep water upwelling results in a frontal boundary over the Icelandic-Faeroe Rise. The relationship of the front to local upwelling topographic mixing may be described by the following process. Figure 14 shows the cross-section diagram of bottom topography of the Wyville-Thomson Ridge. It appears that the tidal current flowing over the ridge through another saddle-like valley on the West-side of the ridge forces the deep water isotherms up toward the surface. To illustrate this mechanism for frontal boundary generation, a schematic diagram of deep water upwelling over the Faeroe Bank Channel is shown in Figure 15. Therefore, the frontal boundary seems to represent simply a surface intersection of the seasonal thermocline. The combination of frontal slope and current
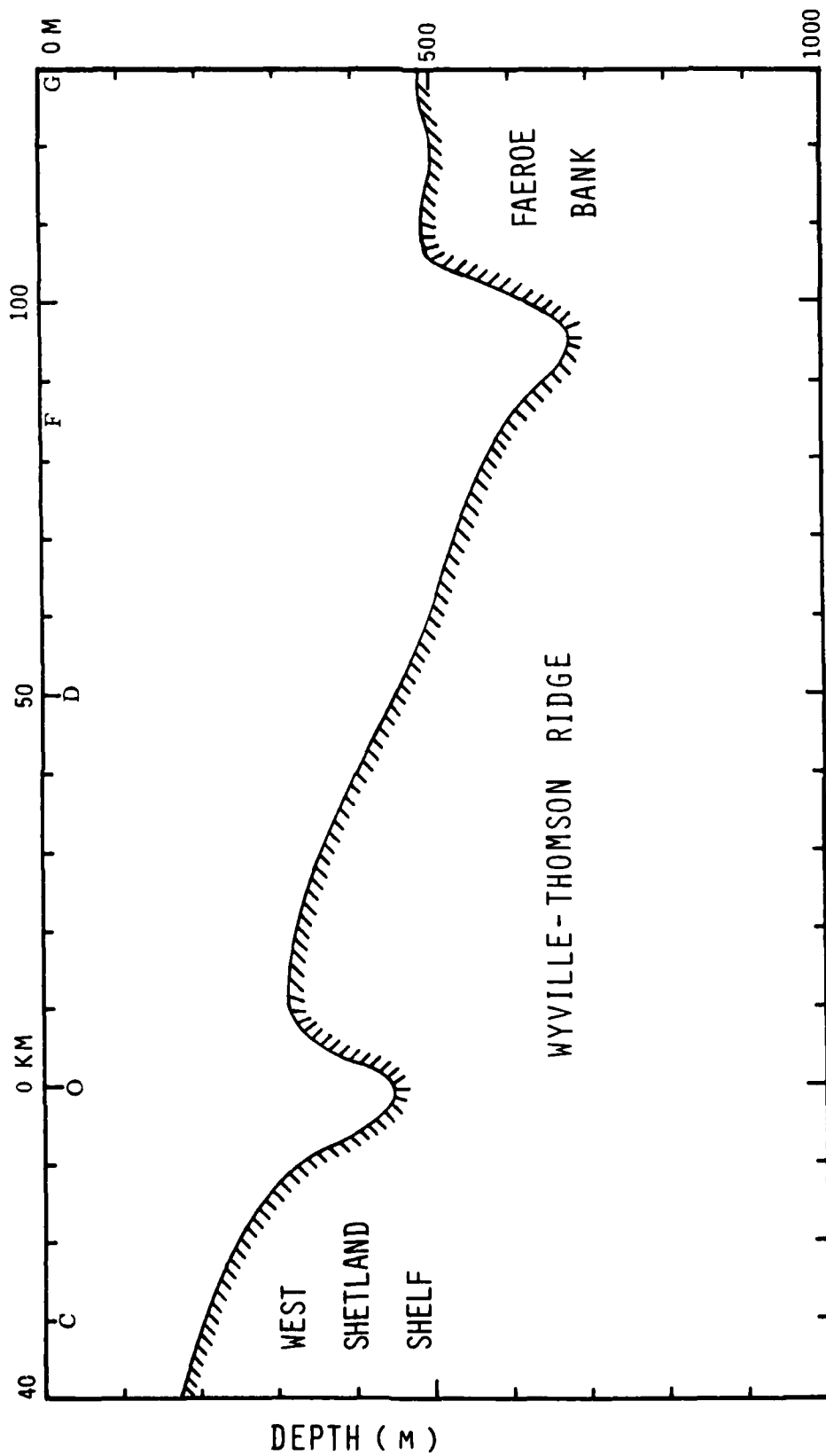
-32-

Figure 14. Cross-section Diagram of Bottom Topography of the Wyville-Thomson Ridge.
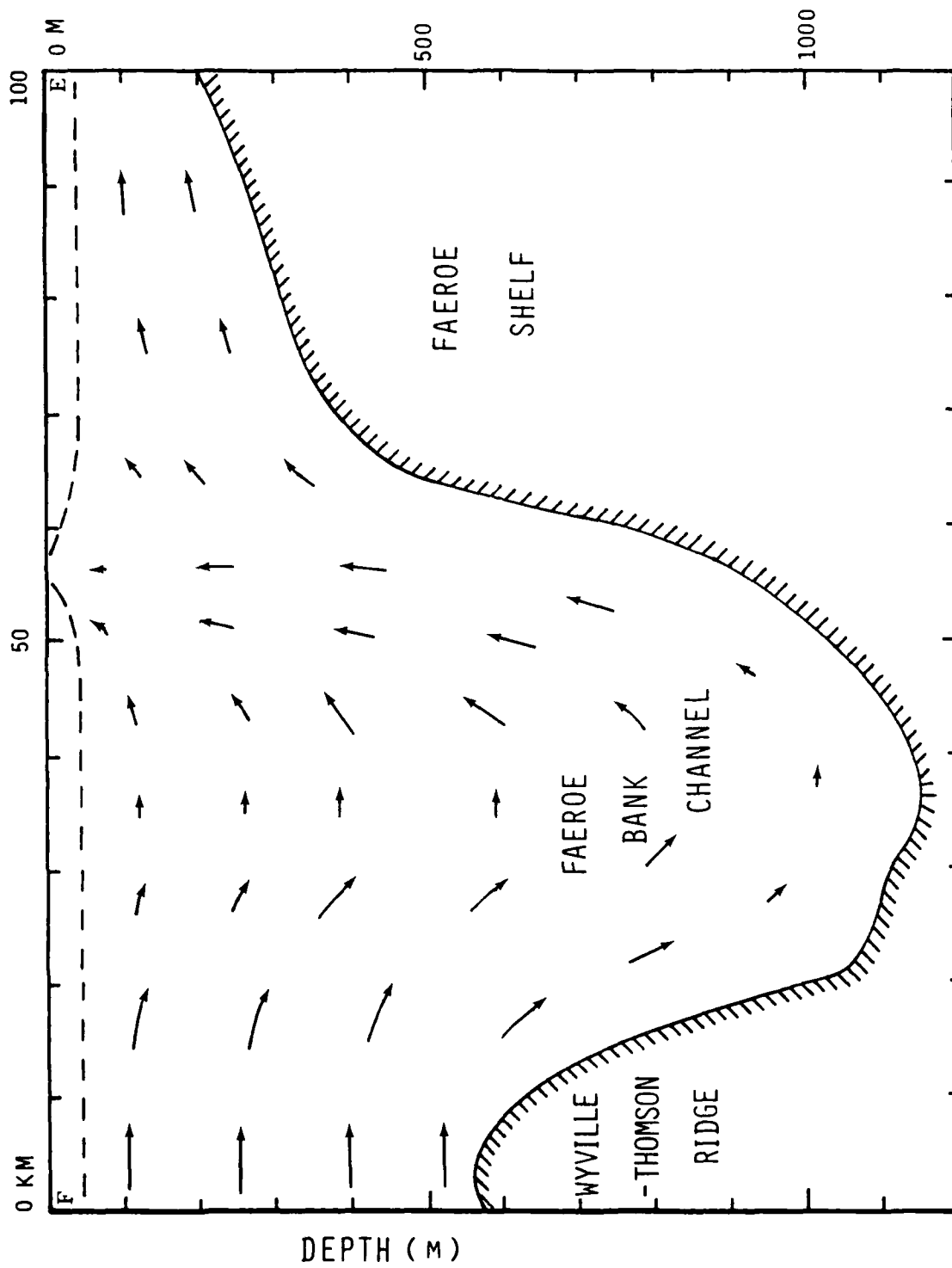
Figure 15. Schematic Diagram Illustrating Deep Water Upwelling over the Faeroe·Bank Channel.

-34-

B-42

shear could yield information on density contrast across the front. The formulation of this upwelling problem is given in Appendix A for reference. The detailed numerical modeling and quantitative estimates are beyond the scope of this investigation, awaiting further study.

The radar imaging mechanism for a frontal boundary is not totally understood at the present time. The surface current field associated with the front is caused by the coastal upwelling, as well as the surface temperature gradient. The effects of such surface currents will perturb the wind wave structure through current-wave interaction. The radar detects these subtle changes in backscatter, thus giving a SAR-detected surface pattern.

3.4 Change in Backscatter Around North Rona Rock

North Rona Rock is an island located approximately 75 km off the northeast tip of Scotland. Figure 16 shows the Seasat SAR imagery and hydrographic chart of North Rona Rock collected during Revolution 762. Detected on this SAR image is a distinct change in radar backscatter in the shoal region designated by the 50 meter depth contour surrounding North Rona Rock. On the SAR imagery, the surface long wave field is also clearly visible. Surfac measurements made concurrently with the Seasat overpass about 300 km west of North Rona Rock indicate that a swell with a dominant wavelength of 210 m, a significant wave height of 5.5 m, and a direction of propagation towards 60° was present in the northeast Atlantic Ocean at this time. A wind from 186° with a surface velocity of 12 m/s was also present. The diffraction of the surface long waves as they pass North Rona Rock can also be seen in Figure 16.

The processes that generate the variations in Bragg scattering observed in the Seasat SAR image most likely involve a combination of modifications of Bragg scattering waves due to tidal flow over topography, current generated by the impingement and refraction of swell and long waves on the shoal, and combined effects. It has been shown by Longuet-Higgins (1967) that islands can trap long-wave energy and this phenomenon was observed at Macquarie

Island in the Southern Ocean. The probable existence of such "edge waves" in the shoal region surrounding North Rona Rock may cause the change in backscatter. Some light can be thrown on the phenomenon of wave trapping by considering the simplest possible case: that of long free waves around a circular sill in shallow water, as shown in Figure 17a. The solution of wavefield is illustrated in Figure 17b, which shows the plan view of the wave crests. Two systems of waves propagate along trajectories inside and outside the sill. In general, the trapping of the energy is essentially due to the waves being reflected internally at the edge of the sill, when their angle of incidence is greater than a critical angle. The brief analysis for this special case is reviewed in Appendix B for reference. This theory seems to explain the SAR-observed pattern, but remains to be directly verified by an *in situ* field measurement.

In general, wave-wave interaction could generate higher harmonic waves which could be trapped around an island. Wave-current interaction could produce wave breaking caused by the blockage phenomenon (Phillips, 1977). A recent paper of Larsen (1980) suggests that wavelets may be trapped in the current field over topography, even when the wave group velocity does not match current speed (non-resonant condition). These mechanisms, if they occur, would enhance the trapping phenomenon and, in turn, the change in backscatter.

As mentioned previously, imaging radars are sensitive to the short Bragg waves. But the trapped waves around an island are generally much longer than the Bragg scattering waves. Short waves riding on long waves are strained by the long waves, and this leads to energy exchange between long and short waves. This long-short wave interaction will modulate the Bragg wave structure, which may result in a SAR-detected surface pattern. The combined effects on modulations of Bragg waves from tidal flow over the sill in the shoal region and the long-short wave interaction seems to be a plausible explanation for the change in backscatter around the North Rona Rock.
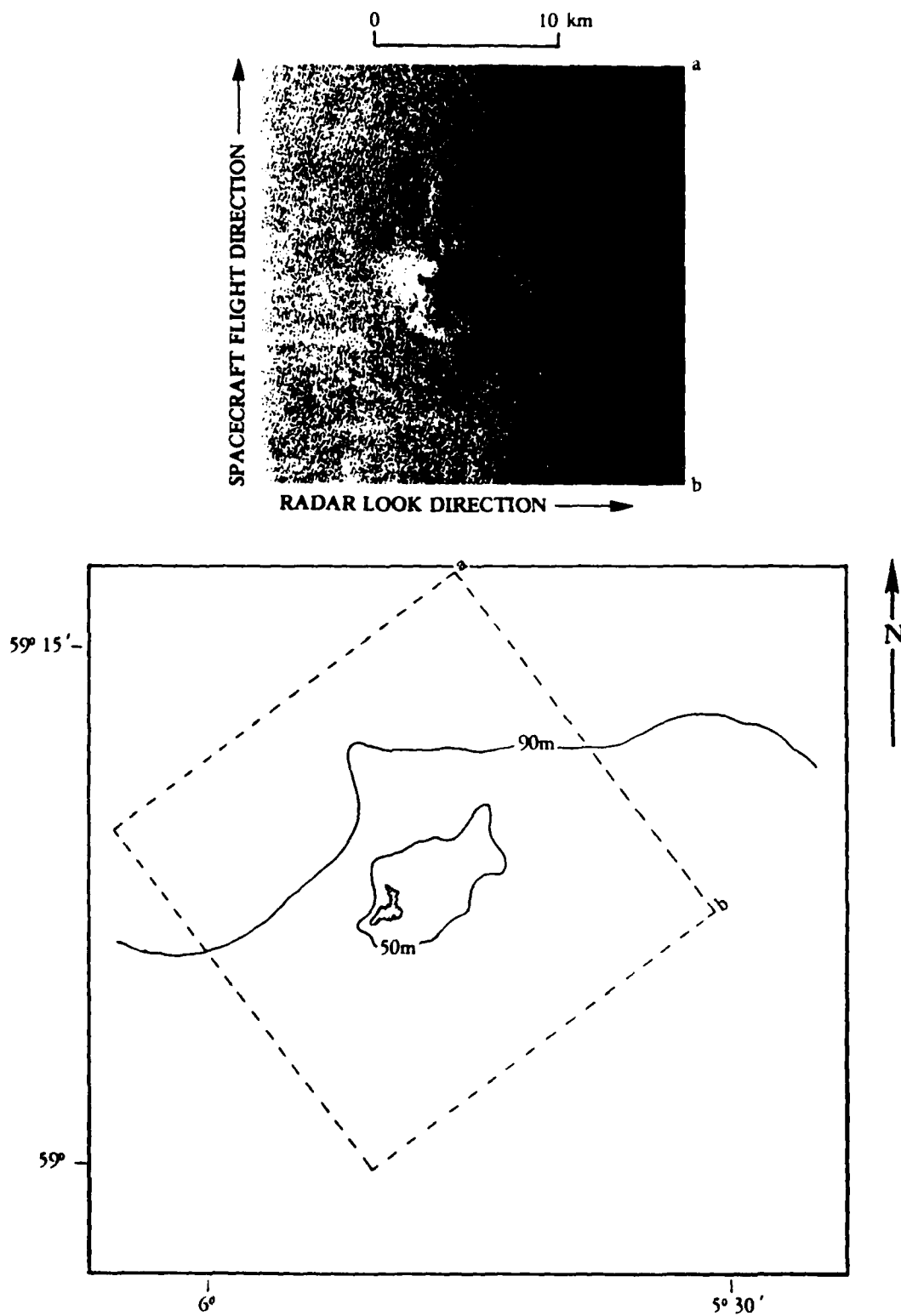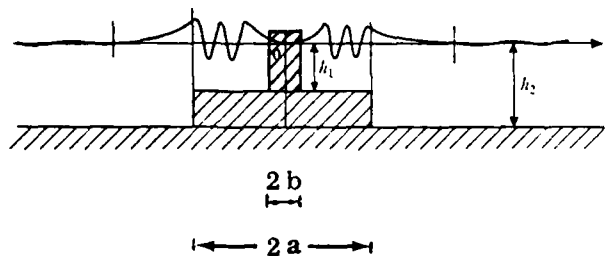
Figure 16. Seasat SAR Imagery and Hydrographic Chart of North Rona Rock. Revolution 762, from ERIM.
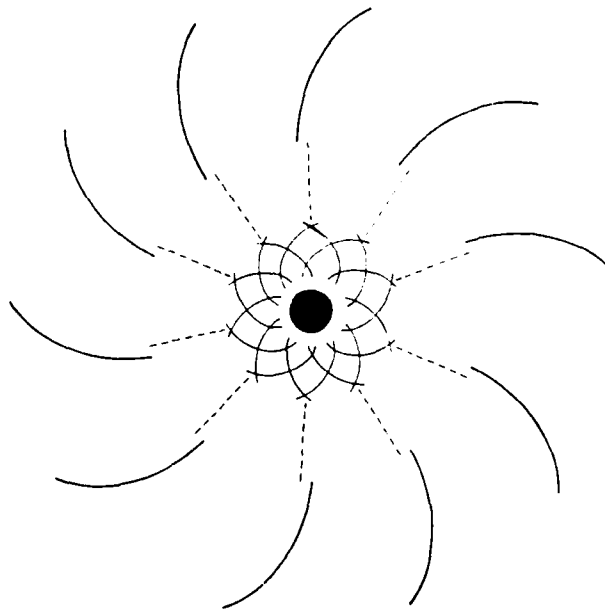
B-45

-37-

(A)

(B)

Figure 17. The Form of Free Waves Trapped by a Circular Island With Sill. (a) A Radial Cross Section; (b) Plan View of the Wave Crests. From Longuet-Higgins (1967).

4.   SUMMARY AND DISCUSSION

This report presents an analytical investigation of the oceanic processes involved in the bottom-related surface signatures observed on the Seasat SAR imagery. Under sponsorship of the DMA, ERIM is currently investigating the potential ability of SAR to provide a rapid survey capability to detect and locate geographically submerged features potentially hazardous to navigation, as well as to provide estimates of water depth. Based on their preliminary investigation, ERIM suggested the data sets for further hydrodynamic analyses. Two sets of data from Seasat orbits during Revolutions 974 and 762 were used to examine the relationship between the bottom features and surface patterns. These SAR-observed patterns occurred in both the shallow, coastal regions, as well as in deep water offshore. For both, the hydrodynamic processes are analyzed in detail to better understand the causes of surface signatures that map bottom features.

Shallow water internal waves on the East Coast and New York Bight appear to be generated at the edge of the continental shelf by shear flow instability at the bottom of the mixed layer. Then, the wave packet propagates up onto the shelf until the mixed layer almost intersects the bottom. The SAR-observed features suggest that these internal waves in each packet are probably rank-ordered solitary waves. Based on a two-layer solitary wave theory and the Seasat SAR image data (Revolution 974), the internal wave field has been constructed. The wind wave modulation induced by the internal waves is formulated by using a spectral transport model. The surface roughness modulation is estimated for different wind and radar operation conditions. The numerically simulated Seasat SAR image shows good visibility of the internal waves, and demonstrates the capability to provide a first order description of the observations.

It is to be noted that the solitary wave theory used in this report is limited to a two-dimensional inviscid fluid without spreading and dissipation. As demonstrated by Liu *et al.* (1983), radial spreading and dissipation effects are important for the internal wave evolution. Also, the effect of shear is important for the calculation of the wave speed and waveform, as shown by Liu and Benney (1980). Therefore, without *in situ* field measurements of environmental conditions, the estimates of surface roughness modulation in the second section are only expected to give order-of-magnitude accuracy.

An alternative mechanism for producing surface effects would be surface films concentrated in current-convergence regions damping the local Bragg waves and hence reducing SAR image intensity. In current-divergence regions the dispersal of surface films would allow higher energy density Bragg waves and hence image enhancement. However, the slicks do not propagate with the internal waves and, unlike the wind waves, may not exist everywhere in the ocean. Therefore, it is felt that the wind wave modulation induced by surface current is probably the dominant mechanism for surface effects. Combination of both mechanisms will definitely enhance the visibility of a surface pattern in SAR images. Nevertheless, at present, the quantitative estimations of both mechanisms are not completely available, awaiting further research.

Three selected features in the northeast Atlantic test site on the Seasat SAR imagery for Revolution 762 have been examined carefully. Deep water internal waves over the Wyville-Thomson Ridge appear to be produced by lee wave formation near a saddle-like valley on the East side of the ridge. A frontal boundary over the Faeroe Bank Channel seems to be generated by deep-water upwelling. The tidal current flowing over the Wyville-Thomson Ridge through another saddle-like valley on the West side of the ridge forces the deep water isotherms up toward the surface. Therefore, the frontal boundary may simply represent a surface intersection of the seasonal thermocline. The change in backscatter around North Rona Rock is probably caused by the trapping of wave energy around the island. The existence of such "edge waves" in the shoal region surrounding North Rona Rock may explain the SAR-observed surface pattern.

In this study, the water depth is related to the SAR observed surface patterns in several ways. For shallow water internal waves on the East Coast and New York Bight, the wave packets are created at the continental shelf edge. Therefore, the location of the first packet seaward is at a water depth of approximately 100 meters. Also, the wave packet disappears at the water depth of 50 to 60 meters. For deep water internal waves, a saddle-like valley on the Wyville-Thomson Ridge can be identified based on the estimated source location of wave packets. The frontal boundary over the Faeroe Bank Channel matches closely the 900 meter bottom contour. The distinct change in radar backscatter in the shoal region is designated by the 50 meter depth contour surrounding North Rona Rock.

This study has demonstrated that these surface patterns can be used for inference about bathymetry and submerged features. Quantitative predictions of SAR-observed phenomena seem to be possible, especially when supported by adequate environmental data (e.g., wind speed and direction), and much of that might also be obtainable remotely. The results of this study lend support to the intended goal of doing the "inverse problem": namely, given remote sensing data, quantify subsurface topography. Therefore, SAR imaging is a powerful technique for high spatial resolution observation under all weather conditions of geographical regions of concern. What is needed is verification of the relationship between oceanic processes and remote sensing imagery, and testing the interpretation of such relationships in research applications and surveys. The following efforts are recommended:

1. Improve the hydrodynamic model by considering the three-dimensional effect and dissipation effect.

2. Estimate the surface roughness modulation based on the spectral transport model to provide a first order description of surface signatures, and limitations of using SAR data.

3. Make detailed quantitative comparisons between the theoretical predictions and SAR observations for some specific case studies.

4. Refine the hydrodynamic transfer function model by comparison with SAR data and other *in situ* field measurements.

5. Apply/modify the model developed above for parametric study and field test planning with various environmental conditions (wind/sea state, stratification, shear) and radar operation conditions (look angle, incidence angle).

This list is still preliminary, and we hope some additional studies will be reported in the near future.

REFERENCES

Allen, J.S., 1973, *"Upwelling and Coastal Jets in a Continuously Stratified Ocean,"* J. Phys. Oceanogr., 3, 245-257.

Alpers, W. and Salusti, E., 1983, *"Scylla and Charybdis Observed From Space,"* J. Geophys. Res., 88, 1800-1808.

Apel, J.R., 1980, *"Satellite Sensing of Ocean Surface Dynamics,"* Annual Review Earth and Planetary Sciences, 8, 303-342.

Apel, J.R., 1981, *"Nonlinear Features of Internal Waves as Derived From the Seasat Imaging Radar,"* in Oceanography From Space, edited by J.F.R. Gower, pp. 525-533, Plenum, New York.

Apel, J.R., Byrne, H.M., Proni, J.R. and Charnell, R.L., 1975, *Observations of Oceanic Internal and Surface Waves From the Earth Resources Technology Satellite,"* J. Geophys. Res., 80, 865-881.

Apel, J.R., Byrne, H.M., Proni, J.R. and Sellers, R.L., 1976, *"A Study of Oceanic Internal Waves Using Satellite Imagery and Ship Data,"* Remote Sensing Environ., 5, 125-135.

Apel, J.R., Holbrook, J.R., 1983, *"The Sulu Sea Internal Soliton Experiment, Part A: Overview and Satellite Data,"* J. Phys. Oceanogr., to appear.

Bainbridge, A.E., 1980, *"Geosecs Atlantic Expedition - Volume 2: Sections and Profiles,"* U.S. Government Printing Office, Washington, D.C., 198 pp.

Beal, R.C., Deleonibus, P. and Katz, I., 1981, Spaceborne Synthetic Aperture Radar for Oceanography, Johns Hopkins Press, Baltimore, Md., 213 pp.

Benjamin, T.B., 1966, *"Internal Waves of Finite Amplitude and Permanent Form,"* J. Fluid Mech., 25, 241-270.

Benney, D.J., 1966, *"Long Non-Linear Waves in Fluid Flows,"* J. Math. and Physics, 45, 52-63.

Fu, L.-L. and Holt, B., 1982, *"SEASAT Views Oceans and Sea Ice With Synthetic Aperture Radar,"* JPL Publication 81-120, Jet Propulsion Laboratory, Pasadena, CA, 200 pp.

Giese, G.S., Hollander, R.B., Fancher, J.E. and Giese, B.S., 1982, *"Evidence of Coastal Seiche Excitation by Tide-Generated Internal Solitary Waves,"* Geophys. Res. Letters, 9, 1305-1308.

Halpern, D., 1971, *"Semidiurnal Internal Tides in Massachusetts Bay,"* J. Geophys. Res., 76, 6573-6584.

Holbrook, J.R., Apel, J.R. and Tsai, J., 1983, *"The Sulu Sea Internal Soliton Experiment, Part B: Observations and Analysis,"* J. Phys. Oceanogr., to appear.

Hughes, B.A., 1978, *"The Effect of Internal Waves on Surface Wind Waves: 2. Theoretical Analysis,"* J. Geophys. Res., 83, 455-465.

Hughes, B.A. and Gower, J.F.R., 1983, *"SAR Imagery and Surface Truth Comparisons of Internal Waves in Georgia Strait, British Columbia, Canada,"* J. Geophys. Res., 88, 1809-1824.

Inoue, T., 1966, *"On the Growth of the Spectrum of a Wind Generated Sea According to a Modified Miles-Phillips Mechanism,"* New York University Geophys. Sciences Lab. Report No. TR 66-6.

Kasischke, E.S., Lyzenga, D.R., Shuchman, R.A., Tseng, Y.S., Termaat, B.S., Burns, B.A. and Meadows, G.A., 1982, *"The Use of Synthetic Aperture Radar to Detect and Chart Submerged Navigation Hazards,"* ERIM FInal Report No. 155200-1-F, Ann Arbor, MI, 221 pp.

Larsen, L.H., 1980, *"Modulation Solitons in Inhomogeneous Media,"* Phys. Fluids, 23, 2359-2361.

Legeckis, R., 1978, *"A Survey of Worldwide Sea Surface Temperature Fronts Detected by Environmental Satellites,"* J. Geophys. Res., 83, 4501-4529.

Lewis, J.E., Lake, B.M. and Ko, D.R.S., 1974, *"On the Interaction of Internal Waves and Surface Gravity Waves,"* J. Fluid Mech., 63, 773-800.

Liu, A.K., Apel, J.R. and Holbrook, J.R., 1983, *"The Sulu Sea Internal Soliton Experiment, Part C: Comparisons with Theory,"* J. Phys. Oceanogr., to appear.

Liu, A.K. and Benney, D.J., 1981, *"The Evolution of Nonlinear Wave Trains in Stratified Flows,"* Studies in Applied Math., 64, 247-269.

Longuet-Higgins, M.S., 1967, *"On the Trapping of Wave Energy Around Islands,"* J. Fluid Mech., 29, 781-821.

Mayer, D.A., Hansen, D.V. and Ortman, D.A., 1979, *"Long-Term Current and Tempertaure Observations on the Middle Atlantic Shelf,"* J. Geophys. Res., 84, 1776-1792.

Osborne, A.R. and Burch, T.L., 1980, *"Internal Solitons in the Andaman Sea,"* Science, 208, 451-460.

Pedlosky, J., 1974, *"Longshore Currents, Upwelling and Bottom Topography,"* J. Phys. Oceanogr., 4, 214-226.

Pedlosky, J., 1978, *"An Inertial Model of Steady Coastal Upwelling,"* J. Phys. Oceanogr., 8, 171-177.

Phillips, O.M., 1977, The Dynamics of the Upper Ocean, 2nd Edition, Cambridge University Press, New York, N.Y., 336 pp.

Pierson, W.J., Jr. and Stacy, R.A., 1973, *"The Evaluation, Slope and Curvature Spectra of a Wind Roughened Sea Surface,"* NASA CR-2247.

Proni, J.R. and Apel, J.R., 1975, *"On the Use of High-Frequency Acoustics for the Study of Internal Waves and Microstructure,"* J. Geophys. Res., 80, 1147-1151.

Shuchman, R.A., 1982, *"Quantification of SAR Signatures of Shallow Water Ocean Topography,"* University of Mich., PhD Dissertation, Ann Arbor, MI, 130 pp.

Trask, R.P. and Briscoe, M.G., 1983, *"Detection of Massachusetts Bay Internal Waves by the Synthetic Aperture Radar on SEASAT,"* J. Geophys. Res., 88, 1789-1799.

Tsai, J. and Apel, J.R., 1979, *"Tidally Induced Shear Flow Instability as a Source of Internal Waves on the Continental Shelf,"* NOAA Pacific Marine Environ. Lab. Contrib. No. 415.

Valenzuela, G.R., 1978, *"Theories for the Interaction of Electromagnetic and Oceanic Waves - A Review,"* Boundary Layer Meteorology, 13, 61-85.

Vesecky, J.F. and Stewart, R.H., 1982, *"The Observation of Ocean Surface Phenomena Using Imagery From the SEASAT Synthetic Aperture Radar: An Assessment,"* J. Geophys. Res., 87, 3397-3430.

Whitham, G.B., 1974, Linear and Nonlinear Waves, John Wiley and Sons, New York, 636 pp.

APPENDIX A: FORMULATION OF COASTAL UPWELLING

Analytical models which attempt to model the seasonal upwelling structure have been studied by Allen (1973) and Pedlosky (1974,1978). Usually, these models depend heavily on both a linearization of the momentum and thermal equations and a very crude parameterization of the turbulent mixing of heat and momentum. These assumptions lead to conceptually useful descriptions of the circulation. In this Appendix, the appropriate governing equations for the coastal upwelling problem over the Faeroe Bank Channel is outlined for the sake of reference. Further quantitative estimates will require numerical modeling and computations.

For an incompressible fluid with the Boussinesq approximation and small aspect ratio, i.e., depth is much smaller than the characteristic horizontal scale, the momentum equations are

$$\frac{\partial u}{\partial t} + \underset{\sim}{u} \cdot \nabla u - fv = - \frac{1}{\rho_0} \frac{\partial P}{\partial x} + \frac{\partial}{\partial z} \left[k_m \frac{\partial u}{\partial z} \right] \quad , \tag{A.1}$$

$$\frac{\partial v}{\partial t} + \underset{\sim}{u} \cdot \nabla v + fu = - \frac{1}{\rho_0} \frac{\partial P}{\partial y} + \frac{\partial}{\partial z} \left[k_m \frac{\partial v}{\partial z} \right] \quad , \tag{A.2}$$

$$0 = - \frac{\partial P}{\partial z} + \rho g \quad , \tag{A.3}$$

where u, v, w are velocity components, P is pressure, ρ is density, f is the Coriolis parameter, and k_m is the eddy viscosity. The continuity equation is

$$\frac{\partial u}{\partial x} + \frac{\partial v}{\partial y} + \frac{\partial w}{\partial z} = 0 \quad . \tag{A.4}$$

For a fluid where effects of compressibilty are minor, the simple state relation

$$\rho = \rho_0 \left[1 - \alpha(T - T_0) \right] \quad , \tag{A.5}$$

(A-1)

B-54

is often adequate, where α is the coefficient of thermal expansion. In this case, the heat equation takes the form

$$\frac{\partial T}{\partial t} + \underset{\sim}{u} \cdot \nabla T = \frac{\partial}{\partial z} \left[k_h \frac{\partial T}{\partial z} \right] \; , \qquad\qquad (A.6)$$

where T is temperataure, and k_h is the eddy diffusivity.

The coastal upwelling is of the unsteady channel-flow type in which the vertical momentum equation reduces to the hydrostatic pressure relation, as shown in (A.3). The eddy viscosity/diffusivity is, of course, an imprecise concept because the value of the coefficients required are a poorly known function of scale, density stratification, and energy input at frequencies above the mean. This formulation nonetheless is useful when analogies can be found to provide guidance for estimating the coefficients.

For future numerical computations, the boundary conditions at the free surface and bottom boundary layer require modeling and matching. The channel flow across the computation boundaries will also need quantitative estimates from the field measurement.

APPENDIX B: TRAPPING OF WAVE ENERGY AROUND AN ISLAND

In this Appendix, the long free waves around a circular sill in shallow water is reviewed. The detailed analysis may be found in the paper by Longuet-Higgins (1967). Assuming that the free surface displacement $\zeta(x,y)$ is small compared to the water depth $h(x,y)$, the equation for ζ in shallow water is

$$\left(\nabla^2 - \frac{1}{gh}\frac{\partial^2}{\partial t^2}\right)\zeta + \frac{1}{h}\nabla h \cdot \nabla\zeta = 0 \quad . \tag{B.1}$$

A circular sill is represented by radius a with an island of radius b, as shown in Figure 17a. The general solution can be expressed by Bessel and Hankel functions,

$$\zeta = \exp\left[i(n\theta - \sigma t)\right] \times \begin{cases} A\,J_n(k_1 r) & ; \quad 0 < r < a \\ B\,H_n^{(1)}(k_2 r) & ; \quad\quad r > a \end{cases} \quad , \tag{B.2}$$

where

$$k_1 = \frac{\sigma}{(gh_1)^{1/2}} \quad , \qquad k_2 = \frac{\sigma}{(gh_2)^{1/2}} \quad , \tag{B.3}$$

and σ is the wave frequency, n is the azimuthal wavenumber.

The solution is illustrated in Figure 17b. Inside the sill the solution consists of two systems of waves propagating along straight trajectories tangent to the circle $k_1 r = n$. Outside the sill, the solution consists of waves propagating outwards, along straight trajectories all tangent to the circle $k_2 r = n$.

From the solution (B.2), it appears that there are three necessary conditions for the existence of trapped modes. First, the ray paths in the interior must make, with the normal at the sill, an angle greater than the critical angle. Hence

$$n > \frac{h_1}{h_2}(k_1 a) \quad . \tag{B.4}$$

(B-1)

Secondly, the outer critical circle must be sufficiently far from the edge of the sill. Thus

$$n \gg 1 + k_2 a . \tag{B.5}$$

Thirdly, the radius of the island must be smaller than the inner critical radius, so that its presence will have little effect on that particular mode. That is,

$$b < \frac{n}{k_1} . \tag{B.6}$$

In general, the trapping of the energy is essentially due to the waves being reflected internally at the edge of the sill, when their angle of incidence is greater than the critical angle. In more general forms of bottom topography, a sufficient condition for trapping of wave energy appears to be the existence of at least one continuous ray-path surrounding the island. However, the curvature of the ray-path must not be so great that appreciable energy is lost at the sharp corners by diffraction.

Around North Rona Rock, $h_1 \simeq 50$ m, $h_2 \simeq 100$ m, with an incoming wave of $2\pi/k_2 \simeq 210$ m, the wavelength over the sill $2\pi/k_1$ is about 150 m. It can be seen that, for the shoal region $a \simeq 1$ km, a fair degree of trapping is achieved only if the azimuthal wavenumber n is greater than about 30 based on Equations (B.4) and (B.5). Then, from Equation (B.6), the radius of the island should be less than 700 m, as observed. This theory seems to provide a reasonable explanation for the SAR observed surface pattern, but remains to be directly verified by an *in situ* field measurement.

(B-2)

APPENDIX C.   PAPERS PUBLISHED USING RESULTS OF
NRL-SPONSORED RESEARCH

1.   Kasischke, E.S. and D.R. Lyzenga, Remote Sensing of Oceanic
     Phenomena Pertinent to Hydrocarbon Resource Development,
     Proceedings of the International Symposium on Remote Sensing
     of Environment, Second Thematic Conference: Remote Sensing for
     Exploration Geology, Ann Arbor, MI, 1983.

2.   Kasischke, E.S., R.A. Shuchman, D.R. Lyzenga, and G.A.
     Meadows, Detection of Bottom Features on Seasat Synthetic
     Aperture Radar Imagery, "Photogrammetric Engineering and
     Remote Sensing, 49, pp. 1341-1353, 1983.

3.   Kasischke, E.S., Y.C. Tseng, and G.A. Meadows, Observations of
     Internal Waves and Frontal Boundaries on Seasat SAR Imagery
     Collected Over the Eastern North Atlantic Ocean, Proceedings
     of the Seventeenth International Symposium on Remote Sensing
     of Environment (in press), Ann Arbor, MI 1983.

REMOTE SENSING OF OCEANOGRAPHIC PARAMETERS

PERTINENT TO HYDROCARBON RESOURCE DEVELOPMENT*

Eric S. Kasischke
David R. Lyzenga

Radar Division
Environmental Research Institute of Michigan
Ann Arbor, Michigan 48107

ABSTRACT

Information obtained from remotely sensed imagery
which is potentially useful to hydrocarbon
resource development is discussed in this paper.
Oceanic phenomena presented include surface
gravity waves, detection of bathymetric features,
and deep ocean internal waves. Techniques used
to extract data are presented along with pertinent
examples.

1. INTRODUCTION

The main emphasis of the papers presented at this meeting has been on the processing and
analysis of remotely sensed data to aid in the detection of oil, gas and mineral deposits.
When the exploration geologist moves from a terrestrial to an off-shore environment, where much
of the world's exploration activities are occuring, remotely sensed data become less useful as
an exploration tool, but more useful in the design and deployment of structures and vessels
operating in oceanic regions. This paper discusses areas where remotely sensed data can be
useful in off-shore hydrocarbon resource development.

This paper focuses on three areas where remote sensing systems can provide important
information in near- and off-shore regions: measuring gravity waves, extracting bathymetric
information, and monitoring oceanic internal waves. The monitoring and classification of sea
ice, an important topic for those interested in off-shore operations in Arctic regions, is
reviewed in other papers presented at this meeting (see Lyden, et al., 1983; Tucker, 1983; and
Mercer, 1983). For an in-depth review of remote sensing for oceanography, the reader is
referred to Gower (1981).

Because of the authors' research interests, the emphasis in this paper will be on imagery
collected by synthetic aperture radars (SARs), with examples from other sensing systems when
appropriate. Because of their sensitivity to changes in the small-scale roughness on the ocean
surface (i.e., the capillary and ultra-gravity wave structure), which is strongly influenced by
many physical oceanic processes, SARs detect a wider variety of oceanic phenomena than any
other imaging spaceborne remote sensing system. The Seasat satellite experiment demonstrated
this capability (see Fu and Holt, 1982; or Beal, et al., 1981). With the number of planned and
proposed spaceborne SARs scheduled for launch during the late 1980's and early 1990's (i.e.,
ERS-1 [Japan], ERS-1 [ESA], SIR-B, SIR-C, SIR-D, Radarsat, MRSE, and SAR-FACILITY), an ever
increasing amount of useful SAR imagery will be available for use by those operating in near-
and off-shore regions.

---

2. DETECTION OF GRAVITY WAVES

Much destruction of property, loss of time and loss of life during operations in off-shore regions can be directly attributed to wind-generated ocean gravity waves. Therefore, the measurement and prediction of the gravity wave environment can be directly translated into significant savings. More specifically, exploration vessels, drilling rigs and port facilities must be designed and constructed to withstand the physical forces of the environment they will operate in.

Recent losses of drilling platforms in the Labrador and North Seas dramatically illustrate the fact that further improvements in the design of such structures are needed, with the forces associated with the expected gravity wave field being a key element in the design. It has been estimated that each additional foot in height of an off-shore drilling platform costs on the order of one million dollars (Raney, 1982). Therefore it is important to design these structures to match their environments as closely as possible.

Accurate gravity wave information is also required for the design of port and loading facilities. This need was dramatically illustrated through the extensive damage to a two-kilometer long breakwater (being constructed for a deep water, bulk cargo port) at Sine, Portugal during a winter storm of moderate strength in February of 1978 (Zwamborn, 1979). A detailed wave refraction analysis after this storm revealed that the waves from this storm were refracted by the bottom and concentrated into several areas along the breakwater. This caused a concentration of wave energy greater than the design specifications of the structure and resulted in extensive damage at these points. More accurate information on the gravity wave environment would probably have prevented the design flaw.

The above two examples illustrate the necessity of accurate gravity information for the design and deployment of vessels and structures in near- and off-shore regions. Recent studies have estimated that annual savings to construction engineering from improved wave data would be in excess of 100 million dollars (Baer, 1982). Traditional oceanographic techniques use a variety of buoy, ship and shore mounted instruments to measure gravity waves at a single geographic location. These data are expensive and often difficult to collect. In any case, for most areas extensive wave records do not exist. When wave information is needed for such areas, or over a wider area of coverage, wave forecasting or hindcasting models are sometimes used (for a review, see Earle, 1981). These models use a combination of meteorological (wind speed, direction and duration) and basin factors (bottom topography, length of fetch, local currents, etc.) to produce an estimate of the wave climate for the area. Hindcast models are used to determine wave conditions that likely occured in the past and forecast models are used to predict what conditions are likely to occur in the future. Both types of models use actual wave data from an area to fine tune the equations within the model.

Because of lack of data records from many regions and the difficulties and costs of collecting gravity wave data via traditional oceanographic techniques (i.e., pier, ship or buoy mounted instruments), recent research efforts have focused on utilizing remote sensing techniques for measuring gravity waves. There are numerous wave measuring methods which could be classified as a remote sensing techniques. In this review, we will only discuss those instruments which are mounted in an aircraft or spacecraft. These include cameras, laser or radar profilometers, short-pulse spectrometers, radar altimeters and real or synthetic aperture radars. (For a comprehensive review of these systems, see Huang, 1982.)

Although the potential for using aerial photography to image wave fields has been recognized since the late 1920's, the first serious investigations were conducted during the 1950's. Through analysis of the sun glitter patterns on an aerial photograph, Cox and Munk (1954) derived the probability density function of the sea surface slope. Cote, et al. (1960) used stereo pairs to construct an ocean surface contour plot, from which a wave energy spectrum was derived. Stillwell (1969) produced a wave number and direction spectrum using a single photograph by taking an optical Fourier transform of the image. Monaldo and Kasevich (1981) have presented a detailed summary of photographic techniques for measuring surface gravity wave statistics.

218

It soon became evident that the use of aerial photography to obtain data about the gravity wave field had serious drawbacks. First, clear weather and no clouds are required for a camera to collect usable data. This virtually eliminates the use of aerial photography during storms, the conditions underwhich it is most desirable to collect wave information. In addition, stereo photography requires a high degree of data reduction, another undesirable trait. Recent investigations have centered on instruments which provide their own source of illumination and can operate during adverse weather conditions.

The basic operating principle behind laser or radar profilometers is to measure the distance between the instrument and the ocean surface. Because profilometers use focused beams, which result in a small footprint, they can create an accurate portrayal of the ocean surface. Recent refinements of the profilometer has led to the development of the surface contour radar, or SCR. The SCR uses a beam transmitter which scans laterally with repect to the platform flight path (see Walsh, 1982). In this manner, an area is covered rather than just a single line which would result if no scanning was used.

The SCR is a microwave instrument and it provides its own source of illumination. It operates independently of solar illumination and can operate through cloud cover. There are limitations to SCR systems. Because it depends on the size of the antenna to create a focused beam (i.e., it is beam-limited), it cannot be operated from higher altitudes. Also, its ground coverage is limited to roughly half the altitude of the aircraft.

The same ranging techniques used for beam-limited profilometers can be used for pulse-limited microwave systems. Pulse-limited radars derive information on the contour of the ocean's surface through use of pulse compression techniques, and are not dependent on the beamwidth of the antenna for their range resolution (see Huang, 1982). Included in this class of instruments are radar altimeters and short-pulse spectrometers. These instruments are still in their developmental stages for use in generating ocean wave spectra, and will not be discussed in detail. Those interested in these systems should see papers by Huang (1982) and Jackson, et al. (1982).

Considerable research has been performed during the past decade exploring the utility of imaging radars to provide gravity wave data. Here we will review the use of synthetic aperture radars (SARs). SARS have a distinct advantage of other microwave remote sensing systems in that they produce fine-resolution images of a large area. These images can be used for purposes other than measuring the surface gravity wave field, which will be illustrated later in this paper.

There are four recognized techniques to extract estimates of the dominant gravity wave period and direction from SAR data. These include two-dimensional Fourier transforms (both optical and digital), a semi-causal technique, and a new one-step spectral estimation routine which extracts the wave period directly from the SAR signal histories.

By passing a monochromatic, collimated beam of light through the film image of the gravity waves imaged by the SAR, a two-dimensional optical Fourier transform (OFT) of the image is created (Barber, 1949; Shuchman, et al., 1977). If a digital image is made, the same process can be accomplished on a computer by taking a fast Fourier transform (FFT) of the data (Shuchman, et al., 1979). Producing an FFT has an advantage over an OFT in that distributional wave spectra, as a function of wave frequency or direction, can also be generated; not just dominant wavelength and direction as obtained from an OFT. Figure 1 presents an example of actual Seasat SAR wave images and the resulting OFT and FFT generated from these data. Figure 2 presents the one-dimensional wave number and wave directional spectra generated from the two-dimensional FFT in Figure 1.

A new two-dimensional spectral estimation algorithm related to maximum entropy, called the semicausal model (Jain and Ranganath, 1978) has been applied to SAR wave imagery (Jackson and Shuchman, 1983). These semicausal spectral estimates were compared to FFT estimates of identical data sets and reference functions. Results indicate the semicausal model can successfully produce spectral estimates of truncated data sets (i.e., 1-2 wave cycles).

Another new technique has been proposed by Hasselman (1980) to extract spectral wave

219

C-4

information directly from the SAR signal history. Hasselman has derived a simple method for the determination of the two-dimensional surface image spectrum from the return signal of a SAR without explicitly forming an image. This algorithm, called a signal-image-Fourier transform (SIFT) has recently been programed at ERIM and is currently undergoing testing and evaluation using Seasat SAR data.

It should be noted that SAR spectral estimates of water gravity waves are wave number/directional spectra of the radar return intensity. The data do not represent wave height information, at least not in a recognizable form. The modulation transfer function (i.e., the SAR gravity wave imaging mechanism) is not totally understood at this time. The determination of the transfer function, as well as determination of wave height using SAR data, will be a major scientific advancement. At that time, it would be possible to use SAR gravity wave data to obtain power density estimates of the sea surface.

During the past eight years, a series of experiments, whose purpose was to demonstrate that SAR data can be used to determine wavelength and direction, has been conducted. The experiments include: Marineland; West Coast; DUCKEX; GOASEX; JASIN; MARSEN; ARSLOE; and Lake Michigan (these experiments are described in detail by Shemdin, 1980; Shemdin, 1980a; Mattie, et al., 1980; Gonzalez, et al., 1981; Allan and Guymer, 1980; Shuchman, et al., 1982; Baer, 1981; and Shuchman and Meadows, 1980). Figure 3 (after Vesecky and Stewart, 1982) is a scatterplot of wavelength information obtained from the Seasat SAR compared to in situ (pitch and roll buoy) ocean wavelength sea truth. Figure 4 (after Vesecky and Stewart, 1982) is the direction of wave propagation obtained from Seasat, again compared to sea truth data. Based on these data, it appears that the Seasat SAR estimates of wavelengths are biased slightly high, with the average error being approximately 12 percent. For wave direction, there appears to be no significant bias and the average error is approximately 15 degrees. To summarize, the Seasat SAR wave analysis indicates dominant wavelength and direction can be measured by the Seasat SAR provided that the waves are visible on the SAR imagery (Vesecky, et al., 1982). Note directional wave data provided from a SAR have an 180° ambiguity. Selective Doppler processing, as reported by Shuchman and Zelenka (1978) and Kasischke and Shuchman (1981), can in some cases resolve this 180° ambiguity.

Figures 5 to 8 are scatterplots of aircraft SAR derived estimates of wavelength and direction versus sea truth of X- and L- band data from Marineland, GOASEX (aircraft) and Lake Michigan. These results indicate that aircraft SAR-derived wavelength information does not appear biased and is accurate to within approximately 13 percent, while directional information is also not biased and accurate to withing approximately 10 degrees.

3. MAPPING OF BATHYMETRIC FEATURES

Up-to-date hydrographic information has always been of utmost importance to navigators and coastal engineers. The advent of sonar sounding techniques and the use of advanced satellite location systems has greatly aided in the generation of more current bathymetric information, but there are still shortcomings in a high percentage of nautical charts. It has been estimated that 62 percent of the world's ocean areas have insufficient hydrographic data to determine the sea-floor topography (Kapoor, 1976).

Recent political developments and economic events have led navigators to seek out and use new shipping lanes, which are not as well surveyed as traditional routes. The construction of deep draft vessels (close to thirty meters) requires a minimum water depth greater than many traditional routes provide. In addition, increasing energy costs have forced many navigators to use shorter, but less well survey routes. In terms of hydrocarbon resource development, many areas where new drilling is occuring are not well surveyed. Also, construction of port and loading facilities often require accurate bathymetric information.

Although the demand for up-to-date nautical charts is high, the ability of the survey vessels of today's hydrographic services to fulfill these needs is deficient. For example, a recent study by the British Hydrography Study Group (Haslam, 1975) indicated that it would require 284 ship-years of work to properly survey the waters around the British Isles, and another 300 ship-years to survey foreign areas for which they were responsible.

220

Recently, the utility of satellite and airborne remote sensing techniques to aid in identifying and mapping bathymetric features has been extensively investigated. These techniques include photogrammetric techniques, radiometric methods, lidar systems, active/passive systems and synthetic aperture radar techniques.

The application of photogrammetric techniques to measurements of water depths was apparently first attempted during World War II (Seiwell, 1949). These techniques were elaborated to include corrections for refraction at the water surface by Tewinkel (1963) and have subsequently undergone extensive field testing and evaluation (Geary, 1968; Umbach and Harris, 1973). As a result, photogrammetric techniques have become an operational tool for nearshore hydrographic charting by several U.S. agencies. These photogrammetric methods use stereo-cartographic techniques to extract estimates of water depths. Disadvantages of this method include errors due to uncompensated refractive effects and limitations imposed by water clarity and bottom contrast (Masry and MacRitchie, 1980). The technique is also not easily adaptable to imagery acquired by satellites.

A second set of methods for the remote measurement of water depth using multispectral scanner technology was initially investigated by Polcyn and Sattinger (1969) and Brown, et al. (1971). The two main techniques resulting from these studies involved the refraction of gravity waves in shallow water and the attenuation of light reflected from the bottom. This latter method has been developed using both aircraft and Landsat MSS data over the past decade (Polcyn and Lyzenga, 1973; Middleton and Barker, 1976; Warne, 1976; Lyzenga, 1981).

Essentially, the method depends upon finding a relationship between the water depth and the observed radiance in one or more wavelength bands. If the water optical properties and bottom reflectance are uniform, a good correlation exists between the depth and the radiance in a single wavelength band. Figure 9 illustrates the reflectance of sunlight from a shallow water region. The radiance in a single wavelength band (L) can be expressed as

$$L = L_s + Kr_b e^{-2Kz} \tag{1}$$

where L_s is the deep water radiance, K is the attenuation coefficient, r_b is the bottom reflectance, and z is the water depth. Eq. (1) can be inverted to estimate water depth (z).

Eq. (1) assumes a constant bottom reflectance (r_b) over the entire region of interest. Figure 10 illustrates a case where there is a vegetated and non-vegetated area in the same scene. From Figure 10 it is clear that use of Eq. (1) would result in different depths according to the bottom type. A two-channel technique to account for this variation is described by Lyzenga, et al. (1982). Using two channels, this algorithm can be written as

$$z = a_0 + a_1 \ln(L_1 - L_{s1}) + a_2 \ln(L_2 - L_{s2}) \tag{2}$$

where the subscripts 1 and 2 designate the two channels used, and the coefficients a_0, a_1, and a_2 are obtained from a regression analysis of the signals over a set of known depths, or from a knowledge of the water attenuation and bottom reflectance parameters.

The advantages of radiometric depth determinations are that they lend themselves well to automatic computation and to data collected from satellites. The disadvantages are their sensitivity to environmental parameters, their restriction to relatively shallow depths, and the need for depth calibration. The problem of sensitivity to environmental parameters has been reduced by the development of multispectral and multitemporal processing algorithms, and may be further reduced by future research. The depth range and accuracy of these techniques are comparable to those of photogrammetric methods if adequate depth calibration information exists. The requirement for depth calibration can be met by coupling with lidar systems, as will be discussed below.

The remote measurement of water depth using pulsed lasers was proposed in the mid-1960's

221

C-6

and was first demonstrated by Hickman and Hogg (1969) in 1968. The basic operating principle behind a lidar is illustrated in Figure 11. A laser directs a pulse of energy towards the water surface. Part of this energy is reflected at the water's surface, and part is reflected from the bottom. The time (t) between these two return pulses (see Figure 12) is

$$t = \frac{2nz}{c} \tag{3}$$

where c is the speed of light and n is the index of refraction of water. Eq. (3) can be inverted to calculate depth, if the returned pulses can be recognized and their separation measured.

Further development of lidar bathymetry systems has been actively pursued by various civilian and military agencies in the U.S. and elsewhere (Kim, 1977; Hoge, et al., 1980). Commercial lidar systems are now available which advertise 0.15 meter rms depth accuracy up to 3.3 times the Secchi depth (Avco Everett Research Lab, 1979). The high accuracy of lidar depth measurements constitutes the primary advantage of this approach over other remote sensing techniques. The disadvatages of this method includes its relatively low sampling density and areal coverage. The sampling density is limited by laser pulse repetition frequencies and data recording rates. Areal coverage is limited by the maximum altitude and scan angles at which usable data can be obtained. In addition, very accurate determinations of platform position and attitude are required in order to provide x-y coordinates corresponding to each depth measurement.

In order to combine the advantages of high spatial resolution inherent in multispectral scanner systems with the accuracy of lidar devices, a hybrid system incorporating both a multispectral scanner and a lidar system was constructed at the Environmental Research Institute of Michigan between 1975 and 1977 (Hasell, et al., 1977), and is called an active/passive scanner. The laser pulse in this device is timed to correspond with known locations in the passive data, allowing the relationship between water depth and the passive signals to be examined statistically for a large number of independent depth samples. Once this relationship is established, the water depth can be calculated at each passive data point, resulting in a sampling density about 7800 times that of the lidar system. Using data collected by the ERIM active/passive scanner system, Lyzenga, et al. (1982) showed that the data could be processed to generate accurate bathymetric maps over a wider area than is possible with lidar alone.

The active/passive scanner described above is subject to the same altitude restrictions as lidar systems, but is capable of operating over a wider range of scan angles and, therefore, has a larger areal coverage than lidar-only systems. Furthermore, the calibration coefficients obtained from the active/passive scanner can be applied to passive data collected at higher altitudes to extend the coverage to still larger areas.

Recent investigations at ERIM have demonstrated the potential of using SAR to detect and chart bottom features (Kasischke, et al., 1980; 1982; 1983; 1983a; Shuchman, 1982; Shuchman and Kasischke, 1979; 1981; and Shuchman, et al., 1981). The objectives of these intitial investigations was to evaluate the potential of SARs to provide data for improving nautical chart products. As a result of these investigations, five different physical oceanographic phenomena were identified as the agents responsible for the appearance of depth-related features on SAR-imagery, as summarize in Table 1.

An example of a Seasat SAR image showing numerous depth-related features is shown in Figure 13. This image was collected over the Nantucket Shoals region on 27 August 1978. At the time of the overpass, a 1.5 knot (0.75 m/s) tidal current was present in this region. The features appearing on this image are thought to be due to the interaction of this tidal current with the bottom, causing a modulation of the wind-generated surface roughness. A comparison of the radar return with the water depth along a transect east of Nantucket Island is shown in Figure 14 (for a complete discussion of this image, see Shuchman, 1982 or Kasischke, et al., 1982). Although there is apparently a strong correspondence between the radar backscatter and

222

bathymetry in this region, much work remains to be done before quantitative depth estimates can be extracted from SAR imagery.

4. MONITORING OF INTERNAL WAVES

Internal waves are waves that propagate beneath the ocean's surface, along the boundary layer between water of greater and lesser density. This layer is usually a thermocline where warm, less saline overlies cold, more saline water. Figure 15 (after Lafond and Cox, 1962) illustrates an internal wave propagating along a thermocline. Internal waves can be caused by several physical forces, but the most common appears to be a tidally driven current flowing over an uneven bottom topography.

Studies by Osborne, et al. (1978) and Osborne and Burch (1980) focused on the effects of internal waves on a drillship operating in 600 to 1000 meters of water in the Andaman Sea. In this region, very large amplitude (greater than 100 meters) internal waves were quite common. These internal waves were characterized by 100 to 200 meter wide swaths of choppy seas with waves 1 to 1.5 meters higher than the surrounding seas which had surface currents of up to 1.5 m/s (3 knots) and currents along the thermocline of .5 to .75 m/s (1 to 1.5 knots). Although the surface drillship from which these data were collected was sufficiently stabalized to withstand these forces, Osborne, et al. (1978) concluded that knowledge of internal wave characteristics were necessary for designing of production facilities for this region.

Internal wave patterns have been detected on a variety of remotely sensed images. They are visible on aerial and spacecraft photography (Osborne and Burch, 1980), Landsat MSS imagery (Apel, et al., 1974; 1975; 1975a; 1976) and aircraft and spacecraft SAR imagery (Brown, et al., 1976; Elachi and Apel, 1976; Shuchman and Kasischke, 1979; Gower and Hughes, 1979; Apel, 1981; Fu and Holt, 1982; Ford, et al., 1983; and Kasischke, et al., 1983). Internal wave patterns have been observed in both shallow, coastal waters as well as deep ocean regions. They appear as well organized wave packets (Figure 16) or as less organized wave-like patterns (Figure 17).

A large amount of information about the characteristics of the internal waves can be inferred from analysis of remotely sensed imagery and data. By examining images collected at different times, the spatial and temporal distribution of internal waves can be determined. Through simple interpretation techniques, the size (wavelength and crest length) of the internal waves can be measured. Recent investigations have shown that through measurement of the phase histories of SAR data, surface current information can be inferred (Lyzenga, et al., 1982a). Finally, the amplitude of the internal waves may also be estimated if the depth of the thermocline is known or estimated (Apel, 1981).

5. CONCLUSIONS

In this paper we have discussed three applications of remote sensing techniques which can provide valuable information for hydrocarbon resource development in oceanic regions. These areas include detection of gravity waves, mapping of bottom features and monitoring of internal waves. Each of these applications can have significant impact on drilling or exploration activities. Remote sensing techniques can provide valuable data for design and deployment of vessels in near- and offshore regions. Since many companies involved in hydrocarbon resource development already have remote sensing processing and analysis capabilities, incorporation of the methods outlined in this paper represent little additional investment to expand these capabilities.

6. ACKNOWLEDGEMENTS

223

C-8

like to acknowledge their associates who participated in the research activities which were reviewed in this paper. These people include Dr. R. A. Shuchman and Mr. J. D. Lyden of ERIM and Dr. G. A. Meadows and Mr. Y. S. Tseng of The University of Michigan.

REFERENCES

Allan, T.D. and T.H. Guymer, Seasat and JASIN, Int. J. Remote Sensing, 1, pp. 261-267, 1980.

Apel, J.R., R.L. Charnell and R.J. Blackwell, Ocean Internal Waves Off the North American and African Coasts from ERTS-1, Proc. Ninth Int. Symp. Remote Sens. Environ., Ann Arbor, MI, pp. 1345-1354, 1974.

Apel, J.R., H.M. Byrne, J.R. Proni and R.L. Charnell, Observations of Oceanic Internal and Surface Waves from the Earth Resources Technology Satellite, J. Geophys. Res., 80, pp. 865-881, 1975.

Apel, J.R., J.R. Proni, H.M. Byrne, and R.L. Sellers, Near-Simultaneous Observations of Inter-mittent Internal Waves on the Continental Shelf from Ship and Spacecraft, Geophys. Res. Lett., 2, p. 128, 1975a.

Apel, J.R., H.M. Byrne, J.R. Proni, and R.L. Sellers, A Study of Oceanic Internal Waves Using Satellite Imagery and Ship Data, Remote Sensing of Environment, 5, p. 125, 1976.

Apel, J.R., Non-Linear Features of Internal Waves as Derived from the Seasat Imaging Radar, in Oceanography from Space, ed. by J.F.R. Gower, Plenum Press, New York, pp. 525-533, 1981.

Avco Everett Research Laboratory, AVCO Airborne Laser Mapping System, Everett, MA, 6 pp., 1979.

Baer, L., Informal Proceedings of the Atlantic Remote Sensing and Ocean Experiment Data and Analysis Workshop, Virginia Beach, VA, 1981.

Baer, L., Operational Needs for Wave Data, in Measuring Ocean Waves - Proceedings of a Sym-posium and Workshop on Wave Measurement Technology, National Academy Press, Washington, D.C., pp. 14-27, 1982.

Barber, N.F., A Diffraction Analysis of a Photograph of the Sea, Nature, 164, p. 485, 1949.

Beal, R.C., P.S. DeLeonibus, and I. Katz (eds.), Spaceborne Synthetic Aperture Radar for Oceanography, John Hopkins Univ. Press, Baltimore, MD, 215 pp., 1981.

Brown, W.L., F.C. Polcyn, and S.R. Stewart, A Method on Calculating Water Depth, Attenuation Coefficients and Bottom Reflectance Characteristics, Proc. Seventh Int. Symp. Remote Sens. Environ., Ann Arbor, MI, pp. 665-682, 1971.

Brown, W.E., Jr., C.E. Elachi and T.W. Thompson, Radar Imaging of Ocean Surface Patterns, J. Geophys. Res., 81, pp. 2657-2667, 1976.

Cote, L.J., J.O. Davis, W. Marks, R.J. McCough, E. Mehr, W.J. Pierson, J.F. Ropek, G. Stephenson, and R.C. Vetter, The Directional Spectrum of a Wind-Generated Sea as Determined from Data Obtained by the Stereo Wave Observation Project, Meteorological Papers, 2(6), Col-lege of Engineering, New York University, 1960.

Cox, C.S. and W.H. Munk, Statistics of the Sea Surface Derived from Sun Glitter, J. Marine Res., 13, pp. 198-227, 1954.

Earle, M.D., Problems in Ocean Wave Hindcasting, in Spaceborne Synthetic Aperture Radar for Oceanography, ed. by R.C. Beal, P.S. DeLeonibus, and I. Katz, Johns Hopkins Univ. Press, Baltimore, MD, pp. 78-109, 1981.

Elachi, C. and J.R. Apel, Internal Wave Observations Made with Airborne Synthetic Aperture Imaging Radar, Geophys. Res. Lett., 3, p. 647, 1976.

Ford, J.P., J.B. Cimino, and C. Elachi, Space Shuttle Columbia Views the World with Imaging Radar: The SIR-A Experiment, JPL Publication 82-95, Pasadena, CA, 166 pp., 1983.

Fu, L. and B. Holt, Seasat Views Oceans and Sea Ice with Synthetic Aperture Radar, JPL Publication No. 81-120, 200 pp., 1982.

Geary, E.L., Coastal Hydrography, Photogrammetric Engineering, 34, pp. 44-50, 1968.

Gonzalez, F.I., R.A. Shuchman, D.B. Ross, C.L. Rufenach and J.F.R. Gower, Synthetic Aperture Radar Wave Observations During GOASEX, Oceanography from Space, ed. by J.F.R. Gower, Plenum Press, New York, pp. 459-467, 1981.

Gower, J.F.R. and B.A. Hughes, Radar and Ship Observations of Coastal Sea Surface Roughness Patterns in the Gulf of Georgia, Proc. Thirteenth Int. Symp. Remote Sens. Environ., Ann Arbor, MI, pp. 103- 115, 1979.

Gower, J.F.R. (ed.), Oceanography from Space, Plenum Press, New York, NY, 977 pp., 1981.

Hasell, P.G., L.M. Peterson, F.J. Thomson, E.R. Work, and F.J. Kriegler, Active and Passive Multispectral Scanner for Earth Resources Applications, ERIM Final Report No. 115800-49-F, Ann Arbor, MI, 93 pp., 1977.

Haslam, D.W., Rear Admiral, O.B.E., F.R.I.C.S., Report by the Hydrographer of the Navy, N.P. 130, Taunton, England, 1975.

Hasselmann, K., A Simple Algorithm for the Direct Extraction of the Two-Dimensional Surface Image Spectrum from Return Signal of a Synthetic Aperture Radar, Int. J. Rem. Sens., 1, pp. 219-240, 1980.

Hickman, G.D. and J.E. Hogg, Application of an Airborne Pulsed Laser for Near Shore Bathymetric Measurements, Remote Sensing of Environment, 1, pp. 47-58, 1969.

Hoge, F.E., R.N. Swift, and E.B. Frederick, Water Depth Measurement Using an Airborne Pulsed Neon Laser System, Applied Optics, 19, pp. 871-883, 1980.

Huang, N.E., Survey of Remote Sensing Techniques for Wave Measurements, in Measuring Ocean Waves - Proceedings of a Symposium and Workshop on Wave Measurement Technology, National Academy Press, Washington, D.C., pp. 38-79, 1982.

Jackson, F.C., W.T. Walton, and P.L. Baker, Aircraft and Satellite Measurement of Ocean Wave Directional Spectra Using Scanning-Beam Microwave Radars, in Measuring Ocean Waves - Proceedings of a Symposium and Workshop on Wave Measurement Technology, National Academy Press, Washington, D.C., pp. 38-79, 1982.

Jackson, P.L. and R.A. Shuchman, A New High Resolution Two-Dimensional Spectral Estimation Technique for SAR Ocean Wave Analysis, J. Geophys. Res., 88, pp. 2593-2600, 1983.

Jain, A.K. and S. Ranganath, Two-Dimensional Spectral Estimation, Proc. of the RADC Spectrum Estimation Workshop, 1978.

Kapoor, D.C., International Cooperation in Hydrography, International Hydrographic Review, Vol. LIII(2), Monaco, 1976.

Kasischke, E.S., R.A. Shuchman and J.D. Lyden, Detection of Bathymetric Features Using SEASAT Synthetic Aperture Radar - A Feasibility Study, ERIM Final Report No. 135900-2-F$_2$, 77 pp., 1980.

225

C-10

Kasischke, E.S. and R.A. Shuchman, The Use of Wave Contrast Measurements in the Evaluation of SAR/Gravity Wave Models, <u>Proc. Fifteenth Int. Symp. Remote Sens. Environ.</u>, pp. 1187-1206, 1981.

Kasischke, E.S., D.R. Lyzenga, R.A. Shuchman, Y.S. Tseng, B.S. Termaat, B.A. Burns, and G.A. Meadows, The Use of Synthetic Aperture Radar to Detect and Chart Submerged Navigation Hazards, <u>ERIM Final Report No. 155200-1-F</u>, Ann Arbor, MI, 232 pp., 1982.

Kasischke, E.S., R.A. Shuchman, D.R. Lyzenga, and G.A. Meadows, Detection of Bottom Features and Seasat Synthetic Aperture Radar Imagery, <u>Photogrametric Engineering and Remote Sensing</u> (in press), 1983.

Kasischke, E.S., R.A. Shuchman, G.A. Meadows, L.D. Lyden, and S.C. Crane, The Use of Satellite and Aircraft SAR to Detect and Chart Submerged Navigation Hazards, <u>ERIM Final Report No. 163000-1-F</u>, Ann Arbor, MI (in press), 1983a.

Kim, H.H., Airborne Bathymetric Charting Using Pulsed Blue-Green Lasers, <u>Applied Optics</u>, 10, pp. 46-56, 1977.

LaFond, E.C. and C.S. Cox, Internal Waves, <u>The Sea</u>, 1, M.N. Hill (ed.), Interscience Publishers, New York, pp. 731-763, 1962.

Lyden, J.D., B.A. Burns, R.A. Shuchman, D.R. Lyzenga, R.W. Larson, and R.T. Lowry, Synthetic Aperture Radar Imagery of Ocean Waves in Sea Ice, <u>Proceedings of the International Symposium on Remote Sensing of Environment, Second Thematic Conference: Remote Sensing for Exploration Geology</u> (in press), Ann Arbor, MI, 1983.

Lyzenga, D.R., Remote Bathymetry Using Active and Passive Techniques, <u>1981 International Geoscience and Remote Sensing Symposium Digest</u>, Washington, D.C., pp. 777-786, 1981.

Lyzenga, D.R., J.S. Ott, and J.P. Livisay, Shallow-Water Bathymetry Using Combined Lidar and Multispectral Scanner Data, paper submitted to <u>Int. J. Remote Sensing</u>, 1982.

Lyzenga, D.R., R.A. Shuchman, and C.L. Rufenach, Synthetic Aperture Radar Measurements of Ocean Surface Currents, <u>Geophys. Res. Lett.</u>, 9, 747, 1982a.

Masry, S.E. and S. MacRitchie, Different Considerations in Coastal Mapping, <u>Photogram. Eng. Remote Sensing</u>, 46, pp. 521-528, 1980.

Mattie, M.G., D.E. Lichy and R.C. Beal, Seasat Detection of Waves, Currents and Inlet Discharge, <u>Int. J. Remote Sensing</u>, 1, pp. 377-398, 1980.

Mercer, J.B., R.T. Lowry, and A.L. Gray, Remote Sensing in Support of Arctic Oil Exploration, <u>Proc. Int. Symp. Remote Sensing Environ. - Second Thematic Conference: Remote Sensing for Exploration Geology</u> (in press), Ann Arbor, MI, 1983.

Middleton, E.M. and J.L. Barker, Hydrographic Charting from Landsat Satellite Data: A Comparison with Aircraft Imagery, <u>MTS-IEEE Oceans-'76</u>, pp. 15F-1 to 15F-6, 1976.

Monaldo, F.M. and R.S. Kasevich, Daylight Imagery of Ocean Surface Waves for Wave Spectra, <u>J. Phys. Oceangr.</u>, 11, pp. 272-283, 1981.

Osborne, A.R. and T.L. Burch, Internal Solitons in the Andaman Sea, <u>Science</u>, 208, pp. 451-460, 1980.

Osborne, A.R., T.L. Burch, and P.I. Scarlet, The Influence of Internal Waves on Deep-Water Drilling, <u>J. Petrol. Tech.</u>, pp. 1497-1504, 1978.

Polcyn, F.C. and D.R. Lyzenga, Calculations of Water Depth from ERTS-MSS Data, <u>Proc. Symp. Significant Results Obtained from ERTS-1</u>, NASA Publication SP-327, 1973.

Polcyn, F.C. and I.J. Sattinger, Water Depth Determinations Using Remote Sensing Techniques, Proc. Sixth Int. Symp. Remote Sens. Environ., Ann Arbor, MI, pp. 1017-1028, 1969.

Raney, R.K., The Canadian Radarsat Program, 1982 International Geoscience and Remote Sensing Symposium Digest, Munich, Germany, pp. TP-6, 3.1-3.6, 1982.

Seiwell, H.R., Oceanographic Factors in Underwater Depth Determination by Aerial Photography, Photogrammetric Engineering, 15, pp. 172-176, 1949.

Shemdin, O.H., The Marineland Experiment: An Overview, Trans. Amer. Geophys. Union, 61, No. 38, pp. 625-626, 1980.

Shemdin, O.H., The West Coast Experiment: An Overview, Trans. Amer. Geophys. Union, 61, No. 40, pp. 649-651, 1980a.

Shuchman, R.A., Quantification of SAR Signatures of Shallow Water Ocean Topography, Univ. of Mich. PhD Dissertation, Ann Arbor, MI, 130 pp., 1982.

Shuchman, R.A., P.L. Jackson and G.B. Feldkamp, Problems of Imaging Ocean Waves with Synthetic Aperture Radar, ERIM Interim Technical Report No. 124300-1-T, Ann Arbor, MI, 111 pp., 1977.

Shuchman, R.A. and J.S. Zelenka, Processing of Ocean Wave Data from a Synthetic Aperture Radar, Boundary-Layer Meteorol., 13, pp. 181-191, 1978.

Shuchman, R.A. and E.S. Kasischke, The Detection of Oceanic Bottom Topographic Features Using SEASAT Synthetic Aperture Radar Imagery, Proc. Thirteenth Int. Symp. Remote Sens. Environ., pp. 1277-1292, 1979.

Shuchman, R.A., K.H. Knorr, J.C. Dwyer, P.L. Jackson, A. Klooster and A.L. Maffett, Imaging Ocean Waves with SAR - A SAR Ocean Wave Algorithm Development, ERIM Interim Technical Report No. 124300-5-T, Ann Arbor, MI, 123 pp., 1979.

Shuchman, R.A. and G.A. Meadows, Airborne Synthetic Aperture Radar Observations of Surf Zone Conditions, Geophys. Res. Lett., 7, pp. 857-860, 1980.

Shuchman, R.A. and E.S. Kasischke, Refraction of Coastal Ocean Waves, in Spaceborne Synthetic Aperture Radar for Oceanography, ed. by R.C. Beal, P.S. DeLeonibus and I. Katz, Johns Hopkins Univ. Press, Baltimore, MD, pp. 128-135, 1981.

Shuchman, R.A., E.S. Kasischke and J.D. Lyden, Observations of Bottom Related Surface Signatures on Seasat Synthetic Aperture Radar Data, paper presented at the IUCRM Symposium on Wave Dynamics and Radio Probing of the Ocean Surface, Miami, Florida, 1981.

Shuchman, R.A., E.S. Kasischke, J.D. Lyden, A. Klooster, and W. Rosenthal, Analysis of MARSEN Synthetic Aperture Radar Wave Imagery, 1982 Int. Geoscience and Remote Sensing Symposium Digest, Munich, Germany, pp. WP-3, 3.1-3.7, 1982.

Stillwell, D., Jr., Directional Energy Spectra of the Sea from Photographs, J. Geophys. Res., 74, pp. 1974-1986, 1969.

Tewinkel, G.C., Water Depths from Aerial Photographs, Photogrammetric Engineering, 24, pp. 1037-1042, 1963.

Tucker, W.B., CRREL Investigations Relevant to Offshore Petroleum Production in Ice Covered Waters, Proc. Int. Symp. Remote Sens. Environ. - Second Thematic Conference: Remote Sensing for Exploration Geology (in press), Ann Arbor, MI, 1983.

Umbach, M.J. and W.D. Harris, Photogrammetric Bathymetry, paper presented at the XII Pan American Consultation on Cartography, Panama, Panama, 10 pp., 1973.

Vesecky, J.F. and R.H. Stewart, The Observation of Ocean Surface Phenomena Using Imagery from the Seasat Synthetic Aperture Radar - An Assessment, J. Geophys. Res., 87, pp. 3397-3430, 1982.

Vesecky, J.F., H.M. Assal, R.H. Stewart, R.A. Shuchman, E.S. Kasischke, and J.D. Lyden, Seasat-SAR Observations of Surface Waves, Large Scale Surface Features and Ships During the JASIN Experiment, 1982 Int. Geoscience and Remote Sensing Symposium Digest, Munich, Germany, pp. WP-3, 1.1-1.6, 1982.

Walsh, E.J., Remote Sensing of Waves by Surface Contour Radar, in Measuring Ocean Waves - Proceedings of a Symposium and Workshop on Wave Measurement Technology, National Academy Press, Washington, D.C., pp. 80-94, 1982.

Warne, D.K., Landsat as an Aid in the Preparation of Hydrographic Charts, Photogram. Eng. Remote Sensing, 44, pp. 1011-1016, 1978.

Zwamborn, J.A., Analysis of Causes of Damage to Sines Breakwater, Coastal Structures 79, Vol. I, American Society of Civil Engineers, New York, NY, pp. 422-441, 1979.

TABLE 1.

Summary of Types of Bottom-Related Surface
Patterns Observed on Seasat SAR Imagery

Bottom/Ocean Interaction	Result on Ocean Surface	Result on SAR Image
1. Gravity Wave Propagating into Shallow Water	1. Refraction of Gravity Waves	Detection of change in gravity wavelength and direction of propagation
	2. Non-linear Gravity wave interaction	Distinct change in radar backscatter resulting in change in image tone over bottom feature
2. Current Flowing over a bottom feature	1. Change in Current velocity	Distinct change in radar backscatter resulting in a banded pattern over the bottom feature
	2. Upwelling	Frontal Boundary
	3. Generation of Internal Waves	Internal Wave Pattern

228

MICROCOPY RESOLUTION TEST CHART

c) Fast Fourier Transform

b) Optical Fourier Transform

a) SAR Image

9 km
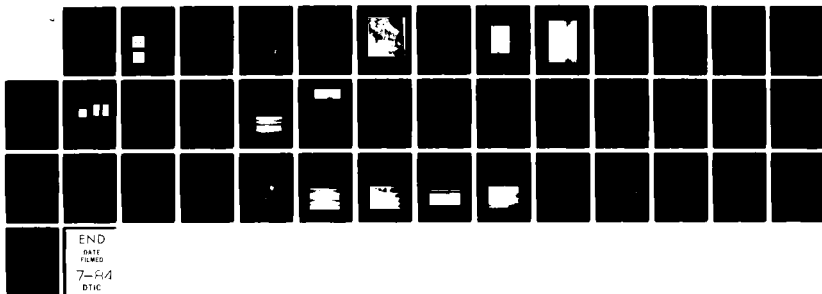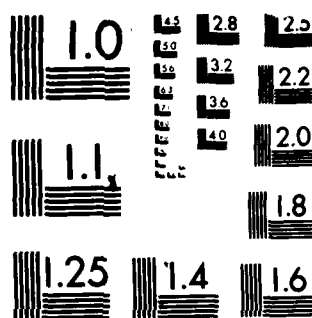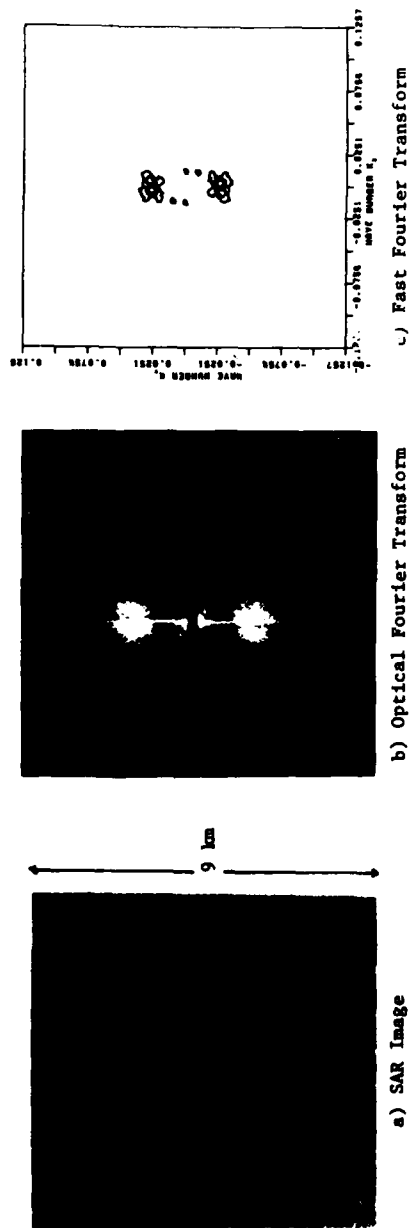
Figure 1. Seasat SAR Image of Ocean Gravity Waves and Their Resultant Two-Dimensional Fourier Transforms (Rev 762, 19 August 1978)
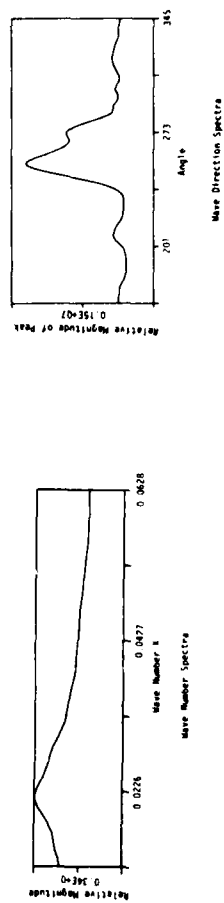
Figure 2. One-Dimensional Wave-Number and Wave Direction Spectra Generated Two-Dimensional Fourier Transform in Figure 1.
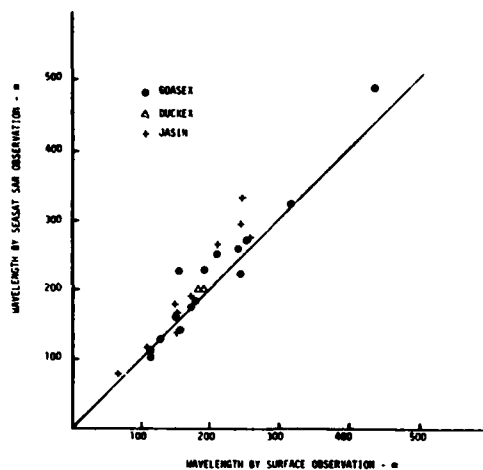
229

C-14

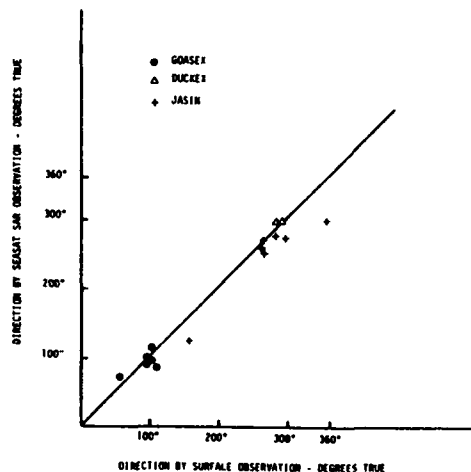Figure 3. Plot of Wavelength, SAR versus Sea Truth, for L-Band Seasat Data (after Vesecky and Stewart, 1982).

Figure 4. Plot of Wave Direction, SAR Versus Sea Truth, for L-Band Seasat Data (after Vesecky and Stewart, 1982).
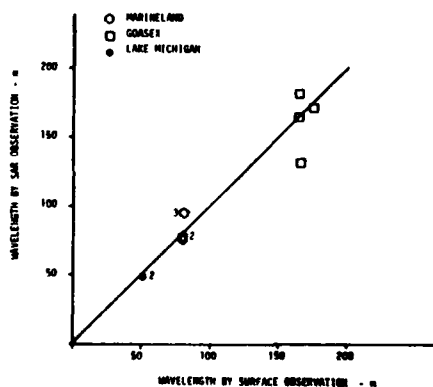
Figure 5. Plot of Wavelength, SAR versus Sea Truth, for X-band Aircraft Data.
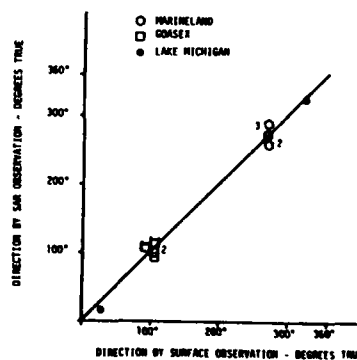
Figure 6. Plot of Wave Direction, SAR versus Sea Truth, for X-band Aircraft Data.

230

C-15
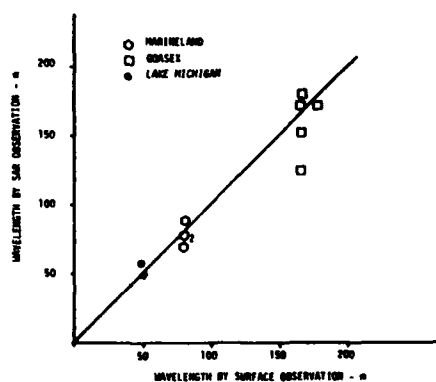
Figure 7. Plot of Wavelength, SAR versus Seatruth, for L-band Aircraft Data.
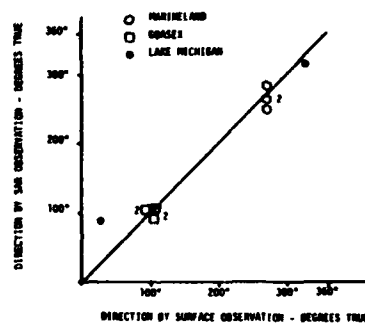
Figure 8. Plot of Wave Direction, SAR versus Seatruth, for L-band Aircraft Data.
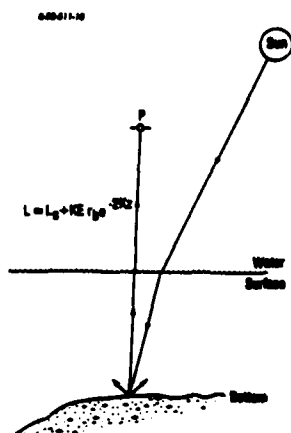
Figure 9. Spectral Reflectance from a Water Surface and Bottom.
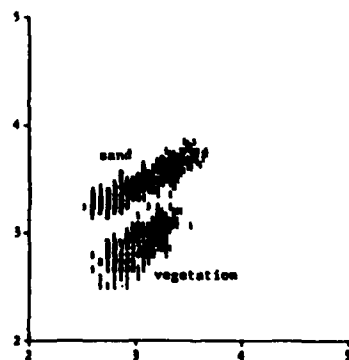
Figure 10. Spectral Reflectance from a Sand and Vegetation Covered Bottom.

231

C-16
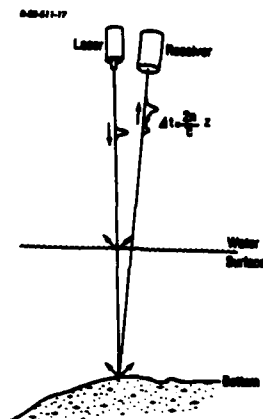
Figure 11. Schematic Diagram of an
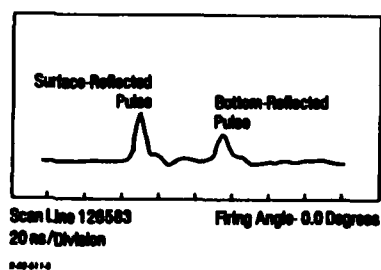Active Laser Bathymetric
Measuring System.

Figure 12. Diagram of a Reflected
Pulse from a Laser System.

232

Figure 13. Seasat SAR Image of Bottom-Related Surface Patterns over the Nantucket Shoals (Rev 880, 27 August 1978; JPL digitally processed data, radiometrically and and geometrically corrected at ERIM).
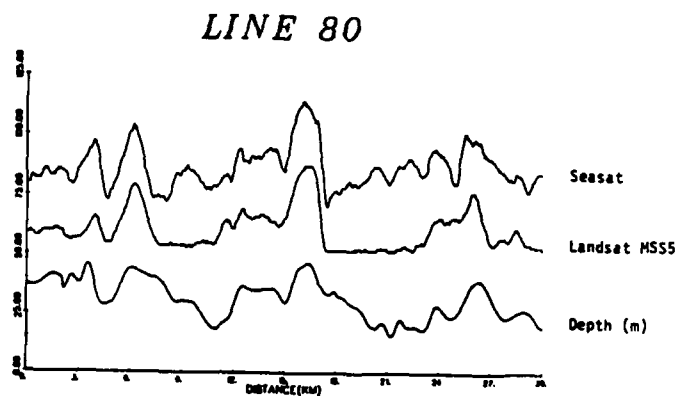
233

C-18

LINE 80

Figure 14. Comparison of Seasat and Landsat
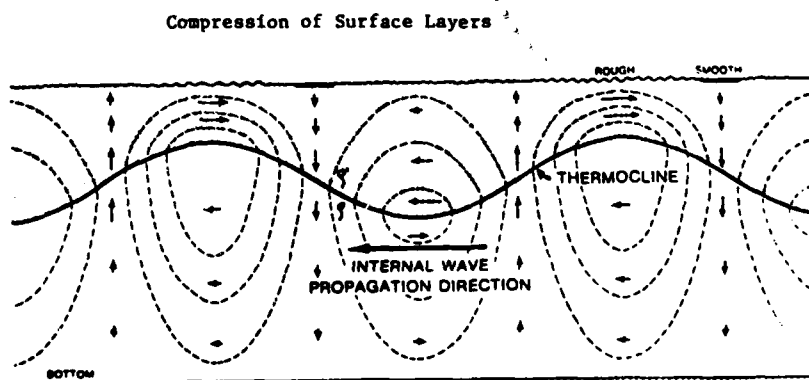Signals with Depth Data for Nantucket
Shoals (see Figure 13).

Figure 15. Schematic of the Structure of
Progressive Internal Wave Motion
Along a Sharp Thermocline Illustra-
ting Alteration of Surface Roughness
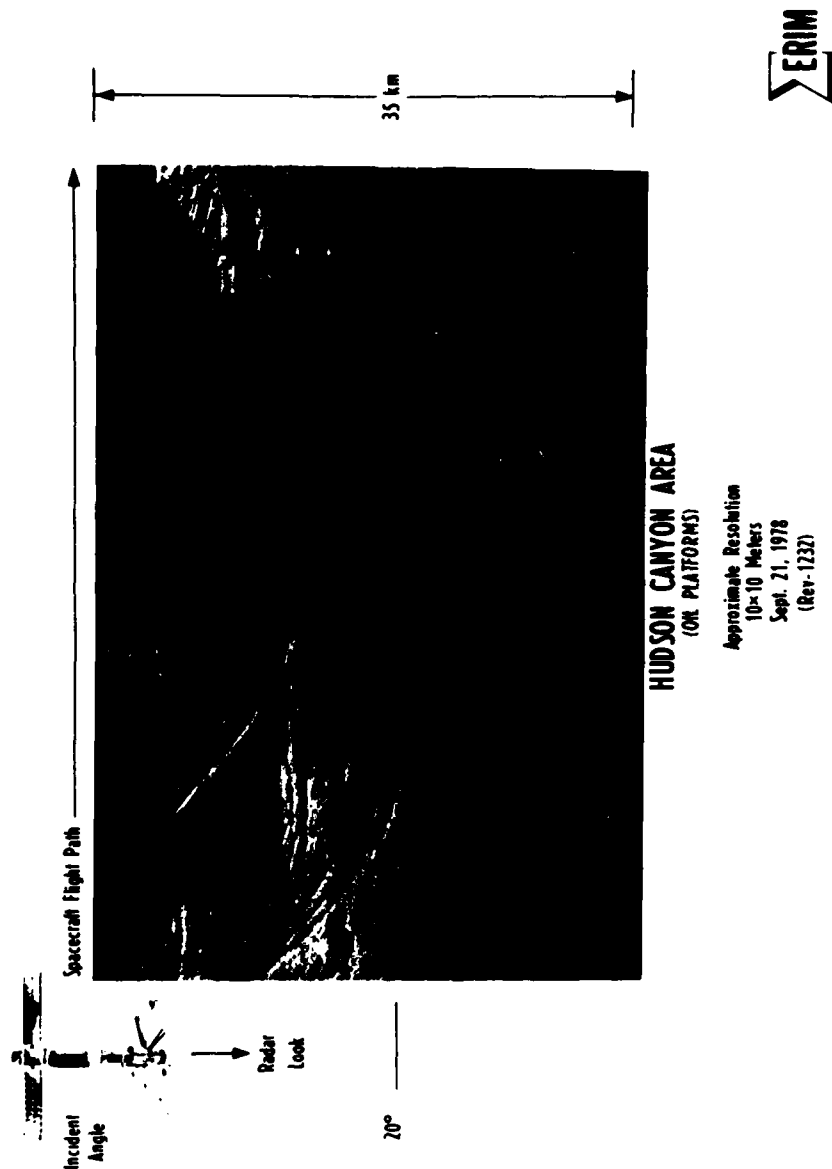(after Lafond and Cox, 1961).

234

C-19

HUDSON CANYON AREA
(ON PLATFORMS)

Approximate Resolution
10×10 Meters
Sept. 21, 1978
(Rev-1232)

35 km

Spacecraft Flight Path

Radar Look

Incident Angle

20°

ΣERIM

Figure 16. Internal Waves on Seasat SAR Imagery Collected Over the Continental Shelf Off the U.S. (Rev 1232, ERIM optically processed imagery).

235
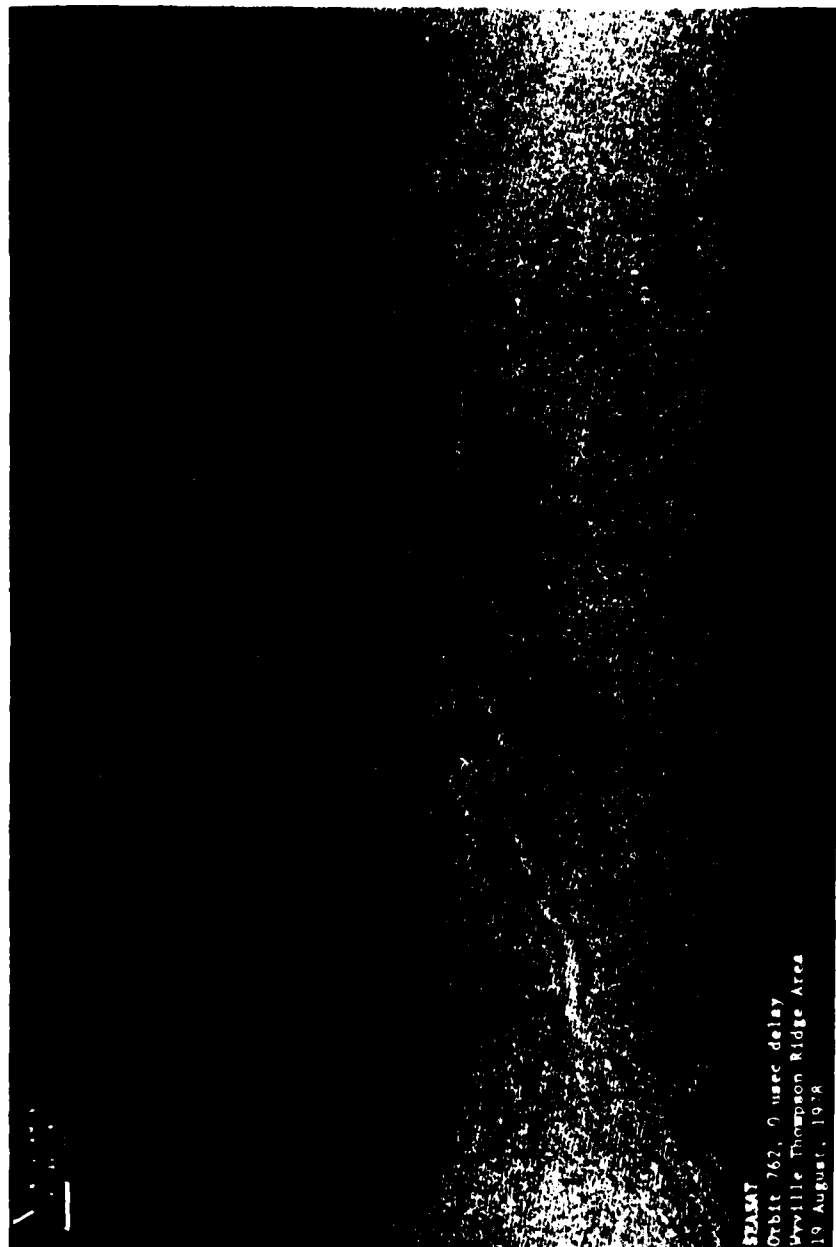
C-20

Figure 17. Deep-Water Internal Waves Imaged by Seasat Over the Nyville-Thomson Ridge (Rev 762, ERIM optically processed imagery).

236

C-21

Eric S. Kasischke
Robert A. Shuchman
David R. Lyzenga
Radar Division
Environmental Research Institute of Michigan
Ann Arbor, MI 48107
Guy A. Meadows*
Department of Atmospheric and Oceanic Science
The University of Michigan
Ann Arbor, MI 48109

Detection of Bottom Features on Seasat Synthetic Aperture Radar Imagery

Seasat SAR imagery was evaluated with respect to its potential to assist hydrographers in identifying submerged hazards.

INTRODUCTION

U P-TO-DATE HYDROGRAPHIC INFORMATION has always been of utmost importance to navigators and coastal engineers. The advent of sonar sounding techniques and the use of advanced satellite location systems has greatly aided in the generation of more current bathymetric information, but there are still shortcomings in a high percentage of nautical charts. It has been estimated that 62 percent of the world's ocean areas have

a minimum water depth which is deeper than many traditional routes provide. In addition, increasing energy costs have forced many navigators to use shorter, but less well surveyed, routes.

Accurate hydrographic information is also required for coastal engineering. This need was dramatically illustrated through the extensive damage to a two-kilometre breakwater (being constructed for a deep water, bulk cargo port) at Sine, Portugal during a winter storm of moderate

ABSTRACT: *A distinct set of surface patterns detected in imagery collected by the Seasat snythetic aperture radar (SAR) have been shown to be the result of an interaction between a physical oceanic process and a bottom topographic feature. These patterns can be used to infer a bottom feature, and thus are a potential source of information for identifying submerged features hazardous to surface navigation. The Seasat SAR imaged bottom-related surface patterns in both deep and shallow water. Examples of these surface patterns are presented in this paper along with explanations of how they occur.*

insufficient hydrographic data to determine the sea-floor topography (Kapoor, 1976).

Recent political developments and economic events have led navigators to seek out and use new shipping lanes, which are not as well surveyed as traditional routes. The construction of deep draft vessels (close to thirty metres) requires

strength in February of 1978. A detailed wave refraction analysis after this storm revealed that the waves from this storm were refracted by the bottom and concentrated into several areas along the breakwater, causing a concentration of wave energy greater than the design specifications of the structure and resulting in extensive damage at these points. Inadequate hydrographic charts were one of the reasons cited for this design flaw (Zwamborn, 1979).

Although the demand for updated nautical

C-22

charts is high, the ability of the survey vessels of today's hydrographic services to fulfill these needs is deficient. For example, a recent study by the British Hydrography Study Group (Haslam, 1975) indicated that it would require 284 ship-years of work to properly survey the waters around the British Isles and another 300 ship-years to survey foreign areas for which they were responsible.

During the 1970s, the U.S. Defense Mapping Agency's Hydrographic/Topographic Center (DMAHTC) began to explore the use of remote sensing techniques to aid in the updating of nautical charts (see Hammack, 1977). The goals of using remote sensing are, in order of priority (J. C. Hammack, DMAHTC, personal communication, 1982):

- To detect uncharted or mispositioned submerged features which are potentially hazardous to surface navigation;
- To define the boundary and location of these hazardous features in either an absolute or relative sense; and
- To extract accurate, detailed, and complete water depth information.

Most remote sensing efforts in this area have utilized aerial photography, multispectral scanners, or lidars (e.g., Hammack, 1977; Lyzenga, 1981). These optical techniques have been able to meet DMAHTC's three goals in shallow-water areas which have clear water. However, these techniques break down when either the water depth or the turbidity exceed certain limits. Recently, DMAHTC has funded research to demonstrate the utility of synthetic aperture radar imagery for meeting its goals in areas where optical techniques are not applicable (Kasischke *et al.*, 1980; 1982). The purpose of this paper is to discuss the phenomena and mechanisms which are responsible for the appearance of depth-related patterns on SAR imagery, and to present examples of patterns on Seasat SAR imagery collected over oceanic regions which can be used to infer the presence of a bottom feature.

BACKGROUND

The data to be presented in this paper were collected by the Seasat satellite. Among the instrumentation carried by Seasat, which was launched on June 28 1978, was an imaging synthetic aperture radar (SAR). This satellite collected over 500 passes of SAR data before suffering a catastrophic power loss in October of 1978. The SAR on board Seasat was an L-band (23.5-cm wavelength) radar. It collected 25 by 25 m resolution imagery with a ground swath-width of 100 km and a length of up to 4000 km, and viewed the surface of the Earth with an average incidence angle of 20°. For a detailed description of the Seasat SAR system and its mission, see Jordan (1980), Beal *et al.* (1981), or Fu and Holt (1982).

Even though the Seasat satellite failed just three months into its expected one-year mission, it provided over one-hundred million square kilometres of SAR imagery. These data provided the oceanography community with an unparalleled opportunity to view the surface of most of the Atlantic Ocean and portions of the Pacific Ocean within the Northern Hemisphere.

An imaging radar such as the Seasat SAR is an active device that senses the environment with short wavelength electromagnetic waves. As an active sensor, the Seasat SAR provided its own illumination in the microwave region of the electromagnetic spectrum and thus was not affected by diurnal changes in emitted or reflected radiation from the Earth's surface. Additionally, the 23.5-cm wavelength utilized by the Seasat SAR allowed for imaging the Earth's surface through clouds and light rain.

The principle in imaging any ocean surface with a radar is that the backscatter of microwave energy (echo) received by the radar contains information on the roughness characteristics (shapes, dimensions, and orientations) of the reflecting area. Parameters that influence the SAR image of the ocean surface include the motion of the scattering surfaces, coherent speckle, system resolution, and noncoherent integration as well as the surface roughness. In addition, the orientation of ocean waves and of bottom topographic features with respect to the radar "look" direction are influencing parameters.

Several scattering models exist that attempt to explain ocean surface image formation with synthetic aperture radars. These models are of two types: static models that depend on instantaneous surface features, and dynamic models that employ surface scatterer velocities.

Three static models have been suggested to describe the radar scattering of energy from large areas on the ocean surface. These three scattering models include (1) the specular point model which is most appropriate for small incidence angles, (2) the Bragg-Rice scattering model, described below, and (3) a Rayleigh scattering model which is often used in terrestrial Earth scattering calculations. There is general consensus within the radio-oceanography scientific community that a Bragg-Rice scattering theory best explains the SAR observed backscatter values obtained from the ocean surface for incidence angles between 20° and 60° (Shuchman *et al.*, 1981). The Bragg-Rice scattering model is based on a well known phenomena in the study of crystals, grating, and periodic structures. If one considers the random ocean surface to be represented by a combination (i.e., spectrum) of periodic surfaces, then the spectrum region which satisfies the backscatter phase matching condition will be the main contributor to the backscatter cross section. Sometimes in the literature, this phase matching of the small ocean

Bragg waves with the radar electromagnetic energy is termed a resonance phenomenon; more correctly stated, it should be termed a constructive interference between the electromagnetic and ocean waves.

Pioneering theoretical and experimental work by Wright (1966) at the Naval Research Laboratory (NRL) demonstrated the general validity of a Bragg scattering model for an ocean surface imaged by radar. In a series of wave tank measurements using 3-cm and 25-cm wavelength continuous wave (CW) Doppler radars, Wright demonstrated that Bragg scattering, that is, transmitted radar energy with wave number K interacts in a resonant or interference fashion with ocean surface waves with wave number K_n such that

$$K_n = 2K \sin \phi. \qquad (1)$$

where $K_n = 2\pi/L$, and $K = 2\pi/\lambda$ (L and λ are the wavelengths of the surface waves and the radar, respectively), and ϕ is the incidence angle. Shuchman et al. (1981) showed that a Bragg scattering equation satisfactorily explained the radar backscatter return from SAR using data collected during the Marineland experiment (for a discussion of the Marineland experiment, see Shemdin (1980)). It should be noted that radar data of large ocean areas (1 by 1 km) were averaged in that analysis. Thus, based on the above, the principal radar reflectivity mechanism of imaging ocean surfaces is via the capillary and small gravity waves which produce Bragg scattering (Raney and Shuchman, 1978).

Synthetic aperture radars are also sensitive to the motion of scatterers present in the imaged scene (Raney, 1971). Effects of scatterer motion on SAR imagery may include (1) image displacement, smearing, and loss of focus in the azimuth direction; and (2) loss of focus in the range direction. Some of these effects can be removed during processing of the SAR signal histories by making appropriate adjustments to the processor (Shuchman, 1981). Effects which cannot be removed during processing may reduce the detectability of gravity waves, but are not expected to have a large influence on the depth-related image features.

Loss of focus in the range direction is due to a rotation of the phase history of the target (i.e., migration through range cells). This loss of focus is proportional to the range velocity and the integration time, and can be corrected by a rotation of the lenses in the optical processor, assuming the range velocity is constant during the integration time.

Loss of focus in the azimuth direction can be caused by the constant velocity in the azimuth direction or a changing velocity (i.e., an acceleration) in the range direction. These effects can be corrected by a change in the azimuth focus setting of the processor, assuming that the azimuth velocity and radial acceleration are constant. Because they are both inversely proportional to the platform velocity, these effects are less important for the Seasat than for aircraft SAR systems.

A variety of processes can alter the surface Bragg waves, resulting in a distinct pattern on SAR imagery. These include oceanic processes (currents, gravity waves, internal waves, slicks, local water depth variations, water temperature, and salinity), climatic processes (wind, rain, and air temperature), and man-made phenomena (ships, buoys, and oil spills). It is the hydrodynamic interaction between several of the oceanic processes and a distinct bottom feature which allows that feature to be detected on SAR imagery. Examples of these bottom-induced surface patterns will be presented in this paper. For examples of other surface patterns on Seasat SAR imagery, see G (1981), Beal et al. (1981), or Fu and Holt ( ).

OBSERVATIONS

This study examined over 100 passes of   SAR imagery for evidence of bottom-relat   r-face signatures. In examining Seasat SAR in   of oceanic areas, those signatures which con   attributed to other oceanic or climatic processes (e.g., gravity waves, wind patterns, rain patterns, etc.) were eliminated from consideration. The positions of the unidentified patterns which were suspected to be bottom-induced were determined by identifying known land areas or through the use of satellite ephemeris records. Hydrographic charts from these areas were examined to determine whether or not the patterns occurred over a distinct bottom feature.

Furthermore, to determine the causes of the bottom-related surface patterns on the SAR imagery, a set of ancillary environmental data was compiled and analyzed for most test areas. These ancillary data included wind speed and direction, tide height, direction and tidal current velocity and gravity wave height, length, and dominant direction of propagation.

Finally, a third analysis was conducted which compared Seasat SAR imagery collected over the same test sites on different dates; i.e., a multitemporal analysis. This analysis was intended to determine how frequently a bottom feature appeared on the SAR imagery in a given area for a set of environmental conditions. Also, when coupled with ancillary environmental data, this technique provides a particularly powerful means for defining the limitations of detecting bottom features on SAR imagery.

Of the 100 orbits of Seasat-SAR imagery examined, approximately 50 percent was found to contain patterns on the imagery which could be correlated to a distinct bottom feature. Of these, 35 orbits were rigorously examined and the surface patterns on the imagery compared with hydrographic charts and ancillary data (environmental conditions coincident with the satellite overpass). These orbits are presented in Table 1. Also in-

TABLE 1. SUMMARY OF SEASAT SAR IMAGERY EXAMINED FOR BATHYMETRIC FEATURES

Study Site (Location)	Seasat Revolution	Date	Time (GMT)	Bottom Feature(s)*	SAR Signature(s)*
Little Bahama Bank—					
Grand Bahama Island	407	25 July 1978	12:46	EB	SB
	651	11 August 1978	12:26	EB	SB
Great Bahama Bank—Bimini	407	25 July 1978	12:46	EB	SB
	651	11 August 1978	12:26	EB	SB
Great Bahama Bank—	407	25 July 1978	12:46	EB	SB
Southern Edge	651	11 August 1978	12:26	EB	SB
Tongue of the Ocean	450	28 July 1978	06:23	EB, SWS	SB, SP
	529	02 August 1978	18:37	EB, SWS	SB, SP
	694	14 August 1978	07:37	EB, SWS	SB, SP
	1024	06 September 1978	09:18	EB, SWS	SB, SP
	1110	12 September 1978	09:43	EB, SWS	SB, SP
	1153	15 September 1978	09:56	EB, SWS	SB, SP
	1196	18 September 1978	10:09	EB, SWS	SB, SP
	1239	21 September 1978	10:21	EB, SWS	SB, SP
	1282	24 September 1978	10:34	EB, SWS	SB, SP
	1325	27 September 1978	10:47	EB, SWS	SB, SP
	1368	30 September 1978	11:00	EB, SWS	SB, SP
	1411	03 October 1978	11:12	EB, SWS	SB, SP
Haiti—Rochelois Bank	492	31 July 1978	11:28	SI	SB, SP
Bermuda	1267	23 September 1978	14:20	SI	SB
Nantucket Shoals	880	27 August 1978	12:25	SWS	SP
Cook Inlet, Alaska	289	17 July 1978	11:50	SWS, MB	SP, OB
North Rona Rock	762	19 August 1978	06:41	SI	OB
Sula Sgier	762	19 August 1978	06:41	SI	OB
English Channel	762	19 August 1978	06:41	SWS, MB	SP, DB
	957	01 September 1978	21:40	SWS	SP, DB
	1430	04 October 1978	20:42	SWS	SP
	1473	08 October 1978	00:15	SWS	SP
North East Atlantic	547	04 August 1978	06:15	DWB, DWR, DWS, DWSM	FB, IW
	556	04 August 1978	21:35	DWB, DWR, DWS, DWSM	FB, IW
	599	07 August 1978	21:43	DWB, DWR, DWS, DWSM	FB, IW
	633	10 August 1978	06:29	DWB, DWR, DWS	FB, IW
	642	10 August 1978	21:50	DWR, DWS, DWSM	FB, IW
	719	16 August 1978	06:43	DWB, DWR, DWS	FB, IW
	757	18 August 1978	22:40	DWB, DWR, DWS	FB, IW
	762	19 August 1978	06:41	DWB, DWR, DWS	FB, IW
	791	21 August 1978	07:24	DWB, DWR, DWS, DWSM	FB, IW
	834	24 August 1978	07:30	DWB, DWR, DWS	FB
	958	01 September 1978	23:54	DWB, DWR	FB, IW
	1006	05 September 1978	08:15	DWB, DWR, DWS	FB, IW
	1044	08 September 1978	00:18	DWB, DWR	FB, IW
	1049	08 September 1978	08:27	DWB, DWR, DWS	FB, IW
	1087	11 September 1978	00:30	DWB, DWR	FB, IW

*Bottom Feature Key
DWB   Deep Water Bank
DWR   Deep Water Ridge
DWS   Deep Water Shelf
DWSM   Deep Water Seamount
EB   Edge of Great or Little Bahama Bank
MB   Mud Bank
SI   Shoal area surrounding an island
SWS   Shallow Water Sand Bank
**SAR Signature Key
DB   Change in radar backscatter or tone (see Figure 2)
FB   Frontal Boundary (see Figure 6)
IW   Internal Wave (see Figure 5)
SB   Stripe along Great or Little Bahama Bank (see Figure 3)
SP   Striated pattern (see Figure 3)

cluded in Table 1 are the study site and its location, the date and time of the Seasat orbits, the type of bottom feature at that site, and the type of SAR surface pattern observed. SAR imagery from four areas which demonstrate SAR's ability to detect bottom features is presented in the following sections.

Table 2 summarizes the types of bottom-related surface patterns observed on Seasat SAR images. This table also includes the hypothesized oceanic process which interacts with a bottom feature to perturb the short surface capillary and ultra-gravity waves, which are then detected by a SAR. The two major ocean processes that result in SAR observation of submerged features are (1) gravity waves propagating into shallow water, and (2) oceanic currents flowing over distinct bottom features. These processes can result in five distinct surface patterns on SAR images, as will be discussed in the following sections.

SHALLOW WATER FEATURES

The first type of commonly observed bottom-related feature with a corresponding expression or surface pattern on SAR imagery is that associated with changes in wavelength and direction of ocean swell entering coastal regions. Utilizing linear gravity wave theory and applying Snell's Law, relative changes in wave phase speed can be successively calculated relative to a bathymetric grid. Hence, topographically induced changes in both surface wavelength and direction can be calculated at each grid location as a function of water depth. Because Seasat SAR imagery can be used to derive accurate estimates of wavelength and direction (see Kasischke, 1980; Gonzalez *et al.*, 1981; Vesecky *et al.*, 1982), the mathematical relationship between wavelength and direction and water depth can be used to calculate water depth. The Seasat SAR's ability to detect changes in wavelength and direction of an ocean swell propagating

into shallow coastal waters was first demonstrated by Shuchman and Kasischke (1981). Figure 1 shows a plot of water depths which were calculated using estimates of wavelength obtained from Seasat SAR imagery compared to water depths from a hydrographic survey.

The second type of bottom-related surface pattern observed on Seasat SAR imagery is associated with an ocean swell propagating over a distinct topographic irregularity in the sea bottom. When a gravity wave field crosses an abrupt change in the water depth, the structure of the gravity wave is changed because the wave begins a transition from a deep water to shallow water wave. As this transformation proceeds, the mass transport and horizontal particle velocity at the surface increases, thus straining the small scale surface roughness field (i.e., the capillary and ultra-gravity waves) and producing a corresponding change in the received electromagnetic backscatter by the radar. An example of one such feature observed by the Seasat SAR is presented in Figure 2. The image in Figure 2 was collected during Revolution 762 (19 August 1978) as Seasat passed over North Rona Rock, an island located approximately 75 km off the northwest tip of Scotland. Detected on this SAR image is a distinct change in radar backscatter in the shoal region (designated by the 50-m line) surrounding North Rona Rock. The gravity wave field present on this date is also clearly evident on the SAR imagery. Surface measurements made concurrently with the Seasat overpass about 300 kilometres west of North Rona Rock indicate a swell with a dominant wavelength of 206 m, a significant wave height ($H_{1/3}$) of 4.3 m, and a direction of propagation towards 60° (True) was present in the northeast Atlantic Ocean at this time. A wind from 186° (True) with a surface velocity of 12 m/s was also present. The diffraction of the waves as they pass North Rona Rock can also be seen.

The third class of SAR-sensed surface pattern is

TABLE 2. SUMMARY OF TYPES OF BOTTOM-RELATED SURFACE PATTERNS ON SEASAT SAR IMAGERY

| Bottom/Ocean Interaction	Result on Ocean Surface	Result on SAR Image
1. Gravity Wave Propagating into Shallow Water	1. Refraction of Gravity Waves	Detection of change in gravity wavelength and direction of propagation
	2. Non-linear Gravity wave interaction	Distinct change in radar backscatter resulting in change in image tone over bottom feature (see Figure 2)
2. Current Flowing over a bottom feature	1. Change in Current velocity	Distinct change in radar backscatter resulting in a banded pattern over the bottom feature (see Figure 3)
	2. Upwelling	Frontal Boundary (see Figure 6)
	3. Generation of Internal Waves	Internal Wave Pattern (see Figure 5)
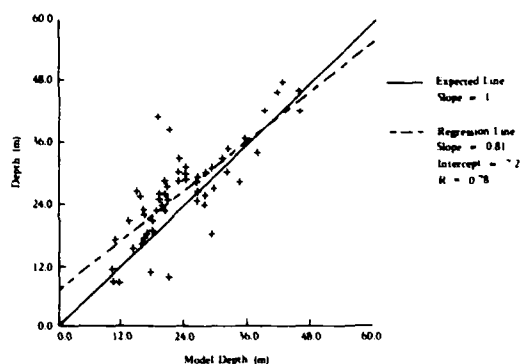
Fig. 1. Plot of water depths calculated using inverted airy wave theory with changes of wavelength extracted from Seasat SAR imagery versus depths obtained from U.S. National Ocean Surveys.
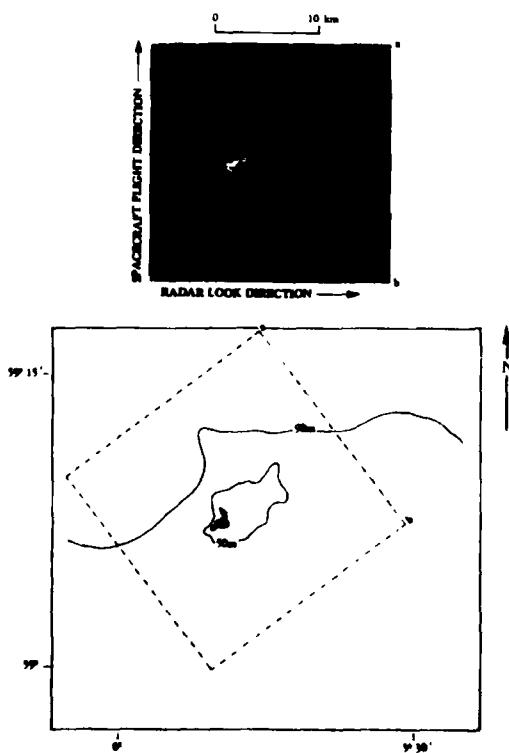
associated with a strong current flowing over a bottom feature in shallow (<50 m) water. These are perhaps the most common and readily identifiable bottom-induced patterns on SAR imagery, and several examples are presented in Figure 3. Because its velocity and internal structure are regulated by the bottom topography, a tidal current will alter the amplitude of the ocean surface Bragg wave to which the SAR is sensitive. The current's modulation of the ocean Bragg wave amplitude enables successful SAR imaging of many bottom features in shallow water.

Several researchers have previously reported surface signatures on radar imagery which are the

Fig. 2. Seasat SAR imagery and hydrographic chart of North Rona Rock (collected during Revolution 762, 19 August 1978) illustrating change in image tone (radar backscatter) associated with the shoal region around the island. (Seasat SAR data collected by the European Space Agency and optically processed at ERIM. Chart reproduced from DMA Chart No. 35200.)
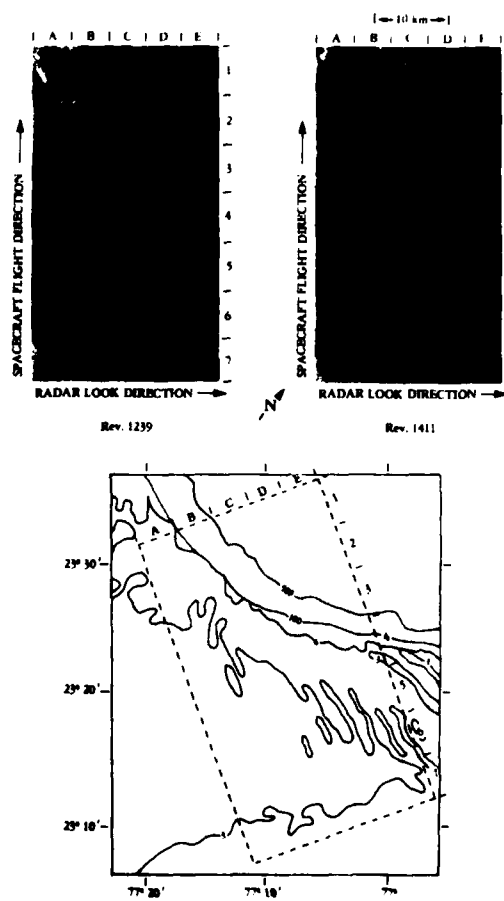
Fig. 3. Seasat SAR imagery and hydrographic chart of the Tongue of the Ocean: (1) Seasat Revolution 1239 (21 September 1978), (b) Seasat Revolution 1411 (8 October 1978), and (c) hydrographic chart of area. (Seasat digitally processed imagery courtesy of the Jet Propulsion Laboratory. Chart reproduced from DMA Chart Nos. 26300 and 27040, depths in fathoms).

result of a current flowing over the bottom feature. DeLoor and Brunsveld Van Hulten (1978) first described this phenomenon using real aperture radar imagery collected over the North Sea. Using Seasat SAR imagery, Kasischke et al. (1980) and Kenyon (1981) have reported detecting sand waves in the southeast corner of the North Sea. McLeish et al. (1981) reported sand waves detected on real aperture, side-looking airborne radar (SLAR) imagery collected off the Dutch coast. Finally, Kasischke et al. (1980) reported detecting sand waves and ridges in the Nantucket Shoals off the Massachusetts coast. The appearance of these current-induced shallow-water signatures is dependent on several factors, including the strength and direction of the tidal current, the shape, orientation, and depth of the bottom feature, and the magnitude of the surface wind. Shuchman (1982) determined the effects of several of these factors through an extensive hydrodynamic and electromagnetic modeling effort. The conditions required to observe these conditions include (1) a tidal current of at least 0.4 m/s (0.8 knots), and (2) a wind of at least 1 m/s (2 knots) but not greater than 7.5 m/s (15 knots), with at least some component in a direction parallel to the radar line-of-sight.

Figure 3 presents two examples of Seasat SAR images collected at the edge of the Great Bahama Bank, over a series of tidal bar belts in the southern end of the Tongue of the Ocean. The two images presented in Figure 3 were collected during Revolution 1411 (3 October 1978) and Revolution 1239 (21 September 1978). Comparison of the SAR images with the corresponding hydrographic chart (in Figure 3) reveals that the pattern located from B1 to E4 corresponds to the edge of the Great Bahama Bank, while the larger features (A2 to E5) correspond to the tidal bar belts in this area.

It should be noted that the patterns located over the tidal bar belts are "banded" in appearance, the pattern consisting of one band darker than the adjacent background image and one band lighter than the adjacent background image, and the patterns are reversed in the two images shown in Figure 3. Both of the images shown in Figure 3 were produced from Seasat SAR data which were digitally processed at the Jet Propulsion Laboratory. The differences in the patterns present over the tidal bar belts are not due to differences in the manner in which the images were processed, but are the result of different environmental conditions at the times the two data sets were collected.

The Tongue of the Ocean (TOTO) is a large (30 km by 120 km) steep-walled channel within the Great Bahama Banks. It has a depth of well over 1300 metres, while the surrounding Great Bahama Bank is generally less than ten metres deep. The tidal bar belts at the southern edge of the TOTO are a series of shallow sand banks (one to two metres

deep) with five to seven metre deep channels between them.

It is postulated that the patterns present on the Seasat imagery in Figure 3 were the result of an interaction between a tidal current flowing over the distinct bottom features in this area. Although the tidal range between high and low water is only about one metre in the Bahamas, tidal currents in the tidal bar belts region of the TOTO have been reported to be between 1 and 1.5 m/s (2 to 3 knots). During a study of tidal bar belts near Schooner Cay in the Bahamas, Ball (1967) noted the tide in this area was of the standing wave variety. Using tide gage and current meter recordings, he observed that maximum current over the tidal bar belts occurred midway between high and low water, with maximum velocities between 1 and 1.5 m/s (2 to 3 knots). In a study of the tidal bar belts of the TOTO, Palmer (1979) also noted that the maximum tidal currents in this region (estimated to be in excess of 1.5 m/s) occurred midway between high and low water.

The strong tidal-driven flow of water over the tidal bar belts and off the edge of Great Bahama Bank into the TOTO may sufficiently disturb the small scale surface roughness structure (i.e., the capillary and ultra-gravity waves) to cause a corresponding change in radar backscatter. It should be further noted that, although the surface patterns occur in the same locations in the two Seasat images in Figure 3, their appearance is different. These differences can be explained through the use of the hydrodynamic/electromagnetic model developed by Shuchman (1982), a qualitative synopsis of which is given in the following paragraphs.

Examination of tide tables for the Bahamas (Kline, 1978) indicates at the time of Revolution 1411 that the tide stage was four hours before low tide, indicating the presence of an ebb flow of water off the Great Bahama Bank into the TOTO. During Revolution 1239, the tide stage was one hour before high water, indicating the presence of a flood tide onto the Great Bahama Bank from the TOTO. Weather records from the Bahama Meteorological Office at Nassau showed a north wind with a velocity of 2.5 m/s was present during Revolution 1411 while an east wind of 4.8 m/s was present during Revolution 1239.

There are three environmental factors influencing the ocean surface roughness sensed by the SAR over sand banks such as those located at the Tongue of the Ocean. These factors are the current speed, the depth of water, and the wind speed and direction. In regions where the depth (and therefore the current speed) is changing rapidly, the roughness is influenced primarily by the rate of change of the current speed. A changing current tends to increase or decrease the amplitude of the

C-28

small capillary and ultra-gravity waves on the surface and make the surface rougher or smoother, depending on the direction of the current relative to the waves.

In areas where the depth is decreasing in the direction of the current, the surface velocity of the water will increase, resulting in a decrease in the amplitude of the surface capillary waves. In areas where the depth is increasing, the surface velocity will decrease, resulting in an increase in the amplitude of the surface capillary waves. This alternating increase and decrease of the water velocity results in the banded patterns imaged by the Seasat SAR over the sand banks.

In areas where the depth and the current are nearly constant, the surface roughness is governed primarily by the wind. The wind can be thought of as a restoring force which tends to bring the wave height or surface roughness into an equilibrium value which depends on the wind speed. Thus, if current variations cause the wave height to be decreased, the wind, given sufficient time, will return the wave height to its original value. These general statements are applied to the two particular cases illustrated in Figure 3 in the following paragraphs.

It should be noted that, although the following discussion is qualitative in nature, the observations made are based on a quantitative hydrodynamic/electromagnetic model developed and tested by Shuchman (1982). Computer simulated SAR imagery generated using this model of a tidal driven current flowing over sand banks in the English Channel and the Nantucket Shoals (almost identical to the situation occurring at the Tongue of the Ocean tidal bar belts) compared favorably to actual Seasat SAR images collected over these regions.

The bottom topography for the southern edge of the TOTO may be modeled and divided into seven regions as illustrated in Figure 4. The pattern of surface roughness variations depends on the current direction. For simplicity, in both of these cases the waves are assumed to be propagating in the same direction as the current. Essentially the same qualitative descriptions hold if the waves are propagating in the opposite direction to the current except that the phenomenon of wave blockage can occur if the current velocity changes from less than the group velocity of the waves to larger than this velocity. For a falling tide (Figure 4a) the following interactions occur:

Region 1: The depth is assumed to be uniform over a large enough area so that the wave height (surface roughness) has reached an equilibrium value for the existing wind speed and current conditions.

Region 2: Decreasing depth causes an increasing water current which in turn causes a progressive smoothing out of the surface roughness pattern
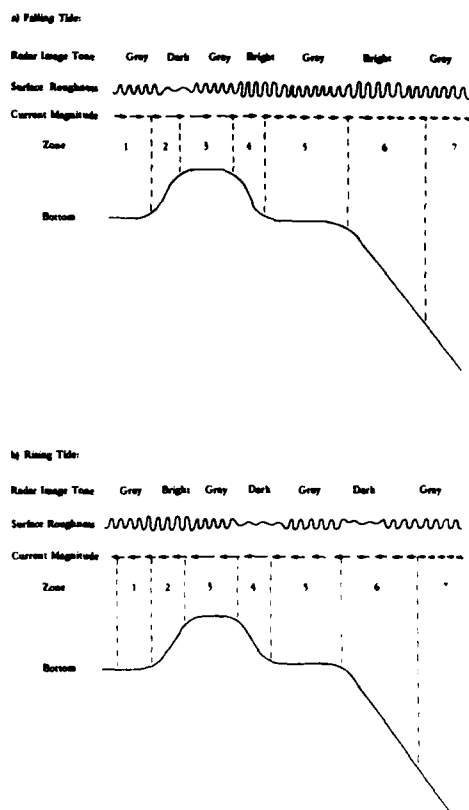

FIG. 4. Schematic diagram of interactions of current, bottom, and capillary waves and the resultant SAR image intensity variation.

(i.e., a decrease in the amplitude of the capillary and ultra gravity waves).

Region 3: The current remains constant while the wave height (surface roughness) is brought back into equilibrium by the action of the wind.

Region 4: Increasing depth causes a decreasing current, thus a compression of the surface, and a progressive roughening of the surface.

Region 5: Depth and current remain constant while the wave height readjusts into equilibrium with the wind.

Region 6: Similar to region 4, i.e., a decreasing current causes an increasing surface roughness.

Region 7: Similar to region 5, i.e., a gradual return to equilibrium with the given wind conditions.

The above model appears to adequately describe the patterns in Figure 3 for Revolution 1411, when an ebb tidal flow was present. Note in the SAR image collected over the southern portion of the TOTO that there exists a series of ridges, each of which has a banded appearance as described in regions 1 through 5 above.

For a rising (flood) tide (i.e., a current flowing onto the bank), the following interactions occur, as illustrated in Figure 4b:

Region 7: The depth is assumed to be uniform over a large enough area so that the wave heights (i.e., surface roughness) have reached an equilibrium with the existing wind speed and current conditions, resulting in an area of uniform radar backscatter.

Region 6: A decreasing water depth causes an increasing current which in turn causes a smoothing out (damping) of the surface capillary and ultragravity waves.

Region 5: Gradual return to equilibrium.

Region 4: Same as Region 6.

Region 3: Gradual return to equilibrium.

Region 2: An increasing water depth causes a decreasing current which in turn causes a compression of the surface waves and a progressive roughening of the surface with respect to the incident radar waves.

Region 1: Gradual return to equilibrium.

This model appears to adequately describe the patterns present on Revolution 1239 during a flood tide.

Thus, the surface patterns present on the two Seasat SAR images in Figure 3 are consistent with the hydrodynamic/electromagnetic model developed by Shuchman (1982) and illustrated in Figure 4. All Seasat SAR images collected over TOTO during ebb flows had patterns similar to those on Revolution 1411 imagery, while all those collected during flood conditions were similar to Revolution 1239 imagery.

DEEP WATER FEATURES

Several types of surface patterns observed on Seasat SAR imagery are believed to be the result of an interaction between a tidal driven current and bottom features in deep water regions such as seamounts, submarine ridges, banks, and edges of continental shelfs. These surface patterns are of two types: internal wave signatures and frontal boundary signatures. Figures 5 and 6 show Seasat SAR imagery collected over the same general region of the northeast Atlantic Ocean, which illustrate the two types of deep water patterns, while Figure 7 illustrates the bathymetry of this area.

Figure 5 presents examples of internal wave signatures. This imagery was collected during Revolution 599 on 7 August 1978 at approximately 2143 (GMT). It can be observed on this SAR image that the internal wave patterns occur over the Wyville-Thomson Ridge, which rises to within approximately 400 metres of the water surface from a surrounding deep water area of over 1000 metres in depth.

Figure 6 presents an example of a frontal boundary observed on Seasat SAR imagery collected during Revolution 762 on 19 August 1978 at approximately 0640 GMT. The curved dark line beginning at A4 and continuing to B9 is believed to
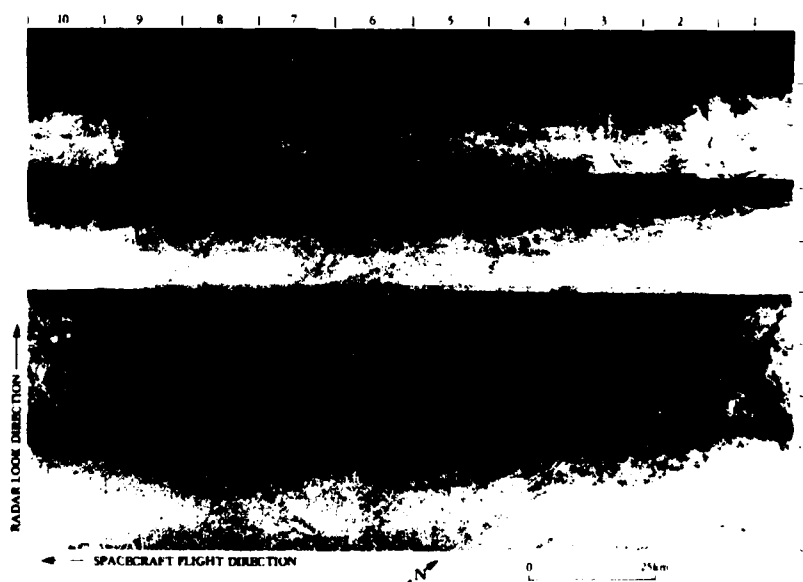

FIG. 5. Seasat SAR imagery of internal waves collected over the Wyville-Thomson Ridge (Revolution 599, 7 August 1978. Optically processed image courtesy of JPL).
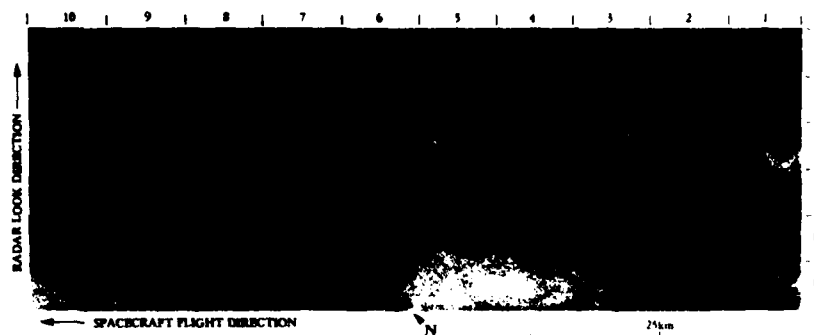
FIG. 6. Seasat SAR imagery of a frontal boundary collected over the Faeroe Bank Channel and Faeroe Ridge (Revolution 762, 19 August 1978. Optically processed image courtesy of JPL).

be a surface pattern caused by a frontal boundary. Its location appears to be in an area where the bottom is rising from the Faeroe Bank Channel to the Faeroe Shelf, over an area with a water depth between 600 and 1000 metres.

It is believed that both of these deep water signatures are the result of an interaction between a tidal current and a deep water bottom topographic feature. A current flowing over a deep water bottom feature can cause both internal waves and
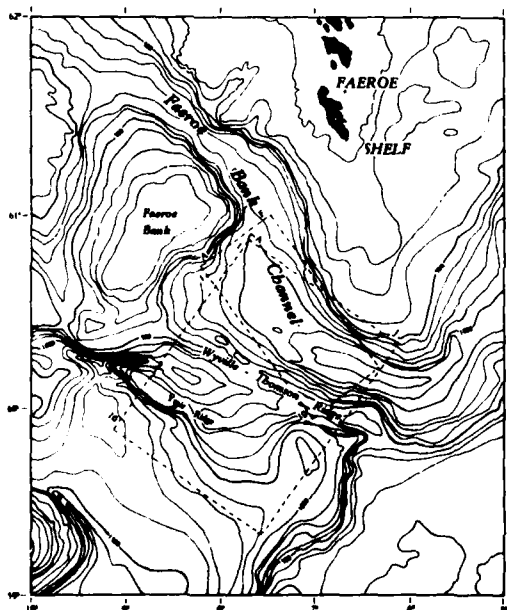

FIG. 7. Hydrographic chart of Northeast Atlantic Ocean showing locations of Figures 5 and 6 (After Institute of Oceanic Science (U.K.) Chart No. C6567, depths in metres).

areas of upwelling, which result in frontal boundaries.

There is little doubt that internal wave signatures have been observed on both aircraft and spaceborne SAR imagery collected over coastal areas (Brown et al., 1976; Shuchman and Kasischke, 1979; Gower and Hughes, 1979; Apel, 1981; Fu and Holt, 1982; Vesecky and Stewart, 1982). These patterns are visible because the energy field associated with the internal wave is sufficient to alter the small scale surface roughness to which the SAR is sensitive. Based on the results of this study and other recent research (Shuchman and Kasischke, 1979; Fu and Holt, 1982), it now appears that internal wave patterns can also be detected in deep water regions.

The generation mechanisms and sources responsible for internal waves have been extensively researched during recent years (Wunch, 1976; Muller and Olbers, 1975; Bell, 1975; Baines, 1979). Even so, the knowledge of the physical processes for internal wave generation is still very limited because a determination of the sources and sinks of internal waves requires a continuous record of the wave spectra (Garrett and Munk, 1975 and 1979).

Several sources for the generation of internal waves have been identified, including surface atmospheric effects, internal (oceanic) effects, and topographic effects (Thorpe, 1975). Surface atmospheric effects include traveling atmospheric pressure and stress, buoyancy flux, surface wave interactions, and Ekman layer instability. Internal (oceanic) generation can be caused by decay of large scale circulations and breaking baroclinic instability (of which there is very little known). The generation of internal waves due to topographic features is similar to the generation of the Lee waves by air flow over irregular surfaces. In the ocean, internal waves can be generated when a current (tidal or otherwise) flows over a deep

water feature such as a seamount, guyot, submarine ridge, or the edge of a continental shelf (Wunch, 1975; Bell, 1975; Baines, 1973).

It is suspected that tidal currents flowing over the bottom topographic features in the northeast Atlantic were forming internal waves along the thermocline present in this area. In many cases, the internal wave fields are felt to have sufficient energy to modulate the surface capillary wave structure, and hence allow the internal waves to be detected on SAR imagery, as illustrated in Figure 5.

The image presented in Figure 5 is not an isolated example of an internal wave pattern in a deep water region. Seasat imagery collected during the Joint Air/Sea Interaction over the northeast Atlantic (see Allan and Guymer, 1980) was examined during the present study. Within the total area covered by the 15 Seasat revolutions, 17 distinct bottom features existed. The bottom features in this area had depths ranging from less than 100 metres (Bill Bailey's Bank) to approximately 1000 metres (Hebrides Terrace Seamount). Seasat imaged the water surface over these features a total of 89 times. On 63 percent of these occasions, an internal wave pattern occurred. No internal wave patterns were present on the Seasat SAR imagery collected over the deep water basins (>2000 m) in the northeast Altantic.

Data presented by Bainbridge (1978) suggest that severe deformation of the thermocline can also occur as the result of a current flowing over a deep water bottom feature. This deformation is sometimes so severe as to force the colder, less saline, deeper water to the surface, resulting in an area of upwelling. This deep water upwelling would result in a frontal boundary between the two water masses. It has been shown that Seasat can detect frontal boundaries (Shuchman et al., 1979; Hayes, 1981; Cheney, 1981; Lichy et al., 1981), and it is believed that patterns like those in Figure 6 are patterns caused by frontal boundaries. On 38 percent of the occasions that Seasat imaged the water surface over a deep water bottom feature in the northeast Altantic, a pattern identified as a frontal boundary was present.

Summary and Conclusions

This study has shown that certain patterns on SAR imagery can be used to infer the presence of a bottom topographic feature located in the vicinity of the pattern. These SAR observed patterns can occur in both shallow coastal regions as well as in deeper offshore water. It has been demonstrated that SAR imagery can be used to detect submerged bottom features which are potentially hazardous to surface navigation.

The frequency with which bottom-induced surface patterns appear on spaceborne SAR imagery

must also be determined in order to define the utility of this data source for providing information in updating nautical charts. Analysis of Seasat imagery collected over the English Channel showed that the larger sand banks were detected 75 percent of the time while the smaller sand banks were detected only 50 percent of the time. Analysis of the Seasat imagery collected over the Tongue of the Ocean showed that distinct surface patterns occurred more than 90 percent of the time over the tidal bar belts and 70 percent of the time over the edge of the Great Bahama Bank. Finally, in the deep water study, an internal wave pattern was present on 63 percent of the Seasat imagery collected over deep water features such as a seamounts, ridges, or banks.

Currently, all SAR imagery collected by the Seasat SAR and the Shuttle Imaging Radar (SIR-A) is being examined and the number of times a surface pattern occurs, or does not occur, over a bottom feature is being tabulated.

Many spaceborne SAR systems will be deployed during the next decade. These SARs include Radarsat (Canada), Earth Resources Satellite-1 (ESA), Earth Resources Satellite-1 (Japan), SIR-B (USA), and the Microwave Remote Sensing Experiment (West Germany), to name a few. It is therefore highly likely that SAR imagery will be collected over areas where insufficient hydrographic information exists. This SAR imagery will certainly represent a data source for identifying and locating uncharted or altered bottom features for those organizations with the responsibility in updating nautical charts.

References

Allan, T. D., and T. H. Guymer, 1980. Seasat and JASIN, Int. J. Remote Sensing, 1, pp. 261–267.

Apel, J. R., 1981. Non-Linear Features of Internal Waves as Derived from the Seasat Imaging Radar, in Oceanography from Space, ed. by J. F. R. Gower, Plenum Press, New York, pp. 525–533.

Bainbridge, A. E., 1980. Geosecs Atlantic Expedition—Volume 2: Sections and Profiles, U.S. Government Printing Office, Washington, D.C., 198 p.

Baines, P. G., 1979. Observations of Stratified Flow Over Two-Dimensional Obstacles in Fluid of Finite Depth, *Tellus, 31*, pp. 351–371.

Ball, M. M., 1967. Carbonate Sand Bodies of Florida and the Bahamas, *Journal of Sedimentary Petrology, 37*, pp. 556–591.

Beal, R. C., P. S DeLeonibus, and I. Katz (eds.), 1981. *Spaceborne Synthetic Aperture Radar for Oceanography*, Johns Hopkins Univ. Press, Baltimore, MD, 215 p.

Bell, T. H., Jr., 1975. Topographically Generated Internal Waves in the Open Ocean, *J. Geophys. Res., 80*, pp. 320–327.

Brown, W. E., Jr., C. E. Elachi and T. W. Thompson, 1976. Radar Imaging of Ocean Surface Patterns, *J. Geophys. Res., 81*, pp. 2657–2667.

Cheney, R. E., 1981. A Search for Cold Water Rings with Seasat, in *Spaceborne Synthetic Aperture Radar for Oceanography*, ed. by R. C. Beal, P. S. DeLeonibus, and I. Katz, Johns Hopkins Univ. Press, Baltimore, MD, pp. 161–170.

DeLoor, G. P. and H. W. Brunsveld Van Hulten, 1978. Microwave Measurements Over the North Sea, *Boundary-Layer Meteorol., 13*, pp. 119–131.

Fu, L., and B. Holt, 1982. *Seasat Views Oceans and Sea Ice with Synthetic Aperture Radar*, JPL Publication No. 81-120, 200 p.

Garrett, C., and W. Munk, 1975. Space-Time Scales of Internal Waves: A Progress Report, *J. Geophys. Res., 80*, pp. 291–297.

———, 1979. Internal Waves in the Ocean, *Ann. Rev. Fluid Mech., 11*, pp. 339–369.

Gonzalez, F. I., R. A. Shuchman, D. B. Ross, C. L. Rufenach, and J. F. R. Gower, 1981. Synthetic Aperture Radar Wave Observations During GOASEX, *Oceanography from Space*, ed. by J. F. R. Gower, Plenum Press, New York, pp. 459–467.

Gower, J. F. R., 1981. *Oceanography from Space*, Plenum Press, New York, NY, 997 p.

Gower, J. F. R., and B. A. Hughes, 1979. Radar and ship Observations of Coastal Sea Surface Roughness Patterns in the Gulf of Georgia, *Proc. Thirteenth Int. Symp. Remote Sens. Environ.*, Ann Arbor, MI, pp. 103–115.

Hammack, J. C., 1977. Landsat Goes to Sea, *Photogrammetric Engineering and Remote Sensing, 43*, pp. 683–391.

Haslam, D. W., 1975. *Report by the Hydrographer of the Navy*, N.P. 130, Tauton, England.

Hayes, R. M., 1981. SAR Detection of the Gulf Stream, in *Spaceborne Synthetic Aperture Radar for Oceanography*, ed. by R. C. Beal, P. S. DeLeonibus, and I. Katz, Johns Hopkins Univ. Press, Baltimore, MD, pp. 146–160.

Jordan, R. L., 1980. The Seasat-A Synthetic Aperture Radar System, *IEEE J. Oceanic Eng., OE-5*, pp. 154–164.

Kapoor, D. C., 1976. International Cooperation in Hydrography, *International Hydrographic Review*, Vol. LIII(2), Monaco.

Kasischke, E. S., 1980. *Extraction of Gravity Wave Information from Synthetic Aperture Radar Data*, Univ. of Mich. M.S. Thesis, 108 p.

Kasischke, E. S., R. A. Shuchman, and J. D. Lyden, 1980. *Detection of Bathymetric Features Using SEASAT Synthetic Aperture Radar—A Feasibility Study*, ERIM Final Report No. 135900-2-F₂, 77 p.

Kasischke, E. S., D. R. Lyzenga, R. A. Shuchman, Y. S. Tseng, B. S. Termaat, B. A. Burns, and G. A. Meadows, 1982. *The Use of Synthetic Aperture Radar to Detect and Chart Submerged Navigation Hazards*, ERIM Final Report No. 15520-1-F, Ann Arbor, MI, 221 p.

Kenyon, N. H., 1981. Bedforms of Shelf Seas Viewed with SEASAT Synthetic Aperture Radar, in *Advances in Hydrographic Surveying*, ed. M. J. Wright, Society for Underwater Technology, London, pp. 67–73.

Kline, H., 1978. *Cruising Guide to the Bahamas*, Miami, Florida.

Licby, D. E., M. G. Mattie, and L. J. Mancini, 1981. Tracking of a Warm Water Ring Using Synthetic Aperture Radar, in *Spaceborne Synthetic Aperture Radar Imagery for Oceanography*, ed. by R. C. Beal, P. S. DeLeonibus, and I. Katz, Johns Hopkins Univ. Press, Baltimore, MD, pp. 171–182.

Lyzenga, D. R., 1981. Remote Bathymetry Using Active and Passive Techniques, *1981 International Geoscience and Remote Sensing Symposium Digest*, Washington, D.C., pp. 777–786.

McLeish, W., D. J. P. Swift, R. B. Long, D. Ross, and G. Merrill, 1981. Ocean Surface Patterns Above Seafloor Bedforms as Recorded by Radar, Southern Bight of North Sea, *Mar. Geol., 43*, pp. M1–M8.

Muller, P., and D. J. Olbers, 1975. On the Dynamics of Internal Waves in the Deep Ocean, *J. Geophys. Res., 80*, pp. 3848–3860.

Palmer, M. S., 1979. *Holocene Facies Geometry of the Leeward Bank Margin, Tongue of the Ocean, Bahamas*, University of Miami, Master's Thesis, Coral Gables, Florida.

Raney, R. K., 1971. Synthetic Aperture Imaging Radar and Moving Targets, *IEEE Trans. Aerospace Elect. Syst., AES-7*, pp. 499–505.

Raney, R. K., and R. A. Shuchman, 1978. SAR Mechanism for Imaging Waves, *Proc. Fifth Canadian Symp. on Remote Sensing*, Victoria, B. C.

Shemdin, O. H., 1980. The Marineland Experiment: An Overview, *Trans. Amer. Geophys. Union, 61*, No. 38, pp. 625–626.

Shuchman, R. A., 1981. Processing Synthetic Aperture Radar Data of Ocean Waves, *Oceanography from Space*, ed. by J. F. R. Gower, Plenum Press, New York, pp. 477–496.

———, 1982. *Quantification of SAR Signatures of Shallow Water Ocean Topography*, Univ. of Mich. PhD Dissertation, Ann Arbor, MI, 130 p.

Shuchman, R. A., and E. S. Kasischke, 1979. The Detection of Oceanic Bottom Topographic Features Using SEASAT Synthetic Aperture Radar Imagery, *Proc. Thirteenth Int. Symp. Remote Sens. Environ.*, pp. 1277–1292.

———, 1981. Refraction of Coastal Ocean Waves, in *Spaceborne Synthetic Aperture Radar for Oceanography*, ed. by R. C. Beal, P. S. DeLeonibus, and I. Katz, Johns Hopkins Univ. Press, Baltimore, MD, pp. 128–135.

Shuchman, R. A., C. L. Rufenach, F. I. Gonzalez, and A. Klooster, 1979. The Feasibility of Measurement of Ocean Surface Currents Using Synthetic Aperture Radar. *Proc. Thirteenth Int. Symp. Remote Sens. Environment*, Ann Arbor, MI, pp. 93–102.

Shuchman, R. A., A. L. Maffett, and A. Klooster, 1981. Static Modeling of a SAR Imaged Ocean Scene, *IEEE J. Oceanic Eng.*, OE-6, pp. 41–49.

Thorpe, S. A., 1975. The Excitation, Dissipation, and Interaction of Internal Waves in the Deep Ocean, *J. Geophys. Res.*, 80, pp. 328–338.

Vesecky, J. F., and R. H. Stewart, 1982. The Observation of Ocean Surface Phenomena Using Imagery from the Seasat Synthetic Aperture Radar—An Assessment. *J. Geophys. Res.*, 87, pp. 3397–3430.

Vesecky, J. F., H. M. Assal, R. H. Stewart, R. A. Shuchman, E. S. Kasischke, and J. D. Lyden, 1982. Seasat-SAR Observations of Surface Waves, Large Scale Surface Features and Ships During the JASIN Experiment, *1982 Int. Geoscience and Remote Sensing Symposium Digest*, pp. WP-1, 1.1–1.6.

Wright, J. W., 1966. Backscattering from Capillary Waves with Application to Sea Clutter, *IEEE Trans. Antenna Propagat.*, AP-14, pp. 749–754.

Wunch, C., 1976. Geographical Variability of the Internal Wave Field: A Search for Sources and Sinks, *J. Phys. Ocean.*, 6, pp. 471–485.

Zwamborn, J. A., 1979. Analysis of Causes of Damage to Sines Breakwater, *Coastal Structures 79, Vol. 8*, American Society of Civil Engineers, New York, NY, pp. 422–441.

(Received 5 September 1982; revised and accepted 13 March 1983)

Eighteenth International Symposium on Remote Sensing of Environment

Paris, France
1-5 October 1984

Organized and conducted jointly by the Centre National d'Etudes Spatiales (CNES) and the Environmental Research Institute of Michigan (ERIM), the Symposium will address state-or-the-art capabilities and techniques, emphasizing current and future capabilities for remote sensing from space.

The technical program will include conventional presentations and multidisciplinary poster sessions formulated to address

- Current techniques and operational applications, emphasizing land and ocean monitoring, including Earth resources and environmental surveys, inaccessible regions, disaster assessment, vegetation mapping, and cartographic applications.
- Advanced techniques and methodology, including statistical methods, inventory strategies, simulation methods, multiple sensors and observations, angular variations, topographic effects, data handling, processing, and analysis.
- Socio-economic considerations, including economic impact, training and technology transfer, commercial operation, and the role of industry.
- Future Earth observation from space. Advanced sensors and sensor systems; data collection, transmission, reception, and dissemination; and data processing and analysis techniques.

For more information please contact

Alain Gaubert
CNES
42, rue Cambronne
75015 Paris, France
Tele. 1.306.26.40

Jerald J. Cook
ERIM
P. O. Box 8618
Ann Arbor, MI 48107
Tele. (313) 994-1200

OBSERVATIONS OF INTERNAL WAVES AND FRONTAL BOUNDARIES ON SEASAT SAR IMAGERY
COLLECTED OVER THE EASTERN NORTH ATLANTIC OCEAN*

E.S. Kasischke

Radar Division
Environmental Research Institute of Michigan
Ann Arbor, Michigan

Y.C. Tseng and G.A. Meadows

Department of Atmospheric and Oceanic Sciences
The University of Michigan
Ann Arbor, Michigan

A.K. Liu

Dynamics Technology, Incorporated
Torrance, California

ABSTRACT

The locations of all frontal bound-
ary and internal wave patterns on 21
passes of Seasat imagery collected over
the eastern North Atlantic Ocean were
plotted on a bathymetric chart of the
region. These plots revealed that the
patterns always occurred over or close
to a deep water bottom feature, such as
a ridge, seamount, bank or shelf. At no
time did a pattern occur over a deep
water basin. An internal wave pattern
appeared in Seasat SAR imagery 67 percent
of the time Seasat passed over a deep
water feature, while frontal boundary
patterns appeared 28 percent of the time.
The causes of internal wave and frontal
boundary patterns on the Seasat SAR
imagery have been identified as Lee wave
generation and deep water upwelling,
respectively. Research which combines
oceanic, subsurface measures with the
Seasat SAR imagery is definitely war-
ranted to further study these patterns.

1. INTRODUCTION

The primary mission of the Seasat synthetic aperture radar (SAR) was to image gravity
waves, ice and other oceanic surface patterns that are a result of interval waves, currents,
frontal boundaries, oil slicks and meteorological occurrences. In collecting over 100 million

1193

square kilometers of SAR imagery from space, Seasat provided the oceanographic and remote sensing communities with an abundance of data to examine.

Numerous studies in the past have documented the presence of internal wave and frontal boundary patterns on SAR images in shallow (<100 m), coastal areas. An early Seasat study of imagery collected during Rev. 762 between Scotland and Iceland reported numerous large wave-like patterns in deep-water (>200 m) regions (Shuchman and Kasischke, 1979). Here, we report on the continuation of this earlier study on the appearance of large-scale surface patterns on Seasat SAR imagery collected over the northeast Atlantic Ocean. These large-scale surface patterns have been tentatively identified as surface manifestations of internal waves and regions of upwelling which result in frontal boundaries.

We will first present a background section which contains discussions on the Seasat SAR, SAR imaging of the ocean surface and past investigations on internal wave and frontal boundary patterns on SAR imagery. This is followed by a section which presents examples of deep-water internal wave and frontal boundary patterns observed on the Seasat SAR imagery and discusses the occurrence of these features on the 21 passes of Seasat data examined during this study. Finally, two first-order hydrodynamic models are presented which explain why the observed patterns were detected by the Seasat SAR.

2. BACKGROUND

The data to be presented in this paper were collected by the Seasat satellite. Among the instrumentation carried by Seasat, which was launched during June of 1978, was an imaging synthetic aperture radar (SAR). This satellite collected over 500 passes of SAR data before suffering a catastrophic power loss in October of 1978. The SAR on board Seasat was an L-band (23.5 cm wavelength) radar. It collected 25 x 25 m resolution imagery with a ground swath-width of 100 km and a length of up to 4000 km, and viewed the surface of the earth with an average incidence angle of 20°. For a detailed description of the Seasat SAR system and its mission, see Jordan (1980); Beal, et al. (1981), or Fu and Holt (1982).

An imaging radar such as the Seasat SAR is an active device that senses the environment with short wavelength electromagnetic waves. As an active sensor, the Seasat SAR provided its own illumination in the microwave region of the electromagnetic spectrum and thus was not affected by diurnal changes in emitted or reflected radiation from the earth's surface. Additionally, the 23.5 cm wavelength utilized by the Seasat SAR allowed for imaging the earth's surface through clouds and light rain.

The principle in imaging any ocean surface with a radar is that the backscatter of micro-wave energy (echo) received by the radar contains information on the roughness characteristics (shapes, dimensions and orientations) of the reflecting area. Parameters that influence the SAR image of the ocean surface include the motion of the scattering surfaces, coherent speckle, system resolution and non-coherent integration as well as the surface roughness. In addition, the orientation of ocean surface patterns with respect to the radar "look" direction can be influencing parameters.

Several scattering models exist that attempt to explain ocean surface image formation with synthetic aperture radars. These models are of two types: static models that depend on instantaneous surface features, and dynamic models that employ surface scatterer velocities.

Three static models have been suggested to describe the radar scattering of energy from large areas on the ocean surface. These three scattering models include: (1) the specular point model which is most appropriate for small incidence angles, (2) the Bragg-Rice scattering model, described below, and (3) a Rayleigh scattering model which is often used in terrestrial earth scattering calculations. There is general consensus within the radio-oceanography scientific community that a Bragg-Rice scattering theory best explains the SAR observed backscatter values obtained from the ocean surface for incidence angles between 20° and 60° (Shuchman, et al., 1981). The Bragg-Rice scattering model is based on a well known phenomena in the study of crystals, grating, and periodic structures. If one considers the random ocean surface to be represented by a combination (i.e., spectrum) of periodic surfaces, then the spectrum region which satisfies the backscatter phase matching condition will be the main contributor to the backscatter cross section. Sometimes in the literature, this phase matching

1194

of the small ocean Bragg waves with the radar electromagnetic energy is termed a resonance phenomenon; more correctly stated, it should be termed a constructive interference between the electromagnetic and ocean waves.

Pioneering theoretical and experimental work by Wright (1966) at the Naval Research Laboratory (NRL) demonstrated the general validity of a Bragg scattering model for an ocean surface imaged by radar. In a series of wave tank measurements using 3 and 25 cm wavelength continuous wave (CW) Doppler radars, Wright demonstrated that Bragg scattering, that is, transmitted radar energy with wave number K, interacts in a resonant or interference fashion with ocean surface waves with wave number K_w, such that

$$K_w = 2K \sin \theta, \tag{1}$$

where $K_w = 2\pi/L$ and $K = 2\pi/\lambda$, (L and λ are the wavelengths of the surface waves and the radar, respectively), and θ is the incidence angle. Shuchman, et al. (1981) showed that a Bragg scattering equation satisfactorily explained the radar backscatter return from SAR using data collected during the Marineland experiment (for a discussion of the Marineland experiment, see Shemdin, 1980). It should be noted that radar data of large ocean areas (1 x 1 km) were averaged in that analysis. Thus based on the above, the principal radar reflectivity mechanism of imaging ocean surfaces is via the capillary and small gravity waves which produce Bragg scattering (Raney and Shuchman, 1978).

Synthetic aperture radars are also sensitive to the motion of scatterers present in the imaged scene (Raney, 1971). Effects of scatterer motion on SAR imagery may include: (1) image displacement, smearing and loss of focus in the azimuth direction, and (2) loss of focus in the range direction. Some of these effects can be removed during processing of the SAR signal histories by making appropriate adjustments to the processor (Shuchman, 1981). Effects which cannot be removed during processing may reduce the detectability of gravity waves, but are not expected to have a large influence on other ocean surface patterns.

A variety of processes can alter the surface Bragg waves, resulting in a distinct pattern on SAR imagery. These include oceanic processes (currents, gravity waves, internal waves, slicks, local water depth variations, water temperature and salinity), climatic processes (wind, rain and air temperature) and man-made phenomena (ships, buoys and oil spills). It is the hydrodynamic interaction between several of oceanic processes and a distinct bottom feature which allows that feature to be detected on SAR imagery. Examples of these bottom-induced, deep-water surface patterns will be presented in this paper. For examples of other surface patterns on Seasat SAR imagery, see Gower (1981); Beal, et al. (1981); or Fu and Holt (1982).

Internal wave patterns have been detected on a variety of remotely-sensed images. They have been detected on aerial and spacecraft photography (Osborne and Burch, 1980; Gower and Hughes, 1979), Landsat MSS imagery (Apel, et al., 1974; 1975; 1975a; 1976) and aircraft and spacecraft SAR imagery (Brown, et al., 1976; Elachi and Apel, 1976; Shuchman and Kasischke, 1979; Gower and Hughes, 1979; Apel, 1981; Fu and Holt, 1982; Ford, et al., 1983; Trask and Briscoe, 1983; Alpers and Salusti, 1983; and Hughes and Gower, 1983). Most of the above studies do not present any direct evidence that the observed patterns are due to internal waves, but the patterns are widely believed to be internal wave surface signatures. An excellent field study by Hughes and Gower (1983; see also Gower and Hughes, 1979) actually measured a tidally-driven internal wave packet as it was being imaged by an aircraft SAR and Seasat. This study verified that SARs can detect surface manifestations of internal wave fields.

An early Seasat study by Shuchman and Kasischke (1979) indicated the presence of internal "wave-like" patterns on Seasat-SAR images in deep-water regions. Since then, deep-water internal wave patterns have been reported on Seasat imagery by Fu and Holt (1982) and SIR-A imagery by Ford, et al. (1983).

There appears to be little question that ocean current or frontal boundaries can frequently be observed on SAR images, although the reason for their appearance is not yet understood. Current boundaries were first noted on aircraft SAR imagery by Moskowitz (1973). Since then, frontal boundaries have been extensively studied by both aircraft SARs (Larson,

1195

et al., 1976; Shuchman, et al., 1977; 1979; Weissman, et al., 1980; Shuchman, et al., 1981) and spaceborne SARs (Hayes, 1981; Shuchman, et al., 1979; Shemdin, et al., 1980a; Mattie, et al., 1980; Cheney, 1981; Lichy, et al., 1981; Shuchman, et al., 1981c). Current velocity gradients (du/dx) on the order of 10^{-3} sec^{-1} appear to be detectable (Larson, et al., 1976), and the sensing of current boundaries apparently occurs for a wide range of wind speeds (3-10 m/s) and air-sea temperature differences (0.1 - 10°C).

The appearance of frontal boundaries on SAR images was at first thought to be due to a Doppler-induced image displacement (Larson, et al., 197·), but this notion has been dis-counted by the observation of current boundaries at all radar look direction orientations on Seasat data (Hayes, 1981). Although the Doppler mechanism may be a contributing factor in some cases, it is now felt that the main reason for the appearance of current boundaries on SAR imagery is either a stress-induced variation in surface roughness in the area of the shear, or a difference in the surface roughness of the water masses.

3. METHODS

The data set for this analysis was the Seasat SAR imagery collected over the eastern half of the North Atlantic Ocean. These data were available because of the satellite receiving station which was operating at Oak Hangar, England for the European Space Agency. The 21 passes of imagery used in this study are summarized in Table 1.

There were two parts to the present analysis. The first part involved investigating the relationship between the internal wave and frontal boundary patterns and the deep-water bottom features in this region. The second part was to develop a first order, hydrodynamic model as to why the patterns appeared on the Seasat imagery.

In order to study the relationship between surface patterns on Seasat SAR imagery and the deep-water bottom features, the following procedure was used: First, the location of the ground coverage of the Seasat SAR was obtained by consulting the satellite data record (SDR) for each pass. (A SDR contains a series of ground latitude and longitude coordinates for specific times during a Seasat pass. Most of the Seasat SAR images contained annotations of the time the data were collected. Therefore, the location of a particular surface pattern could be identified by noting the time when the pattern occurred during that orbit.) The ground coverage of each pass was then marked on an overlay placed on the chart. Next, the locations of all internal waves and frontal boundaries detected on each pass were noted and then these locations marked on the overlay. Finally, a surface pattern was said to be asso-ciated with a bottom feature if its location was within 10 kilometers of that feature.

The bottom morphology of the eastern North Atlantic Ocean is quite well known due to the extensive hydrographic surveys conducted in this region (see e.g., Roberts, et al., 1979). This area contains a large number of submarine ridges, seamounts, banks and shelfs. Table 2 lists the major bottom features in this area, along with the shallowest contour interval charted for that feature and the depth of the adjacent deep water.

The second part of the analysis was performed by analyzing the environmental conditions which were most likely present at specific sites for a given set of patterns observed in a single pass of Seasat SAR imagery, and then formulating a first-order hydrodynamic/ electromagnetic model which explains the SAR-observed surface pattern.

4. OBSERVATIONS

In this section, we will first present examples of internal wave and frontal boundary patterns from the study area. This will be followed by a summary of the relationship of these patterns to the deep-water bottom features. Figure 1 is a diagram of the positions of the Seasat images presented in this section.

The JPL-optically processed SAR imagery in Figure 2 was collected during Rev. 599 (7 August 1978) as Seasat passed over the Wyville-Thomson Ridge. The corresponding bathymetric chart for this coverage is presented in Figure 3. From Figure 2, it can be seen that there are numerous internal wave signatures. Note on the SAR image that the internal waves are both range (e.g., C/D1 to C/D2) and azimuth (e.g., A9 to D9) traveling. The internal waves in the

1196

lower left corner of the SAR image appear to occur over the Ymir Ridge; the internal waves in the middle of the image appear over the Wyville-Thompson Ridge; and those at the top of the image occur over the Faeroe Bank Channel.

Surface measurements collected at the time of the Seasat overpass indicate a wind of 6.9 m/s from the north, and a wave field with a significant wave height of 1.1 meters, and a dominant wavelength of 71 meters propagating towards 200°(T).

The SAR imagery in Figure 4 was collected during Revolution 958 (1 September 1978) as Seasat passed over the Iceland-Faeroe Rise. The corresponding bathymetric chart for this area is presented in Figure 5. The internal wave patterns in the top half of Figure 4 occur in an area where the water depths are between 600 and 1000 meters. It is in an area where the ocean floor is rising from the deep (>2500 m) Iceland Basin to the relatively shallow (500 m) Iceland-Faeroe Rise. The dark areas of Figure 4 (J7 and D2) are believed to be atmospheric events.

Surface measurements obtained near the test area indicates the gravity wave field present at the time of Revolution 958 had a significant wave height of 1.4 meters, a dominant wavelength of 147 meters and was propagating towards 176°(T). Surface winds had a speed of 7.2 m/s, but no direction was given.

Figure 6 presents Seasat SAR imagery collected during Rev. 762 (19 August 1978). The corresponding bathymetric chart for this region is presented in Figure 7. This image contains both internal wave patterns as well as a frontal boundary pattern. There are two distinct sets of internal wave packets present. One set (F5 to J8) can be seen on the West Shetland Shelf, while the other lies along the southern edge of the Wyville-Thompson Ridge (C3 to H4). The frontal-boundary pattern in this image can be seen to lie along the edge of the Faeroe Shelf (A6 to B9).

Surface measurements obtained near the time of the Seasat overpass indicate a strong wind (12.5 m/s) from the south and a swell with a significant wave height of 3.0 m/s and a wavelength of 210, propagating toward 60°(T) was present.

Not all surface signatures believed to be related to deep-water, bottom topographic features are as clear and distinct as the examples presented previously. Figure 8 was collected by Seasat during Rev. 791 (21 August 1978) as it passed over the Anton Dohrn Seamount. The corresponding bathymetry for this imagery is presented in Figure 9. The internal wave signatures collected over the Anton Dohrn Seamount are quite subtle. Three groups of internal waves (B6 to C6, D/E6 to D/E8, and A8) occur over this seamount , which is quite steep sided, as can be seen by the narrow spacing of the contour lines in Figure 9.

The sea truth collected near the test area indicates the winds were quite strong, with a speed of 13 m/s from the southwest. The surface gravity wave field had a significant wave height of 3.1 m, a dominant wavelength of 151 m and was propagating towards 45°(T).

Table 3 summarizes the occurrences of the internal wave and frontal boundary patterns over the 26 deep-water bottom features in the study area. Table 4 summarizes the number of times each Seasat revolution passed over a deep-water bottom feature and the total number of internal wave and frontal boundary patterns appeared over a bottom feature in that pass.

At no time did an internal wave pattern or frontal boundary pattern appear on the Seasat imagery over a deep-water region without a bottom feature in the immediate vicinity. From Table 3, it can be seen that 67 percent of the time the Seasat SAR imaged the ocean surface over a deep-water bottom feature, an internal wave pattern was present. The corresponding figure for frontal boundary patterns was 28 percent. The figure for internal waves and frontal boundary patterns combined is 82 percent. These figures suggest a strong correlation between the bottom features and the SAR-observed surface patterns. This relationship will be further analyzed in the next section.

1197

5. HYDRODYNAMIC MODELS

The Seasat SAR imagery presented in Figure 6 was used as a base to formulate first-order hydrodynamic models to explain why the internal wave and frontal boundary patterns occur. Figure 10 combines a line drawing of the internal waves and a frontal boundary observed in Figure 6 with the corresponding bathymetric chart for this area. From Figure 10, it can be seen that there are numerous internal wave signatures. The internal waves in the middle of the image appear to be generated over the Wyville-Thomson Ridge. Near the lower right corner of the image, three wave packets are visible. It is to be noted that no waves were generated on the north side of the ridge.

The dominant bottom features in this region are a broad, saddle-like valley on the east side of the ridge, and a 90° sector of deep water extending out from the ridge, as shown in Figure 11. The ridge has the characteristic scales of approximately 10 km in both the longitudinal and transverse direction. The minimax of the bathymetric saddle is at a depth of about 450 m.

Based on the bathymetry, it seems that the wave packets are produced by lee wave formation—a mechanism similar to the undulation of the jet stream as it passes over a mountain ridge. Figure 12 schematically illustrates the stages that are hypothesized during the production of solitary internal wave packets. As the strong semidiurnal tidal current flows north into the Faeroe Bank Channel, an internal lee wave forms on the northern edge of the ridge. As the tidal flow goes to zero six hours later, the lee wave, trying to maintain its group velocity relative to the current, escapes south over the ridge barrier back into the deep water, emerging as a packet of solitary waves. This phenomenon has previously been studied by Holbrook, et al. (1983) in the Sulu Sea. The initial waveform then can be viewed as a localized source that immediately begins to propagate, and evolves into a series of solitary waves while undergoing radial spreading, encountering variable topography and slowly losing energy through dissipation. The disappearance of internal waves on the north side of the ridge is probably because there is no strong tidal current flowing south across the ridge; most of the tidal current may flow along the Faeroe Bank Channel.

Based on the Seasat SAR image, the wave packets in deep water over the Wyville-Thomson Ridge have the following properties:

1. Wave packets are separated by distances of the order of 14 km.

2. Wave speed is estimated to be 0.31 m/s based on the assumption of a semidiurnal tidal origin.

3. Wave packets in this region contain about five waves with packet width about 5 km.

4. Wavelengths are between 500 m and 1000 m.

5. The crests are curved in a horizontal plane with their convex sides pointed in the direction of propagation.

Although no _in situ_ measurements are available, it is believed this area is dominated by tidal currents with velocities of less than 0.5 m/s at the surface. Figure 13 shows the profiles of potential temperature, salinity and sigma theta generated from data collected over the Iceland-Faeroe Rise during the Atlantic Expedition in August 1972 (Bainbridge, 1980). Station 19 is the measurement closest to the Wyville-Thomson Ridge area. As evident from Figure 13, a mixed layer of 40 m is dominant in this area during the summer. Based on the two-layer finite depth model, the linear wave speed is given by

$$C_0 \simeq \left[\frac{\Delta\rho}{\rho} \frac{g}{k} \frac{1}{\coth kH_1 + \coth kH_2} \right]^{1/2}. \qquad (2)$$

Near the Wyville-Thomson Ridge, $\Delta\rho/\rho \simeq 0.6 \times 10^{-3}$, $H_1 \simeq 40$ m, $H_2 \simeq 260$ m, $2\pi/k \simeq 500$ m, and thus the wave speed is approximately 0.40 m/s, depending on the water depths. This value is consistent with the estimated wave speed of 0.31 m/s from the SAR image. Based on the

1198

wavelength, the wave amplitude is estimated to be between 10 and 15 m. Note that the effect of shear is important in this case, since the wave speed is slow compared with the background current. Also, the bottom topography near the West Shetland Shelf is complex, which influences the evolution of wave packets, as shown in Figure 10. A similar solitary wave theory developed by Liu, et al. (1983) can be applied here. However, due to the limited scope of this investigation, the detailed analysis and calculations will have to wait until sea-truth data are available.

Liu (1983) also modeled the surface strain rate produced by shallow water (coastal) internal waves. He then used this surface strain as an input to an electromagnetic model and simulated a SAR image of the internal wave, which compared favorably to the Seasat image. A similar surface strain is expected to occur for the deep-water internal waves, resulting in the patterns observed on the JASIN imagery.

The curved, dark line, as indicated by the dashed line in Figure 10, is believed to be a surface pattern caused by a frontal boundary. Its location appears to be over the edge of the Faeroe Shelf, and closely matches the 800 meter bottom contour.

As shown in Figure 13, the deep water upwelling results in a frontal boundary over the Icelandic-Faeroe Rise. The relationship of the front to local upwelling topographic mixing may be described by the following process. Figure 14 shows the cross-section diagram of bottom topography of the Wyville-Thomson Ridge. It appears that the tidal current flowing over the ridge through another saddle-like valley on the west-side of the ridge forces the deep water isotherms up toward the surface. To illustrate this mechanism for frontal boundary generation, a schematic diagram of deep water upwelling over the Faeroe Bank Channel is shown in Figure 15. Therefore, the frontal boundary seems to represent simply a surface intersection of the seasonal thermocline. The combination of frontal slope and current shear could yield information on density contrast across the front.

6. SUMMARY

Twenty-one passes of Seasat SAR imagery collected over the eastern North Atlantic Ocean were examined for the presence of internal wave and frontal boundary patterns. All passes contained such signatures, and the geographic position of all signatures were found to be within 10 kilometers of a deep-water bottom feature, such as a seamount, submarine ridge, bank, or shelf. It was determined that on 67 percent of the occasions the Seasat SAR passed over the geographic location of a deep-water bottom feature, an internal wave pattern was present at that location. The corresponding figure for frontal boundary patterns was 28 percent.

A first-order hydrodynamic model was developed to explain the appearance of the Seasat SAR-observed surface patterns. These models indicate that the internal wave patterns are formed by lee-wave internal waves, which are generated as tidally-driven currents flow over the deep-water bottom features. The frontal boundary patterns were shown to be due to the upwelling of deeper water to intersect the surface layer. This upwelling is generated by tidal currents flowing against a deep-water bottom feature.

7. ACKNOWLEDGEMENTS

1199

8. REFERENCES

Alpers, W. and E. Salusti, Scylla and Charybdis Observed from Space, J. Geophys. Res., 88, pp. 1800-1808, 1983.

Apel, J.R., R.L. Charnell and R.J. Blackwell, Ocean Internal Waves Off the North American and African Coasts from ERTS-1, Proc. Ninth Int. Symp. Remote Sens. Environ., Ann Arbor, MI, pp. 1345-1354, 1974.

Apel, J.R., H.M. Byrne, J.R. Proni and R.L. Charnell, Observations of Oceanic Internal and Surface Waves from the Earth Resources Technology Satellite, J. Geophys. Res., 80, pp. 865-881, 1975.

Apel, J.R., J.R. Proni, H.M. Byrne, and R.L. Sellers, Near-Simultaneous Observations of Intermittent Internal Waves on the Continental Shelf from Ship and Spacecraft, Geophys. Res. Lett., 2, p. 128, 1975a.

Apel, J.R., H.M. Byrne, J.R. Proni, and R.L. Sellers, A Study of Oceanic Internal Waves Using Satellite Imagery and Ship Data, Remote Sensing of Environment, 5, p. 125, 1976.

Apel, J.R., Non-Linear Features of Internal Waves as Derived from the Seasat Imaging Radar, in Oceanography from Space, ed. by J.F.R. Gower, Plenum Press, New York, pp. 525-533, 1981.

Bainbridge, A.E., Geosecs Atlantic Expedition - Volume 2: Sections and Profiles, U.S. Government Printing Office, Washington, D.C., 198 pp., 1980.

Beal, R.C., P.S. DeLeonibus and I. Katz (eds.), Spaceborne Synthetic Aperture Radar for Oceanography, Johns Hopkins Univ. Press, Baltimore, MD, 215 pp., 1981.

Brown, W.E., Jr., C.E. Elachi and T.W. Thompson, Radar Imaging of Ocean Surface Patterns, J. Geophys. Res., 81, pp. 2657-2667, 1976.

Cheney, R.E., A Search for Cold Water Rings with Seasat, in Spaceborne Synthetic Aperture Radar for Oceanography, ed. by R.C. Beal, P.S. DeLeonibus and I. Katz, Johns Hopkins Univ. Press, Baltimore, MD, pp. 161-170, 1981.

Elachi, C. and J.R. Apel, Internal Wave Observations Made with Airborne Synthetic Aperture Imaging Radar, Geophys. Res. Lett., 3, p. 647, 1976.

Ford, J.P., J.B. Cimino, and C. Elachi, Space Shuttle Columbia Views the World with Imaging Radar: The SIR-A Experiment, JPL Publication 82-95, Pasadena, CA, 166 pp., 1983.

Fu, L. and B. Holt, Seasat Views Oceans and Sea Ice with Synthetic Aperture Radar, JPL Publication No. 81-120, 200 pp., 1982.

Gower, J.F.R. and B.A. Hughes, Radar and Ship Observations of Coastal Sea Surface Roughness Patterns in the Gulf of Georgia, Proc. Thirteenth Int. Symp. Remote Sens. Environ., Ann Arbor, MI, pp. 103- 115, 1979.

Gower, J.F.R. (ed.), Oceanography from Space, Plenum Press, New York, NY, 977 pp., 1981.

Hayes, R.M., SAR Detection of the Gulf Stream, in Spaceborne Synthetic Aperture Radar for Oceanography, ed. by R.C. Beal, P.S. DeLeonibus and I. Katz, Johns Hopkins Univ. Press, Baltimore, MD, pp. 146-160, 1981.

Holbrook, J.R., J.R. Apel, and J. Tsai, The Sulu Sea Internal Soliton Experiment, Part B: Observations and Analysis, J. Phys. Oceanogr. (in press), 1983.

Hughes, B.A. and J.F.R. Gower, SAR Imagery and Surface Truth Comparisons of Internal Waves in Georgia Strait, British Columbia, Canada, J. Geophys. Res., 88, pp. 1809-1824, 1983.

1200

Larson, T.R., L.I. Moskowitz and J.W. Wright, A Note on SAR Imagery of the Ocean, IEEE Trans. Antenna Propag., pp. 393-394, 1976.

Lichy, D.E., M.G. Mattie and L.J. Mancini, Tracking of a Warm Water Ring Using Synthetic Aperture Radar, in Spaceborne Synthetic Aperture Radar Imagery for Oceanography, ed. by R.C. Beal, P.S. DeLeonibus, and I. Katz, Johns Hopkins Univ. Press, Baltimore, MD, pp. 171-182, 1981.

Liu, A. K., Detection of Bottom Features on Seasat Synthetic Aperture Radar Imagery, Dynatech Report No. DT-8312-01, Torrance, CA, 45 pp., 1983.

Liu, A.K., J.R. Apel, and J.R. Holbrook, The Sulu Sea Experiment, Part C: Comparisons with Theory, J. Phys. Oceanogr. (in press), 1983.

Mattie, M.G., D.E. Lichy and R.C. Beal, Seasat Detection of Waves, Currents and Inlet Discharge, Int. J. Remote Sensing, 1, pp. 377-398, 1980.

Moskowitz, L.I., The Feasibility of Ocean Current Mapping via Synthetic Aperture Radar Methods, Proc. Amer. Soc. of Photogrammetry, Part II, pp. 760-771, 1973.

Osborne, A.R. and T.L. Burch, Internal Solitons in the Andaman Sea, Science, 208, pp. 451-460, 1980.

Raney, R.K., Synthetic Aperture Imaging Radar and Moving Targets, IEEE Trans. Aerospace Elect. Syst., AES-7, pp. 499-505, 1971.

Raney, R.K. and R.A. Shuchman, SAR Mechanism for Imaging Waves, Proc. Fifth Canadian Symp. on Remote Sensing, Victoria, B.C., 1978.

Roberts, D.G., P.M. Hunter, and A.S. Laughton, Bathymetry of the Northeast Atlantic: Continental Margin Around the British Isles, Deep-Sea Res., 26A, pp. 417-428, 1979.

Shemdin, O.H., The Marineland Experiment: An Overview, Trans. Amer. Geophys. Union, 61, No. 38, pp. 625-626, 1980.

Shemdin, O.H., A. Jain, S.V. Hsiao and L.W. Gatto, Inlet Current Measured with Seasat-1 Synthetic Aperture Radar, Shore and Beach, 48, pp. 35-39, 1980a.

Shuchman, R.A., Processing Synthetic Aperture Radar Data of Ocean Waves, Oceanography from Space, ed. by J.F.R. Gower, Plenum Press, New York, pp. 477-496, 1981.

Shuchman, R.A., P.L. Jackson and G.B. Feldkamp, Problems of Imaging Ocean Waves with Synthetic Aperture Radar, ERIM Interim Technical Report No. 124300-1-T, Ann Arbor, MI, 111 pp., 1977.

Shuchman, R.A. and E.S. Kasischke, The Detection of Oceanic Bottom Topographic Features Using SEASAT Synthetic Aperture Radar Imagery, Proc. Thirteenth Int. Symp. Remote Sens. Environ., pp. 1277-1292, 1979.

Shuchman, R.A., C.L. Rufenach, F.I. Gonzalez, and A. Klooster, The Feasibility of Measurement of Ocean Surface Currents Using Synthetic Aperture Radar, Proc. Thirteenth Int. Symp. Remote Sens. Environ., Ann Arbor, MI, pp. 93-102, 1979.

Shuchman, R.A., E.S. Kasischke and G.A. Meadows, Detection of Coastal Zone Environmental Conditions Using Synthetic Aperture Radar, 1981 International Geoscience and Remote Sensing Symposium Digest, Washington, D.C., pp. 756-767, 1981a.

Shuchman, R.A., A.L. Maffett and A. Klooster, Static Modeling of a SAR Imaged Ocean Scene, IEEE J. Oceanic Eng., OE-6,, pp. 41-49, 1981.

Shuchman, R.A., D.R. Lyzenga, and A. Klooster, Exploitation of SAR Data for Measurement of Ocean Currents and Wave Velocities, ERIM Report No. 137600-1-F, Environmental Research Institute of Michigan, Ann Arbor, 1981c.

1201

Trask, R.P. and M.G. Briscoe, Detection of Massachusetts Bay Internal Waves by the Synthetic Aperture Radar (SAR) on Seasat, J. Geophys. Res., 88, pp. 1789-1899, 1983.

Weissman, D.E., T.W. Thompson and R. Legeckis, Modulation of Sea Surface Radar Cross Section by Surface Stress: Wind Speed and Temperature Effects Across Gulf Stream, J. Geophys. Res., 85, pp. 5032-5042, 1980.

Wrignt, J.W., Backscattering from Capillary Waves with Application to Sea Clutter, IEEE Trans. Antenna Propagat., AP-14, pp. 749-754, 1966.

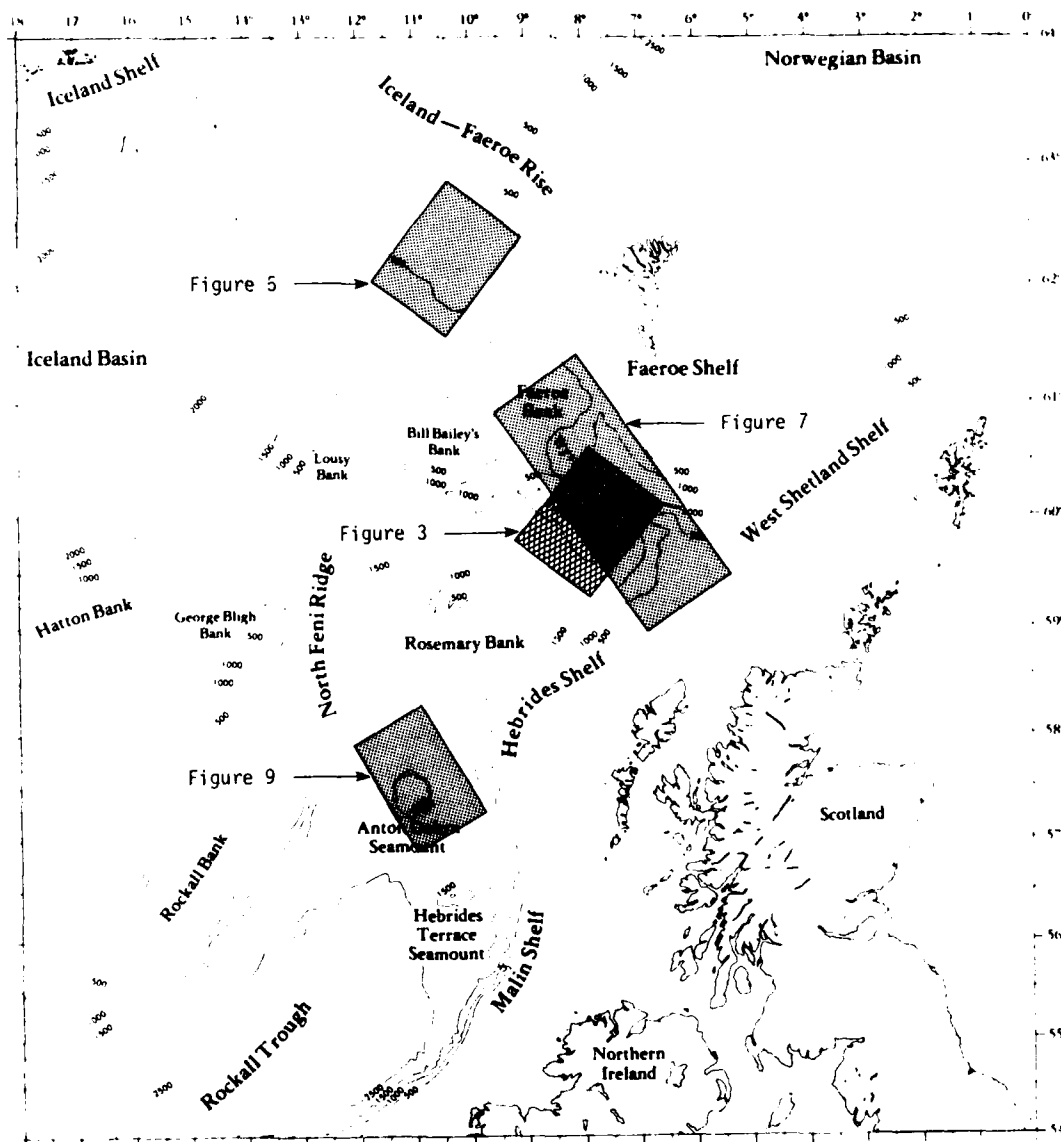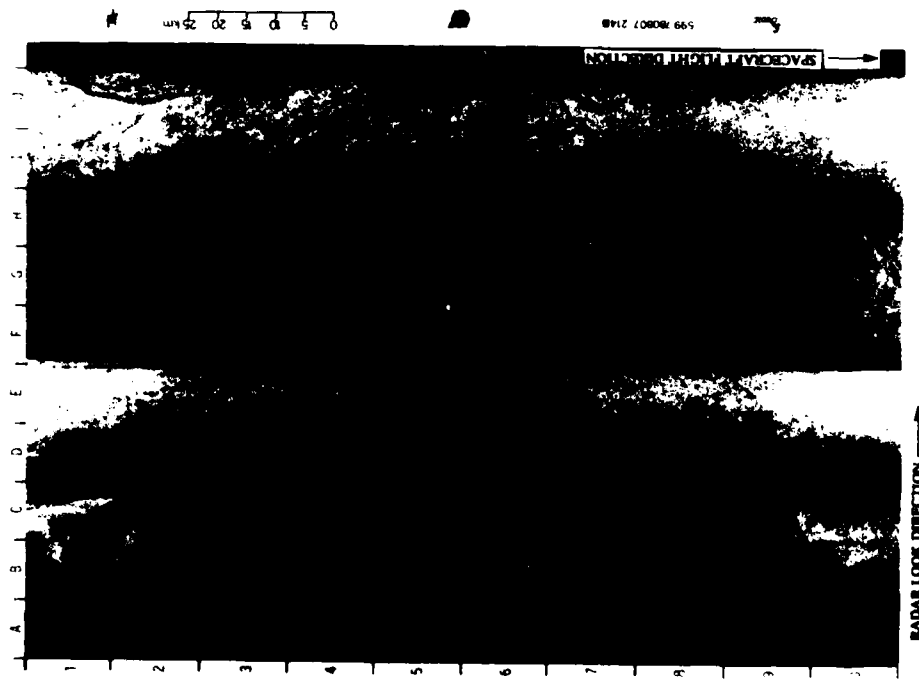Figure 1. Location of Major Bottom Features in Eastern North Atlantic and Positions of Seasat SAR Images
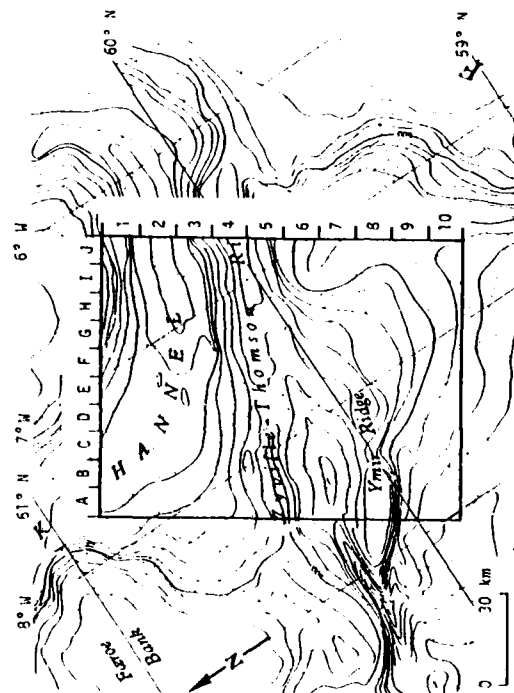
1202

Figure 3. Ground Coverage Corresponding to Seasat SAR Rev. 599. (After IOS Chart No. C6567, Contour Intervals in 100-Meter Increments.)
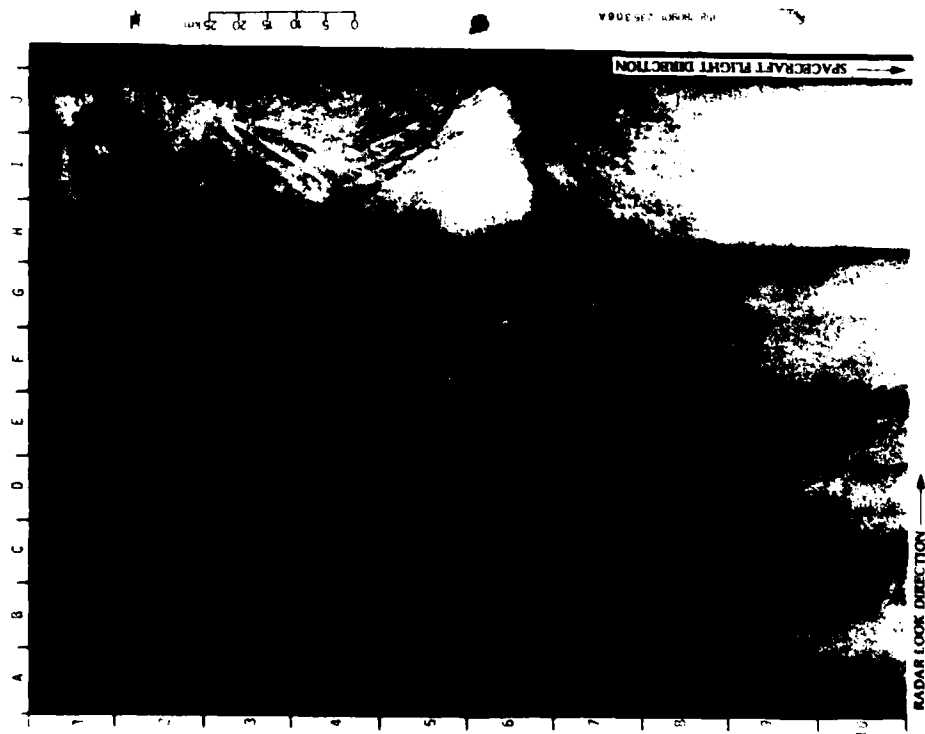

Figure 2. Seasat SAR Imagery Collected Over the Wyville-Thomson Ridge During Rev. 599
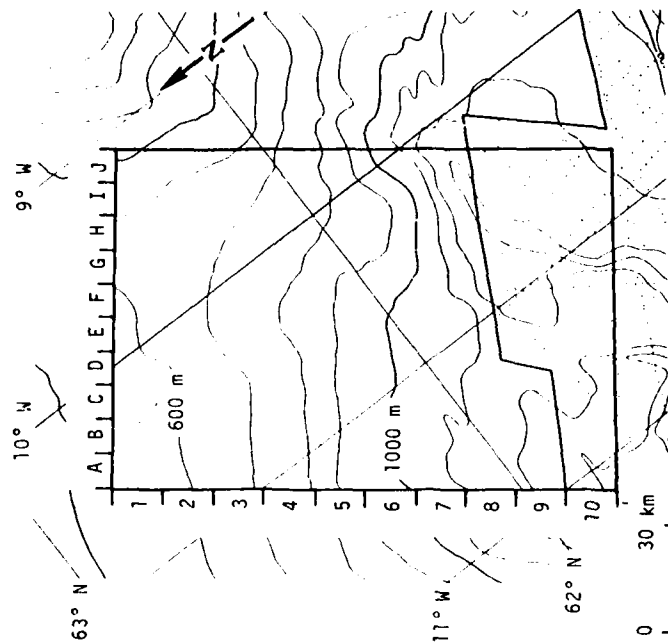
1203

C-45

Figure 5. Ground Coverage of Seasat Rev. 958 Over Iceland-Faeroe Rise. (After IOS Chart No. C6567, Depth Contours in 100-Meter Increments.)

Figure 4. Seasat SAR Imagery Collected Over the Iceland-Faeroe Rise During Rev. 958

1204

C-46

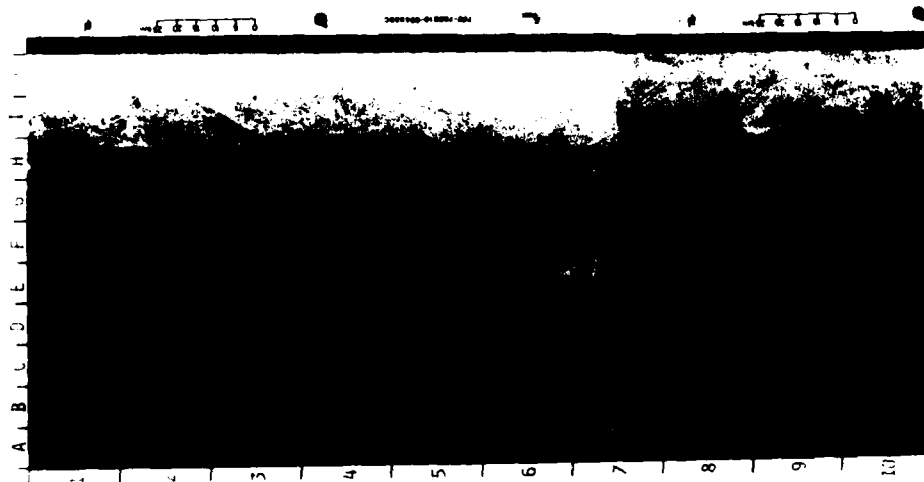Figure 7. Ground Coverage of Rev. 762 Over Wyville-Thomson Ridge. (After IOS Chart No. C6567, Depth Contours in Meters.)

Figure 6. Seasat SAR Imagery Collected Over Wyville-Thomson Ridge During Rev. 762

1205

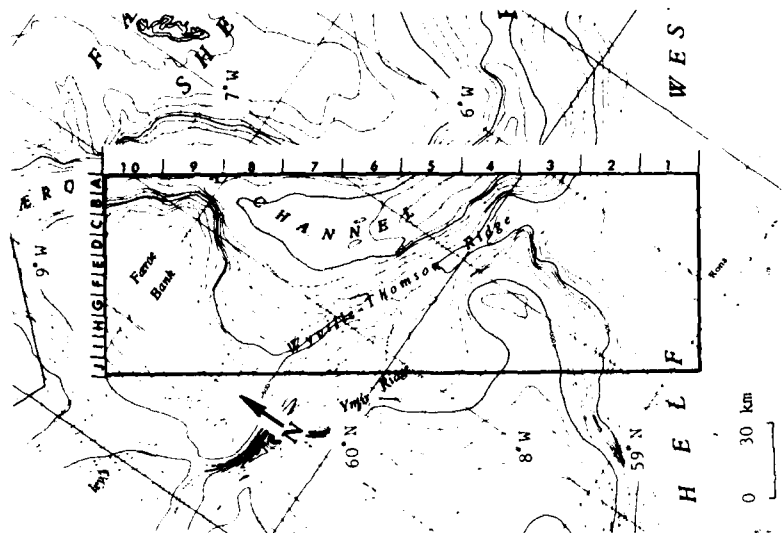Figure 9. Ground Coverage of Rev. 791 Over Anton Dohrn Seamount. (After IOS Chart No. C6567, Depth Contours in 100-Meter Increments.)
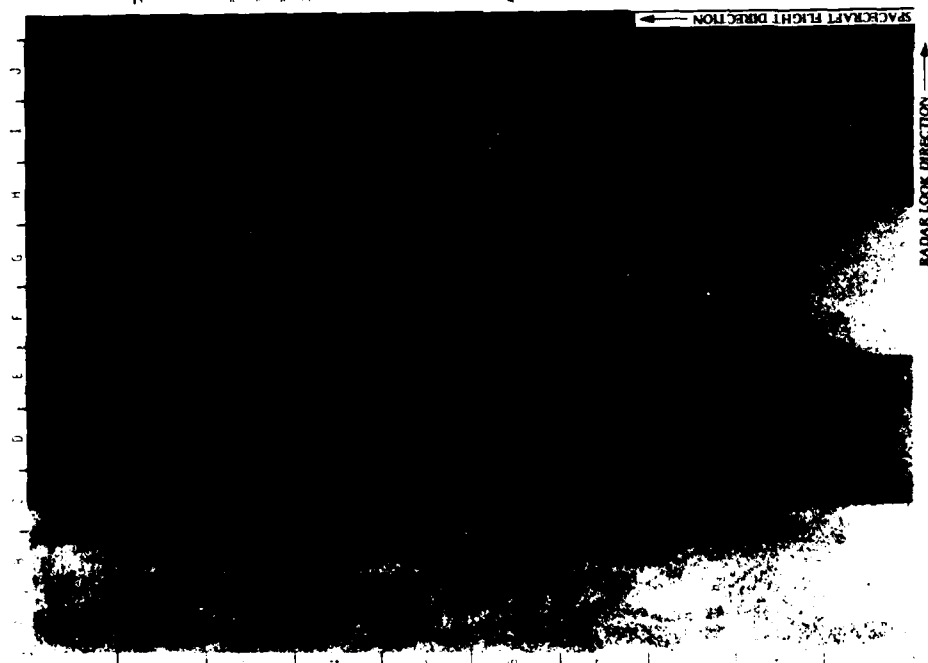
Figure 8. Seasat SAR Imagery Collected Over Anton Dohrn Seamount During Rev. 791

1206

C-48
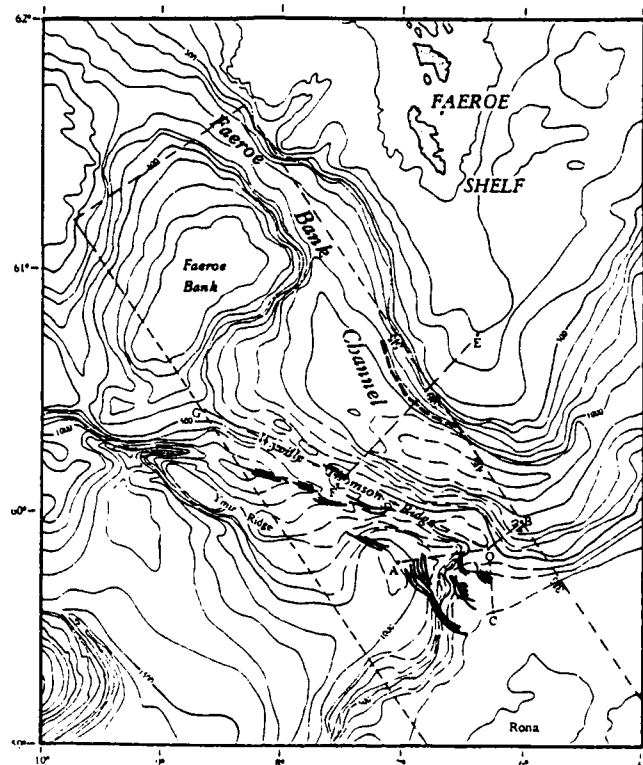
Figure 10. Line Drawings of Internal Waves and a Frontal Boundary Observed
in Figure 6 Superimposed on the Hydrographic Chart of the
Northeast Atlantic Ocean
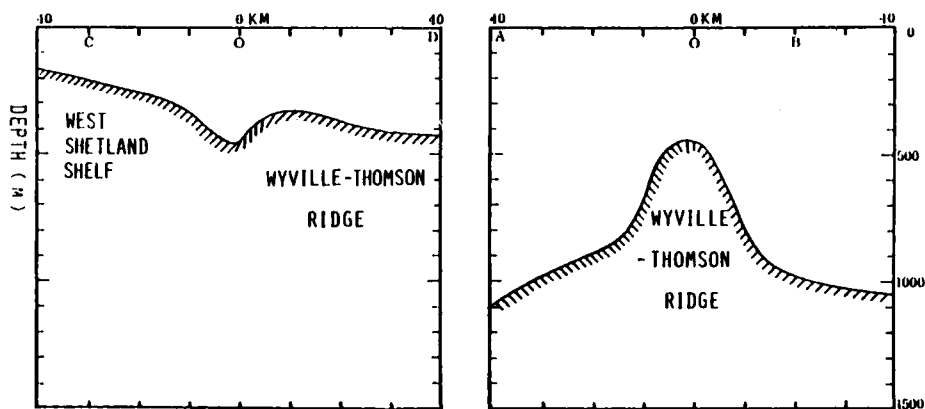
Figure 11. Longitudinal and Transverse Bathymetric Profiles Across Ridge,
with a Saddle-Like Valley at 0. Locations of Letters A, B, C,
D and 0 are Indicated in Figure 10.

1207

C-49
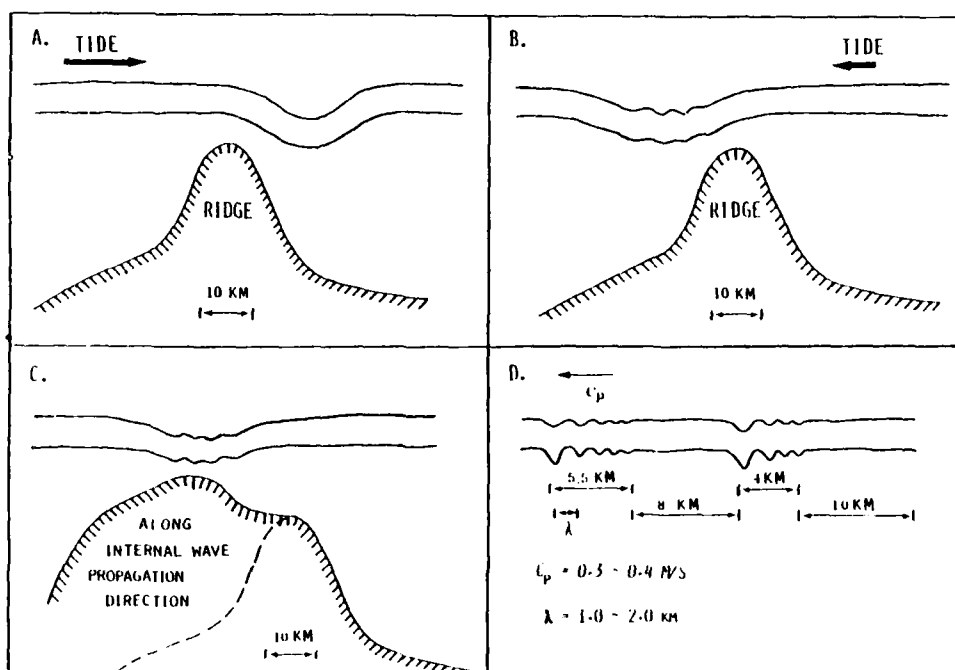
Figure 12. Schematic Diagram Summarizing the Generation and Evolution of an Internal Wave Packet Over the Wyville-Thomson Ridge

Figure 13. Profiles of Potential Temperature, Salinity and Sigma Theta From Data Collected Over the Icelandic-Faeroe Rise. (From Bainbridge, 1980)

1208

Figure 14.   Cross-Section Diagram of Bottom Topography of the Wyville-Thomson Ridge

Figure 15.   Schematic Diagram Illustrating Deep Water Upwelling Over the
Faeroe Bank Channel

1209

C-51

TABLE 1
SUMMARY OF SEASAT SAR PASSES COLLECTED OVER EASTERN NORTH ATLANTIC OCEAN

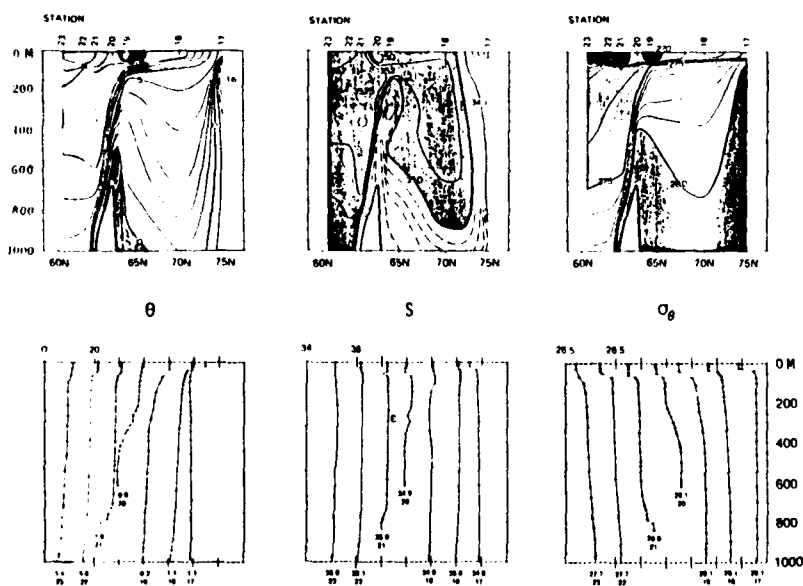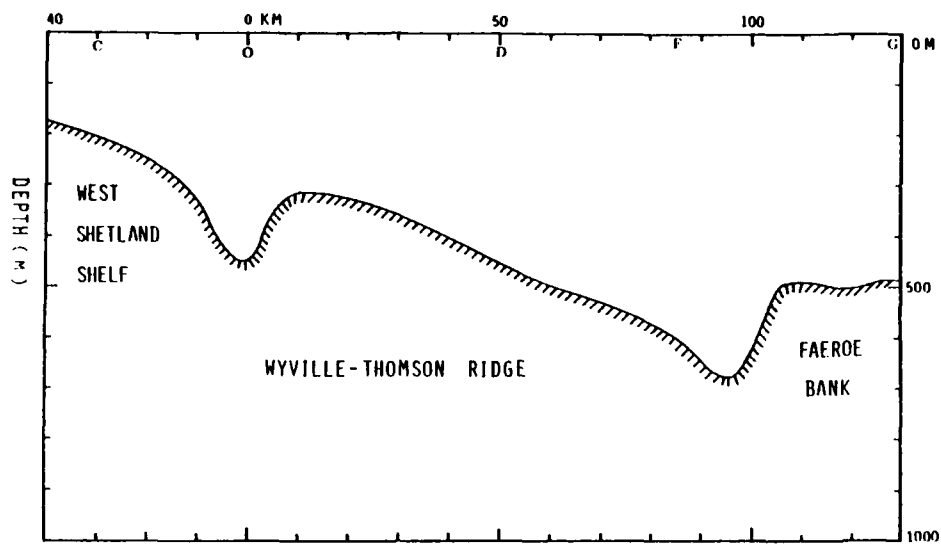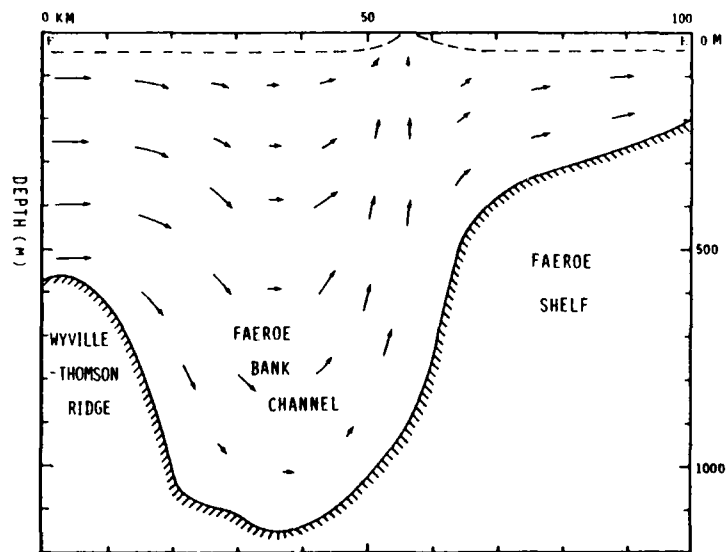| Seasat Revolution	Date	Time (GMT)
547	4 August 1978	06:15
556	4 August 1978	21:35
590	7 August 1978	06:20
599	7 August 1978	21:45
633	10 August 1978	06:30
642	10 August 1978	21:50
714	15 August 1978	22:35
719	16 August 1978	06:40
757	18 August 1978	22:40
762	19 August 1978	06:45
785	20 August 1978	21:40
791	21 August 1978	07:25
834	24 August 1978	07:30
958	1 September 1978	23:53
1006	5 September 1978	08:15
1044	8 September 1978	00:18
1049	8 September 1978	08:27
1087	10 September 1978	00:30
1149	15 September 1978	08:20
1307	26 September 1978	09:45
1359	30 September 1978	01:15

TABLE 2
BOTTOM TOPOGRAPHIC FEATURES IN THE NORTHEASTERN ATLANTIC

Bottom Feature	Shallowest Point (m)	Depth of Deep Water Adjacent (m)
Iceland-Faeroe Rise	300	1000
Bill Bailey's Bank	100	1200
Lousy Bank	300	1500
Hatton Bank	500	2000
George Bligh Bank	500	1100
Faeroe Bank	100	1000
Faeroe Shelf	300	1000
Wyville-Thomson Ridge	400	1200
Ymir Ridge	600	1500
North Feni Ridge	1200	2000
Rosemary Bank	500	2000
Rockall Bank	300	2300
Anton Dohrn Seamount	600	2100
West Shetland Shelf	300	1000
Malin Shelf	200	2000
Hebrides Terrace Seamount	1000	2400
Hebrides Shelf	200	1500
Iceland Continental Shelf	200	2000
Norway Contentinal Shelf	200	600
Ormonde Seamount	100	2500
Gettysburg Seamount	100	2500
Coral Patch Seamount	500	2500
Ampere Seamount	100	2500
Porcupine Bank	300	3000
Mid-Atlantic Ridge	700	1500
South Feni Ridge	2300	3000

1210

TABLE 3. SUMMARY OF OCCURRENCES OF BOTTOM-RELATED SURFACE PATTERNS
ON SEASAT SAR IMAGERY COLLECTED OVER THE NORTHEAST ATLANTIC

Bottom Feature Covered by Seasat SAR	SAR Revolution Number	SAR-Observed Pattern Internal Wave	SAR-Observed Pattern Frontal Boundary
Rockall Bank	547	X	
	556		X
	714	X	
	757	X	
	791	X	
	958	X	X
	1044		
	1087		X
Anton Dohrn Seamount	547	X	X
	556	X	
	599	X	
	791		
West Shetland Shelf	642	X	
	762	X	
	1359	X	
Malin Shelf	547		X
	633	X	
	791	X	
	834		
Hebrides Terrace Seamount	547	X	
	642	X	
	791		
Hebrides Shelf	590	X	
	599		
	633		
	642		
	719		
	762	X	
	834		X
	1006		X
	1049		
	1307		
Iceland-Faeroe Rise	719	X	
	762	X	X
	958	X	
	1044	X	X
	1087	X	
	1149	X	
Bill Bailey's Bank	719	X	X
	757		
	1006		X
	1044		
	1049	X	X
	1087	X	
	1307		
Lousy Bank	633	X	X
	590	X	
	791		X
	834	X	
	958	X	
	1006		
	1044	X	X
	1049	X	X
	1087	X	
Hatton Bank	547		
	791		X
	958		X
	1044	X	
George Bligh Bank	547	X	
	791		X
	958	X	
	1044	X	
	1087	X	
Faeroe Bank	556		X
	719		X
	757	X	X
	762	X	X
Faeroe Shelf	556		X
	599	X	X
	642	X	X
	714	X	
	757		
	762	X	X
	1149	X	
Wyville-Thomson Ridge	556	X	
	599	X	
	642		X
	719	X	
	757		
	762	X	X
Ymir Ridge	556	X	
	599	X	
	642	X	
	719	X	
	757	X	
	1049	X	

1211

TABLE 3. SUMMARY OF OCCURRENCES OF BOTTOM-RELATED SURFACE PATTERNS ON SEASAT SAR IMAGERY COLLECTED OVER THE NORTHEAST ATLANTIC (CONTINUED)

Bottom Feature Covered by Seasat SAR	SAR Revolution Number	SAR-Observed Pattern	
		Internal Wave	Frontal Boundary
North Feni Ridge	547	X	X
	556		X
	590	X	
	633		
	757		
	791	X	X
	834		
	1006	X	X
	1049		X
South Feni Ridge	556	X	
Rosemary Bank	556	X	
	599	X	
	633	X	X
	757		
	834	X	
	1006	X	X
	1049	X	
	1307		
Iceland Continental Shelf	547		
	590	X	
	633	X	
	719	X	
	762	X	
	791	X	
	834		
Norway Continental Shelf	556	X	
	599		
	757	X	
Ormonde Seamount	785	X	
Gettysburg Seamount	785	X	
Ampere Seamount	785		
Coral Patch Seamount	785	X	
Porcupine Bank	599	X	
	642	X	
Mid-Atlantic Ridge	556	X	
	599	X	
	642	X	
	714	X	
	757	X	

TABLE 4. SUMMARY OF DETECTIONS OF DEEP WATER TOPOGRAPHIC FEATURES BY SEASAT SAR IMAGERY USING DATA COLLECTED OVER THE NORTHEAST ATLANTIC

Seasat Revolution	Total Number of Deep-Water Bottom Features Covered	Total Number of Occurrences of Internal Waves Over Features	Total Number of Occurrences of Frontal Boundaries Over Features
547	8	6	3
556	11	7	4
590	4	4	0
599	9	6	1
633	6	4	2
642	8	6	3
714	3	3	0
719	7	5	2
757	10	5	1
762	7	7	4
785	4	2	0
791	9	5	4
834	6	3	0
958	5	4	2
1006	5	2	4
1044	6	4	2
1049	6	4	2
1087	5	4	1
1149	2	2	0
1307	3	0	0
1359	1	1	0
Total	125	84	35
Percent		67%	28%

1212